

Pallav Kumar Shrestha

**Toward accurate boundary conditions for
flood early warning systems with global
hydrology models in managed river
basins**

PHD DISSERTATION 5 | 2024

Helmholtz Centre for Environmental Research –UFZ
Department of Computational Hydrosystems

Toward Accurate Boundary Conditions for Flood Early Warning System with Global Hydrological Models in Managed River Basins

Pallav Kumar Shrestha

CUMULATIVE DISSERTATION

submitted in partial fulfilment of the academic degree of

“Doctor rerum Naturalium”

(Dr. rer. nat.)

in the scientific discipline “Hydrology”

Department of Geoecology
Faculty of Mathematics and Natural Sciences
Institute of Environmental Science and Geography
University of Potsdam

Potsdam, October 2024

This work is protected by copyright and/or related rights. You are free to use this work in any way that is permitted by the copyright and related rights legislation that applies to your use. For other uses you need to obtain permission from the rights-holder(s).

<https://rightsstatements.org/page/InC/1.0/?language=en>

FIRST SUPERVISOR:

Prof. Dr. Luis Samaniego

SECOND SUPERVISOR:

Prof. Dr. Sabine Attinger

MENTOR:

Dr. Martin Schrön

FIRST REVIEWER:

Prof. Dr. Sabine Attinger

SECOND REVIEWER:

Prof. Dr. Marc Bierkens

THIRD REVIEWER (INDEPENDENT):

Asso.-Prof. Dr. Shannon Sterling

EXAMINATION COMMITTEE MEMBERS:

Prof. Dr. Axel Bronstert

Prof. Dr. Luis Samaniego

Prof. Dr. Sabine Attinger

Prof. Dr. Marc Bierkens

Asso.-Prof. Dr. Shannon Sterling

Prof. Dr. Thorsten Wagener

Copyright ©2024 by Pallav Kumar Shrestha.

All rights reserved. No part of the material protected by this copyright notice may be reproduced or utilised in any form or by any means, electronic or mechanical, including photocopying, recording or by any information storage and retrieval system, without the prior permission of the author.

Toward Accurate Boundary Conditions for Flood Early Warning System with Global Hydrological Models in Managed River Basins / Pallav Kumar Shrestha

Helmholtz Centre for Environmental Research – UFZ

Printed in Germany.

Published online on the

Publication Server of the University of Potsdam:

<https://doi.org/10.25932/publishup-67838>

<https://nbn-resolving.org/urn:nbn:de:kobv:517-opus4-678385>

DECLARATION

I declare that the thesis has not been submitted to any other university and has been completed independently by me and only with the means indicated.

Leipzig, October 2024

Pallav Kumar Shrestha

For my mother and father

Today, one third of the world's people, mainly in least developed countries and small island developing states, are still not covered by early warning systems . . . This is unacceptable, particularly with climate impacts sure to get even worse. Early warnings and action save lives. To that end, today I announce the United Nations will spearhead new action to ensure every person on Earth is protected by early warning systems within five years.

— UN Secretary-General António Guterres on World Meteorological Day (2022)

ABSTRACT

Floods are one of the most prevalent natural disasters, impacting 55 millions lives yearly. Floods in small catchments have substantial implications, yet their risks and impacts remain difficult to predict using the state-of-the-art Global Hydrological Model (GHM)s and Flood Early Warning Systems (FEWS). This dissertation focuses on addressing these limitations by developing new methods to improve flood impact forecasting. Through the integration of improved large-scale streamflow modeling, machine learning, and real-time flood mapping, the research aims to enhance FEWS capabilities and make them more responsive to localized flooding events.

One key innovation explored in this research is the use of 2D hydrodynamic models to generate real-time flood inundation maps and impact indicators. Existing FEWS either interpolated flood hazard maps (e.g., Global Flood Awareness System (GloFAS), European Flood Awareness System (EFAS)) or relay only the local rainfall depths or gauge levels to the users. This results in inaccuracies for unprecedented extreme events in the first case and misinformed actions in the second. We demonstrate the feasibility of the ICON-D2-EPS-mHM-RIM2D operational FEWS for the 2021 European Summer Flood in the Ahr valley. Parallelized RIM2D high resolution flood inundation ensemble runs on GPUs reduce the total forecast runtime of the FEWS to under three hours. The FEWS forecasts lead time to specified inundation thresholds and at-risk infrastructure factoring in forecast uncertainty, which are crucial information for emergency response teams and policymakers.

Representation of catchment shape presents a unique challenge for GHMs. D8, arguably the most widely used method of catchment upscaling in GHMs, struggles to accurately represent catchment shapes smaller than 30 times the area of the grid pixel. This dissertation introduces a novel stream upscaling technique – Subgrid Catchment Contribution (SCC) – as a solution. SCC improves the accuracy of streamflow simulations by allowing multiple downstream connections within a single grid cell, thereby addressing the limitations of the widely-used D8 method, which only permits a single outflow direction per cell. This advancement in stream network upscaling significantly enhances the precision of modelled catchments, ensuring that even the smallest contributing areas are properly accounted for.

The effectiveness of SCC is demonstrated through experiments in the Rhine basin and at the global scale. In these experiments, SCC not only improves the accuracy of streamflow simulations but also offers up to a five-fold increase in computational efficiency compared to existing methods. This directly contributes to the real-time applications of FEWS, where speed and accuracy are paramount. Furthermore, SCC ensures accurate streamflow across modeling resolutions, eliminating the need for GHMs to reach sub-kilometer scales for streamflow precision. This, combined with the advantage that SCC can be integrated with

any land surface or hydrological model, significantly expands its use in global flood forecasting systems.

Small catchments have historically been under-served by global models but are often the location for catastrophic flood events. This research makes an important contribution by addressing the “catchment size problem”, a long-standing problem in GHMs where representation accuracy diminishes with smaller catchments. SCC improves the upscaling of catchment areas irrespective of catchment size, solving the catchment size problem entirely and allowing GHMs to deliver locally relevant streamflow at given points of interest. This represents a major opportunity in flood forecasting technology, allowing FEWS to rely on fluvial boundary conditions from a unified GHM setup for flood events at any scale, whether local or regional, eliminating the need for separate hydrological model setups and the associated resolution challenges.

The SCC method also offers a novel solution to the issue of simulating streamflow at multiple points of interest within a single grid cell. Current methods (e.g., D8) are limited to providing a single streamflow value per grid cell. The multiple downstream connectivity of SCC allows for a grid to have multiple routing fractions with the corresponding values, overcoming the limitation of single streamflow values within the same cell. This feature is especially important for regions with complex hydrological setting such as multiple tributaries, intricate river networks, dense networks of monitoring stations, or high density of reservoirs, where capturing the full scope of hydrological interactions is crucial for accurate streamflow predictions.

In addition to these advancements in catchment representation, the dissertation explores the use of Machine Learning (ML) to improve the simulation of streamflow downstream of regulated reservoirs. Reservoirs have the potential to introduce significant discontinuities in natural streamflow patterns. These discontinuities are often difficult to model using traditional hydrological approaches. The research presents a ML based method to predict non-consumptive demand at hydropower reservoirs based using downstream streamflow observations as control point. The ML demand model, when fed to the hydrological model, enables more precise simulation of daily streamflow downstream of 31 global reservoirs. This is particularly important for FEWS, as regulated rivers often pose significant forecasting challenges due to the variability in reservoir operations based on water demand. The improved simulations would allow FEWS to generate more accurate predictions, which can help mitigate flood risks in communities downstream of large/disruptive reservoirs. While the current focus of the ML model is on non-consumptive reservoirs, its methodology could be extended to consumptive uses like irrigation if reliable data is available.

Another novel aspect of this research is the investigation into the role of reservoir bathymetry, the underwater topography of reservoirs, on lake surface evaporation. Reservoirs contribute substantially to global evaporation, yet their shapes are often oversimplified in GHMs. The dissertation quantifies the impact of bathymetric assumptions on evaporation and streamflow predictions, finding that oversimplifications can lead to

significant overestimation of evaporation. A new function for estimating reservoir surface reflectivity based on latitude and the solar elevation angle is introduced, offering a more physically accurate approach to modeling reservoir evaporation dynamics in GHMs. These findings enhance the accuracy of evaporation estimates and improve upstream fluvial boundary conditions for FEWS to forecast downstream flood risks.

The final contribution of the dissertation addresses the computational challenges of large-scale hydrological modeling. Current global database includes 38 000 georeferenced dams. Simulating every reservoir in a large model domain is computationally expensive, so this study introduces a prioritization method based on reservoir “disruptivity” – the degree to which a reservoir alters natural streamflow patterns. By establishing thresholds for excluding less disruptive reservoirs from simulations, the dissertation offers a way to reduce computational costs while still maintaining accuracy in GHMs. This is particularly valuable for regional scale FEWS, where real-time forecasting requires a balance between precision and computational efficiency.

In summary, this dissertation makes significant contributions to the development of more accurate, efficient, and reliable flood forecasting systems. Through the integration of fast 2D hydrodynamic models, the introduction of the SCC method, and investigation of reservoir representation methods, the research enhances the capabilities of GHMs in generating fluvial boundary conditions in FEWS to forecast “flood impacts” in small catchments and regulated rivers. The advancements made in this dissertation offer transferable tools and methodologies that provide a foundation for future work in global hydrological modeling and flood forecasting and the opportunity to reduce flood impacts on communities worldwide.

ZUSAMMENFASSUNG

Überschwemmungen gehören zu den häufigsten Naturkatastrophen und betreffen jährlich 55 Millionen Menschen. Überschwemmungen in kleinen Einzugsgebieten haben erhebliche Auswirkungen, doch ihre Risiken und Folgen sind mit den modernsten globalen hydrologischen Modellen (GHMs) und Frühwarnsystemen für Überschwemmungen (FEWS) schwer vorherzusagen. Diese Dissertation befasst sich mit der Lösung dieser Einschränkungen durch die Entwicklung neuer Methoden zur Verbesserung der Vorhersage von Überschwemmungsauswirkungen. Durch die Integration von verbesserten großskaligen Abflussmodellen, maschinellem Lernen und Echtzeit-Überschwemmungskartierung zielt diese Forschung darauf ab, die Fähigkeiten von FEWS zu verbessern und sie reaktionfähiger auf lokale Überschwemmungsereignisse zu machen.

Eine zentrale Innovation, die in dieser Forschung untersucht wird, ist die Verwendung von 2D-hydrodynamischen Modellen zur Erstellung von Echtzeit-Überschwemmungskarten und Impact-Indikatoren. Bestehende FEWS interpolieren entweder Gefahrenkarten (z.B. GloFAS, EFAS) oder übermitteln den Nutzern lediglich die lokalen Niederschlagsmengen oder Pegelstände. Dies führt im ersten Fall zu Ungenauigkeiten bei beispiellosen Extremereignissen und im zweiten zu missinformierten Handlungen. Wir demonstrieren die Machbarkeit des operationellen FEWS ICON-D2-EPS-mHM-RIM2D für die europäische Sommerflut 2021 im Ahrtal. Parallelisierte hochauflösende Überschwemmungsläufe von RIM2D auf GPUs reduzieren die Gesamtlaufzeit der Vorhersage des FEWS auf unter drei Stunden. Die Vorhersagen des FEWS bieten Vorlaufzeiten bis zu bestimmten Überflutungsschwellen und gefährdeten Infrastrukturen unter Berücksichtigung von Prognoseunsicherheiten, diese sind wichtige Informationen für Notfallteams und Entscheidungsträger.

Die Darstellung der Einzugsgebietsform stellt eine besondere Herausforderung für GHMs dar. Das D8-Verfahren, das wohl am häufigsten verwendete Upscaling-Verfahren für Einzugsgebiete in GHMs, hat Schwierigkeiten, Einzugsgebietsformen abzubilden, die kleiner als 30-mal die Fläche des Rasterpixels sind. Diese Dissertation stellt eine neuartige Methode zur Skalierung von Flüssen vor, das Subgrid-Catchment-Contribution Verfahren (SCC). SCC verbessert die Genauigkeit der Abflusssimulationen, indem es mehrere Abflussverbindungen für eine Rasterzelle ermöglicht und so die Einschränkungen des weit verbreiteten D8-Verfahrens behebt, das nur eine einzige Abflussrichtung pro Zelle zulässt. Diese Weiterentwicklung in der Skalierung von Flussnetzen verbessert die Präzision der modellierten Einzugsgebiete erheblich und stellt sicher, dass auch die kleinsten beitragenden Flächen angemessen berücksichtigt werden.

Die Wirksamkeit von SCC wird durch Experimente im Rheineinzugsgebiet und im globalen Maßstab demonstriert. In diesen Experimenten verbessert SCC nicht nur die

Genauigkeit der Abflusssimulationen, sondern bietet auch eine bis zu fünfmal höhere Recheneffizienz im Vergleich zu bestehenden Methoden. Dies trägt direkt zu den Echtzeitanwendungen von FEWS bei, wo Geschwindigkeit und Genauigkeit von größter Bedeutung sind. Darüber hinaus stellt SCC sicher, dass der Abfluss unabhängig von der Modellierungsaufösung präzise ist, wodurch GHMs nicht auf Sub-Kilometerskalen operieren müssen, um genaue Abflussvorhersagen zu gewährleisten. Dies, zusammen mit dem Vorteil, dass SCC in jedes Landoberflächen- oder hydrologische Modell integriert werden kann, erweitert seine Anwendungsmöglichkeiten in globalen Hochwasservorhersagesystemen erheblich.

Kleine Einzugsgebiete wurden historisch gesehen von globalen Modellen vernachlässigt, sind jedoch oft Schauplatz katastrophaler Hochwasserereignisse. Diese Forschung leistet einen wichtigen Beitrag zur Lösung des „Einzugsgebietsgrößenproblems“, eines langjährigen Problems in GHMs, bei dem die Darstellung mit kleineren Einzugsgebieten an Genauigkeit verliert. SCC verbessert das Upscaling von Einzugsgebieten unabhängig von deren Größe und löst das Größenproblem vollständig, sodass GHMs lokale Abflüsse für bestimmte Punkte liefern können. Dies stellt eine bedeutende Chance für die Hochwasservorhersagetechnologie dar und ermöglicht es FEWS, auf fluviale Randbedingungen aus einer einheitlichen GHM-Konfiguration für Hochwasserereignisse jeder Größenordnung – ob lokal oder regional – zurückzugreifen, wodurch separate hydrologische Modellkonfigurationen und die damit verbundenen Auflösungsprobleme überflüssig werden.

Die SCC-Methode bietet auch eine neuartige Lösung für das Problem der Abflusssimulation an mehreren Interessenspunkten innerhalb einer einzigen Rasterzelle. Aktuelle Methoden (z.B. D8) sind auf die Bereitstellung eines einzigen Abflusswerts pro Rasterzelle beschränkt. Die Mehrfachverbindungen von SCC ermöglichen es einer Zelle, mehrere Abflussfraktionen mit den entsprechenden Werten zu haben, wodurch die Einschränkung eines einzigen Abflusswerts pro Zelle überwunden wird. Diese Funktion ist besonders wichtig für Regionen mit komplexen hydrologischen Gegebenheiten, bei denen es entscheidend ist, das gesamte Spektrum der hydrologischen Interaktionen für genaue Abflussvorhersagen zu erfassen. Solche sind zum Beispiel Regionen mit mehreren Nebenflüssen oder verzweigten Flussnetzen sowie solche mit einem dichten Netzwerk von Überwachungsstationen oder einer hohen Dichte an Stauseen.

Neben diesen Fortschritten in der Einzugsgebietsrepräsentation untersucht die Dissertation den Einsatz von maschinellem Lernen (ML) zur Verbesserung der Simulation von Abflüssen unterhalb regulierter Stauseen. Stauseen haben das Potenzial, erhebliche Diskontinuitäten in den natürlichen Abflussmustern zu verursachen. Diese Diskontinuitäten sind oft schwer mit traditionellen hydrologischen Ansätzen zu modellieren. Die Forschung stellt eine auf maschinellem Lernen basierende Methode zur Vorhersage des nicht-konsumptiven Bedarfs an Wasserkraftstauseen unter Verwendung von Abflussbeobachtungen als Kontrollpunkt vor. Das ML-Nachfragemodell ermöglicht es dem hydrologischen Modell, den täglichen Abfluss unterhalb von 31 globalen Stauseen ge-

nauer zu simulieren. Dies ist besonders wichtig für FEWS, da regulierte Flüsse aufgrund der Variabilität des Stauseebetriebs in Abhängigkeit vom Wasserbedarf häufig erhebliche Herausforderungen bei der Vorhersage darstellen. Die verbesserten Simulationen würden es FEWS ermöglichen, genauere Vorhersagen zu treffen, was dazu beitragen kann, Hochwasserrisiken für Gemeinschaften stromabwärts großer/ disruptiver Stauseen zu mindern. Während sich das aktuelle ML-Modell auf nicht-konsumptive Stauseen konzentriert, könnte seine Methodik auf konsumtive Nutzungen wie Bewässerung ausgeweitet werden, wenn zuverlässige Daten verfügbar sind.

Ein weiterer neuartiger Aspekt dieser Forschung ist die Untersuchung der Rolle der Stauseebathymetrie – der Unterwassertopographie der Stauseen – auf die Verdunstung an der Seeoberfläche. Stauseen tragen erheblich zur globalen Verdunstung bei, doch ihre Formen werden in GHMs oft stark vereinfacht dargestellt. Die Dissertation quantifiziert die Auswirkungen bathymetrischer Annahmen auf Verdunstungs- und Abflussvorhersagen und stellt fest, dass Vereinfachungen zu erheblichen Überschätzungen der Verdunstung führen können. Eine neue Funktion zur Abschätzung der Reflexivität der Stauseeoberfläche basierend auf Breitengrad und dem Sonnenhöhenwinkel wird eingeführt, die einen physikalisch genaueren Ansatz zur Modellierung der Verdunstungsdynamik von Stauseen in GHMs bietet. Diese Erkenntnisse verbessern die Genauigkeit der Verdunstungsschätzungen und optimieren die fluvialen Randbedingungen für FEWS, um Hochwasserrisiken stromabwärts besser vorhersagen zu können.

Der letzte Beitrag der Dissertation befasst sich mit den rechentechnischen Herausforderungen großskaliger hydrologischer Modellierung. Die aktuelle globale Datenbank enthält 38.000 georeferenzierte Staudämme. Da die Simulation jedes Stausees in einem großen Modellgebiet aufwendig ist, wird in dieser Studie eine Priorisierungsmethode eingeführt, die auf der „Disruptivität“ der Stauseen basiert, das heißt dem Ausmaß, in dem ein Stausee die natürlichen Abflussmuster verändert. Durch die Festlegung von Schwellenwerten für den Ausschluss weniger disruptiver Stauseen aus den Simulationen bietet die Dissertation einen Weg, die Rechenkosten zu senken und gleichzeitig die Genauigkeit in GHMs zu erhalten. Dies ist besonders wertvoll für regionale FEWS, bei denen die Echtzeitvorhersage ein Gleichgewicht zwischen Genauigkeit und Recheneffizienz erfordert.

Zusammenfassend leistet diese Dissertation bedeutende Beiträge zur Entwicklung genauerer, effizienterer und zuverlässigerer Hochwasservorhersagesysteme. Durch die Integration schneller 2D-hydrodynamischer Modelle, die Einführung der SCC-Methode und die Untersuchung von Methoden zur Stauseedarstellung verbessert die Forschung die Fähigkeiten von GHMs, FEWS für die Vorhersage von Hochwasserauswirkungen in kleinen Einzugsgebieten und regulierten Flüssen zu initialisieren. Die in dieser Dissertation erzielten Fortschritte liefern übertragbare Werkzeuge und Methoden, die die Grundlage für zukünftige Arbeiten in der globalen hydrologischen Modellierung und Hochwasservorhersage bilden und die Möglichkeit eröffnen, die Auswirkungen von Hochwasserereignissen auf globaler Ebene zu reduzieren.

Imagine yourself as a baby. You would look at that baby and think they lacked nothing. That baby came complete. Their value did not depend on external things like wealth or appearance or politics or popularity. It was the infinite value of human life. And that value stays with us, even as it becomes easier to forget it. We stay precisely as alive and precisely as human as we were the day we were born. The only thing we need is to exist. And to hope. — Matt Haig (2021)

ACKNOWLEDGMENTS

First and foremost I would like to pay tribute to my father Nirmal Kumar and mother Nirmal Prabha, my sculptors. Mom and Dad, your life decisions during my youth are directly responsible for where I stand today. This dissertation is merely a chapter of the project you started 37 years back.

I feel thankful and lucky to have the unconditional love of my wife, Srijana, during my PhD. Srijana, apart from being the muse of my life, you have also been the parachute of my PhD. Your compassion healed me whenever I fell from the PhD wall. My PhD journey wouldn't have been complete without your calming support.

I am grateful to my “Doctorvater”, my primary supervisor, Luis Samaniego. Thanks Luis, for taking me under your wing and teaching me the ways of persistence, rallying the team towards ambitious projects, fighting for us and supporting us through the thick and thin. Whenever I needed more time to reach my goals, you were always there with bountiful of faith and patience. Your championing of work quality over quantity guided my “scientific compass” throughout these years and will continue to do so in future. I am indebted for the time and energy you have invested on me, for being my scientific sculptor, for carving out the Dr. rer. nat. out of me. I also want to say thank you to Sabine Attinger, our department leader. Without Luis and Sabine's funding ideas, I would neither be compiling a PhD dissertation today nor have had met the prominent scientists of my field at international conferences. I would also like to thank Martin Schrön, my mentor, for inoculating me with PhD motivation whenever I needed it.

I will forever be thankful to Oldrich Rakovec, who took care of me like his younger brother from the day I landed in Germany. I am convinced that I can write a mini wikipedia based on the tips and tricks I learned from Olda regarding work as well as living in Leipzig. I consider myself privileged to have had mHM veterans Stephan Thober and Rohini Kumar as my collaborators. Developing the concept of SCC with Stephan and realizing the need for it during my discussions with Rohini are two of the most exciting research moments of my PhD. I would also like to thank Husain Najafi, my collaborator in the Ahr flood project. Brainstorming the figures for the Nature Communication paper with Husain was some of the most enjoyable hours I have spent on visualization ideas.

I would like to expend few sentences of appreciation to all the people with whom I have worked with at my department (CHS). CHS has helped me survive three tests of

time – the bureaucracy of Germany in my early PhD days, complications of reuniting with my wife during the pandemic, and when I briefly experienced depression in 2023. I am lucky to have worked at CHS, where I received helping hands and listening ears on countless occasions. I would also like to thank my colleagues, mainly Husain Najafi, Matthias Kelbling, and Ehsan Modiri, who took work off my shoulders facilitating the final push for the dissertation chequered flag. A special acknowledgment goes to Simon Lüdke for translating the abstract into German.

I've always believed that if there were best secretary award at UFZ, the team of our amazing secretaries would undoubtedly win. Sindy, Nora, and Catharina, kindly accept my words of gratitude for solving our problems year-in year-out, you are the best. I would also like to thank my (ex-) office mates, Estanis, Toma, Bahar, Robert, Simon, and Majid, for bearing with my habits and the noise of the keystrokes from my mechanical keyboard.

I am deeply indebted to the creators of the ecipy repository. Stephan and Matthias, your ecipy code has been worth its weight in gold and proved to be a timely blessing for my dissertation. I would also like to take this opportunity to thank WKDV, the IT support team at UFZ. WKDV tirelessly maintain and update the UFZ computer cluster infrastructure (EVE), like a well-oiled machine, which makes computer simulations based dissertations like mine possible. I owe special thanks to Toni Harzendorf and Robin Peters for their proactive support on all matters related to EVE and MacOS.

This document was typeset using the typographical look-and-feel classicthesis developed by André Miede and Ivo Pletikosić.

<https://bitbucket.org/amiede/classicthesis/>

CONTENTS

I Overarching Introduction

1 Introduction	3
1.1 A mythological perspective of floods	3
1.2 The socio-economy of floods since time immemorial	4
1.3 Impact based forecasting for FEWS	6
1.4 The elusive eagle vision in large scale streamflow modelling	7
1.5 (In-)accurate representation of reservoirs in large scale modeling	8
1.6 Subject of the dissertation	10
1.7 Structure of the dissertation and the research statements	11
1.8 Contribution to publications	13

II Publication Chapters

2 Impact-based early warning system for local floods	17
2.1 Introduction	17
2.2 Results	24
2.2.1 Ensemble precipitation and probabilistic water level forecasts	24
2.2.2 Comparison between the official and experimental water ...	26
2.2.3 Lead-time maps and impact-based warning	27
2.2.4 Enhancing Flood Forecast Communication for Informed ...	31
2.3 Discussion	31
2.4 Methods	34
2.4.1 Extended warning chain	34
2.4.2 Hydrological model setup and calibration	35
2.4.3 Computational resources and data requirements	36
2.4.4 Definition of forecast persistency	36
3 Integrating small catchments in global hydrological models	37
3.1 Introduction	37
3.2 Methods	43

3.2.1	mHM – the mesoscale Hydrological Model	43
3.2.2	SCC – a novel stream network upscaling scheme	44
3.2.3	Visualizing the advantages of the SCC scheme in a real case	48
3.2.4	Data and modeling procedure	48
3.2.5	Modeling domain and experiment design	50
3.3	Results and Discussion	52
3.3.1	Solving the “catchment size problem”	52
3.3.2	Error and performance regimes for D8	53
3.3.3	Improved scalability of streamflow simulations	56
3.3.4	Locally relevant streamflow simulations	58
3.3.5	Resolving multiple stations in a model grid	63
3.4	Conclusions and Outlook	65
4	Improved regulated streamflow in global hydrological models	69
4.1	Introduction	70
4.2	Methodology	80
4.2.1	Establishment of a Lake Module for mHM	80
4.2.2	Reservoir Water Balance	81
4.2.3	Estimating Non-consumptive Demand with a Surrogate Model	84
4.2.4	Demand Hedging	87
4.2.5	Estimating Reservoir Outflow Components	88
4.2.6	Reservoir Disruptivity	89
4.3	Experiment Design	91
4.3.1	Data and Setup	91
4.3.2	Modelling Procedure	93
4.3.3	Experiments	93
4.4	Results and Discussion	95
4.4.1	Performance Evaluation of mHM-LM and RF Model	95
4.4.2	Sensitivity of Reservoir Shape on Reservoir Simulations	100
4.4.3	Reservoir Disruptivity Analysis	107
4.5	Conclusions and Outlook	109
5	Synthesis and Outlook	113
5.1	Synthesis and conclusions	113
5.2	Outlook	116
5.3	The irony of myths: A final reflection	120

III Appendices

A Appendix A	125
A.1 Ensemble water level forecasts	125
A.2 Ensemble median - Without persistence	128
A.3 Ensemble Maximum - Without persistence	129
A.4 Forecasting Chain for the Impact-based FEWS	129
A.5 mHM Performance Evaluation	131
A.6 Persistency Map Schematics	132
A.7 Location Map	133
B Appendix B	135
B.1 Global distribution of data availability ...	135
B.2 Schematics of the resolution levels in mHM	137
B.3 Algorithms for upscaling the stream network with SCC	137
B.4 Routing flow using stream network upscaled by SCC	138
B.5 Equations for the benchmarks	139
B.6 Comparison of model upscaled catchment area with the GRDC ...	140
B.7 Additional figures for the scalability hypothesis	141
C Appendix C	143
c.1 Overall Algorithm for mHM-LM	143
c.2 Lake Module Parameters	144
c.3 Lake Evaporation	144
c.4 Reservoir Water Balance Solution	147
c.5 Random Forest based Prediction of Non-consumptive Demand	148
c.6 Routing of the Reservoir Outflow	148
c.7 Percolation from Reservoir Bottom	149
c.8 Water Balance for Aquifer Storage	150
c.9 Reservoir spill	150
c.10 Consumptive Water Use at Reservoir	151
c.11 Information on reservoirs used in the experiment	152
c.12 Data sources	154
c.13 Derivation of bathymetric relationships for half of pyramid ...	155

c.14 Performance evaluation at Tres Marias	157
c.15 Sensitivity of reservoir shape at Tres Marias	159
c.16 hV plots comparing the surveyed bathymetry to shape approximations	159
Bibliography	161

LIST OF FIGURES

Figure 1.1	Artistic representation of the “Descent of Ganga”	3
Figure 1.2	Giant current ripples formed by the Missoula Floods	4
Figure 1.3	Implications of natural disasters in the 21 st century	5
Figure 1.4	Global map of population exposed to flood risk	8
Figure 1.5	Overview of the dissertation subject	11
Figure 2.1	A holistic end-to-end impact-based flood forecasting modelling chain. The state-of-the-art flood early warning system is extended with components of quasi-real-time hydrodynamic and ...	20
Figure 2.2	Ensemble of precipitation and water level forecasts from the Icosahedral Nonhydrostatic (model) (ICON)_D2_EPS-mesoscale Hydrologic Model (mHM) chain. Ensemble ...	25
Figure 2.3	The maximum flood lead-time warning based on the ICON_D2_EPS-mHM-Raster-based Inundation Model 2D (RIM2D) FEWS chain. A maximum lead-time raster-based flood warning map is ...	28
Figure 2.4	Uncertainty representation of the forecasted inundated area downstream of the Altenahr gauge. Uncertainty is quantified ...	32
Figure 3.1	Genealogy of stream network upscaling methods in hydrological modeling. Double Maximum Method (DMM) – double maximum method, Cell Outlet Tracing with an Area Threshold (COTAT) – cell outlet tracing with ...	41
Figure 3.2	Schematic representation illustrating the differences between the Directions of a grid to its Eight neighbors (D8) and SCC stream ...	45
Figure 3.3	Example showing upscaling of subgrid streamflow (skyblue lines) to model streamflow network (black arrows) using SCC. (a-d) delineation of catchment ...	47
Figure 3.4	Hengduan Mountains at one degree resolution, with the Irrawady, Salaween, Mekong, and Yangtze rivers running parallel to each other. Comparison of ...	49

- Figure 3.5 a) The global scale experiment domain comprising of 62 hydrological domains and 5 256 streamflow stations. b) The regional scale experiment ... 51
- Figure 3.6 Scatterplots of input catchment area on x-axis and modeled catchment area on y-axis evaluating performance of (a) Flexible LOcation of Waterways (FLOW), (b) Döll and Lehner (2002), and ... 54
- Figure 3.7 D8 catchment area error regimes as a function of the Digital Elevation Model (DEM) based catchment area (A_d) and the model resolution size (A_g). The area ... 55
- Figure 3.8 (a) Performance improvement regimes, on replacement of D8 with SCC, as a function of the DEM based catchment area (A_d) and the model resolution size (A_g). The ... 55
- Figure 3.9 CDFs comparing streamflow performance across 1 km to 100 km model resolutions, and subgrid stream network upscaling using SCC and D8, for the regional experiment. (a) CDFs of ... 57
- Figure 3.10 Hydrographs resulting from the upscaling of subgrid stream network to 6 km employing SCC and D8. The catchment areas of the selected locations ... 59
- Figure 3.11 Comparison of daily model performance at 5 256 streamflow station catchments, worldwide, with subgrid stream networks up-scaled to 25 km using ... 61
- Figure 3.12 Comparison of computational cost (x-axis) among SCC, multi-domain D8, and single-domain D8, showing variation with number of streamflow stations ... 63
- Figure 3.13 Map of the Rhine basin showing 187 stations (red dots), their corresponding catchments, and the 25 km modeling grid. The bar plots, beneath ... 64
- Figure 4.1 (a) Computational grid map of Três Marias reservoir (as an example) in mHM-Lake Module (LM) showing the delineated reservoir lake, reservoir catchment, lake inlet nodes ... 82
- Figure 4.2 (a) Global map showing the geographical distribution of $n = 31$ reservoirs considered for the experiment. Red dots ... 91
- Figure 4.3 Schematics of bathymetry approximations for rectangular prism (Linear), half-pyramid (Liebe et al., 2005 (L2005)), and Reservoir Geometry dataset (ReGeom) shapes (Yigzaw et al., 2018 (Y2018)) 94

Figure 4.4	mHM-LM prediction efficiency at the Rappbode reservoir compared against observed streamflow. (a) mHM without dam (N), (b) $Q^{d,RF}$ fitted ...	96
Figure 4.5	CDFs depicting the streamflow performance at downstream gauges ($n = 31$, F-reservoirs) with LM and mHM parameters optimized (M), only LM parameters ...	98
Figure 4.6	Comparison of the mean annual values of M^0 and M simulations for (a) runoff at the location of gauge downstream of the reservoir, and (b) aET from the ...	99
Figure 4.7	Sensitivity of the reservoir shape on streamflow, volume, elevation, surface area and evaporation at the ...	100
Figure 4.8	hA plots comparing the surveyed bathymetry to Y_{2018} , L_{2005} and Linear shape approximations at (a) H-reservoirs, and (b) 88 Texan reservoirs. The ...	102
Figure 4.9	Comparison of surveyed and Global Reservoirs and Dam database (GRanD) (v1.3) values of (a) reservoir surface area at full capacity (A_f), and reservoir capacity (V_f) at 88 Texan reservoirs. The ...	104
Figure 4.10	Cumulative distribution functions of the mHM lake module performance in 31 reservoirs (F) using two distinct reservoir shape approximations (Y_{2018} and linear V-h). The ...	105
Figure 4.11	(a) Barplot depicting the ratio of mean annual evaporation using L_{2005} shape approximation (\bar{E}_{2005}) to reservoir capacity (V_f). Larger the ...	106
Figure 4.12	Scatterplots between (a) Amended Annual Proportional Flow Deviation (AAPFD) vs c , (b) AAPFD vs c' , and (c) c vs c' . Dark blue dots in (a), (b) and (c) are the F-reservoirs, light ...	108
Figure 5.1	A screenshot of Windy.com	121
Figure 5.2	The “Descent of Ganga” in the 21 st century	122
Figure A.1	Ensemble water level forecasts ($n=20$) at gauge Altenahr for 16 initialisations between July 13, 2021 (02 Central European Summer Time (CEST)) and ...	126
Figure A.2	Raster-based lead-time map of water level downstream Altenahr gauge exceeding 100 years return period flood (HQ ₁₀₀) levels based on ensemble median from ICON_D2_EPS-mHM-RIM2D ...	128
Figure A.3	Raster-based lead-time map of water level downstream Altenahr gauge exceeding HQ ₁₀₀ levels based on ...	129

Figure A.4	Schematic of the ICON_D2_EPS-mHM-RIM2D flood warning chain. Data ...	130
Figure A.5	Time series of streamflow simulations and observation at (a) hourly, (b) daily, (c) monthly time step for the Altenahr gauge. Monthly climatology is ...	131
Figure A.6	(a) Raster-based inundation forecast and water level shown for three forecast initialisations for a given pixel (b) Definition of maximum lead-time ...	132
Figure A.7	Topographic map of the Ahr catchment	133
Figure B.1	Attributes of 5 256 streamflow stations of the global experiment. (a) Temporal extent of daily time series streamflow ...	136
Figure B.2	Resolution levels used in mHM with two possible cases between ℓ_1 and ℓ_{11} . Note that there is ...	137
Figure B.3	Scatterplots of Global River Discharge Centre (GRDC)/Centro de Estudios y Experimentación de Obras Públicas (CEDEX) reference area (A_r) on x-axis and model upscaled catchment area (\hat{A}) on ...	140
Figure B.4	CDFs comparing streamflow performance across 25 km to 100 km model resolutions, and subgrid stream network upscaling using SCC and D8, for the ...	141
Figure B.5	Hydrographs resulting from SCC and D8 across 1 km to 100 km model resolutions at three different streamflow stations in the Rhine: ...	142
Figure C.1	Albedo of still water for reservoir evaporation. Grishchenko measurements taken from Cogley (1979)	146
Figure C.2	Percolation in mHM	150
Figure C.3	Schematics for half pyramid	155
Figure C.4	Performance evaluation of RF and mHM simulations at Três Marias reservoir. Rows 1 to 3 show ...	157
Figure C.5	Sensitivity of reservoir shape on streamflow, volume, elevation, surface area and evaporation for Três Marias reservoir.	158
Figure C.6	hV plots comparing the surveyed bathymetry to Y_{2018} , L_{2005} and Linear shape approximations at (a) H-reservoirs, and (b) 88 Texan reservoirs. The ...	160

LIST OF TABLES

Table 1.1	Selected notable small catchment floods of the 21 st century	9
Table 2.1	Existing State-of-the-Art FEWS around the World	21
Table 2.2	Comparison of impact-based forecasted damages to buildings, railways, and roads to benchmark. A 100% percentage indicates that the damage ...	30
Table 3.1	A non-exhaustive list comparing the stream network representation of recent studies assessing streamflow hydrology at large scale	39
Table 4.1	Comparison with the state-of-the-art of reservoir representation	76
Table 4.2	Predictors used in constructing random forest model for estimating non-consumptive demand at reservoirs ...	86
Table C.1	Parameters of LM	144

LIST OF ALGORITHMS

Algorithm 1	Delineation of basins at points of interest	137
Algorithm 2	Node initialisation	138
Algorithm 3	Setting the upscaled stream network	138
Algorithm 4	Streamflow routing	139
Algorithm 5	Overall Algorithm for mHM-LM	143
Algorithm 6	Reservoir Water Balance Solution	147
Algorithm 7	Random Forest based Prediction of Non-consumptive Demand	149

DEFINITION OF KEY TERMS

Lead time to exceed 100-yr flood

The return period HQ₁₀₀, or 100-year return period flood, refers to a statistical estimate of the frequency at which a certain flow magnitude (discharge) is expected to be equaled or exceeded on average once every 100 years. Lead time to exceed 100-yr flood is the time remaining for the water level at a particular location to exceed the water level corresponding to HQ₁₀₀. Greater the lead time the more time there is for evacuation.

Impact based flood forecasts

An eminent flood event inundates the flood plains, which may impact infrastructure such as (residential) buildings, roads, railways, etc. Prediction of flood outcomes as maps, continuous in space (i.e., 2D), is intuitive and are called impact based forecasts. In comparison, the traditional flood forecasting only includes forecasting of water level at an observation gauge upstream of an area of interest. Inferring impacts to area of interest from such point forecast has been found to be non-intuitive, hence the need of impact based flood forecasts.

Hydrodynamic modeling

Hydrodynamic modeling is the numerical simulation of water movement in natural or engineered environments based on fluid dynamics principles. It aims to predict the spatiotemporal behavior of water flow, such as water levels, velocities, and discharges, under varying boundary and forcing conditions. The Saint-Venant equations, a depth-averaged, simplified form of the Navier-Stokes equations, are the core mathematical foundation of hydrodynamic modeling, especially for surface water systems (rivers, floodplains, canals).

Fluvial boundary conditions

To simulate riverine floods using a hydrodynamic (inundation) model, it is essential to define the fluvial boundary conditions, which specify the volume of water entering the modeling domain. These conditions are typically provided as discharge time series at upstream or lateral inflow points and can be derived from observed streamflow data or simulated outputs from hydrological models. Accurate specification of fluvial

boundary conditions is critical for representing the timing, magnitude, extent, and depth of inundation, and directly affects the reliability of the model's flood predictions.

Forecast persistency

Operational flood early warning systems (FEWS) provide instances of forecasts at a particular interval in time. Exceedance of an impact criteria, say 100 year return period flood water level, by consecutive forecast instances is valuable for decision-making in situations where reliability is prioritized over lead time. Forecast persistency is the count of the consecutive forecast hits, and helps to quantify the uncertainty in the forecasting system.

Disruptivity index

Not all reservoirs are built the same or in the same hydrological and geographical context. Their influence on the natural streamflow regime varies significantly depending on factors such as storage capacity, the draining catchment, and operational rules. Therefore, quantifying a reservoir's potential to alter the natural flow patterns of the river it regulates is useful, and the metrics that quantify this potential are disruptivity indices.

ACRONYMS

AAPFD	Amended Annual Proportional Flow Deviation
ACCESS	Australian Community Climate and Earth-System Simulator
AHPS	Advanced Hydrologic Prediction Service
AT	Austria
AWIPS	Advanced Weather Interactive Processing System
BUEK ₂₀₀	Bodenübersichtskarte 1:200,000
C ₃ S	Copernicus Climate Change Service
CamaFlood	Catchment-based Macro-scale Floodplain model
CDF	Cummulative Distribution Function
CEDEX	Centro de Estudios y Experimentación de Obras Públicas
CEMS	Copernicus Emergency Management Service
CEST	Central European Summer Time

CH	Switzerland
CHPS	Community Hydrologic Prediction System
CLM	Community Land Model
CLSM	Catchment Land Surface Model
CMIP6	Intercomparison Project 6
COTAT	Cell Outlet Tracing with an Area Threshold
COSMO	Consortium for Small-scale Modeling
CWatM	Community Water Model
CYGNSS	Cyclone Global Navigation Satellite System
D8	Directions of a grid to its Eight neighbors
DBH	Distributed Biosphere-Hydrological model
DCL	Dam Crest Level
DE	Germany
DDS	Dynamically Dimensioned Search
DEM	Digital Elevation Model
DHVSM	Distributed Hydrology Vegetation Soil Model
DMM	Double Maximum Method
DROP	Dynamic Routing of Overland Flow and Pooling
DRT	Dominant River Tracing
DTM	Digital Terrain Model
DWD	Deutscher Wetterdienst
EAM	Effective Area Method
ecFlow	ECMWF's workflow management system
ECMWF	European Centre for Medium-Range Weather Forecasts
EDK	External Drift Krigging
EFAS	European Flood Awareness System
EMS	Emergency Management Service
EPS	Ensemble Prediction System
FEWS	Flood Early Warning Systems
FLOW	Flexible LOcation of Waterways
FR	France
FUNCEME	Fundação Cearense de Meteorologia e Recursos Hídricos

GADM	Global Administrative Areas database
GHM	Global Hydrological Model
GIS	Geographical Information System
GLDAS	Global Land Data Assimilation System
GLiM	Global Lithological Map
GLOBathy	Global Reservoir Bathymetry dataset
GloFAS	Global Flood Awareness System
GLDAS	Global Land Data Assimilation System
GFM	Global Flood Map
GIMMS	Global Inventory Modeling and Mapping Studies
GMLZ	Geoinformation und Monitoring bei Landnutzung und Zivil- und Katastrophenschutz
GMTED	Global Multi-resolution Terrain Elevation Data
GR4J	Génie Rural à 4 paramètres Journalier
GRanD	Global Reservoirs and Dam database
GRDC	Global River Discharge Centre
GPU	Graphics Processing Unit
hAV	Elevation Area Volume
HD-Model	Hydrological discharge model
HEFS	Hydrologic Ensemble Forecast Service
HM	Hydrological Model
HQ ₁₀₀	100 years return period flood
HQ ₅₀	50 years return period flood
HQ _{extreme}	the most extreme scenario of the flood
HTESSSEL	Hydrology Tiled ECMWF Scheme for Surface Exchanges over Land
HydroSHEDS	Hydrological Data and Maps Based on Shuttle Elevation Derivatives at Multiple Scales
HYDRA	Hydrological Routing Algorithm
HyFS	Hydrologic Forecasting System
HYPERstream	HighLY Parallelizable and scalable Routing scheme
ICON	Icosahedral Nonhydrostatic (model)
ICON-D ₂	Icosahedral Nonhydrostatic - 2 km resolution model for Germany

IFS	Integrated Forecast System
IHU	Iterative Hydrography Upscaling
KGE	Kling-Gupta Efficiency
L2005	Liebe et al., 2005
LARSIM	Large Area Runoff Simulation Model
LEPS	Limited Area Ensemble Prediction System
LfU	Landesamt für Umwelt
LHFD	Large-Scale Hydrological and Fluvial Dynamics
LM	Lake Module
LPJmL	Lund-Potsdam-Jena managed Land model
LSM	Land Surface Model
MATSIRO	Minimal Advanced Treatments of Surface Interaction and Runoff
ME	Model Efficiency
MERIT	Multi-Error-Removed Improved-Terrain
MESH	Modélisation Environnementale Communautaire - Surface and Hydrology
ML	Machine Learning
MOZART	Model for Scale Adaptive River Transport
MPI-HM	Max Planck Institute Hydrological Model
MPR	Multiscale Parameter Regionalization
mHM	mesoscale Hydrologic Model
mRM	multiscale Routing Model
NL	The Netherlands
NRMSE	Normalized Root Mean Square Error
NSE	Nash-Sutcliffe Efficiency
NWP	Numerical Weather Prediction
ODbL	Open Database License
ORCHIDEE	Organising Carbon and Hydrology In Dynamic Ecosystems
OSM	OpenStreetMap
PDM	Probability Distributed Model
PCR-GLOBWB	PCRaster Global Water Balance model
PET	Potential Evapotranspiration

RAPID	Routing Application for Parallel computation of Discharge
RADOLAN	Radar Online Aneichung
ReGeom	Reservoir Geometry dataset
RF	Random Forest
RIM2D	Raster-based Inundation Model 2D
RMSE	Root Mean Square Error
RP	Rhineland-Palatinate
S2023	Sadki et al. (2023)
SAR	Synthetic Aperture Radar
SCC	Subgrid Catchment Contribution
SPHY	Spatial Processes in HYdrology
SWAT	Soil and Water Assessment Tool
TRIP	Total Runoff Integrating Pathways
TRL	Technology Readiness Level
ULYSSES	mULTi-model hYdrological SeaSonal prEdictionS system
URBS	Unified River Basin Simulator
VIC	Variable Infiltration Capacity
WaterGAP	Water - Global Assessment and Prognosis model
WBM	Water Balance Model
WL	Water Level
WMO	World Meteorological Organization
WUR	Wageningen University and Research
Y2018	Yigzaw et al., 2018

Part I

OVERARCHING INTRODUCTION

INTRODUCTION

1.1 A MYTHOLOGICAL PERSPECTIVE OF FLOODS

The Ganges River, or Ganga, is held in high regard in Hindu mythology, particularly in the context of floods. According to the *Ramayana*, an ancient hindu text, Ganga was a celestial river residing in the heavens. King Bhagiratha performed intense penance to bring Ganga down from the heavens to earth to purify the ashes of his ancestors. However, the force of Ganga descending from the heavens would have been catastrophic, causing a widespread flood on earth. Bhagiratha sought help of Lord Shiva, who with his immense power, caught Ganga in his matted hair, controlling her mighty flow, slowing her descent. This act by Shiva ensured that Ganga could fulfill her purpose of purifying the earth without causing destruction (Figure 1.1).

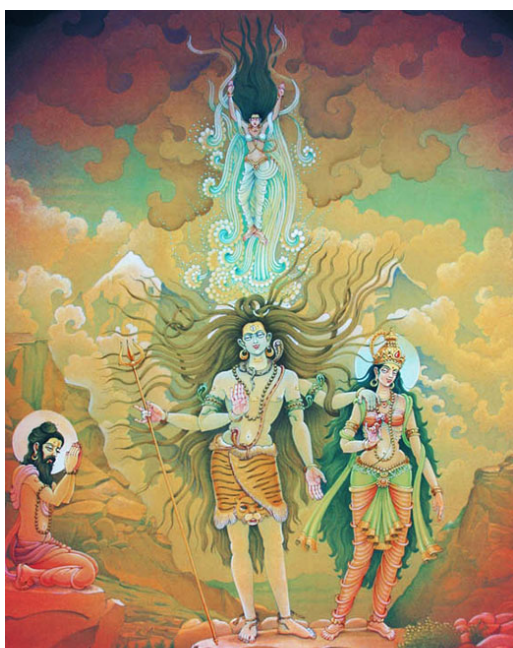


Figure 1.1: Artistic representation of the “Descent of Ganga” featuring Shiva (middle), Ganga (top), and King Bhagiratha (left). (source: <https://blog.sagarworld.com/itihaas/>)

Floods in mythology not only symbolize physical destruction but also serve as metaphors for the emotional and spiritual turmoils we face. In spiritual traditions, water often represents the subconscious mind, and floods signify the overwhelming surge of suppressed emotions or unresolved issues. Just as Shiva tamed the powerful Ganga, we are reminded of the need to control and channel our emotions constructively.

The “Descent of Ganga” also offers a compelling parallel to modern humanity’s efforts to manage and control floods. Just as Shiva subdued the mighty Ganga, carefully channeling her powerful flow, transforming chaos into calm, contemporary societies construct dams and other infrastructures to regulate river flows and mitigate seasonal flooding. Just as the gods foresaw the potential catastrophic impact of Ganga’s descent, modern FEWS stand at the forefront of humanity’s defence against floods.

1.2 THE SOCIO-ECONOMY OF FLOODS SINCE TIME IMMEMORIAL

Long before human civilization took root, the Earth experienced cataclysmic floods that shaped its geology and topography. One of the most dramatic of such ancient floods took place in North America circa 13 000 BCE. The Missoula Floods, triggered by the breach of ice dams holding back glacial lakes, created the Channeled Scablands of Washington state, characterized by deep channels, and massive erosion patterns through basalt deposits (Bretz, 1923), some of which were up to 15 m tall (Baker, 2009) (Figure 1.2). The corresponding flow rate of the flood is estimated to have been ten times the flow of all current rivers combined (Bjornstad, 2006).



Figure 1.2: An abandoned homestead is dwarfed by giant current ripples formed by the Missoula Floods that occurred c.a. 15 000 years ago. Flow direction is toward the camera, looking upstream to the north. (Bjornstad, 2021)

Relationship between human civilization and floods has been complex and often fraught with challenges. Early human civilizations often settled along fertile river valleys prone to seasonal flooding. For instance, the ancient Egyptians settled along the banks of the Nile River. Similarly, Mesopotamian civilizations flourished between the Tigris and Euphrates rivers. The unpredictability of floodwaters posed severe risks to ancient societies, sometimes leading to the collapse of entire civilizations such as the Sumerian city of Ur in Mesopotamia (c. 2000 BCE), Mohenjo-Daro in the Indus Valley (c. 1900 BCE), and the ancient Egyptian Old Kingdom in the Nile Delta (c. 1150 BCE).

Recent history, too, has not been spared by floods. Prolonged heavy rainfall and the overflow of the Yangtze, Yellow, and Huai rivers led to the Great Flood of 1931 in China, one of the deadliest floods on record (Courtney, 2018). The 1970 Bhola cyclone brought

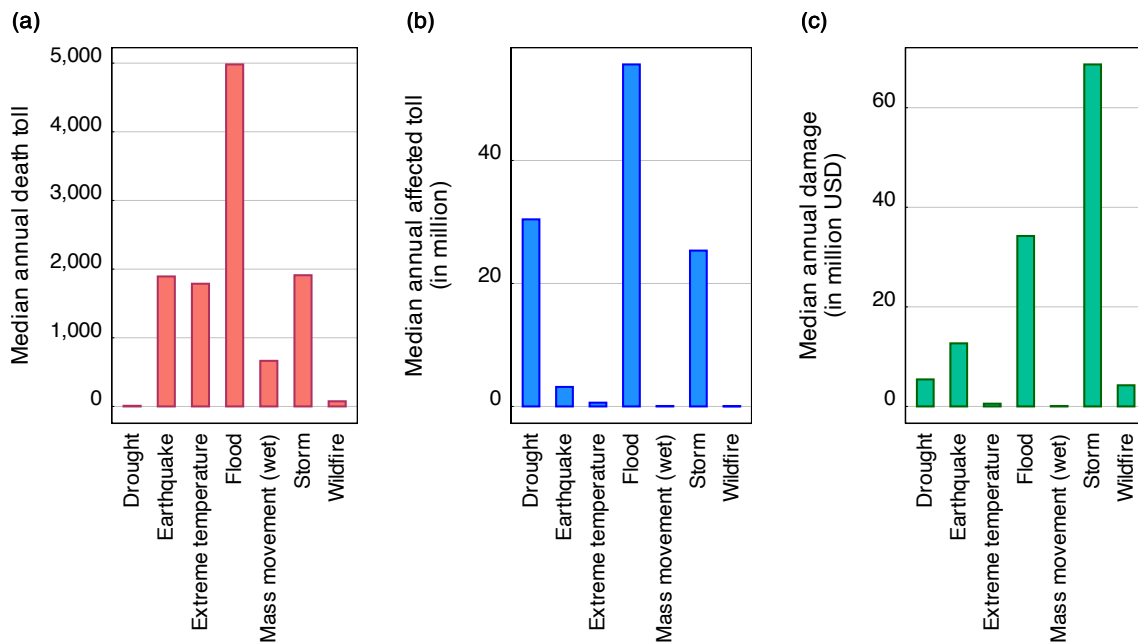


Figure 1.3: Implications of natural disasters in the 21st century. Subplots illustrate the (a) median annual death toll, (b) median annual affected toll, and (c) median annual damage, attributed to each natural disaster type. Data source: EM-DAT (<https://www.emdat.be>). The implications of storms and floods are differentiated based on the primary cause of damage. Impacts from strong winds are included under storms while those from river overflowing are included under floods.

devastating floods that led to a humanitarian crisis in Bangladesh (WMO, n.d.). Similarly, Hurricane Katrina in 2005 brought catastrophic flooding to New Orleans (Daniels et al., 2006). In 2021, a 8600 years return period (Vorogushyn et al., 2022) catastrophic flood in the Ahr River, Germany, took life of 134 people (LfU, 2022) with the total economic loss surmounting in excess of 40 billion EUR (Szönyi et al., 2021).

Flood risk is global and flood impacts are significant and profound. According to Mazzoleni et al. (2022), globally 1.81 billion people are exposed to medium-level flood risk, facing inundation depths greater than 0.15 meters in the event of 100 year return period flood. The EM-DAT database, which tracks disasters globally, indicates that floods have been the most consistently deadly and disruptive natural disaster, with nearly 5 000 fatalities and affecting 55 million people each year since 2000 (refer to Figure 1.3a-b). In terms of annual damage, floods are only surpassed by storms in the 21st century, with inflation-adjusted losses over 34 million USD each year (Figure 1.3b). This makes floods the most enduringly fatal and one of the most persistently costly natural disasters. The sustained and deeply consequential global impacts of floods highlight the urgent need to improve current flood management and disaster response strategies (Daniels et al., 2006; Najafi et al., 2024).

In figure 1.3, a storm is a meteorological event involving intense atmospheric conditions like heavy rainfall, strong winds, or lightning, while a flood is a hydrological event where water overflows onto normally dry land. Storms can cause floods, particularly when rainfall exceeds the land's or drainage system's capacity to absorb or convey water. However, floods can also result from other factors such as snowmelt, dam failure, or tidal surges. In essence, storms are a cause, and floods are often a consequence.

Climate change increases the risk and severity of flooding through several key mechanisms. According to the Clausius-Clapeyron relation, warmer air holds about 7% more moisture per degree Celsius of warming, leading to more intense and frequent rainfall events that can overwhelm drainage systems and cause flash or riverine floods. In colder regions, rising temperatures cause snow to melt earlier and more rapidly, resulting in sharper spring flood peaks. Additionally, sea-level rise driven by melting ice and thermal expansion of sea water amplifies coastal flooding and storm surges, especially during high tides and storms. Warmer ocean temperatures also fuel more powerful tropical storms and hurricanes, which bring intense rainfall and storm surges that can cause widespread inland and coastal flooding. All of this underscores how a warming climate intensifies the hydrological cycle, making flood events more frequent, severe, and unpredictable across diverse regions.

1.3 IMPACT BASED FORECASTING FOR FEWS

Throughout history, humanity has actively sought solutions to flooding, ranging from basic stilt houses in Southeast Asia (c.a. 3000 BCE) to advanced flood control systems in the Netherlands that can withstand up to 10 000 year floods (Rentschler et al., 2022). This evolution spans concepts such as adaptation, control, protection, minimization, and more recently sustainability (Katyál and Petrisor, 2011). But with climate change, the extreme and unprecedented flood events are expected to occur more often than in the past (Gründemann et al., 2022). As flood defences often fail to cope with these extremes, the role of FEWS in safeguarding lives and reducing financial losses has become widely acknowledged (UNDRR, 2015) and applied (Schumann et al., 2013; Pappenberger et al., 2019; Samaniego et al., 2019; Gomez et al., 2019; Ivanov et al., 2021). However, the general public (Quiggin et al., 2021) and the media (Harrabin, 2021) speculate why these scientific advances do not translate into reductions in socioeconomic and human costs (Najafi et al., 2022).

The traditional FEWS provide river gauge water levels or discharge, which is hard to translate to impact of the imminent flooding (Najafi et al., 2022). Post event analysis has revealed that early warnings solely on water level at a gauge site resulted in misinformed actions, delayed responses, and at times, no action at all (Szönyi et al., 2021). Therefore, the communication baton pass between flood forecasting and decision-making is yet to achieve perfect synchrony. There is a need for a system that delivers flood depth and flow velocities not only at a few gauge locations, but continuously and consistently in

space. Such information would enable quantification of affected assets, and anticipated losses, thus, improve the richness of “impact forecasting”, the significance of which has been recently addressed by the UK MET office (Harrowsmith et al., 2020) and the WMO (Zhongming et al., 2020).

2D hydrodynamic models are key tools to simulate the spatio-temporal dynamics of flood inundation. While high-resolution models offer precision, they come with substantial computational demands and has long been considered unfeasible for ensemble forecasting (Wu et al., 2020). Operational FEWS, hence, are yet to integrate flood impact forecasting at the local scale via the utilisation of 2D hydrodynamic modelling (Ivanov et al., 2021). To circumvent this limitation, FEWS systems worldwide have adopted various approaches. For instance, GloFAS (Alfieri et al., 2013) interpolates pre-calculated flood hazard maps to provide an estimate of potential inundation areas. However, these estimates are spatially inconsistent and do not retain continuity (Najafi et al., 2022). State-of-the-art FEWS would, thus, benefit from incorporating fast, real-time hydrodynamic modeling, enhancing the impact-based forecasts and ensuring a more seamless transfer of information to the decision-makers.

1.4 THE ELUSIVE EAGLE VISION IN LARGE SCALE STREAMFLOW MODELLING

Nearly one in four people worldwide are exposed to medium-level flood risk (Rentschler et al., 2022). As shown in Figure 1.4a, this exposed population and flood-prone areas are distributed globally. Tellman et al. (2021) estimated the proportion of the global population exposed to floods to have increased from 2000 to 2015 by 20-24%. While Mazzoleni et al. (2022) indicated a general rise in the annual maximum flood extent across 106 perennial river basins worldwide. The takeaway is clear: *Flood risk is, and will continue to be, a global issue – along with the need for flood forecasting.*

Flood Early Warning Systems (FEWS) with inundation simulation capability requires fluvial boundary conditions to its hydrodynamic model with streamflow time series at upstream river reaches. The Hydrological Model (HM) generates these boundary conditions within the FEWS. Setup and maintenance of individual HMs for FEWS at various location on globe is challenging and computationally inefficient due to overlapping coverage between the individual setups. GHM, with its continental scale streamflow simulations, helps address this issue and thus holds great value for generating fluvial boundary conditions for FEWS on-demand, globally.

While there have been plenty of work involving state-of-the-art GHMs accurately simulating streamflow at large catchments (Polcher et al., 2023; Hou et al., 2023; Grogan et al., 2022; Aerts et al., 2022; Eilander et al., 2021; Stacke and Hagemann, 2021; Harrigan et al., 2020; Burek et al., 2020; Droppers et al., 2020; Müller Schmied et al., 2020; Thober et al., 2019; Hanasaki et al., 2018; Sutanudjaja et al., 2018; Zhao et al., 2017; Li et al., 2015), none have demonstrated the ability to maintain that accuracy at local-scale using continental domains, commonly setting a catchment cutoff at 10 000 km². Table 1.1 provides historical

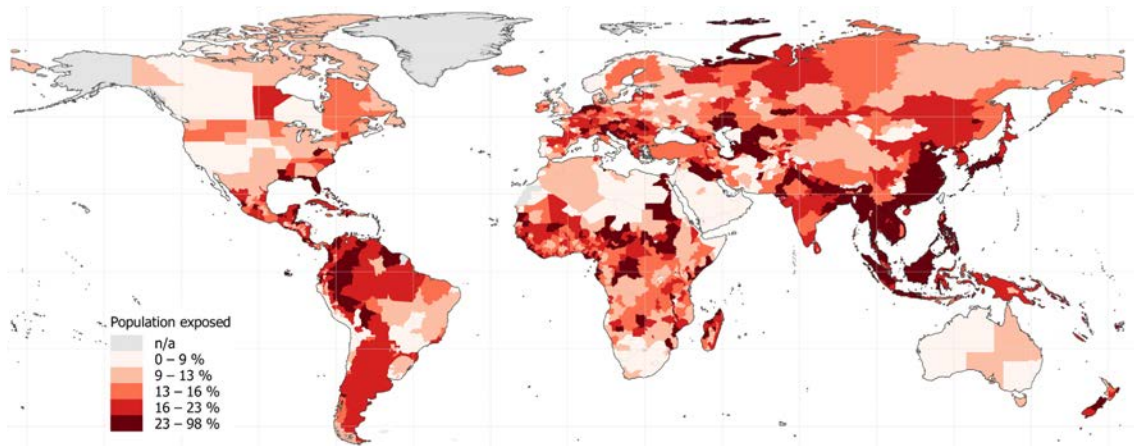


Figure 1.4: Percentage of population exposed to at least medium-level flood risk at the sub-national level. Medium-level flood risk corresponds to an inundation of 15 cm or more during 100-year return period flood. Map source: Rentschler et al. (2022)

evidence that floods in local small catchments can also result in significant losses. Considering small catchments to produce smaller flood extents compared to large catchments, the EM-DAT database reveals floods affecting areas of 10,000 km² or less made up 24% of the flood events in the 21st century, accounting for 18% of flood-related deaths and 19% of the damages – figures that are far from insignificant. It is clear that local floods at smaller catchments needs FEWS just as much as larger basins. Yet the state-of-the-art GHM remain ineffective for generating boundary conditions for FEWS at local-scale. Therefore, it is imperative to develop solutions that enhance GHMs with “eagle vision”, enabling them to produce accurate streamflow simulations for small catchments as well.

1.5 (IN-)ACCURATE REPRESENTATION OF RESERVOIRS IN LARGE SCALE MODELING

According to the GRanD v1.3 (Lehner et al., 2011), one in five reservoirs worldwide serves flood control as one of its purposes, with half of these primarily built for this specific function. In comparison, natural dams are more commonly associated with the triggers of flooding. For example, glacial lakes and their sudden outbursts are frequently linked to catastrophic flooding and downstream destruction (Mool et al., 2011). Additionally, the interplay of heavy rainfall and terrain can give rise to landslide dams that, when breached, release severe floodwaters, as witnessed in the Melamchi flood of 2020 (Adhikari et al., 2023). Thus, flood-prone regions are generally characterized by the presence of dams, whether natural or artificial, and the reservoirs they impound. In order to effectively support Flood Early Warning Systems (FEWS) in such flood-prone regions, it is crucial for Global Hydrological Model (GHM)s to accurately represent these reservoirs.

Table 1.1: Selected notable small catchment floods of the 21st century

Year	Flood event	Catchment of the flooding rivers (km ²)	Hydrometeorological conditions	Aftermath	Source/s
2004	Boscastle flood, UK	20	τ_r : 400 yr 200 mm rain in 5 hr	70+ properties	Fenn et al. (2005) and Ross (2012)
2004	Caribbean floods, Haiti, Dominican Republic	500 – 9 500	250 mm in 24 hr	3353 dead	<i>Flood Disaster Hits Hispaniola</i> (2004); EM-DAT
2009	The Philippines floods	340 – 3 800	442 mm in 12 hr 2x typhoons: Ondoy, Pepeng	241 dead 12 563 homeless	Yumul et al. (2013) and Sato and Nakasu (2011)
2010	Leh floods, Ladakh, India	103	356 mm rain in 2 hr Cloudburst in high altitude cold desert	193 dead 945 houses	Bhatt et al. (2011) and Mueller et al. (2019)
2010	Madeira floods, Portugal	8.8 – 40.9	333 mm rain in 24 hr	45 dead	Fragoso et al. (2012)
2012	Krymsk flood, Krasnodar Krai, Russia	11 – 179	τ_r : 500 – 1000 yr 156 mm rain in 12 hr	172 dead 5500 homeless	Kotlyakov et al. (2013); EM-DAT
2013	Uttarakhand floods, India	50 – 11 800	595 mm in 48 hr	4 190 dead 110 000 stranded 30+ hydropower plants damaged	Patel et al. (2022) and Champati Ray et al. (2016); EM-DAT
2017	Freetown floods Sierra Leone	10 622	1 040 mm rain in 45 d	1 141 dead 3 000 homeless	World Bank Group (2017)
2020	Melamchi flood, Nepal	958	τ_r : 1000 yr landslide dam break	46 dead 539 houses	Adhikari et al. (2023); EM-DAT
2021	Ahr flood, Germany	746	τ_r : 8000 yr 119 mm rain in 14 hr	196 dead 44.9 billion USD	Najafi et al. (2024) and Vorogushyn et al. (2022); EM-DAT

τ_r – estimated return period of the flood event

Telteu et al. (2021) highlighted that only six out of 16 GHMs included reservoirs in their comprehensive review, indicating a lack of sufficient attention to reservoir representation by global hydrologic and land surface modelers. Models that have tried to incorporate reservoirs have typically relied on overly simplified representations (Turner et al., 2021). A common simplification involves modeling reservoir catchments at the scale of the model grid, which can lead to significant discrepancies with coarse model resolutions. The “one grid leads to one reservoir” strategy imposes a limit of one reservoir per grid, which becomes a constraint when multiple reservoirs are located within the same grid

cell (Haddeland et al., 2006a; Haddeland et al., 2006b; Biemans et al., 2011; Terink et al., 2015; Zhao et al., 2016; Zajac et al., 2017; Sutanudjaja et al., 2018; Shin et al., 2019; Shin et al., 2020; Dang et al., 2020). Alternatively, some studies have categorized reservoirs into different types (e.g., “major” and “minor”) and treated them accordingly (Wisser et al., 2010; Hanasaki et al., 2018; Burek et al., 2020; Müller Schmied et al., 2020; Gharari et al., 2024), leading to a partial representation of reservoirs. The problem of reservoir catchments mirrors the small catchment problem, as discussed in Section 1.4.

Evaporation from reservoir lakes is another commonly overlooked topic in GHMs. Some large-scale hydrological applications that include reservoirs have neglected lake surface evaporation, even in recent work such as Salwey et al. (2024). Many studies oversimplify the issue due to inaccurate assumptions about reservoir shapes as pointed out by Shrestha et al. (2024). For instance, studies employing well established GHMs like CWatM (Burek et al., 2020), WaterGAP (Döll et al., 2003), and LISFLOOD (Zajac et al., 2017), have made unrealistic assumption – reservoirs are rectangular prisms with time-invariant water surface area. Addressing these inadequate representation of reservoir catchment, shape, and evaporation in large-scale HMs and GHMs is essential to ensure their suitability to track floods using FEWS in managed river basins.

1.6 SUBJECT OF THE DISSERTATION

This dissertation contributes towards the idea of deploying a single global hydrological model, incorporating realistically represented reservoirs, for efficient, accurate, and on-demand fluvial boundary conditions for impact-based FEWS, at any location of the world.

Challenges such as hydrological modelling of entire earth’s land surface and incorporation of anthropogenic interventions are not the foci of this study, nor is the hydrodynamic modeling of floods. These topics have already been covered by pioneering works such as Vörösmarty et al. (2000), Alcamo et al. (2003), Haddeland et al. (2006a), Hanasaki et al. (2006), Feldhaus et al. (1992), Bates et al. (1995), Bates et al. (1998), and Bates and De Roo (2000). The subject of this dissertation work are rather the niches discussed in Sections 1.3, 1.4, 1.5, which are also shown in Figure 1.5. The first subject examines the potential for real-time impact-based flood forecasting using a hydrodynamic model. The second subject involves a novel method to accurately extract streamflow from GHMs, irrespective of catchment size, grid size, and number of gauges on the grid. The third subject of this work is improving the state-of-the-art representation of reservoirs in GHMs, especially regarding the reservoir catchment, shape, and evaporation.

Another noteworthy contribution of this dissertation is the development of open-source codes, mainly the new reservoir module and the novel stream network upscaling method. The latter is integrated to the routing model of mHM. This implies the gridded runoff from any HM or Land Surface Model (LSM) can be routed by the routing model of mHM to benefit from the new stream network upscaling method.

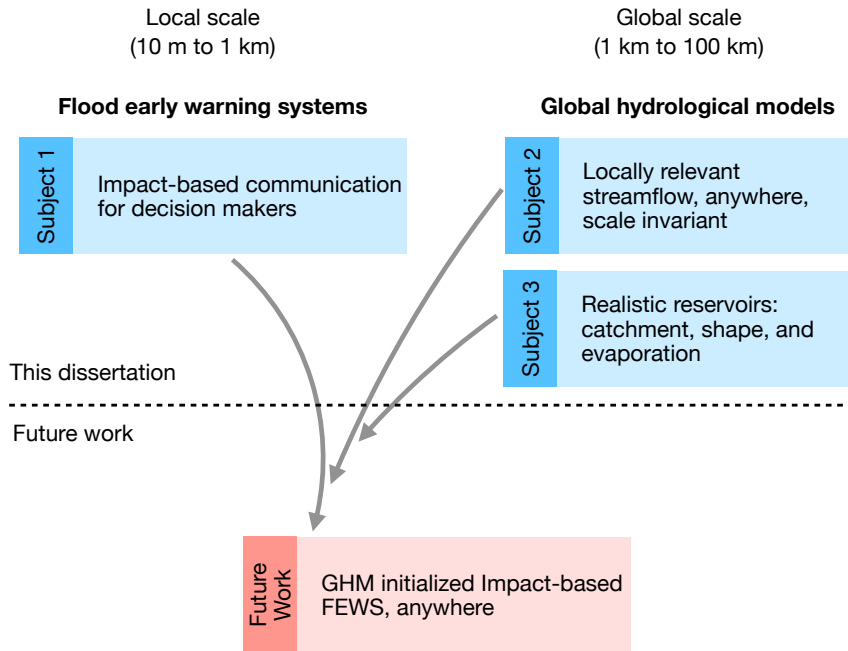


Figure 1.5: Overview of the dissertation subject

1.7 STRUCTURE OF THE DISSERTATION AND THE RESEARCH STATEMENTS

This dissertation consists of four chapters – three publication chapters, and a closing chapter for synthesis and outlook. Out of the three publication chapters, two are published open-access, while the third one is a preprint and currently under consideration for open-access publication in *Water Resources Research* journal. The sequence of the chapters, the three subjects shown in Figure 1.5, follows local to global scale transition, where a local-scale, impact-based FEWS is evaluated in the first chapter, while the second and the third chapters together improve GHMs for better accuracy of regulated streamflow at local scale, in order to generate reliable fluvial boundary conditions for the FEWS. The second chapter introduces a novel method for accurate catchment estimation and invariance to multiple points per grid which benefits the reservoir modeling in the third chapter, hence the logical order.

It is worth noting that the sequence of the published chapters may not be in chronological order. This is partly due to the timing of the funding and partly due to the length of the peer-review process. The corresponding Appendix and Supporting Information for the three chapters are compiled as Appendices A, B, and C.

Below is a summary of the three publication chapters along with their primary research statements. The research statements are denoted hereafter with the letter $\mathcal{R}_{p,i}$. The index

p denotes the publication chapter and i a running number. Each chapter has its own research hypotheses which have undergone rigorous testing and peer-review.

Chapter 2 Impact-based early warning system for local floods

Najafi, H., Shrestha, P. K., Rakovec, O., Apel, H., Vorogushyn, S., Kumar, R., Thober, S., Merz, B., & Samaniego, L. (2024). High-resolution impact-based early warning system for riverine flooding. Nature Communications, 15(1), 3726.

The primary aim of this paper is to demonstrate that state-of-the-art FEWS can deliver more sophisticated, impact-based flood information, thereby improving disaster preparedness. To showcase our system's capabilities, we present a floodplain inundation hindcast ensemble for the 2021 European Summer Flood. This study acts as a proof-of-concept, establishing the foundation for the development and testing of prototypes for impact-based operational systems.

The main thesis put forward in this study is:

$\mathcal{R}_{1.1}$: 2D hydrodynamic models can be incorporated in FEWS for production of near-real-time flood inundation maps and other relevant impact indicators with associated uncertainties.

Chapter 3 Integrating small catchments in global hydrological models

Shrestha, P. K., Samaniego, L., Rakovec, O., Kumar, R., Mi, C. X., Rinke, K., & Thober, S. (preprint). Enhancing Global Streamflow Modeling to Enable Locally Relevant Simulations. ESS Open Archive.

This paper presents, for the first time, global-scale simulations with locally relevant streamflow at catchments as small as 1 km^2 . Catchment area is fundamental to correctly estimating streamflow, which is the basis for Subgrid Catchment Contribution (SCC), a novel stream network upscaling scheme we developed for the routing of river flow in mHM. We test streamflow simulations using SCC against D8 at 5 256 measurement stations, distributed over 62 large-scale domains for global coverage, across model grid size of 1 km to 100 km.

The main theses put forward in this study are:

$\mathcal{R}_{2.2}$: SCC preserves the catchment area at predefined points of interest.

$\mathcal{R}_{2.3}$: SCC eliminates the catchment size problem and enables locally relevant streamflow simulations in gridded hydrological models.

$\mathcal{R}_{2.4}$: SCC enables streamflow estimation at multiple points of interest within a grid cell.

Chapter 4 Improved regulated streamflow in global hydrological models

Shrestha, P. K., Samaniego, L., Rakovec, O., Kumar, R., & Thober, S. (2024). Toward Improved Simulations of Disruptive Reservoirs in Global Hydrological Modeling. Water Resources Research, 60(4).

In this study, we augment the mHM with a newly developed Lake Module (LM) and modified an existing reservoir regulation scheme (Hanasaki et al., 2006) for the module. With a set of 31 global reservoirs, we tested the utility of non-consumptive demand predictions from random forest, evaluated the sensitivity of reservoir simulations to its shape, and propose criteria for in-/exclusion of reservoirs in the model. We compared our results with the state-of-the-art modeling approaches for capturing daily streamflow regulations, reservoir shape representation, and reservoir in-/exclusion strategy.

The main theses put forward in this study are:

$\mathcal{R}_{3.5}$: Machine learning based demand improves the reservoir regulated streamflow simulation.

$\mathcal{R}_{3.6}$: The bathymetry of the reservoir is critical for the lake surface fluxes.

$\mathcal{R}_{3.7}$: Only a subset of global reservoirs are disruptive enough to add value to the modelled streamflow.

1.8 CONTRIBUTION TO PUBLICATIONS

Following are my contributions to the publication chapters that are part of this cumulative dissertation. Please note that the contributions correspond to those reported in the published articles themselves.

Najafi, H., Shrestha, P. K., Rakovec, O., Apel, H., Vorogushyn, S., Kumar, R., Thober, S., Merz, B., & Samaniego, L. (2024). High-resolution impact-based early warning system for riverine flooding. Nature Communications, 15(1), 3726.

- Provided input to the first author for coding the forecasting system.
- Led the development of the flood impact indicator processing program
- Conducted the analyses and produced graphs, alongside the first author
- Added functionality in the mHM code base for sub-daily analysis, alongside a co-author.
- Contributed to interpreting results and the revision of the manuscript, together with the co-authors.

Shrestha, P. K., Samaniego, L., Rakovec, O., Kumar, R., Mi, C. X., Rinke, K., & Thober, S. (preprint). Enhancing Global Streamflow Modeling to Enable Locally Relevant Simulations. ESS Open Archive.

- Conceptualization – lead
- Formal analysis – lead
- Investigation – lead
- Data curation – lead
- Software – independent
- Validation – independent
- Visualisation – independent
- Writing – original draft and all revisions thereafter

Shrestha, P. K., Samaniego, L., Rakovec, O., Kumar, R., & Thober, S. (2024). Toward Improved Simulations of Disruptive Reservoirs in Global Hydrological Modeling. Water Resources Research, 60(4).

- Conceptualization – lead
- Formal analysis – lead
- Investigation – lead
- Methodology – lead
- Software – lead
- Validation – independent
- Visualisation – independent
- Writing – original draft and all revisions thereafter

Part II

PUBLICATION CHAPTERS

HIGH-RESOLUTION IMPACT-BASED EARLY WARNING SYSTEM FOR RIVERINE FLOODING

H Najafi¹, PK Shrestha^{1,2}, et al.

¹Computational Hydrosystems, Helmholtz Centre for Environmental Research – UFZ

²Institute of Environmental Science and Geography, University of Potsdam

Originally published at:

Najafi, H., Shrestha, P. K., Rakovec, O., Apel, H., Vorogushyn, S., Kumar, R., Thober, S., Merz, B., & Samaniego, L. (2024). High-resolution impact-based early warning system for riverine flooding. Nature Communications, 15(1), 3726.

SUMMARY

Despite considerable advances in flood forecasting during recent decades, state-of-the-art, operational flood early warning systems (FEWS) need to be equipped with near-real-time inundation and impact forecasts and their associated uncertainties. High-resolution, impact-based flood forecasts provide insightful information for better-informed decisions and tailored emergency actions. Valuable information can now be provided to local authorities for risk-based decision-making by utilising high-resolution lead-time maps and potential impacts to buildings and infrastructures. Here we demonstrate a comprehensive floodplain inundation hindcast of the 2021 European Summer Flood illustrates these possibilities for better disaster preparedness, offering a 17-hour lead time for informed and advisable actions.

2.1 INTRODUCTION

Flooding affects more people worldwide than any other natural hazard does (UNSIDR and CRED, 2018) and represents one of the four key climate change hazards (Intergovernmental Panel on Climate Change, 2021). Approximately 1.81 billion individuals, constituting 23% of the global population, are found to be directly exposed to 100-year floods (Rentschler et al., 2022). Anthropogenic climate change, inadequate investments of governments and the private sector, and cognitive biases in human perception and decision making are usually blamed for disastrous flood impacts (Merz et al., 2021; Lahsen and Ribot, 2022). Since the 1990s, the observed number of record-breaking rainfall events has deviated substantially from a stationary climate and this deviation has occurred at an increasing rate (Robinson et al., 2021). The rarest rainfall events are projected to

experience the most substantial relative increase in magnitude under future climate change (Gründemann et al., 2022). Extreme and even unprecedented rainfall events, and the associated flooding, are thus expected to occur much more often than in the past. As flood preparedness and defences are often overwhelmed by such extremes, forecasting and early warning systems are perceived as crucial tools to safeguard human life and reduce monetary losses (UNDRR, 2015).

For decades, science and state agencies have been developing hydro-meteorological monitoring and forecasting systems (Pappenberger et al., 2019; Samaniego et al., 2019). Recent improvements in model resolution, process representation, parameterisation, data assimilation, and computational efficiency have advanced numerical weather prediction (Numerical Weather Prediction (NWP)) and hydrological forecasting, and early warning systems have benefited from that alike (Pappenberger et al., 2015). Efforts to enhance the monitoring of atmospheric variables and hydrological fluxes and conditions have also contributed to achieving more accurate initial conditions within the forecasting chain. However, the general public (Quiggin et al., 2021) and the media speculate why these scientific advances do not translate into similar reductions in socio-economic and human costs once a catastrophic event occurs – even in developed countries with advanced flood early warning systems (FEWS) as demonstrated by the floods in Western Europe in July 2021.

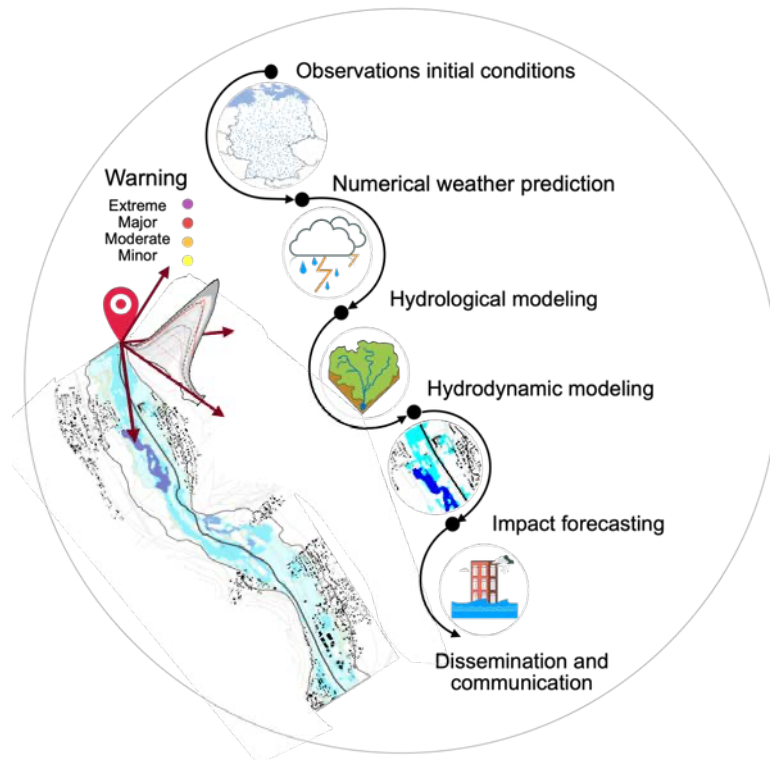
The components of the forecasting chain for a technologically advanced FEWS are depicted in Figure 2.1. First, observed meteorological data is needed for generating hydrological initial conditions. The next component is the NWP system. The skill of NWP models is constrained by several factors, including intrinsic atmospheric chaos, errors in the initial conditions, the spatiotemporal resolution of the model, limited knowledge of physical processes, model errors, and limited computational power. However, with the steady progress of forecasting technology and skill over the past 40 years (Bauer et al., 2015), NWP systems now provide improved quantitative precipitation forecasts because of the increased resolution to the scale of convective-permitting schemes (1-4 km), incorporating several sources of uncertainties and better representation of physical processes (Emerton et al., 2016). A substantial challenge in NWP pertains to the uncertainties in precipitation forecasts, particularly for rare events (Boelee et al., 2019). These uncertainties propagate throughout the model chain and require quantification.

NWP model outputs are then passed to hydrological models to forecast discharge/water levels. Hydrological forecasting technology has also seen substantial progress. A decade ago, producing global hydrological forecasts from land surface models at a hyper-resolution of 0.1-1 km was viewed as a formidable challenge (Wood et al., 2011b). Achieving the high-resolution hydrological forecasting is still ongoing within the research field. Delivering it would be possible with the availability of input data at high resolution and with the implementation of methods that derive seamless parameter fields as well as downscaled forcings and initial conditions (Samaniego et al., 2017). Despite the widespread application of ensemble forecasting in NWP, ensemble flood forecasting is

considered to be in its infancy even in countries with advanced operational FEWS (Adams and Pagano, 2016; Wu et al., 2020). This is mainly related to the challenges of transferring ensemble forecasts into operational decision-making and flood management (Wu et al., 2020). Large-scale operational FEWSs that provide ensemble forecasts (e.g., the European Flood Awareness System-EFAS (Smith et al., 2016)) do not often satisfy the expectations of regional flood managers requiring hydro-meteorological forecasts at river gauge locations with high spatio-temporal resolutions and update frequencies (LfU, 2022).

Flood warnings are usually provided for river gauge locations. Extending flood forecasts from streamflow and water levels at selected river gauges to spatially distributed information on inundation, flow velocities and further impacts has been considered unfeasible for many years (Wu et al., 2020) because of two main reasons: first, the extensive runtime required by fine-resolution (high-fidelity) hydrodynamic models to produce an ensemble forecast in real-time, and second, the lack of river cross-section data at a reasonably high resolution along the river network (Bates, 2022). Despite the existing computational and operational challenges, flood managers need forecasted impact maps in real-time for issuing more targeted flood warnings and for better emergency response (Merz et al., 2020). By extending the forecast model chain with high-resolution (1-10 m grid size) hydrodynamic and impact forecasting, shown in Figure 2.1, it would be possible to provide essential information for emergency response downstream of the river gauge. For examples, expected consequences of imminent flooding impacts, extending beyond traditional hazard data like river gauge water levels, affected assets and anticipated losses can be delivered. It holds a considerable promise for enhancing disaster risk management by considering physical characteristics of the event, as well as socio-economic systems affected.

Local authorities and civil protection agencies benefit from impact forecasting, gaining actionable insights for initiating safety measures and evacuation protocols during floods. However, operational FEWS still need to integrate flood impact forecasting at the local scale of disaster management, particularly through the utilisation of 2D hydrodynamic modelling (Ivanov et al., 2021). Table 2.1 provides an overview of the key components within existing state-of-the-art FEWS. Notably, both GloFAS (Alfieri et al., 2013) and EFAS employ an approach to inundation and impact forecasting, relying on the interpolation of pre-calculated flood hazard maps for a limited set of return periods (Dottori et al., 2017). This provides a rough estimate of potential inundation areas, and the so-produced flood maps are spatially inconsistent and do not retain continuity. This integration presents two major challenges:



Model/characteristic	Daily updates	Technology readiness level	Spatial Resolution	Ensemble member
Numerical weather prediction	1 - 8	7 - 9	1 - 4 km	10 - 51
Hydrological forecasting	1 - 8	7 - 9	100 m - 5 km	10 - 51
Hydrodynamic modeling and impact forecasting	Not yet operationalized	4 - 6	1 - 10 m	-

Figure 2.1: A holistic end-to-end impact-based flood forecasting modelling chain. The state-of-the-art flood early warning system is extended with components of quasi-real-time hydrodynamic and impact forecasting. Observational initial conditions are obtained based on data from ground, radar, satellite, and reanalysis. The Technology Readiness Level (Technology Readiness Level (TRL)) (*Technology Readiness Level (TRL) n.d.*) serves as a scale for evaluating the developmental stage and maturity of a technology. At TRL 1, the technology is in the initial scientific research phase, while TRL 9 signifies that the system has been successfully demonstrated in a real-world operational environment. Data sources: OpenStreetMap (OSM) rivers, roads and buildings: OpenStreetMap (OpenStreetMap, 2017) contributors 2021, distributed under the Open Data Commons Open Database License (Open Database License (ODbL)) v1.0. National German boundary: Global Administrative Areas database (GADM). Meteorological stations (Deutscher Wetterdienst)

Table 2.1: Existing State-of-the-Art FEWS around the World

Platform /System	Scale	Atmospheric Model	Atmospheric Model Resolution	Hydrologic Model	Hydrologic Model Resolution	Forecast Update	Ref. No.
GloFAS	Global	European Centre for Medium-Range Weather Forecasts (ECMWF)-Integrated Forecast System (IFS)	18 km	Hydrology Tiled ECMWF Scheme for Surface Exchanges over Land (HTESSEL)-Lisflood	0.1° - 0.05°	12-hourly	Alfieri et al. (2013)
EFAS	Continental (Europe)	Consortium for Small-scale Modeling (COSMO)-Limited Area Ensemble Prediction System (LEPS)/ICON/ICON-EU	6.5 - 13 km	Lisflood	5 km	6-hourly	Dottori et al. (2017)
Flood early warning system*	National (Germany)	ICON-D2/ICON-D2-Ensemble Prediction System (EPS)	2.2 km	Large Area Runoff Simulation Model (LARSIM)	Spatial Units of 0.25-10 km ²	3-hourly	LfU (2022)
Advanced Hydrologic Prediction Service (AHPS), Hydrologic Ensemble Forecast Service (HEFS), NWM†	National (USA)	Advanced Weather Interactive Processing System (AWIPS)‡	3 - 25 km	Community Hydrologic Prediction System (CHPS)	100 m / 250 m and 1 km††	1- 12 hour	Adams and Pagano (2016)
Hydrological Forecasting System (Hydrologic Forecasting System (HyFS))	National (Australia)	Australian Community Climate and Earth-System Simulator (ACCESS) (Australian Community Climate and Earth-System Simulator)	4-40 km	Unified River Basin Simulator (Unified River Basin Simulator (URBS)), Génie Rural à 4 paramètres Journalier (GR4J)‡‡	Semi-distributed	at least daily	Adams and Pagano (2016) and Hapuarachchi et al. (2022)

* (Hochwasserfrühwarnsystem) The described model chains are implemented in flood forecasting centres in the German Federal States of Baden-Württemberg, Bavaria, Hesse, Northern Rhine-Westphalia, Rhineland-Palatinate, and Saarland Adams and Pagano (2016). Flood forecasting centres in other German Federal States are using similar approaches.

†‡ Flexible, specified by User (from HRR, NAM, GFS, RAM, and ECMWF)

‡‡ The National Water Model 3 provides 18-hour deterministic short-range forecast the contiguous United States (CONUS).

‡‡ SWIFT (GR4H-hourly) is used as part of Short-term Water Information Forecasting Tools (SWIFT) hydrologic modelling package for 7-day streamflow forecast.

1. **Computational Efficiency Challenge:** Computationally efficient FEWS are imperative for promptly generating inundation and impact information, including associated uncertainties. Several studies have developed prototypes of flood forecasting modelling chains that include probabilistic flood inundation forecasting (see e.g., (Schumann et al., 2013; Gomez et al., 2019; Ivanov et al., 2021)). While high-fidelity models offer precision, they come with substantial computational demands. Strategies such as non-physics-based (simplified) methods (Teng et al., 2017) and model emulation, as demonstrated by Ivanov et al. (Ivanov et al., 2021) and Fraehr et al. (Fraehr et al., 2023), seek to strike a balance between computational efficiency and prediction accuracy. Sustaining prediction accuracy requires accounting for a wide range of flooding scenarios and inundation behaviours (Fraehr et al., 2023). However, these approaches may encounter challenges when adapting to diverse flood scenarios or diverse landscape contexts (Bout et al., 2023). Simplified methods, for instance, are particularly suitable for applications where dynamic effects play a minimal role, and the focus is primarily on the final or maximum flood extent and water levels (Teng et al., 2017). Moreover, surrogate models may struggle when faced with inputs outside their training scope or complex, non-linear interactions among flood drivers (Schubert et al., 2022). Notably, they may also face difficulties accurately simulating unprecedented extremes compared to high-fidelity models (Schubert et al., 2022).
2. **Propagation and representation of uncertainties in probabilistic impact forecast for better informed disaster management:** Recent research demonstrates the potential usefulness of probabilistic forecasts for emergency managers facing real-world constraints. However, the exact impact of these forecasts on user decision-making remains unquantified (Fundel et al., 2019). The challenge resides in propagating the uncertainties along the entire forecast model chain and represent the uncertainty of impact indicators in a suitable way.

To address these challenges, the advancements in inundation and impact-based forecasting are demonstrated by comparing the common practice of pre-calculated/flood hazard maps with our proposed forecasting chain. Utilizing real-time forecasts as an extra layer enriches pre-calculated hazard maps by considering antecedent conditions (Speight et al., 2021). In addition, fast hydrodynamic modeling captures real-time flood dynamics, overcoming the limitation of pre-calculated maps assuming seamless connection between real-time forecasting models and static inundation and impact assessments, potentially leading to inaccuracies, especially for unusual flood events. Furthermore, these maps rely on several factors which might not be valid for all flood events (Speight et al., 2021). We leverage fast and real-time hydrodynamic modeling while transparently communicating uncertainties for decision-makers. Our method, featuring dynamic simulation, provides crucial timing information for effective emergency responses. Additionally, it offers im-

proved adaptability in flood hazard map resolution, particularly with high-resolution Digital Elevation Models, ensuring accuracy without sacrificing computational efficiency.

The need for impact-based warnings for disaster risk management has been addressed recently in various guidelines and studies (Kox et al., 2018; Harrowsmith et al., 2020). For instance, the shift from weather forecasts and warnings to impact-based forecasts and warning services is outlined by the World Meteorological Organization (World Meteorological Organization (WMO)) guidelines (Zhongming et al., 2020). This shift also underlines the need for decision-making protocols tailored to align with the distinct dynamics of specific hazards, geographical locales, institutional capabilities, and cultural nuances. The initiative on impact-based early warnings is gaining global support, as more national hydro-meteorological services align their strategies and investments with this approach.

The effectiveness of an experimental impact-based flood early warning system is showcased in this study by utilising the catastrophic flood event that occurred in the Ahr River, Germany in 2021. During the July 2021 flood event, 134 people in the Ahr Valley lost their lives (LfU, 2022). The total economic loss in Germany exceeded 40 billion EUR (Szönyi et al., 2021). The return period of the event based on observed annual peak discharge gauge data between 1946-2019 and four historical floods between 1888 and 1920 is estimated to about 8600 years (Vorogushyn et al., 2022). The magnitude of the flood and its damage to buildings and infrastructure required the most extensive response and recovery operation in German history (Szönyi et al., 2021). The German Weather Service, Deutscher Wetterdienst (DWD), predicted a heavy precipitation event several days prior to the event (DWD–Deutscher Wetterdienst, 2021). In addition, the official hydrological forecasts indicated unprecedented water levels at several gauges. Post-event analysis has revealed that early warnings solely on hazard metrics such as maximum local rainfall depths or maximum water level at a gauge site resulted in misinformed actions, delayed responses, and at times, no action at all (Szönyi et al., 2021). Local weather and civil protection officials underscored that their limited knowledge to understand about the potential impacts of 150 mm or 200 mm of rainfall, or a gauge level of 6 m, prevented them from giving clear guidance on the specific problems or damage expected from the forecasted rainfall or water levels (Szönyi et al., 2021).

Here, we show how a state-of-the-art flood forecasting modelling chain can provide more sophisticated information, enhancing disaster preparedness. To illustrate the capabilities of our system, we provide a floodplain inundation hindcast ensemble for the 2021 European Summer Flood. The proposed approach allows for a more dynamic and responsive early warning system, offering enhanced insights into potential flood impacts and facilitating more effective decision-making. By employing high-resolution, object-based impact forecasting techniques, we are able to generate near-real-time flood inundation maps and other relevant impact indicators with associated uncertainties. This serves as a practical example to highlight the potential of our approach in accurately predicting and visualising flood impacts for better decision-making and preparedness in

the face of such devastating events. It provides lessons that contribute to the improved management of future events and highlight why users need to put rare but severe events into perspective (Fundel et al., 2019). The current study serves as a proof-of-concept, laying the groundwork for the further development and testing of prototypes for such operational systems.

2.2 RESULTS

2.2.1 *Ensemble precipitation and probabilistic water level forecasts*

Here, we use the DWD's latest NWP limited area ensemble prediction system (ICON_D2_EPS) for generating ensemble forecasts of water level for the event. The operational NWP ensemble prediction system generates 20 ensemble forecasts at a spatial resolution of 2.2 km. It considers different sources of forecast uncertainty arising from initial conditions and model error, in addition to the uncertainty in the boundary conditions for limited area ensembles (Reinert et al., 2020). For the hindcast experiment, ensemble forecasts were retrieved for every 3-h initialisation between 13 July 2021 (02:00 CEST) and 14 July 2021 (23:00 CEST), thus covering a window of opportunity of 47 h to 2 h prior to the flood peak.

Probabilistic forecasts are considered much more valuable than deterministic forecasts especially for extreme and rare events (Cloke and Pappenberger, 2009). Therefore, to evaluate the predictability of the flood event in Ahr Valley, with the catchment area of 746 km², the mHM (Samaniego et al., 2010) is forced with 320 ensemble predictions (16 initialisations × 20 members) from ICON_D2_EPS to generate streamflow and water level predictions at the gauge Altenahr. The mHM has been evaluated as a prospective choice for a continental-scale operational flood forecasting in Europe (Kauffeldt et al., 2016). Ensemble medians and the water level forecasts for all 16 initialisations are depicted in Figure 2.2. Hydrological predictions for each initialisation can be elaborated in Supplementary Figure S1.

The Altenahr gauge was wrecked by the flood; therefore, water levels reconstructed by the responsible authority (Rhineland-Palatinate (RP) State Office for the Environment; Landesamt für Umwelt (LfU)) are used for the evaluation of the ensemble water level predictions (refer to Figure 2.2). The probabilities of exceeding warning levels are shown in Figure 2.2 for each initialisation as well, assuming that all ensemble members have an equal likelihood (Cloke and Pappenberger, 2009). The classification of official flood notification levels varies across Germany's federal states. In Rhineland-Palatinate (RP), the categorisation of flood situations hinges on the concept of return periods. Specifically, flood occurrences with return periods equal to or exceeding that of a 50-year flood are labeled as extreme events. The 100-year flood (HQ₁₀₀) serves as the critical benchmark for potential risks to life, property (Cloke and Pappenberger, 2009), and infrastructure.

Figure 2.2 displays a considerable variation in water level predictions among the ensemble members. This wide range of predictions can be attributed to the inherent

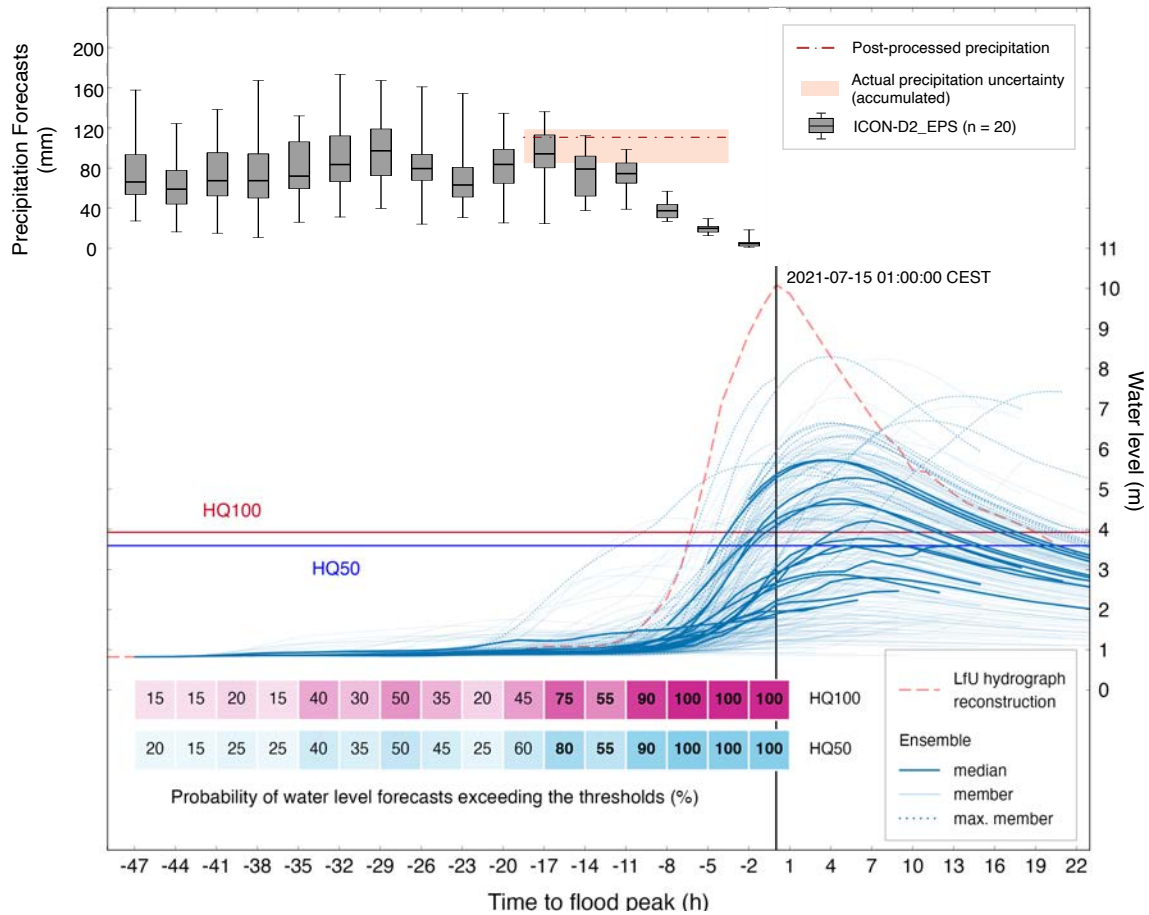


Figure 2.2: Ensemble of precipitation and water level forecasts from the ICON_D2_EPS-mHM chain. Ensemble forecasts initialised every 3-hour before the reconstructed flood peak at Altenahr gauge. The probabilities of exceeding the 50-year (50 years return period flood (HQ₅₀)) and 100-year (HQ₁₀₀) flood thresholds are displayed for 16 forecast initialisations (See Supplementary Figure S1 for more details). The range of 48-hour areal precipitation forecasts for the Ahr basin is shown as whisker plots for each initialisation from ICON_D2_EPS. The whisker plots of precipitation forecast for each initialisation represent the minima, maxima, the bounds of the box (25 and 75 percentiles) and the center (median) based on 20 ensemble members. The uncertainty of quantitative precipitation estimation for the event is shown for the target period of 07/14 07:00 to 07/14 21:00 CEST (LfU, 2022)

uncertainties in the flood forecasting modelling chain, primarily stemming from ensemble precipitation predictions (Cloke and Pappenberger, 2009). The precipitation forecasts derived from the ICON_D2_EPS (shown in Figure 2.2) reveal substantial variations. These variations can reach up to 80 mm among distinct NWP ensemble members and across diverse forecast initialisations. The quantitative estimation of precipitation for the event exhibits uncertainty. The most realistic estimate indicates 119 mm of precipitation between the period 07/14 07:00 to 07/14 21:00 CEST (LfU, 2022). This amount surpasses the ensemble median forecasts, sometimes even doubling them. Because this flood was an exceptionally rare event, and the calibration period has not had many such extreme events to tailor the model parameters, precipitation amounts higher than 119 mm were necessary to accurately predict the flood peak. For these reasons, water level ensemble forecasts are substantially lower than reconstructed water level at gauge Altenahr. Despite the discrepancies in ensemble precipitation forecast, the primary focus remains on assessing the exceedance probability of the warning threshold as key variable (Alfieri et al., 2019).

The expected precipitation amounts from high-resolution and convection-permitting NWP (ICON_D2_EPS) differentiate largely depending on the forecast time (LfU, 2022). This uncertainty is propagated to water level forecasts and finally to the probability of exceedance of warning thresholds. This complicates the task for flood managers, making it challenging to arrive at a confident decision (LfU, 2022). For example, the probability of exceeding HQ₁₀₀ increased by 30% from the forecast initialisation 20 h prior to the flood peak to that of 17 h but dropped by 20% in the next issued forecast.

For all water-level forecasts issued within the lead-time of 17 h to the flood peak, the probability of exceeding HQ₁₀₀ is greater than 50% ($P_{WL > HQ_{100}} \geq 50\%$) based on the Icosahedral Nonhydrostatic - 2 km resolution model for Germany (ICON-D2)_EPS-mHM forecast chain. Additionally, at the 11-hour mark in advance (14 July, 14:00 CEST initialisation), the probability of a flood exceeding the HQ₁₀₀ threshold surged to 90% (Figure 2.2). This dramatic increase in probability further emphasises the urgency for appropriate flood response measures and is a confirmation of the adequacy of the modelling chain.

2.2.2 Comparison between the official and experimental water level forecasts

Ten official deterministic water level forecasts were published by LfU within a time window ranging of 22 h to 1 h prior to the reconstructed maximum level for Altenahr (LfU, 2022). LfU forecasts ranged from 225 cm in the morning of July 14 to 707 cm in the late evening. This wide range of predicted maximum levels illustrates the uncertainty associated with atmospheric forecasts, and observation errors of the rain gauges and water levels at gauge Altenahr (LfU, 2022). LfU uses the LARSIM water balance model (Ludwig, 2006) as an operational forecast model. The Ahr catchment is represented by 561 sub-basins in their model. The real-time forecasts on July 14 2021 were generated

based on a LARSIM calibration from the period ranging between 1993 and 2016 (LfU, 2022).

In the post-assessment report by LfU (LfU, 2022), an ensemble forecast was provided based on the ICON_D2_EPS for the 14 July 2021 (14:00 CEST) initialisation. The ensemble water-level forecasts based on the ICON_D2_EPS – mHM are quite similar to the official forecasts for the same initialisation. Ensemble median water levels based on the ICON_D2_EPS – mHM were approximately 1 m lower than the deterministic water-level forecasts of the LfU within the window of 5 h to the flood peak. Differences between water-level forecasts may be due to the post-processing method used in the radar-adjusted quantitative precipitation estimate, the structural and parameter uncertainty, and the initialisation of the hydrologic model. In our proposed modelling chain, the LfU reconstructed hydrograph is used as a reference for the hindcast experiment.

2.2.3 *Lead-time maps and impact-based warning*

Probabilistic water level forecasts at a gauge location do not provide sufficient information for emergency measures downstream. To address this shortcoming, the provision of lead-time maps to reach critical levels, along with high-resolution near-real-time inundation maps, and flow velocities are crucial and may ultimately save human lives and reduce socio-economic impacts (Weyrich et al., 2018; Campbell et al., 2018; Kreibich et al., 2021).

Here, we demonstrate that near-real-time impact forecasting for floods is possible, even for comparatively small and fast-reacting rivers. The NWP-hydrologic forecasting chain is extended with the high-resolution (10 m grid) hydrodynamic model RIM2D, which proved to reliably simulate inundation for the Ahr valley (Apel et al., 2022). In this study, the uncertainty along the modelling chain is considered, which is the added value compared to studies which have used only a single forecast (e.g., see Apel et al. (Apel et al., 2022)). The near-real-time forecasts of inundation depth are compared first to HQ₁₀₀ raster-based water depth map to identify regions with extreme flood hazard. For the grid cells, for which the water depth forecast exceeds HQ₁₀₀, the lead-time is calculated based on forecast outputs from hydrodynamic modelling. By running the ensemble inundation prediction, information on the most likely estimate of flood impacts can be derived from the ensemble mean. In addition, the ensemble members that have generated the minimum and maximum water levels can provide the uncertainty of inundation extent in each forecast initialisation.

In the presence of considerable uncertainties within the forecasting chain, effectively communicating forecast persistency is imperative for informed decision-making. Communication with local authorities should encompass the persistent impacts of flood forecasts, providing guidance for effective emergency response operations. Here, the selection of three consecutive forecast initialisations is considered. The lead-time is calculated for each grid cell across consecutive forecast initialisations (Pappenberger et al., 2015) when the water level surpasses the HQ₁₀₀ threshold. To account for prediction uncertainty,

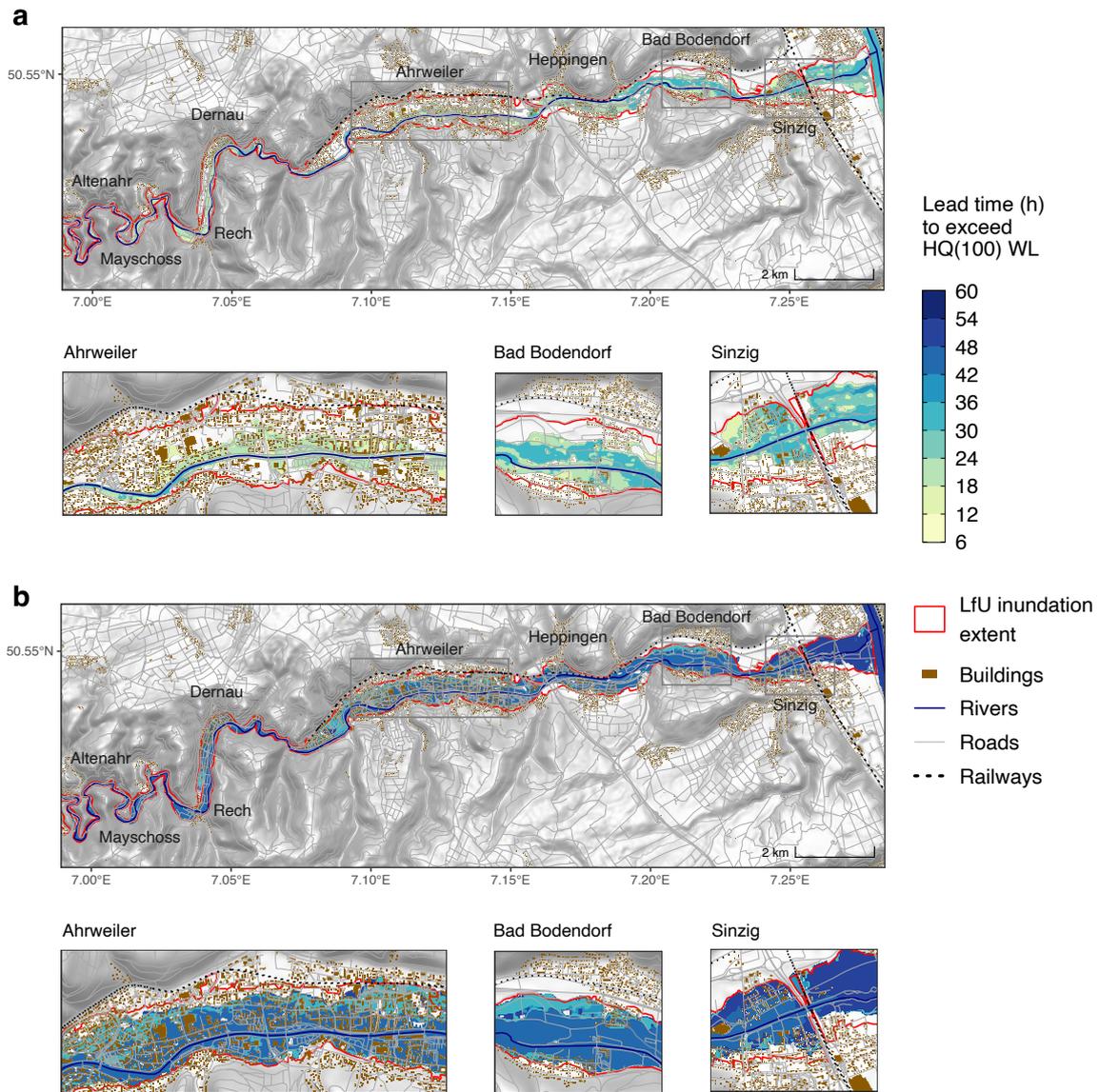


Figure 2.3: The maximum flood lead-time warning based on the ICON_D2_EPS-mHM-RIM2D FEWS chain. A maximum lead-time raster-based flood warning map is a geospatial representation that highlights the maximum available time for flood preparedness and response. The lead time is calculated downstream Altenahr gauge based on water levels (Water Level (WL)) exceeding HQ_{100} . Panel (a) displays the lead time map derived from 16 ensemble median water levels (i.e., median over 20 members for each NWP initialisation). Panel (b) shows the same but obtained with 16 maximum water levels. These lead time maps are obtained when three consecutive initialisations exceed the HQ_{100} for a given 10 m grid cell. Please refer to the Forecast Persistency section in the 2.4 for additional details. The red extent delineates the inundation area mapped by the LfU of Rhineland-Palatinate. Supplementary data sources: OSM river, roads and buildings: OpenStreetMap/OpenStreetMap (2017) contributors 2021 distributed under the Open Data Commons Open Database License (ODbL) v1.0. Hillshade: Digital Terrain Model (DTM) vo.3 (CC BY)Hengl et al. (2021)

we select ensemble members that produce the lowest and highest water levels at the gauge, in addition to the ensemble median, as well as the 25th and 75th percentiles. In Figure 2.3(a) and Figure 2.3(b), lead-time maps for the ensemble median and maximum are presented for the river reach downstream of the Altenahr gauging station, covering multiple settlements. The high-resolution raster-based lead-time map shows a time-window ranging from 6 to 30 h, which could have been used for on the most likely outcome (i.e., ensemble median). The maximum water level predictions indicate a lead-time map ranging from 24 to 48 h before the forecasts exceed the HQ₁₀₀ warning threshold. The predicted inundation extent from the ensemble median underestimates the actual flood extent mapped by LfU. The maximum ensemble member, i.e., one member out of 20, matches well with this estimate, (Figure 2.3(b)). For this specific event, the assessment of the predicted inundation areas suggests that the flood extents generated by the maximum rainfall estimate from the ICON_D2_EPS model could closely resemble the actual conditions. This conclusion is confirmed by a recently published report (LfU, 2022), which shows that the observed precipitation was predominantly within the range of the maximum values of the ensemble forecast. Relying on lead-time estimation from a single forecast can extend the window of the opportunity for response, yet it may also elevate the occurrence of false alarms. Supplementary Figure S2 and S3 present lead-time maps for median and maximum water levels without considering forecast persistence.

To validate the impact forecasts, we compared the affected buildings footprint as well as road and railway length to those estimated from the Copernicus Emergency Management Service (Copernicus Emergency Management Service (CEMS)) Rapid Mapping as a benchmark. The service activated by the German Joint Information and Situation Centre (Geoinformation und Monitoring bei Landnutzung und Zivil- und Katastrophenschutz (GMLZ)). The figures are compared for different ensemble members related to different percentiles (Table 2.2). For example, the maximum ensemble member, issued 47 hours in advance of the flood peak, overestimated inundated building footprint by 10% compared to Copernicus Rapid Mapping. Notably, the maximum ensemble member for several forecast initialisations closely aligns with the benchmark for several forecast initialisations. Our estimates for the number of affected buildings and infrastructure often turn out to be less severe compared to the post-event surveys. This aligns with the underestimation of water levels and consequently of the inundation areas.

Table 2.2: Comparison of impact-based forecasted damages to buildings, railways, and roads to benchmark. A 100% percentage indicates that the damage equals that of the benchmark while values exceeding (falling below) 100 signify an overestimation (underestimation) of the forecasted damage.

Infrastructure	Benchmark	Ensemble statistic	Forecast (Time to Flood Peak in hours)																
			47	44	41	38	35	32	29	26	23	20	17	14	11	8	5	2	
Building footprint	Copernicus EMS Rapid Mapping	Max	110	73	71	75	60	117	104	104	91	90	90	85	89	72	84	70	
		75P	5	1	15	15	25	50	47	32	16	16	51	71	52	74	52	72	70
		Median	1	1	1	1	1	4	12	14	1	1	15	44	29	57	41	70	70
		25P	1	1	1	1	1	1	1	1	2	1	3	20	1	46	32	69	70
		Min	1	1	1	1	1	1	1	1	1	1	1	1	1	1	4	26	64
Building footprint	LfU	Max	76	51	49	52	42	81	72	72	63	63	63	59	62	50	59	49	
		75P	3	1	10	11	17	35	33	22	11	35	49	36	51	36	50	49	49
		Median	1	1	1	1	1	3	8	9	1	10	31	20	40	29	49	49	49
		25P	1	1	1	1	1	1	1	1	2	1	2	14	1	32	22	48	49
		Min	1	1	1	1	1	1	1	1	1	1	1	1	1	3	18	45	49
Railways	LfU/Copernicus EMS Rapid Mapping	Max	124	97	95	97	90	132	117	118	103	102	102	100	102	97	100	94	
		75P	40	32	58	59	69	84	82	73	59	84	95	85	97	85	97	94	94
		Median	29	29	29	29	32	39	55	56	30	57	80	70	90	78	94	94	94
		25P	29	29	29	29	29	29	29	36	29	38	65	29	82	72	94	94	94
		Min	29	29	29	29	29	29	29	29	29	29	29	29	29	39	69	91	94
Roads	LfU/Copernicus EMS Rapid Mapping	Max	111	83	81	84	73	115	106	107	95	94	94	91	94	82	90	81	
		75P	22	15	37	38	48	67	65	54	38	67	81	68	84	69	82	81	81
		Median	14	14	14	14	15	22	35	36	15	37	63	51	71	60	81	81	81
		25P	14	14	14	14	14	14	14	18	14	20	43	14	65	54	80	81	81
		Min	14	14	14	14	14	14	14	14	14	14	14	14	14	21	49	76	81

2.2.4 *Enhancing Flood Forecast Communication for Informed Decision-Making and Risk Management*

Decision-makers frequently encounter the task of issuing deterministic directives based on inherently probabilistic data (Pappenberger et al., 2015). Although FEWS capabilities may limit the provision of high-resolution flood impact forecasts and introduce uncertainties, effective communication of this information can still enhance user trust (Anderson et al., 2022). In the domain of emergency response, theoretical models and decision analysis methods abound, with notable contributions like the Protective Action Decision Model (PADM) (Lindell and Perry, 2012) and cumulative prospect theory (Tversky and Kahneman, 1992). In cases where official risk thresholds are not defined by relevant agencies, decision-makers often need to set their own probability thresholds that align with their specific needs and organizational goals, as illustrated by Fundel et al. (2019) (Fundel et al., 2019). In this respect, Figure 2.4 provides a useful visualization of how probabilistic information, based on lead-time, can support flood managers. The whisker plot visually represents the predicted inundated area downstream of the Ahr river, with an estimated coverage of 8.37 km². Visual representations like this effectively contextualize infrequent yet severe events, providing valuable perspective (Fundel et al., 2019).

The convergence line in Figure 2.4 falls short when compared to the 11.33 km² extent mapped by LfU due to the uncertainties inherent in forecasting rainfall, which subsequently impacts the predicted water levels and inundation extent. Nevertheless, the ensemble median inundation map has revealed that the affected area would potentially match or surpass the the most extreme scenario of the flood (HQ_{extreme}) level. Regarding Figure 2.4, the ensemble median consistently surpassed the inundation areas of HQ₁₀₀ and HQ_{extreme} by 20 and 17 lead-hours, respectively. This time frame provides a potential warning lead-time for preparation and response in the face of impending floods. For this particular event, it was demonstrated that the maximum forecast ensemble member was more closely aligned with the post-event inundation area mapping compared to the median forecast. However, more events should be investigated to better understand how to use the full ensemble for decision making. We advise flood managers to adjust the thresholds based on their daily experience in making warning decisions, as proposed by Fundel et al. (Fundel et al., 2019), or in accordance with national regulations.

2.3 DISCUSSION

We demonstrate that recent advancements in hydrologic and hydrodynamic models and computational capabilities enable high-resolution flood inundation and impact forecasting within operational FEWS even for comparatively small and fast-reacting rivers. These forecasts encompass probabilistic inundation maps and identify buildings and transportation infrastructure at risk of flooding. Operational inundation and impact modelling provides much richer information on the space and time dynamics of flooding

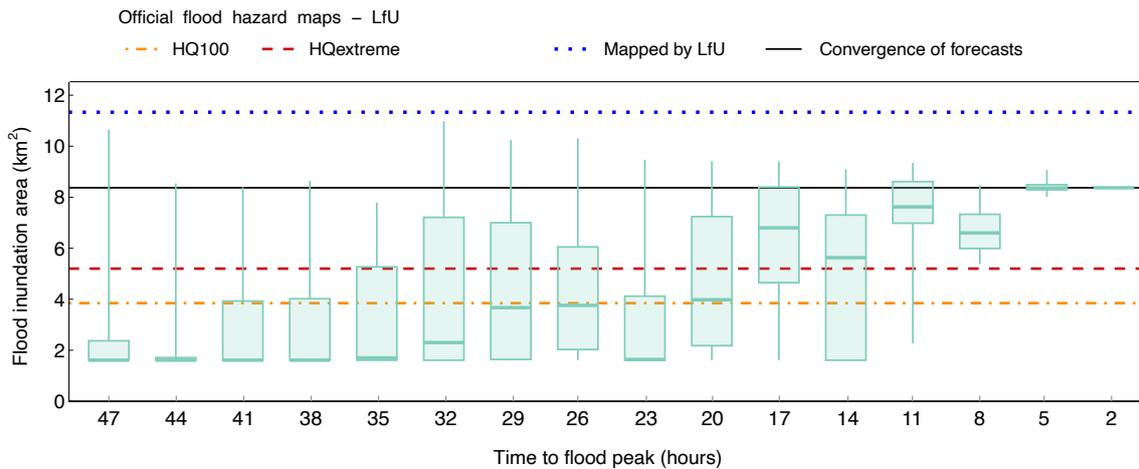


Figure 2.4: Uncertainty representation of the forecasted inundated area downstream of the Al-tenahr gauge. Uncertainty is quantified based on 16 initialisations issued 47 h to 2 h prior to the 2021 European Summer Flood. The uncertainty of the atmospheric forecast t based on 20 ensemble members ($n=20$) is propagated through the modelling chain to the hydrological and inundation prediction. The whisker plots of inundation prediction for each initialisation represent the minima, maxima, the bounds of the box (25 and 75 percentiles) and the center (median) based on this ensemble.

and its effects. Flood depth and flow velocities are not only available at a few gauge locations, but continuously and consistently in space. Time-varying characteristics such as lead time to specific depth thresholds or the rate of water rise can be provided during the course of the entire event. At last, the prediction of affected buildings and critical infrastructure are compared against emergency mapping products derived from satellite data. This multi-faceted information is very instrumental for more targeted and tailored emergency response. Current satellite inundation maps, given their prioritization of rapid mapping over quality, should not be regarded as absolute truth, leading to inherent uncertainties (Bates, 2023). Depending on Synthetic Aperture Radar (Synthetic Aperture Radar (SAR)) for emergency mapping introduces limitations, such as misclassification and timing issues. This highlights the need for caution and an acknowledgment of the upper limits of SAR-based flood detection methods when identifying affected areas and assessing damages (Ajmar et al., 2017).

The feasibility of the operational flood impact forecasting was demonstrated in the hindcast of the 2021 European Summer Flood event in the Ahr basin in this study. Several challenges, however, remain as we progress in adopting impact-based FEWS: 1) An increasing number of national hydro-meteorological services are investing in a paradigm shift from traditional FEWS to high-resolution, impact-based FEWS. However, implementing real-time services on a national scale poses challenges, given the trade-offs involving computational power, operational service scheduling, and data storage archiving. 2) Availability of quality data and computational resources is crucial for

implementing near-real-time flood impact forecasting. Many regions, especially flood-prone areas, lack essential datasets such as high-resolution soil and terrain data, real-time meteorological observations, and high-resolution atmospheric forecasts. Continuous and long-term discharge measurements are also essential for flood monitoring, model calibration and warning threshold establishment. 3) NWP's still have uncertainties due to factors like ensemble size, model structure, and how e.g., small-scale convection processes are represented. Real-time quantitative precipitation by radar systems is underestimated and needs further post-processing. 4) The complexity of data integration and validation poses an additional challenge. The integration of workflow managers like ECMWF's workflow management system (ecFlow) (Bahra, 2011), complemented by a user-friendly graphical interface, streamlines the scheduling of operational services. This not only enhances user engagement and accessibility but also contributes to the optimisation of service delivery in real-time hydrodynamic modelling and forecasting. 5) Evaluating the performance of FEWS can be difficult, especially when hindcast data is not available and NWP models have limited operational history. Ensuring the reliability of FEWS is critical to respond quickly to predicted events. It helps avoid the cry wolf effect, where too many false alarms make people and authorities less likely to act promptly during real flood threats. 6) The prediction of rare, extreme flood events with return periods of more than a century is a challenge due to the limited data available, which emphasises the need for comprehensive training of flood-managers. 7) The introduction of real-time impact-based warnings should go along with the development of specific customised warning messages, action instructions and emergency decisions. In order to tackle this problem effectively, interdisciplinary cooperation with social and psychological sciences is required. 8) In a world where the likelihood of unprecedented rainfall and subsequent flooding is increasing, impartiality in the communication of information is critical. Ongoing calibration of hydrological component of operational FEWS is important to better anticipate flood events. Moreover, there is a growing demand to account for the most extreme events to avoid surprises of megafloods similar to the 2021 European Summer Flood (Bertola et al., 2023). The shift in thinking beyond national flood risk assessment and removal of cognitive biases are necessary to prevent unexpected surprises (Bertola et al., 2023; Merz et al., 2021).

Finally, more attention needs to be paid to the effective communication of forecast uncertainties. Uncertainties need to be propagated along the entire forecast chain delivering the plausible ranges of flood impact indicators. We believe that better informed decisions can be made given transparently presented uncertainties rather than single deterministic values. Future studies are needed to find out how the proposed impact-based FEWS can be used for better communicating the flood impacts to users, decision makers and the public. A subsequent investigation could involve seeking input from decision makers regarding their preferences for ensemble ranges.

2.4 METHODS

2.4.1 *Extended warning chain*

The extended warning chain (ICON_D2_EPS-mHM-RIM2D) is illustrated in Supplementary Figure 4. This model chain produces high-resolution impact forecasts indicating inundation depth and flow velocity at buildings and infrastructure. The four components of this chain are described below.

Meteorological inputs: The regional ensemble prediction system ICON-D2 EPS provides operational forecasts for a 48-h forecast horizon, covering the entire German territory. High-resolution forecasts of ICON-D2 (2.2 km) are initialised every 3 h with a convection-permitting model set-up suitable for early warning of local heavy rainfall events. Hydrological initial conditions are derived from near-real-time radar adjusted gridded hourly precipitation data provided by the DWD. The gridded fields of temperature were generated by using the External Drift Krigging (EDK) method (Zink et al., 2017) using variograms derived from DWD station observations.

Ensemble Hydrological forecasting: Streamflow and water level forecasts are generated based on mHM at a resolution of 1.1 km. The mHM uses multiscale parameter regionalisation for estimating distributed parameter fields (Samaniego et al., 2010) and is forced with real-time forecasts from DWD-ICON_D2_EPS for hindcast evaluation and hydrological predictability of the Ahr flood.

Hydrodynamic forecasting: The RIM2D hydrodynamic model was set-up and validation are described in a recent flood inundation simulation of the 2021 flood event for the Ahr valley (Apel et al., 2022). Flood inundation depth for HQ₁₀₀ was mapped first by running RIM2D. Then, the lead-time of water level forecasts exceeding the HQ₁₀₀ level was calculated for each raster cell at 10 m resolution downstream of the gauge Altenahr. The locations of buildings, roads and railways were extracted from the OpenStreetMap (OSM) layers. Hydrodynamic forecasts are triggered only upon reaching or exceeding pre-established warning thresholds customised for selected percentiles based on the user's specific interest. This automated trigger mechanism enhances the responsiveness and adaptability of the system accommodating real-time services easier. The RIM2D simulations are executed on the Graphical Processor Units (GPUs) to achieve high computational performance. Each ensemble run is allocated to a single Graphics Processing Unit (GPU) device allowing for parallel processing. While 20 ensemble members are available, our real-time forecasting focuses on selected percentiles with respect to peak discharge at the upstream boundary (minimum, 25%, median, 75%, and maximum). This approach ensures timely forecasts every 3 hours and is able to accommodate larger ensembles if needed.

Quantitative impact forecasting: Several criteria can be provided for impact forecasting including the object-based forecasting (e.g., buildings footprint), the length of roads and railways. This information are calculated based on the synthesis of data extracted from

open geographic database such as OSM (OpenStreetMap, 2017), and hydrodynamic forecasting outputs.

Copernicus Emergency Management Service (EMS) Mapping products: The Copernicus Emergency Management Service (CEMS) employs satellite imagery and additional geospatial data to respond to natural disasters, including floods. CEMS offers a variety of products that provide insights into the impact and reach of the event, including overall flood extent and detailed assessments of damage severity (*Copernicus EMS Mapping products, EMSR517 2023*). It provides information on affected buildings and infrastructures based on several detection methods such as semi-automatic and automatic extractions. We utilised the standard spatial datasets (vector data) from CEMS, which are publicly available free of charge (*Copernicus EMS Mapping products, EMSR517 2023*).

Comparison between forecasts of inundated building footprint with a benchmark: In this research, we analysed the number of affected building footprints, as well as the total lengths of roads and railways from RIM2D inundation forecasts by benchmarking them against established data sources. Our study utilised datasets from OSM and CEMS. The CEMS dataset provides valuable information on the extent and severity of flood impacts based on damage grades (ranging from damaged to potentially damaged and destroyed), their spatial distribution. The processing of this data involved several key steps: (1) CEMS data points corresponding to OSM building centroids were linked to the respective OSM building footprints; (2) in cases where multiple CEMS data points reported damage to the same OSM building, the OSM footprint was counted only once to eliminate duplication; and (3) CEMS data points lacking corresponding OSM building polygons were excluded from the analysis. We leveraged OSM data to furnish building footprints for structures affected according to the CEMS dataset. The processing and analysis were carried out using a combination of Python and R scripts, encompassing geospatial matching, damage statistics, and assessments of spatial distribution. Moreover, we compared the predicted inundation impact on building footprints for each initialisation with the total building footprint within the flood extent, as mapped by the LfU. This comparative analysis allowed us to thoroughly evaluate the accuracy and reliability of our predictive models.

2.4.2 Hydrological model setup and calibration

The mHM setup used in this study is based on Bodenübersichtskarte 1:200,000 (BUEK200) soil dataset (BGR, 2020). Soil layers are vertical discretized in four layers (0–5, 5–25, 25–60 cm and 60 cm - variable) in the mHM. More details regarding the mHM setup is described by Boeing et al. (Boeing et al., 2022). The corresponding mHM global parameters were calibrated using the Dynamically Dimensioned Search (DDS) (Tolson and Shoemaker, 2007) algorithm with 500 iterations, against observed hourly time series of river discharge at Altenahr gauge. A detail description of the procedure for calibrate mHM can be found in Rakovec et al. (Rakovec et al., 2019b). In the present case, we considered a 10-year simulation period (1.1.2011–31.12.2020) with five years of warm-up; thus the

July 2021 flood peak was excluded from the calibration exercise. Hourly Radar Online Aneichung (RADOLAN) grids of precipitation (Bartels et al., 2004; Winterrath et al., 2012) are adjusted to 24-h total precipitation (Rauthe et al., 2013) and used for model calibration. The mHM historical performance is provided in Supplementary Figure S5.

2.4.3 *Computational resources and data requirements*

The implemented near-real-time flood impact forecasting chain is applicable to other region around the world contingent upon the availability of specific quality data and appropriate computational resources. To ensure effective operation, it is necessary to generate frequent NWP of precipitation and temperature. Near real-time access to hourly precipitation and temperature observations is required for the regular reinitialisation of the mHM model. For the RIM2D hydrodynamic model, a high-resolution DEM and land-use information is required. We tackled the computational challenge inherent in real-time inundation forecasting through the utilisation of the massively parallelised Graphical Processing Units (GPUs) (Apel et al., 2022). Using the state-of-the-art NVIDIA Tesla P100 device, we achieved a 22-minute runtime for a 48-hour event simulation (one ensemble member) for the entire domain of about 30 km river length with a spatial resolution of 10 m by 10 m. We would like to emphasis here that all the underlying datasets and modelling tools which have been used in this study are available freely. To develop a similar system in other regions, high-resolution terrain information (DEM) along with morphological datasets (e.g., soil, vegetation, etc) would be needed. Additionally, access to near-real-time meteorological forcings and river gauge station data for model calibration can be acquired from responsible agencies. To this end, growing availability of remote-sensing and satellite based information can provide additional opportunities to reliably establish the FEWS in data-scarce regions.

2.4.4 *Definition of forecast persistency*

Probability of exceedance of a predefined warning threshold can rapidly change with subsequent forecast initialisations. A definition is provided for the confidence in the forecast information across different initialisations. Once three consecutive forecast initialisations show water levels above HQ_{100} for a given grid cell, the time span between the time point of the forecast initialisation and model time step corresponding to $WL \geq HQ_{100}$ for the third forecast is calculated as the lead-time. Definition of lead-time with and without confidence is provided in Supplementary Figure S6. Selecting the ideal number of forecast initialisations to establish forecast persistency can be determined by balancing the frequency of operational NWPs and the required preparedness time.

ENHANCING GLOBAL STREAMFLOW MODELING TO ENABLE LOCALLY RELEVANT SIMULATIONS

PK Shrestha^{1,2}, et al.

¹Computational Hydrosystems, Helmholtz Centre for Environmental Research – UFZ

²Institute of Environmental Science and Geography, University of Potsdam

Under consideration for publication in Water Resources Research

Shrestha, P. K., Samaniego, L., Rakovec, O., Kumar, R., Mi, C. X., Rinke, K., & Thober, S. (preprint). Enhancing Global Streamflow Modeling to Enable Locally Relevant Simulations. ESS Open Archive.

SUMMARY

Large-scale hydrological models are advancing towards sub-kilometer resolutions, aiming to achieve “locally relevant hydrological simulations”. However, grid-based domain representations create significant errors in small catchments, underscoring the catchment size problem, a conundrum unsolved by the state-of-the-art modelling schemes (e.g, D8). Here, we equip the grid-based mesoscale Hydrologic Model (mHM) with a novel stream network upscaling scheme called Subgrid Catchment Conservation (SCC) that preserves the subgrid catchment area, and allow for a seamless predictions of water fluxes and storage at different spatial resolutions and across a variety of catchment sizes. We employ a global setup with 62 domains encompassing 5 256 streamflow measurement stations, and a regional setup encompassing 187 stations in the Rhine river basin. SCC produces consistent performance over various catchment sizes globally, outperforming the D8 and other state-of-the-art routing schemes. The widely used D8 scheme’s efficacy diminishes drastically for catchments under 30 times the grid size, while SCC excels when D8 area errors exceed 1%. SCC demonstrates remarkable streamflow scalability in the regional experiment with nine out of 10 stations exceeding the mean flow benchmark across 1 km to 100 km model resolutions (and eight out of 10 stations in the global setup across 25 km to 100 km). In addition to the improved streamflow scalability, SCC’s ability to resolve multiple points of interests in a grid leads to greater modelling flexibility. By addressing the catchment size problem, SCC marks a significant advancement for global-scale simulations producing locally relevant streamflow.

3.1 INTRODUCTION

Global hydrological models (GHMs) are predominantly gridded (Bierkens, 2015). The gridded simulation of hydrological states and fluxes enables distributed analyses at

any point in the domain (Kumar et al., 2010; Rakovec et al., 2016b), which is a major advantage of gridded hydrological models over others. Moreover, input data typically come in grid format (Sood and Smakhtin, 2015), encompassing a wide array of sources including remote sensing products, reanalysis datasets, climate change projections, and (sub-)seasonal forecasts. Gridded hydrological models, thus, eliminate the need for extensive aggregation or manipulation of data, streamlining the modeling processes.

In spite of the advances such as incorporation of reservoirs (Hanasaki et al., 2006; Haddeland et al., 2006a; Shin et al., 2019; Sadki et al., 2023; Shrestha et al., 2024), water use (domestic, irrigation, industrial)(Döll and Siebert, 2002; Alcamo et al., 2003; Wada et al., 2013; Flörke et al., 2013), groundwater abstraction (Wada et al., 2010), hydrodynamic routing (van Beek et al., 2011), floodplain inundation (Yamazaki et al., 2011), and streamflow temperature (Wanders et al., 2019), global hydrological models have not been able to abolish the “catchment size problem” (Fekete et al., 2001; Hanasaki et al., 2006; Yamazaki et al., 2008; Wu et al., 2011; Thober et al., 2019; Eilander et al., 2021; Aerts et al., 2022; Polcher et al., 2023):

While modeling a large domain with multiple catchments, grid based representation incurs errors in modelled catchment area, the magnitude of which might be hardly noticeable for large catchments and beyond acceptable for smaller catchments, simultaneously. Compounding the issue, the size of the catchment is relative to the grid size. The catchment size problem hampers continental-scale streamflow modeling, constraining analyses to larger basins and resulting in diminished accuracy for smaller catchments in global hydrological models. Ironically, the majority of the discharge stations worldwide are small e.g., 75% of Global River Discharge Centre (GRDC) stations have a drainage area of 10 000 km² or less (GRDC, n.d.). It is undeniable that accurate streamflow simulations are as important at the local points of interest as at the outlets of large basins. Achieving locally relevant streamflow (Bierkens et al., 2015a) is akin to, thus, possessing “eagle vision” in global streamflow modeling – a capability that the current GHMs lack.

Table 3.1 provides insight into recent studies on large-scale streamflow applications, highlighting three major characteristics of the state-of-the-art. Firstly, to circumvent the catchment size issue, the majority of studies predominantly exclude small catchments, commonly setting a cutoff at 10 000 km². Second, none of the referenced studies demonstrate scenarios where multiple streamflow stations fall within the same grid. This absence is largely anticipated, given the substantial cutoff values applied to catchment areas, inherently preventing such occurrences. Thirdly, the majority of cited works involve analyses relying on streamflow simulations at a single routing resolution. Notably, Thober et al. (2019) was among the first to conduct multiscale routing experiment at large-scale (Europe) which was then followed by more recent works (Eilander et al., 2021; Aerts et al., 2022; Polcher et al., 2023). Scalability of streamflow simulations in adopted modelling schemes, however, hugely depends on the precision of catchment area modelled across the spatial resolutions, thereby reiterating the connection back to the catchment size problem.

Table 3-1: A non-exhaustive list comparing the stream network representation of recent studies assessing streamflow hydrology at large scale

Study/ hydrology or land surface/ routing model or scheme	A cutoff/ stations included	Resolves multi-station grids?	Routing resolutions employed	Grid outflow	Stream network scheme
This study / mesoscale Hydrologic Model (mHM) / mRM	$A \geq 1 \text{ km}^2 / n = 5256$	yes (demonstrated)	1, 3, 6, 12, 25, 50, and 100 km	≥ 1	SCC (in-built upscaling)
State-of-the-art in chronological order (most recent to older)					
Polcher et al. (2023) / ORCHIDEE / Linear reservoir	$A > 2500 \text{ km}^2 / n = 35$	yes (theoretically)	11, 20 km, 0.25°, 0.5°	> 1	HTU (pre-processor)
Hou et al. (2023) [†] / 12 Climate models (CMIP6), 6 GHMs (ISIMIP2a), 3 LSMs (GLDAS) / CaMa-flood	$A > 10000 \text{ km}^2 / n = 840$	no	0.25°	1	FLOW with Unit catchment (MERIT Hydro)
Grogan et al. (2022) / WBM v1.0.0 / Linear reservoir	A cutoff NA / $n = 666$	no	5'	1	D8 (MERIT 5')
Aerts et al. (2022) / wflow_sbm / Kinematic wave	A cutoff NA / $n = 454$	no	200 m, 1 km, 3 km	1	D8 (MERIT Hydro)
Eilander et al. (2021) / Synthetic runoff / Kinematic wave	A cutoff NA / $n = 500$	no	30'', 5', 15'	1	IHU (D8) (in-built)
Stacke and Hagemann (2021) / HydroPy (previously MPI-HM) / HD-Model	A cutoff NA / $n = 100$	no	0.5°	1	D8 (input)
Harrigan et al. (2020) / HTESEL / LISFLOOD	$A \geq 575 \text{ km}^2 / n = 1801$	no	0.1°	1	D8 (input)
Burek et al. (2020) / CWaM / Kinematic wave	$A > 9000 \text{ km}^2 / n = 1366$	no	5', 30'	1	D8 (input)
Droppers et al. (2020) / VIC-WUR (based on VIC-5) / VIC-5	$A > 20000 \text{ km}^2 / n = 462$	no	0.5°	1	D8
Müller Schmied et al. (2020) / WaterGAP 2.2d / Linear reservoir	A cutoff NA / $n = 1319$	no	0.5°	1	Döll and Lehner (2002) (D8) (input)
Thober et al. (2019) / mHM / mRM	$A > 100 \text{ km}^2 / n = 622$	no	1, 2, 3, 4, 6, 8, 12, 16, 24, 48 km	1	Döll and Lehner (2002) (D8) (in-built upscaling)
Hanasaki et al. (2018) / Ho8 / TRIP	A cutoff NA / $n = 12$	no	0.5°	1	Döll and Lehner (2002) (D8) (input)
Sutanudjaja et al. (2018) / PCR-GLOBWB v1 and v2 / Travel time routing	$A \geq 10000 \text{ km}^2 / n = 3597$	no	5', 30'	1	Döll and Lehner (2002) (D8) (input)
Zhao et al. (2017) [‡] / 9 GHMs (ISIMIP2a) / CaMa-flood	$A > 9000 \text{ km}^2 / n = 2906$	no	0.25°	1	FLOW with Unit catchment (HydroSHEDS and GDBD)
Li et al. (2015) / CLM4 / MOZART	$A > 10000 \text{ km}^2 / n = 1674$	no	0.5°	1	D8 (input)

[†] - CMIP6: CABLE2.4, CLM4.5, CLM5, HAL1.0, JSBACH2.0, MATSIRO6.0, Noah v2.7.1; ISIMIP2a: DBH, Ho8, LPjml, MATSIRO, PCR-GLOBWB, VIC; GLDAS: CLSM, Noah, VIC

[‡] - ISIMIP2a: CLM, DBH, Ho8, LPjml, MATSIRO, MPI-HM, ORCHIDEE, PCR-GLOBWB, WaterGAP2

To minimize errors at the smallest of the catchments and, thus, achieve locally relevant (streamflow) simulations, the global hydrological modeling community has seen recent efforts in the direction of high resolution simulation, ushering the era of hyperresolution modeling at global scale (Wood et al., 2011a; Bierkens et al., 2015a). However, computational cost remains as the major bottleneck in hyperresolution streamflow modeling, a fact underscored by the constrained geographical coverage evident in the few applications observed thus far ($1^\circ \times 1^\circ$ block, USA (Chaney et al., 2021), and Kyushu, Japan (Hanasaki et al., 2022)).

This begs the question: *Is there an alternative to hyperresolution modeling for achieving locally relevant streamflow simulations?*

The answer to the above question lies in the manner in which river networks are represented, a sub-field of hydrological modeling which has undergone a long and evolving history of development (refer Figure 3.1). O'Callaghan and Mark (1984) coined the concept of eight flow directions (D8) whereby all runoff from a grid has to flow to one of its eight neighboring grids i.e., a grid-to-grid routing method. D8 formed the basis for lateral flow directions in major large-scale routing models such as TRIP (Oki and Sud, 1998), mRM (Samaniego et al., 2010; Kumar et al., 2010; Thober et al., 2019), LISFLOOD (Burek et al., 2013), MOSART (Li et al., 2013), and is still the de-facto method in many state-of-the-art applications (refer Table 3.1). There have been many versions of the D8 over the years (Döll and Lehner (2002), double maximum method (Olivera et al., 2002), cell outlet tracing with an area threshold (Reed, 2003; Paz et al., 2006), effective area method (Yamazaki et al., 2008)), all of which can be traced back to one of the three pioneering D8 methods: O'Donnell et al. (1999), Wang et al. (2000), and Fekete et al. (2001). One of the common drawback of the D8 methods is the need for manual correction wherever an automatic upscaling algorithm leads to breaking of the upstream-downstream grid relationships, especially at the small catchments. The iterative hydrography upscaling approach (Eilander et al., 2021) automatized this correction through a 12-step iterative procedure. Yamazaki et al. (2009), however, argued such correction weakened the connection between the upscaled river network map and the original flow direction map, consequently nullifying the fine-resolution information. The issue was circumvented by the introduction of methods such as the flexible location of waterways method (Yamazaki et al., 2009) and the dominant river tracing method (Wu et al., 2011) that deviated from the traditional D8, allowing non-neighboring grids to be related as upstream-downstream, giving a "jumping" impression on the upscaled stream network map (refer to Sect. 3.2.3 for further discussions).

Despite of the improvements, the major drawback of the grid-to-grid methods remained – the least count of the modelled catchment area is the grid size. This lead to vector based routing concepts and models like Routing Application for Parallel computation of Discharge (RAPID) (David et al., 2011), unit catchment (Yamazaki et al., 2013), HydroROUT (Lehner and Grill, 2013), Highly Parallelizable and scalable Routing scheme (HYPERstream) (Piccolroaz et al., 2016), MizuRoute (Mizukami et al., 2016), and

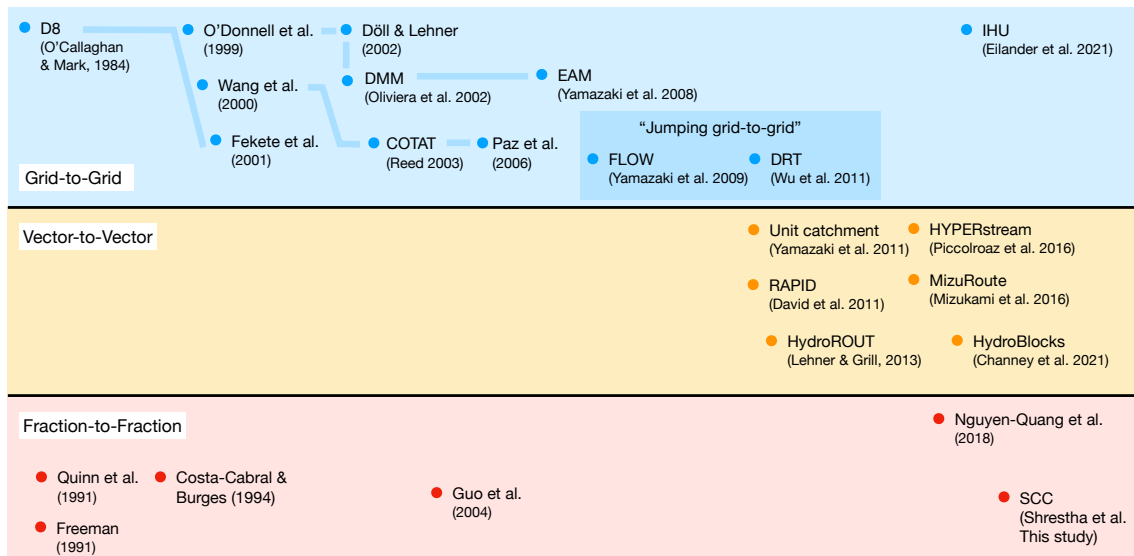


Figure 3.1: Genealogy of stream network upscaling methods in hydrological modeling. DMM – double maximum method, COTAT – cell outlet tracing with an area threshold, Effective Area Method (EAM) – effective area method, FLOW – flexible location of waterways, Dominant River Tracing (DRT) – dominant river tracing, IHU – iterative hydrography upscaling, SCC – subgrid catchment contribution.

more recently, HydroBlocks (Chaney et al., 2021). These vector-to-vector methods rout the gridded runoff from a vector shape to the downstream vector shape, thus, completely preserving the basin shape and drainage area at the vector outlets. However, this meant vector-to-vector methods had to decouple from the grid system of global hydrological or land-surface models.

It became increasingly clear that tackling the catchment size issue and preserving grid compatibility would necessitate the development of methods enabling multiple outflow directions from a grid i.e., multiple downstream connectivity (Mateo et al., 2017). Wu et al. (2011) highlighted such multiple flow direction algorithm could be the best way to preserve subdominant rivers. Early attempts of multiple downstream connectivity allocated flow fractions from a grid to downstream grids with the help of slope (Quinn et al., 1991; Freeman, 1991) or aspect angle (Costa-Cabral and Burges, 1994). Guo et al. (2004) proposed to use accumulated contribution area of outlet pixels on each of the four edges of a grid to allocate flow fractions to the cardinal flow directions. Nguyen-Quang et al. (2018) improved this approach, renamed the accumulated contribution area as hydrological transfer units (HTUs), and check the HTUs for user defined threshold for size and minimum count per grid. These (grid-)fraction-to-(grid-)fraction methods have shown improved scalability and preservation of small catchments relative to the grid-to-grid methods (Guo et al., 2004; Liang et al., 2004; Wen et al., 2012; Nguyen-Quang et al., 2018; Polcher et al., 2023).

Streamflow spatially and temporally integrates the range of meteorological variables and basin characteristics (Burek and Smilovic, 2023), has an extensive history of measurement, is the focal point of seminal hydrologic research over the years, making it the fundamental variable in hydrological modeling. Consequently, it is imperative for GHMs to possess flexibility in accurately predicting streamflow at predefined “points of interest” in a range of model applications, such as seasonal flood forecasting at particular sets of river reaches (Copernicus Climate Change mULTi-model hYdrological SeaSonal prEdictionS system (ULYSSES) project, <https://www.ufz.de/index.php?en=47367>) or evaluating the state of global water resources based on specific basin outlets (WMO, 2023a). From this perspective, the current fraction-to-fraction methods still present two major drawbacks. First, runoff partitioning is either system generated or user controlled, as fractions per grid. This means the catchment areas at predefined locations are again dependent on the resolution of the fractions, leading us back to the catchment size problem. Vector-to-vector methods share this drawback since the vector outlets are also system generated. Second, unnecessary partitioning of grids elsewhere in the domain by employing four (Guo et al., 2004) or eight grid fractions (a minimum as recommended by Nguyen-Quang et al. (2018)) substantially escalates the overall routing runtime.

Motivated by these gaps identified, we developed Subgrid Catchment Contribution (SCC) technique which leverages subgrid catchment at predefined locations, such as streamflow stations and dams, to partition grid runoff. SCC can be considered as a user-driven enhancement of the D8 technique, enabling contiguous representation of streamflow network schemes for a seamless streamflow predictions across a variety of spatial resolutions and catchment sizes. In summary, the modeller has now the possibility to provide as many points of interest as necessary to obtain accurate streamflow simulations regardless of the modeling resolution of the hydrological model. SCC is model agnostic and can be easily integrated in any routing algorithm. The user-driver enhancement of the upscaled stream network ensures perfect catchment conservation while minimizing grid partitioning, thereby, optimizing computational cost of routing for any given set of points, at any model resolution. We test the following three hypotheses in this study:

1. SCC preserves the catchment area at predefined points of interest across all model resolutions.
2. Maintaining the catchment area results in improved and consistent model performance across all resolutions and catchment sizes. Therefore, *SCC effectively eliminates the catchment size problem* in gridded hydrological models.
3. By preserving the catchment area, it becomes possible to estimate streamflow at multiple gauging stations or points of interest within a grid cell, regardless of the resolution.

It is important to clarify that the error in the modeled catchment area comprises of two components. The first component is the error in the catchment area as modeled by the upscaling scheme at the model resolution, relative to the DEM-based catchment area, which is the model input at the subgrid resolution. The second component is the error in the DEM-based catchment area relative to the reference catchment area, such as the reported values in the GRDC database. Numerous past studies have focused on this second error component, leading to improved global-scale DEM products like MERIT Hydro (Yamazaki et al., 2019) and the forthcoming HydroSHEDS version 2 (Warmendinger et al., 2023). However, the focus of this study is on evaluating the ability of upscaling schemes to model the input DEM-based catchment. Therefore, errors in the input DEM itself fall outside the scope of this study.

We integrate SCC into the mesoscale Hydrologic Model (mHM) (Samaniego et al., 2010; Kumar et al., 2013; Thober et al., 2019), as an enhancement to the default D8 (Döll and Lehner, 2002) method. The user has the option to activate SCC and conserve the catchment at input locations of interests such as streamflow gauges and dams. In this study, mHM internally upscales a high resolution DEM (220 m) (level-0) and we validate the resulting streamflow simulations globally, at 5 256 locations, across 25 km to 100 km grids. Additionally, we conduct regional validation in the Rhine River Basin, examining 187 locations, across 1 km to 100 km grids. The catchment sizes of the locations span from 1 km² to 4 680 000 km². It should be noted that the higher the resolution of the level-0 DEM, the greater the accuracy of the catchment delineation, and the higher the computational cost for the river network upscaling. This task however can be done a single time and stored in the restarting file of mHM.

3.2 METHODS

3.2.1 mHM – the mesoscale Hydrological Model

The mHM (Samaniego et al., 2010; Kumar et al., 2013; Thober et al., 2019) is a fully distributed hydrologic model developed to provide seamless prediction of hydrological fluxes and storages at multiple spatial resolutions and locations (Samaniego et al., 2017) across the globe (Zink et al., 2016; Thober et al., 2018; Rakovec et al., 2019a; Saha et al., 2021). The model includes process representations for canopy interception, snow accumulation and melt, soil moisture and evapotranspiration, surface and subsurface runoff generations, deep percolation and baseflow, flood routing along with a river network, and reservoirs and lakes. mHM uses the Multiscale Parameterization Regionalization technique (Samaniego et al., 2010) which includes the regionalization and spatial scaling approaches to generate a set of regionalized model parameter fields at required modeling resolutions, while explicitly accounting for the sub-grid variability of the fine-scale information on terrain, soil, vegetation, and other landscape properties (Kumar et al., 2013; Rakovec et al., 2016a; Samaniego et al., 2017).

mHM has four different resolutions for data and simulations (refer B.2). The subgrid data and the meteorological data are represented by ℓ_0 and ℓ_2 , respectively. The two remaining model resolutions, ℓ_1 and ℓ_{11} , are hydrological and routing resolutions, respectively. ℓ_1 and ℓ_{11} are user-prescribed where ℓ_{11} could be set greater or lesser than ℓ_1 depending on whether we want to reduce runtime resulting from streamflow routing or enhance the intricacy of streamflow representation. mHM uses the ℓ_1 cell as a primary hydrologic unit for water balance. Prior to this study, mHM considered the ℓ_{11} cells as the primary routing unit for streamflow. In this previous approach, ℓ_0 stream network was upscaled to ℓ_{11} by the multiscale routing model, mRM (Samaniego et al., 2010; Thober et al., 2019) following the nomenclature of the D8 method (O’Callaghan and Mark, 1984), employing the method of Döll and Lehner (2002) i.e., the flow direction at ℓ_{11} is equal to the flow direction in the underlying ℓ_0 with the highest flow accumulation (Thober et al., 2019).

3.2.2 SCC – a novel stream network upscaling scheme

In this study we equip the multiscale Routing Model (mRM), the routing module of mHM, with the newly developed Subgrid Catchment Contribution (SCC) upscaling scheme. SCC was initially tested in Shrestha et al. (2024) for delineating water bodies and estimating the inflow. Figure 3.2 is a schematic representation showing the difference between SCC and the D8. The figure includes two points of interest, π_1 and π_2 , and their corresponding catchments at subgrid (ℓ_0) level. For simplicity, here we select four grids, G_1 to G_4 , as representation of the modeling grid system, G , at ℓ_{11} resolution.

For the D8, the stream network, \mathcal{N} , is comprised of nodes N and links L as depicted in Figure 3.2. Each ℓ_{11} grid can only have a single node located at its centre. Furthermore, a given link routes the runoff generated within a grid towards its neighboring cell, which is also represented by a single node. The concentration time within a grid is neglected considering that the resolution of the cells is nowadays less than 100 km (this a common assumption in D8 implementations). It should be noted that the routing algorithm need to adjust the routing time for the corresponding spatial resolution (see Thober et al. (2019)). The direction of the link goes in the direction of the edge at which the maximum flow accumulation is at the ℓ_0 level. The catchments at the points of interest π_1 and π_2 do not have any effect on \mathcal{N} for the D8 scheme.

In contrast, the SCC allows a ℓ_{11} grid to have more than one node based on the catchments at π_1 and π_2 . For instance, grid G_2 has three nodes, two corresponding to the points π_1 and π_2 and one that is not flowing towards any of the input points denoted here by π_0 . Each of these nodes, η_2^1 , η_2^2 , and η_2^0 , route water individually to neighboring node. Similar to the D8, the links λ_1^1 , λ_3^2 , and λ_5^0 follow the edge containing the maximum flow accumulation at ℓ_0 level. In this sense, SCC can be considered as an improved version of the D8, where the nodes N are split into η s and links L are split into λ s, based on the catchments at π s, to form the stream network \mathcal{N} . In general, η_i^k denotes a split node at grid i originated by the point of interest k . Likewise for λ_l^k , l indicates a running index

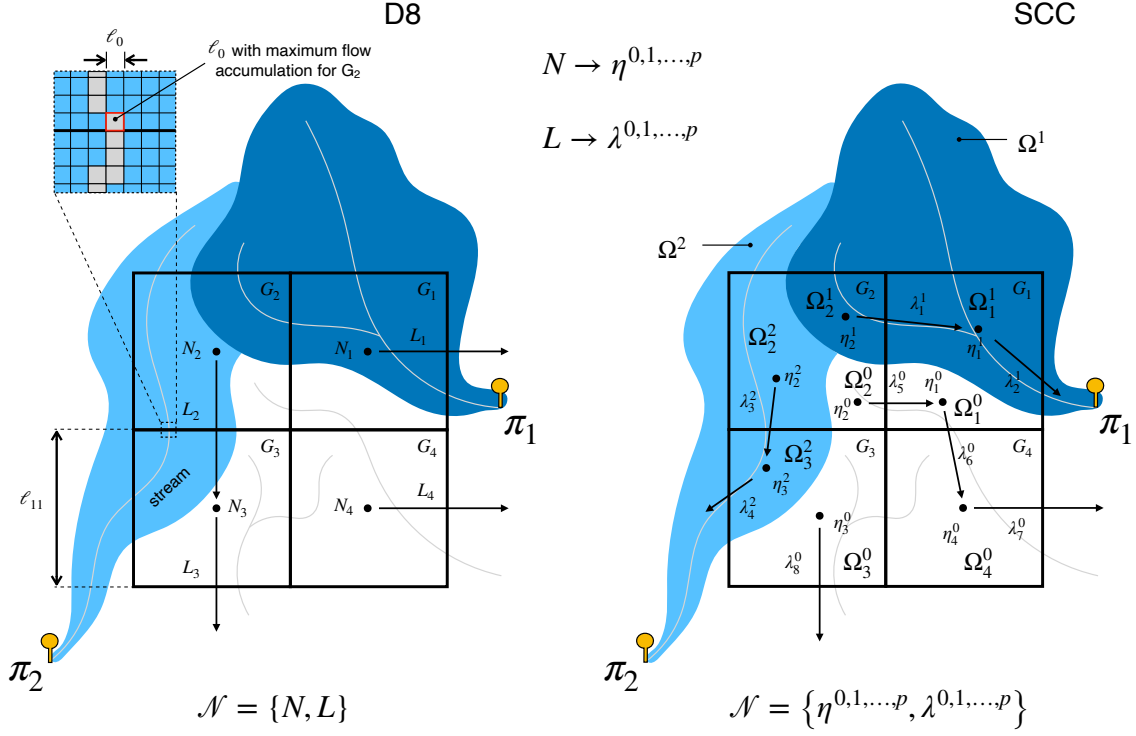


Figure 3.2: Schematic representation illustrating the differences between the D8 and SCC stream network upscaling schemes. π - user-provided points of interest, Ω - (fraction of) catchments at π s, G - model grid structure, ℓ_0 - subgrid resolution, ℓ_{11} - model resolution, \mathcal{N} - upscaled (model) stream network comprising of nodes and links. N & L - nodes and links for D8, η & λ - nodes and links for SCC. p - number of points of interest.

for the network and k is the point of interest that generates the link. It should be noted that in the SCC scheme, all points of interest π_k , except for π_0 , are user-provided.

It is noteworthy that the nodes at the grids contributing solely to π_0 (e.g., G_4) remain intact with SCC, and behave exactly as it would with D8. We would also like to point out that the following two relationship always holds true for SCC:

$$(\Omega^k \cap G) \stackrel{!}{=} \sum_{i=1}^n \Omega_i^k \quad (3.1)$$

$$G_i \stackrel{!}{=} \bigcup_{k=0}^m \{\Omega_i^k\}, \quad (3.2)$$

where, i is the index for each model grid, k is the index for each user-provided point of interest. Ω^k is the catchment shape at π_k , and Ω_i^k is the fraction of this catchment shape at grid i . G denotes the overall modeling domain, and G_i denotes a given individual grid

i. m is the number of nodes in G_i , which could be one or more, and n is the total number of model grids in G . Relationship 3.1 ensures the intersection of the catchment shape of π_k and model grid to be equal to the sum of all grid fractions corresponding to π_k , across the model domain. Relationship 3.2 ensures the area of each ℓ_{11} grid to be equal to the union (sum) of all fractions within a given grid i .

SCC internally upscales the subgrid (ℓ_0) stream network to the routing resolution (ℓ_{11}) specified by the user. We illustrate the procedure with a real world example shown in Figure 3.3. This example domain consists of four points of interest consisting in four streamflow gauge stations, $D1$ to $D4$. Using ℓ_{11} as the routing unit leads to several challenges in this domain. Firstly, the points $D1$, and $D3$ fall under the same ℓ_{11} grid, leading to both being assigned the same streamflow value (refer to panel *e*). Secondly, the catchment at point $D4$ is smaller than a single ℓ_{11} grid, resulting in an overestimated outflow at $D4$. Lastly, the inherent irregular shapes of all catchments deviate significantly from regular grids, introducing varying degrees of error in the estimated catchment area. By permitting routing units to be fractions of the ℓ_{11} grid (refer to panel *h*), SCC ensures the preservation of catchment drainage areas (at the prescribed locations), resolving the aforementioned challenges. This refined approach results in individual outflows being accurately issued at points $D1$ and $D3$. The outflow at small catchments such as $D4$ is generated from an unbiased drainage area, mitigating overestimation. Furthermore, all irregular shapes of the catchments are preserved, ensuring the correct contribution of the drainage area to outflows at each streamflow gauge.

Generally, SCC upscales the ℓ_0 stream network as follows. The first step is to produce a map (\mathcal{M}') of catchments delineated at all the points of interest (Figure 3.3a-d). Special care is taken to preserve smaller upstream catchments in this map. It's worth highlighting that the correct location of the points of interest on the ℓ_0 flow accumulation, F_a , is crucial for accurate catchment delineation. To ensure this alignment, we employ Basinex (Developers, 2022) (see the Software Availability section) to associate the station locations to the nearest stream that would give the least error in the recorded catchment area. The second step includes initialization of the routing units denoted by the nodes depicted in Figure 3.3e-f. The node geometries are derived from the features resulting from the spatial union of ℓ_{11} grid and \mathcal{M}' . Hence, each sub-catchment, i.e., the fraction of catchment at each grid, is established as a node geometry. The final step finds the upstream-downstream pairs of nodes and connects them in the direction of flow (Figure 3.3g-h). These upscaled flow direction forms the upscaled stream network of the domain. The detailed procedure for these three steps are provided by the algorithms in B.3. It should be noted that for a grid cell where no point of interest is prescribed (see panel *h* top left cell), the standard mRM (D8) procedure is still applied as was originally in mHM (Samaniego et al., 2010) and in mRM (Thober et al., 2019) as stand alone routing algorithm.

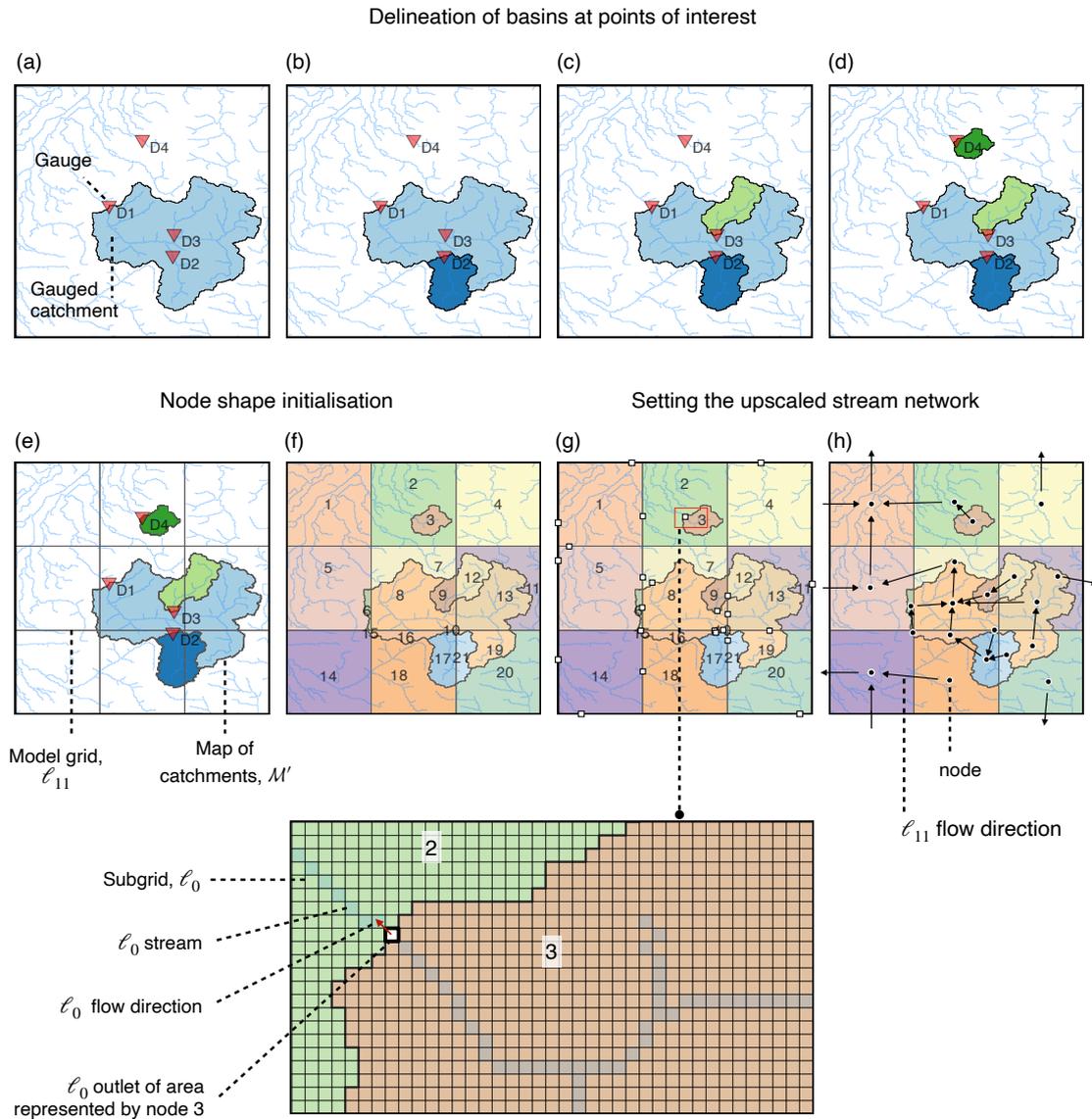


Figure 3.3: Example showing upscaling of subgrid streamflow (skyblue lines) to model streamflow network (black arrows) using SCC. (a-d) delineation of catchment at GRDC stations and merging of the catchments in the order of subgrid flow accumulation at the stations. (e) overlaying of the map of catchments, \mathcal{M}' , with the ℓ_{11} grid. (f) establishing of nodes shapes with node ID shown as labels. (g) identification of subgrid outlets at each node shape. (h) upscaled streamflow shown as flow direction arrows joining the upstream and downstream nodes. Note: the centroids represent nodes for linking the upscaled flow direction. The centroids of nodes with irregular shapes could fall outside the node geometry.

Once the upscaled stream network is ready, mRM routes the streamflow through the links connecting the subgrid outlets of the upstream and downstream nodes. The routing scheme employed could be the Muskingum-Cunge or the kinematic wave equation. In both cases, their link parameters are regionalized as explained in (Thober et al., 2019). The step-by-step algorithm for routing streamflow is provided in B.4.

3.2.3 Visualizing the advantages of the SCC scheme in a real case

Figure 3.4 compares the stream network upscaled to 1° using D8, Flexible LOcation of Waterways (FLOW) (Yamazaki et al., 2009; Yamazaki et al., 2013), and SCC against the base map of subgrid stream network, at the Hengduan Mountain region. Both FLOW and SCC are seen to preserve the subgrid river network e.g., the Mekong starts from pixel *A1* and ends at pixel *J6*. At 1° routing resolution, D8 incorrectly drains the upstream areas of Mekong and Salaween to the Yangtze. Similarly, both FLOW and D8 incorrectly allocate all the runoff generated at pixel *E4* to the Salaween river, at the given resolution. A notable aesthetic issue in visualisation with FLOW is the unnatural “jumping” artifact. For example, FLOW requires external specification on the stream network to jump from pixel *D4*, over neighbouring grids, to reach pixel *G5* and preserve the continuity of the Mekong river in the model. In contrast, SCC stands out and distributes the streamflow from the *E4* pixel to the Irrawady, Salaween, Mekong and Yangtze rivers alongside the corresponding routed streamflow from upstream. By doing so, SCC automatically delineates and conserves the subgrid catchments of Mekong in the *D4*, *E4*, *F4*, and *F5* pixels as individual nodes, connecting each node to the corresponding downstream node to finally arrive at pixel *G5*. Hence, SCC produces a more realistic catchment-continuum over the neighboring grids – a capability not attainable with FLOW.

3.2.4 Data and modeling procedure

The mHM model input includes subgrid data, meteorological forcings, and the streamflow data. All the subgrid input were pre-processed at $\ell_0 = 1/512^\circ$ resolution. This includes the Global Multi-resolution Terrain Elevation Data (GMTED) (USGS and NGA, 2018) as the DEM. The ℓ_0 flow direction (F_d), flow accumulation (F_a), and other DEM derivatives were based on GMTED. We use the SoilGrids (ISRIC - World Soil Information, 2017) soil maps and Global Lithological Map (GLiM) (Hartmann and Moosdorf, 2012) geological maps to derive the subsurface properties. The land cover is based on GlobCover (European Space Agency (ESA), Universit Catholique de Louvain, 2009) with monthly leaf area index climatology from Global Inventory Modeling and Mapping Studies (GIMMS) (Tucker et al., 2004). The model is forced with daily ERA5 (Copernicus Climate Change Service, 2017) meteorological forcings at $\ell_2 = 1/4^\circ$. The daily streamflow observation time series are taken from the Global River Discharge Centre (GRDC)(<http://www.bafg.de/GRDC/>),

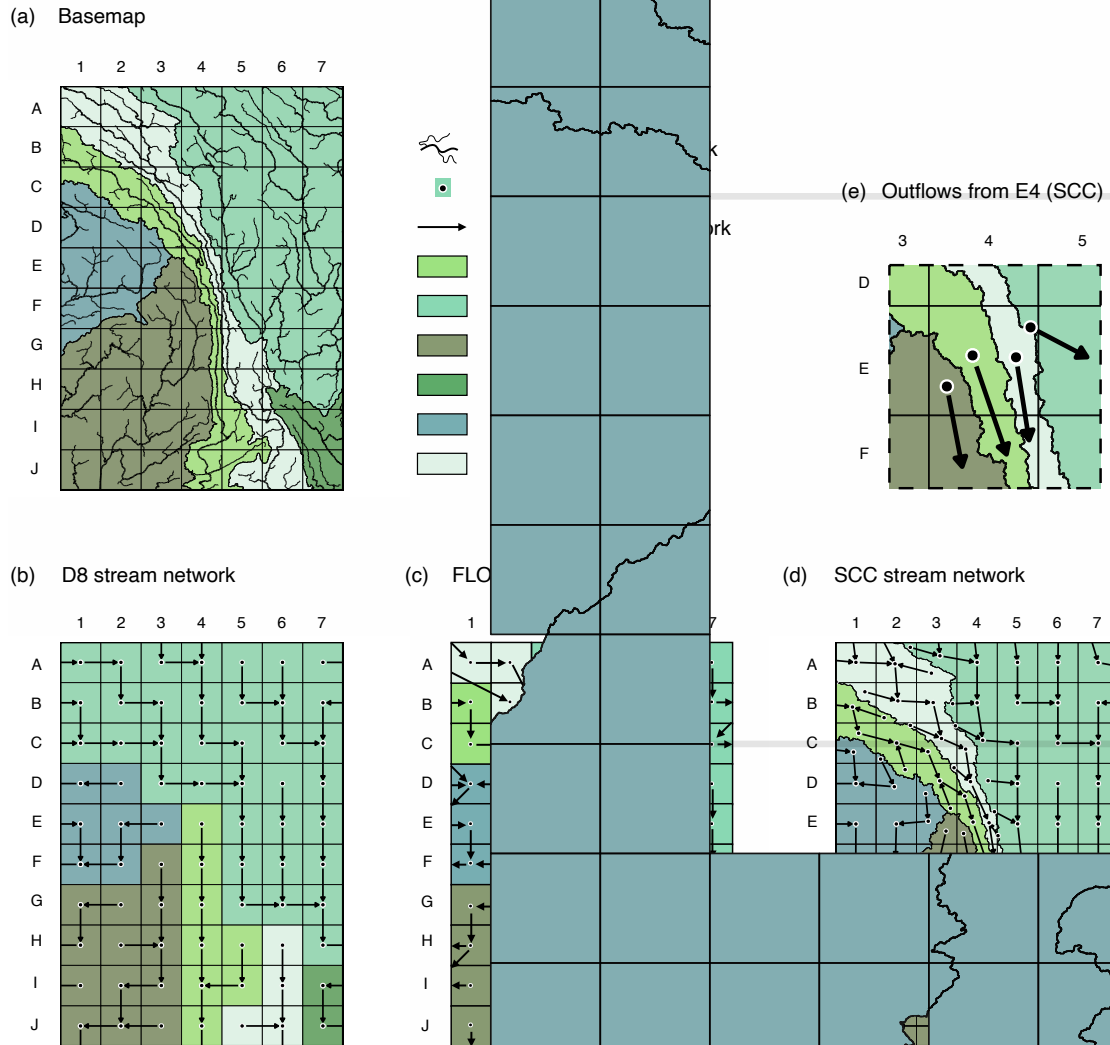


Figure 3.4: Hengduan Mountains at one degree resolution, with the Irrawaddy, Salaween, Mekong, and Yangtze rivers running parallel to each other. Comparison of (a) the base map subgrid stream network (source: HydroRIVERS, <https://www.hydrosheds.org/products/hydrorivers> downloaded on 27.08.2023 ©HydroSHEDS), against the stream network upscaled by the (b) D8, (c) FLOW, and (d) SCC schemes. (e) Zoom-in of the pixel E4 showing the multiple outflowing links using SCC. The stream network upscaled using FLOW is an adapted version of Figure 6 in Yamazaki et al. (2009).

and Centro de Estudios y Experimentación de Obras Públicas (CEDEX). The records of the station coordinates and catchment area are also taken from the corresponding database.

The hydrologic model parameters are set to default values, which are previously obtained from Kumar et al. (2013). We evaluate the performance of mHM using the streamflow observations available between 1961 and 2020, while keeping the preceding

ten years as spin up to stabilize relevant states of mHM (e.g., root-zone soil moisture). The availability of daily streamflow data is presented in Figure B.1a.

3.2.5 Modeling domain and experiment design

This paper presents two sets of experiments. First, the regional scale experiment that involves testing the model at seven different resolutions of $1/64^\circ$, $1/32^\circ$, $1/16^\circ$, $1/8^\circ$, $1/4^\circ$, $1/2^\circ$, and 1° . For simplicity, from this point onwards, these resolution will be referred to as 1 km, 3 km, 6 km, 12 km, 25 km, 50 km, 100 km, respectively. This experiment focused on the Rhine River basin and incorporated 187 (internal) streamflow gauging stations (refer to Figure 3.5b). The second experiment focused on the global scale analysis that is conducted at resolutions of 25 km, 50 km, and 100 km. This encompasses 5 256 streamflow stations distributed across 62 model domains defined by the HydroBASINS (Lehner and Grill, 2013) level 2 classification (see Figure 3.5a). This approach enables the examination of the effects of SCC both globally and at a fine resolution of 1 km.

The choice of HydroBASINS level 2 classification for the global scale setup was deliberate, ensuring computational feasibility for upscaling the 220 m subgrid stream network to a 25 km model resolution within the largest domain. The Rhine basin, on the other hand, contains a wide range of catchment sizes at provided streamflow stations (1 km^2 to over $150\,000 \text{ km}^2$). Some of the stations are in close proximity to each other which helps to test SCC's ability to resolve streamflow at multiple stations within a grid. Further more, the data availability on average is 47 years, making the Rhine basin an apt case for the regional scale experiment.

The streamflow stations included in this study meet the criteria of having daily measurements for a minimum span of five years since 1961 (see Figure B.1a). For approximately 90% of these stations, the DEM based catchment area (A_d) is within $\pm 10\%$ of the GRDC or CEDEX reference values (A_r) (see Figure B.1b). Nevertheless, as our primary focus is on evaluating the model's ability to preserve subgrid details of the DEM and the error in the DEM is merely a side note. In other words, we use the DEM catchment area (A_d) as the reference for evaluating the modelled area (\hat{A}).

To examine the first hypothesis – that “SCC preserves the catchment area at predefined points of interest across all model resolutions” – we conduct a comparative analysis between the modeled catchment areas and the DEM based catchment areas within the context of the global-scale experiment. We compare the results against the reported results of the state-of-the-art stream network upscaling schemes including FLOW (Yamazaki et al., 2009; Yamazaki et al., 2013) and IHU (Eilander et al., 2021).

Testing the first part of the second hypothesis – “Maintaining the catchment area results in improved and consistent model performance across all resolutions” – we check the hydrographs at selected stations of the regional scale experiment to see the effect of scalability across 1 km to 100 km. Finally, we inspect the CDFs of performance metrics

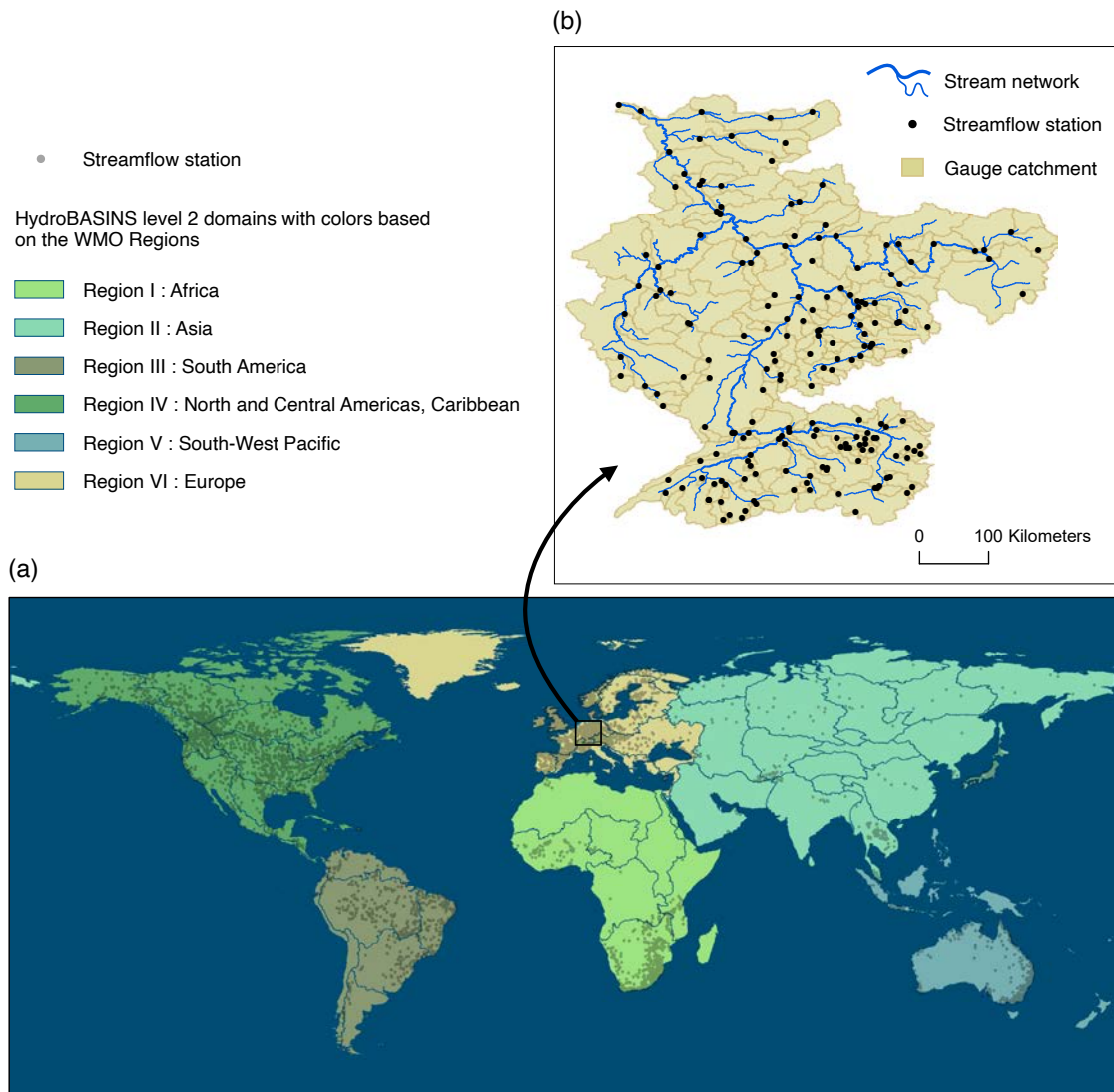


Figure 3.5: a) The global scale experiment domain comprising of 62 hydrological domains and 5 256 streamflow stations. b) The regional scale experiment domain of the Rhine river basin consisting of 187 streamflow stations.

for consistency of streamflow simulations, across model resolutions, for both the global and the regional scale setup.

Addressing the second part of the second hypothesis – “Maintaining the catchment area results in improved and consistent model performance across all catchment sizes i.e., SCC effectively eliminates the catchment size problem in gridded hydrological models” – involves assessing the consistency in the model performance across the stations, regardless of the geographical location, especially whether model performance is compromised at small catchments. We evaluate the hydrographs at selected stations with catchment area

ranging from 1 km^2 to over $100\,000 \text{ km}^2$. Subsequently, we analyze model performance globally to elucidate the relationship between performance, catchment size, and the method of stream network upscaling. Special attention is given to the model performance at small catchments ($<1\,000 \text{ km}^2$).

For the investigation of the third hypothesis – “By preserving the catchment area, it becomes possible to estimate streamflow at multiple gauging stations or points of interest within a grid cell, regardless of the resolution” – we employ the regional scale 25 km setup focused on the Rhine basin and analyze the mean annual streamflow simulated at stations that are situated within the same modeling grid.

3.3 RESULTS AND DISCUSSION

3.3.1 Solving the “catchment size problem”

SCC emerges as the most successful method in accurately representing catchment sizes, demonstrating its successful application, regardless of model resolution. The scatterplots in Figure 3.6, panels *a* to *f*, depict the agreement between the modeled catchment area (\hat{A}) and the DEM based catchment area (A_d), the latter being the reference. The first three subplots represent a global comparison taken from Yamazaki et al. (2009), utilizing three stream network upscaling methods: FLOW (Yamazaki et al., 2009), Döll and Lehner (2002), and Double Maximum Method (Olivera et al., 2002), at a 50 km model resolution. Panels *d*, *e*, and *f* correspond to this study and compare D8 and SCC globally at resolutions of 25 km, 50 km, and 100 km, respectively. FLOW exhibits satisfactory agreement only in the catchments larger than $100\,000 \text{ km}^2$, while the performance of the remaining methods, including D8, shows poorer alignment between A_d and \hat{A} . Panels *d* to *f*, also highlight how majority of the \hat{A} for D8 (the default in mHM) is constrained by the grid size limit of the modeling resolution (ℓ_{11} – the area of one grid pixel at the modelling resolution). In contrast, SCC proves to be independent of the grid boundary (blue dots along the 1:1 line). In fact, the error in the estimation of the basin area by SCC is only given by the area of the DEM resolution, i.e., $\pm \ell_0^2 \text{ m}^2$. Consequently, it is almost negligible for most practical applications. Interestingly, for some catchments, the error with D8 is quite low in panels *d* to *f*, even below the grid limit. This is likely due to chance, particularly if the catchment is situated at the boundary of the domain such that the domain mask favorably clips the grid resulting in improved \hat{A} . Figure B.6 shows similar plots, but with the area values reported in the GRDC/CEDEX database (A_r) used as the reference instead. Overall, inaccuracies from the upscaling scheme, such as the D8 method, can be orders of magnitude higher than the error in the DEM if not properly addressed.

Panel *g* and *h* present boxplots illustrating the error in \hat{A} . Panel *g*, sourced from Eilander et al. (2021), compares the Double Maximum Method (DMM), Effective Area Method (EAM), and Iterative Hydrography Upscaling (IHU) methods for upscaling stream networks across approximately 1 km, 12 km, and 25 km model resolutions, globally. The

boxplots in panel *h* are outcomes of this study, comparing SCC and D8 across 25 km, 50 km, and 100 km resolutions globally. SCC is again the most consistent method, demonstrating absolute scalability in modeling A_d . Among the other methods, IHU effectively conserves A_d at 1 km resolution but struggles to maintain this level of performance at coarser resolutions.

Similar demonstration of the catchment size problem has been included in the past literature, even before Yamazaki et al. (2011) and Eilander et al. (2021) (Fekete et al., 2001; Reed, 2003; Hanasaki et al., 2006; Yamazaki et al., 2008). Despite of improvements, the problem had not been eradicated by the state-of-the-art as seen in Figure 3.6. Vector-based methods also lead to errors in \hat{A} at local point (of interest), as the catchment areas and outlets are generated by the system. SCC is the first stream network upscaling method capable of achieving absolute conservation and scalability of \hat{A} , for systems with pre-decided points of interests. SCC also makes it possible to recalculate the discharge at other, originally unspecified points of interest. In this case, the gridded simulated discharge only needs to be post-processed with mRM, without the need for time-consuming start-up, warm-up and calibration procedures.

3.3.2 Error and performance regimes for D8

The suitability of D8 is highly conditional and dependent on the combination of the model resolution size (A_g) and the DEM based catchment size (A_d), as evident in Figure 3.6d-h. Granted SCC's superiority over the D8, the latter is still seen as the go-to method for stream network upscaling in the latest large-scale streamflow modeling studies (see Table 3.1). Therefore, it is important to examine the conditions under which D8 is suitable (or unsuitable) for modeling purposes.

The shapes of the points in Figure 3.7 represent error in modelled catchment area (ϵ_A) at the streamflow stations of the regional experiment, across the modelled resolutions, using D8. Here, ϵ_A is calculated as the absolute difference between A_d and the modeled catchment area \hat{A} . We utilize the results from the regional experiment owing to the wider range of model resolutions included. Three distinct error regimes appear based on the values of ϵ_A . The large error regime (upper left) for D8 is bounded by the 1:1 line to its right and includes catchments smaller than the grid limit or grid size. In this error regime, large ϵ_A is virtually guaranteed. We delineate the small error regime (bottom right) for the D8 such that ϵ_A is limited to 10% at 80% of the catchments, at a particular model resolution. It is worth noting that the maximum width of the transition regime is about one and a half order of magnitude of A_d . Thus, the gist of this graph can be put into a thumb rule as:

$$A_d \begin{cases} < 10^{1.5} A_g \approx 30 A_g, & \text{D8 small error regime} \\ > A_g, & \text{D8 large error regime,} \end{cases} \quad (3.3)$$

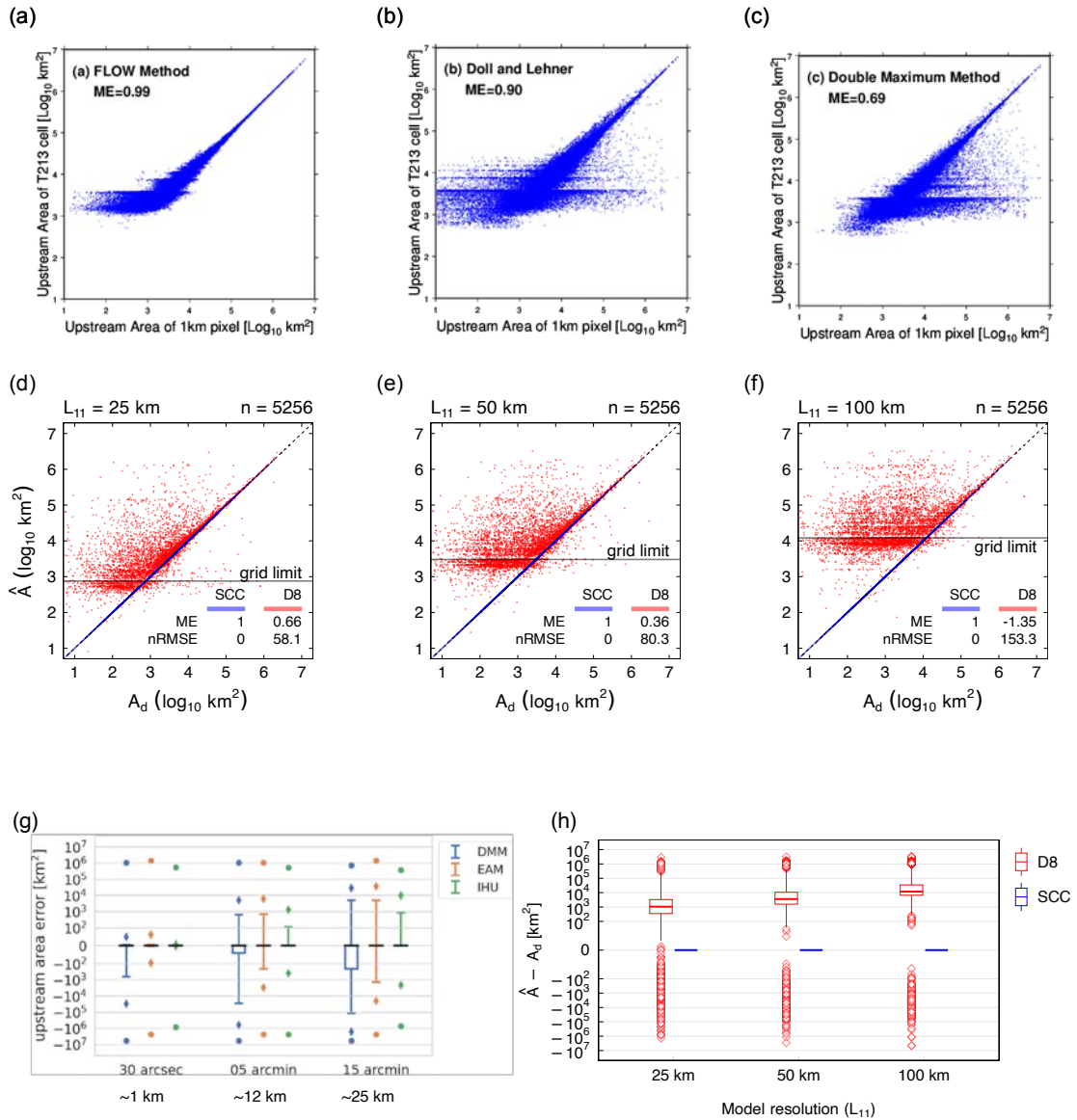


Figure 3.6: Scatterplots of input catchment area on x-axis and modeled catchment area on y-axis evaluating performance of (a) FLOW, (b) Döll and Lehner (2002), and (c) Double Maximum Method at 50 km model resolution (source: Figure 8 in Yamazaki et al. (2009)). Similar scatterplots with DEM based catchment area (A_d) on x-axis and modeled catchment area (\hat{A}) on y-axis evaluating SCC vs D8 (this study) at model resolutions of (d) 25 km, (e) 50 km, and (f) 100 km corresponding to the 5256 streamflow stations worldwide. The goodness of fit of \hat{A} on A_d is given by the Model Efficiency (ME)(dimensionless) and Root Mean Square Error (RMSE) (km^2) normalized using standard deviation. The grid limit represents the area of the model grid (ℓ_{11}) and is estimated at the equator. Boxplots showing error in the upscaled catchment area using (g) DMM, EAM, and IHU schemes across individual model grids, globally (source: Figure 4 in Eilander et al. (2021)), (h) SCC and D8 schemes across the 5256 streamflow stations (this study). The kilometers approximation is added in panel g for comparability. The box represents the 25th–75th percentiles, the whiskers depict the 1st–99th percentiles, the diamonds depict the 0.1th–99.9th percentiles. Additionally, the dots represent the minimum and maximum errors in panel g.

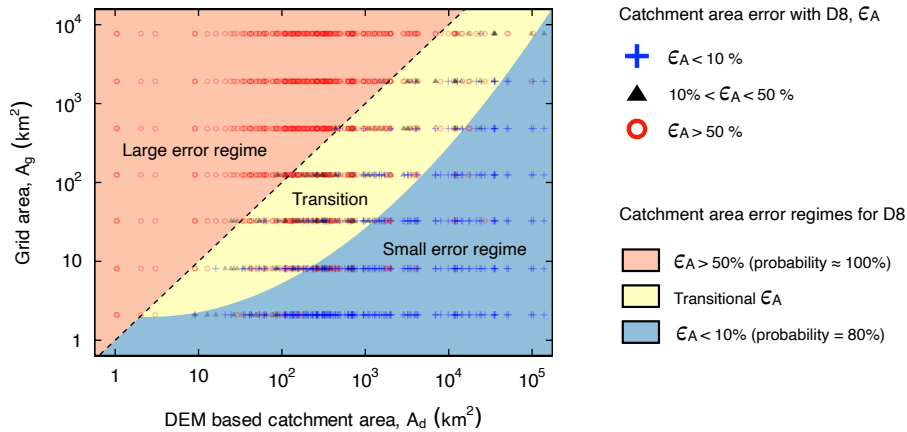


Figure 3.7: D8 catchment area error regimes as a function of the DEM based catchment area (A_d) and the model resolution size (A_g). The area error (ϵ_A) is calculated as the absolute difference between A_d and the modeled catchment area \hat{A} . The data points for ϵ_A belong to the D8 runs from the regional experiment (187 stations \times 7 model resolutions). The error regimes are developed based on ϵ_A . The dashed line is the 1:1 relationship i.e., the grid limit.

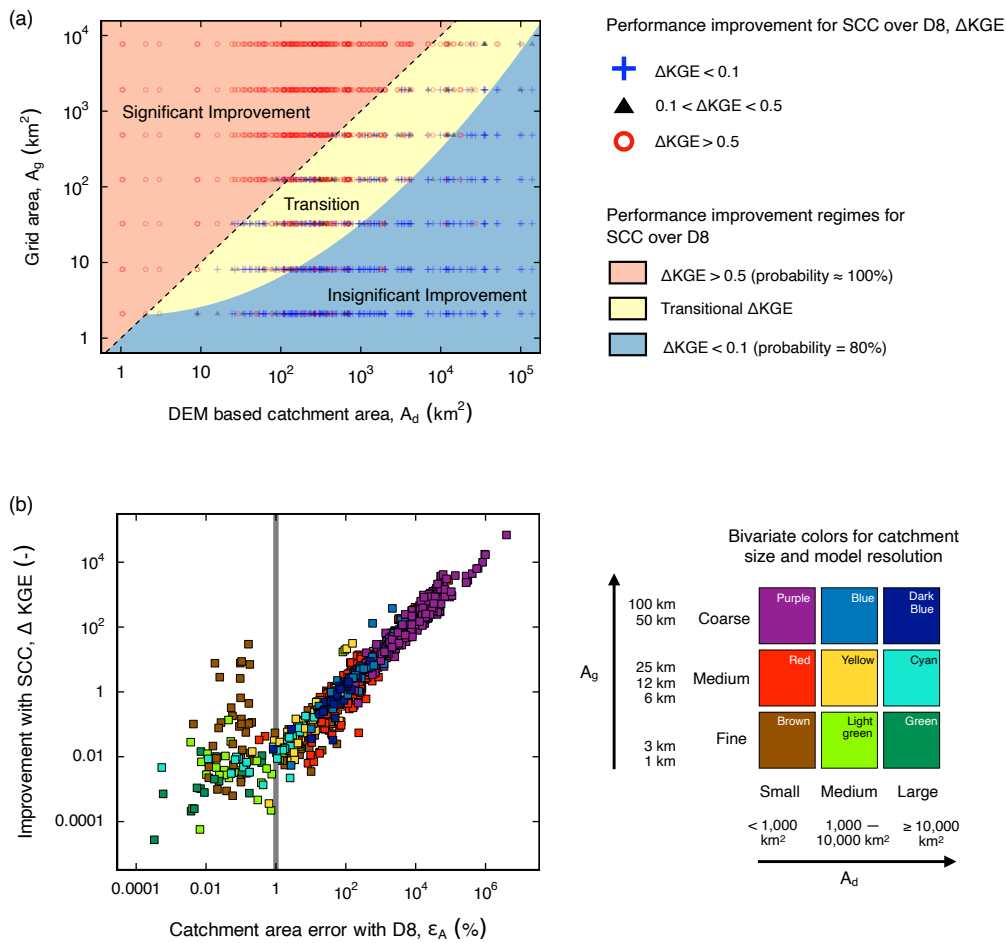


Figure 3.8: (a) Performance improvement regimes, on replacement of D8 with SCC, as a function of the DEM based catchment area (A_d) and the model resolution size (A_g). The dashed line is the 1:1 relationship i.e., the grid size limit. The improvement regimes are developed based on Δ Kling-Gupta Efficiency (KGE) at the data points. (b) Scatterplot between performance gain (ΔKGE) using SCC instead of D8, and the catchment area error (ϵ_A) while using D8. The bivariate colors represent three groups each of the DEM based catchment size (A_d) and the model resolution (A_g). Both (a) and (b) belong to the regional experiment (187 stations \times 7 model resolutions).

Figure 3.8a shows the improvement regimes for replacing D8 by SCC in the model performance for streamflow (Q) simulations. We use ΔKGE (refer B.5) of 0.1 and 0.5 as the thresholds to quantify the significance of performance improvement. These performance improvement regimes are virtually identical to the error regimes in Figure 3.7, which implies the Equation 3.3 is valid for the performance improvement regimes as well. This correlation is further explored in the scatterplot of Figure 3.8b, which reveals ΔKGE to be linearly correlated to ϵ_A as long as the error in catchment area estimated by D8 is larger than 1%. The bivariate colors, which represent the combination of sizes of catchment area and model resolution, spotlights larger model improvements with coarser model resolution, for each catchment size. The small catchments at fine resolution (the brown cluster) is seen to depart from the otherwise linear relationship, with large performance gains with SCC even if D8 introduced small ϵ_A (around 0.1%). This could be attributable to the fact that, for very small catchments, in addition to the size, the shape of the catchment plays a significant role in model performance. For instance, a 18 km² catchment can be modelled by D8 with two 3 km pixels resulting in a small value for ϵ_A and yet there could be drastic performance gains with SCC, simply due to the accuracy in catchment shape and the resulting routing.

To the best of our knowledge, our analyses on the applicability of D8 is first of its kind. These outcomes are evidently useful for modellers, employing the D8 method, to determine the appropriate spatial resolution using the regime maps and the rule of thumb derived herein.

3.3.3 Improved scalability of streamflow simulations

The condensed view of model performance (KGE and its components) from the regional experiment is showcased in Figure 3.9. The near conformity of the CDFs for SCC across a range of spatial resolutions (1 km to 100 km) highlights its ability to produce scalable Q . It can be stated that the absolute scalability previously demonstrated by SCC in modeling the DEM based catchment (A_d) extends to the scalability of Q simulations. This remarkable streamflow scalability results in nine out of 10 stations exceeding the mean flow benchmark, $KGE = -0.41$ (Knoben et al., 2019), across all model resolutions. In contrast, D8 barely manages to outperform the mean flow benchmark at 50% of the stations at 12 km model resolution. Moreover, the significant nonconformity of the CDFs for D8 exhibits its disability to produce scalable Q . Analysis of the KGE components reveals that the significant gain in the model performance primarily stems from improvements in the variability (α) and the mean (β), while the correlation (r) is the least influenced. This is plausible since erroneous catchment area (\hat{A}) might still produce strong Q correlation but would struggle to accurately capture the variability and the mean. Similar conclusions can be drawn from Figure B.4 in B.7, corresponding to the global experiment, where SCC enables eight out of 10 stations to outperform the mean flow benchmark, across 25 km to 100 km model resolutions. Figure B.4 of B.7 shows the scalability of hydrograph

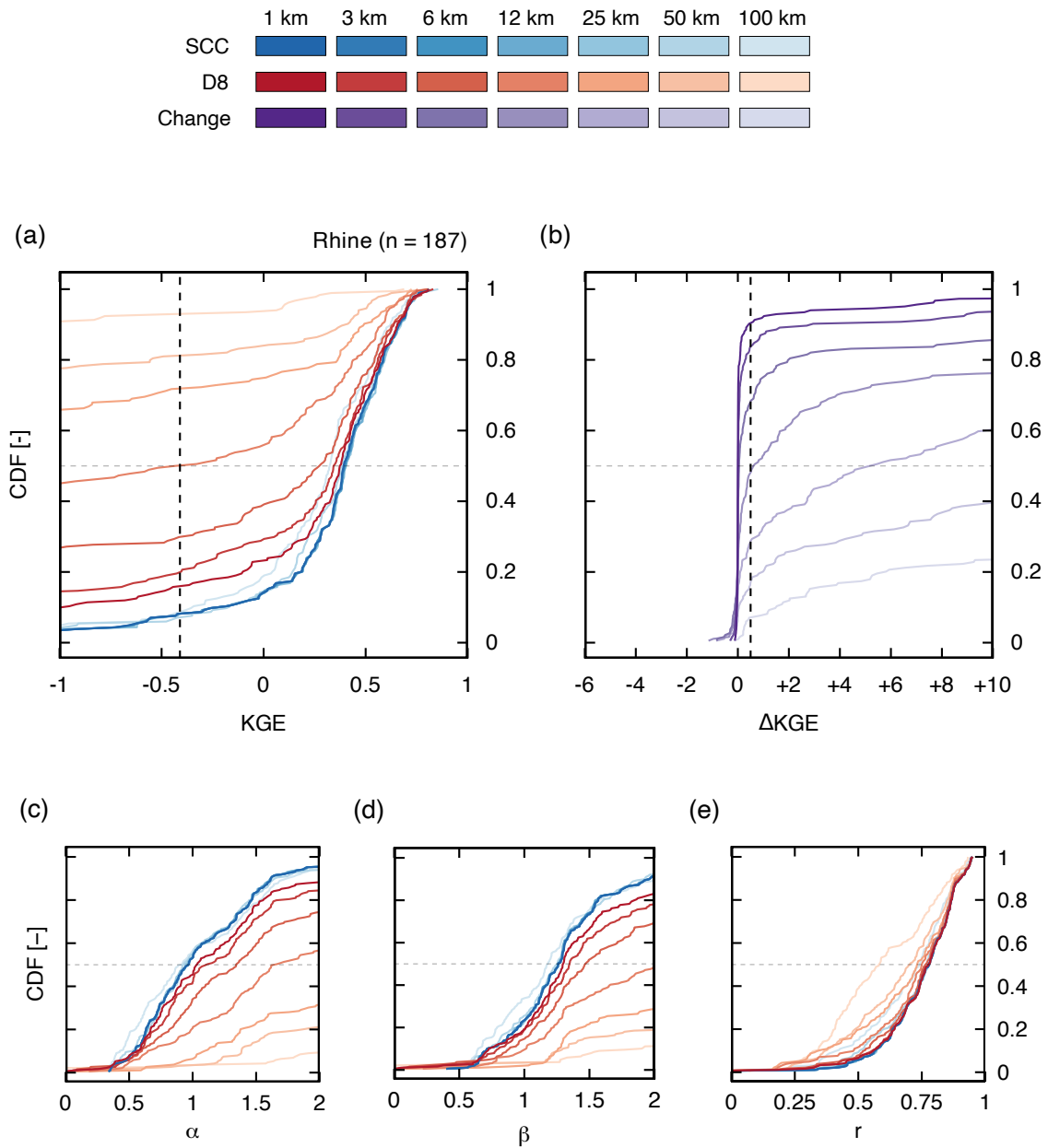


Figure 3.9: CDFs comparing streamflow performance across 1 km to 100 km model resolutions, and subgrid stream network upscaling using SCC and D8, for the regional experiment. (a) CDFs of KGE. (b) CDFs showing the corresponding improvements gained by using SCC instead of D8 (i.e., Δ KGE). (c) – (e) CDFs of KGE components namely variability measure (α), bias (β), and correlation (r). The vertical line in the panel (a) corresponds to the mean flow benchmark ($KGE = -0.41$). The vertical line in the panel (b) corresponds to $\Delta KGE = +0.5$.

simulations with SCC at three streamflow stations from the regional experiment, across 1 km to 100 km model resolutions. Overall, the results underscores the significance of scalable process representation in hydrological modeling, a principle that SCC adheres to.

Sutanudjaja et al. (2018) compared the streamflow at 3 597 GRDC stations globally, across 5' and 30' model resolutions. They employed D8 upscaled stream network to obtain median KGE difference of ≈ 0.15 , across the two resolutions, at gauges below 1000 m elevation and ≈ 0.45 at gauges above 1000 m. Aerts et al. (2022) tested the D8 across 454 stations of the USA, at model resolutions of 3 km, 1 km, and 200 m. Surprisingly, even with a hyperresolution model of 200 m, 18% of the stations failed to surpass the mean flow benchmark using the D8 method, which indicates potential deficiencies in process representation. Eilander et al. (2021) shows significant reduction in median errors in flood peak magnitude timing using IHU (1.8%, 2 h) relative to EAM (2.8%, 3 h) and DMM (14.2%, 5 h), using model resolutions of 30'', 15', and 30'. Polcher et al. (2023) partitioned runoff from grids of varying resolutions (11 km, 20 km, and 0.25°) into up to 55 hydrological transfer units (HTUs), per grid, for downstream routing. While their approach demonstrated improved scalability in evaluating streamflow at 35 locations compared to earlier studies, there is tremendous escalation in computational load from this approach. Other land-surface or hydrological models could, thus, benefit from the scalability provided by SCC, which is integrated into mRM. Such coupling exercises have been successfully carried out in the past by Wanders et al. (2019) and in the Copernicus Climate Change ULYSSES project where mRM has been coupled to route the simulated runoff from PCR-GLOBWB, VIC, Noah-MP, JULES, and HTESSEL.

3.3.4 Locally relevant streamflow simulations

The “catchment size problem” inherent in global hydrological models restricts their application primarily to large catchments in continental-scale modeling (see Table 3.1). Figure 3.10 illustrates the hydrograph comparison at the outlet of six catchments, from the 6 km regional experiment. The catchments are selected such that each successive catchment is approximately one order of magnitude larger than the previous one. D8 produces large discrepancies between \hat{A} and A_d on panels *a* and *b* i.e., catchments which are smaller than the grid limit for 6 km model resolution. These discrepancies in catchment area are translated to simulated streamflow, posing challenges in sustaining model performance across different catchment sizes while utilizing D8. On the contrary, SCC is seen to generate reasonable hydrograph match, at all locations, from large catchments exceeding 100 000 km² in panel *f*, down to small catchments spanning just 1 km² in panel *a*. Interestingly, panels *c* and *d* display superior KGE values for D8 compared to SCC. This is evidently due to the overestimation of A_d compensating for the underestimation of streamflow, exemplifying a common scenario of *achieving right results for the wrong reasons*. A similar occurrence is observed in Aerts et al. (2022) where three hydrographs showed the best performance (KGE) with three different model resolutions (3 km, 1 km, 200 m),

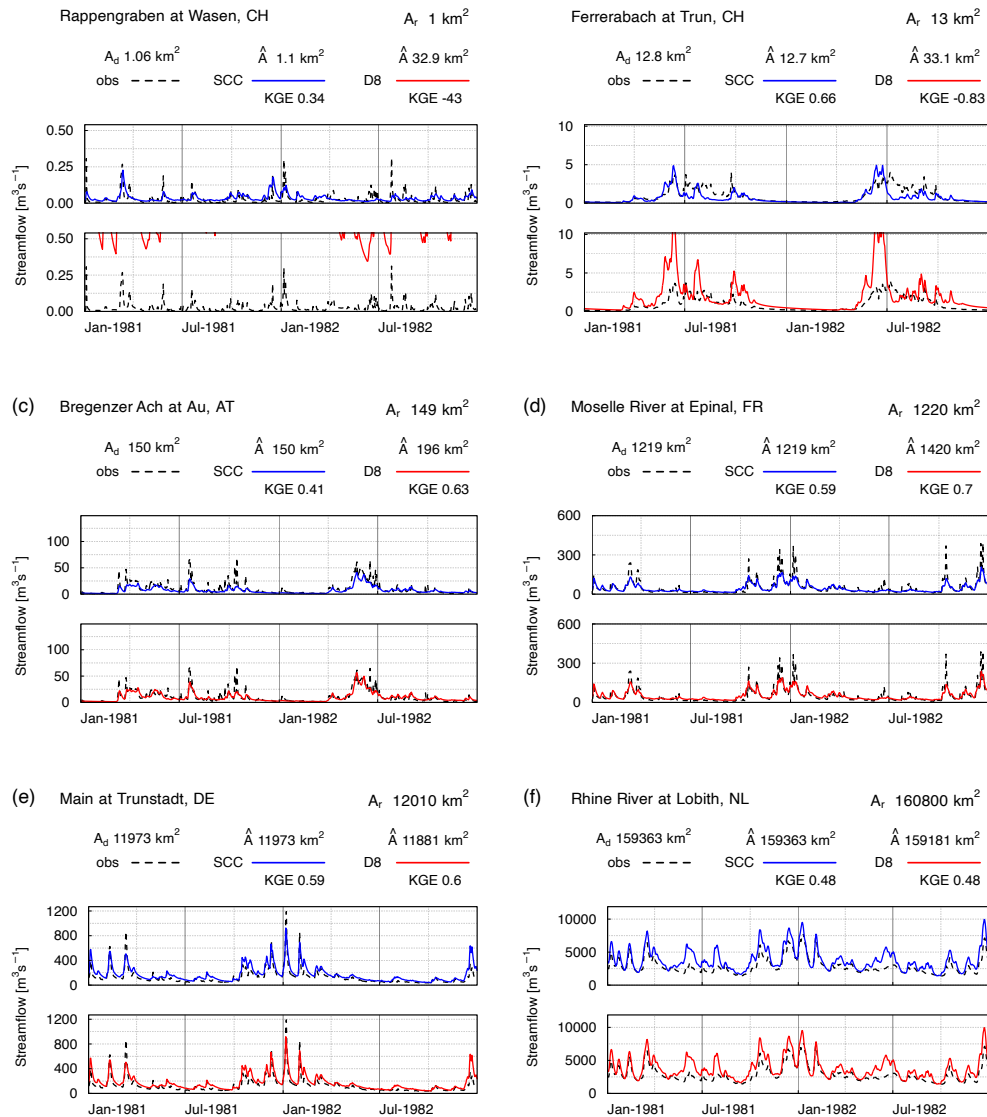


Figure 3.10: Hydrographs resulting from the upscaling of subgrid stream network to 6 km employing SCC and D8. The catchment areas of the selected locations span over six orders of magnitude and are taken from the regional experiment. (a) Rappengraben at Wasen, Switzerland (CH), (b) Ferrerabach at Trun, CH, (c) Bregenzer Ach at Au, Austria (AT), (d) Moselle River at Epinal, France (FR), (e) Main at Trunstadt, Germany (DE), and (f) Rhine River at Lobith, The Netherlands (NL). Each graph displays the recorded catchment area (A_r) and the DEM based catchment area (A_d). The modeled (upscaled) catchment area (\hat{A}) and the KGE values for SCC and D8 are provided next to the corresponding legends. Note: The KGE values correspond to the full evaluation period (1961 – 2020) while the graph viewport zooms to the years 1981 – 1982.

using the D8. Nevertheless, the study did not investigate the potential association between these results and inaccuracies in the modeled catchment area.

Figure 3.11 shows the spatial distribution of model performance (KGE) for the global experiment, for 25 km model resolution. The SCC map (panel *a*) in comparison to the D8 map (panel *b*) has darker shades of blue as well as greater number of small catchments outperforming the mean flow benchmark (87% with SCC compared to 24% with D8). This is more evident in the Western and the Central Europe (zoom-in insets), where a large number of small catchments, underperforming with D8 (light green in panel *b*), improve and exceed the mean flow benchmark with SCC (shades of blue in panel *a*).

The CDFs in Figure 3.11 summarize the model performance, categorizing catchments as either small or large using a threshold area of 1 000 km². The threshold split the total gauges into 2168 (41%) small and 3088 (59%) large catchments. The global Cumulative Distribution Function (CDF) illustrates a notable improvement in KGE for small catchments, with a 63% increase in small catchments surpassing the meanflow benchmark upon transitioning from D8 to SCC. This significantly narrows the performance gap between small and large catchments, reducing the difference in meanflow exceedance from nearly 40% with D8 to just 6% with SCC. Individual CDFs across the continents show similar reductions in performance disparities between the catchment sizes. These findings underscore two key points: Firstly, streamflow at small catchments are disproportionately affected by errors stemming from catchment area upscaling with D8. Secondly, SCC effectively mitigates this issue, enabling distributed models like mHM, to produce locally relevant streamflow at catchments as small as 1 km², in a global-scale setup.

Previous studies, employing the D8, have reported variations in model performance across catchment size groups. Sutanudjaja et al. (2018) found performance disparity where the fraction of small catchments decreased with KGE. Burek et al. (2020) also noted that better performance was predominantly evident for larger basins in their study, which encompassed 1366 GRDC stations. The results from Harrigan et al. (2020) also concur, where they observed median KGE skill score to be better than 0.5 for catchments larger than 10 000 km² and 0.21 for catchments smaller than 2 000 km². Interestingly, the GloFAS observation database, used in their analysis, contains only 7% of stations with catchments smaller than 10 000 km², contrasting with our study where 77% of the 5 256 locations fall into this category (refer Figure B.1c). An alternative method to SCC involves manually employing a mask for each catchment, a technique already available in mHM and demonstrated in Thober et al. (2019). The study managed to achieve acceptable performance for catchments as small as 100 km² using the multi-domain basin setup. The study also includes a brief analysis of catchment area errors using a single-domain setup, though limited to catchments larger than 100 000 km². However, the study did not demonstrate any enhanced scalability for multiple stations in one catchment, as is frequently the case for large scale applications. In contrast to these studies using D8, Polcher et al. (2023) employed HTUs and demonstrated performance invariance across catchment size comparable to this study. Despite its limited inclusiveness, analyzing

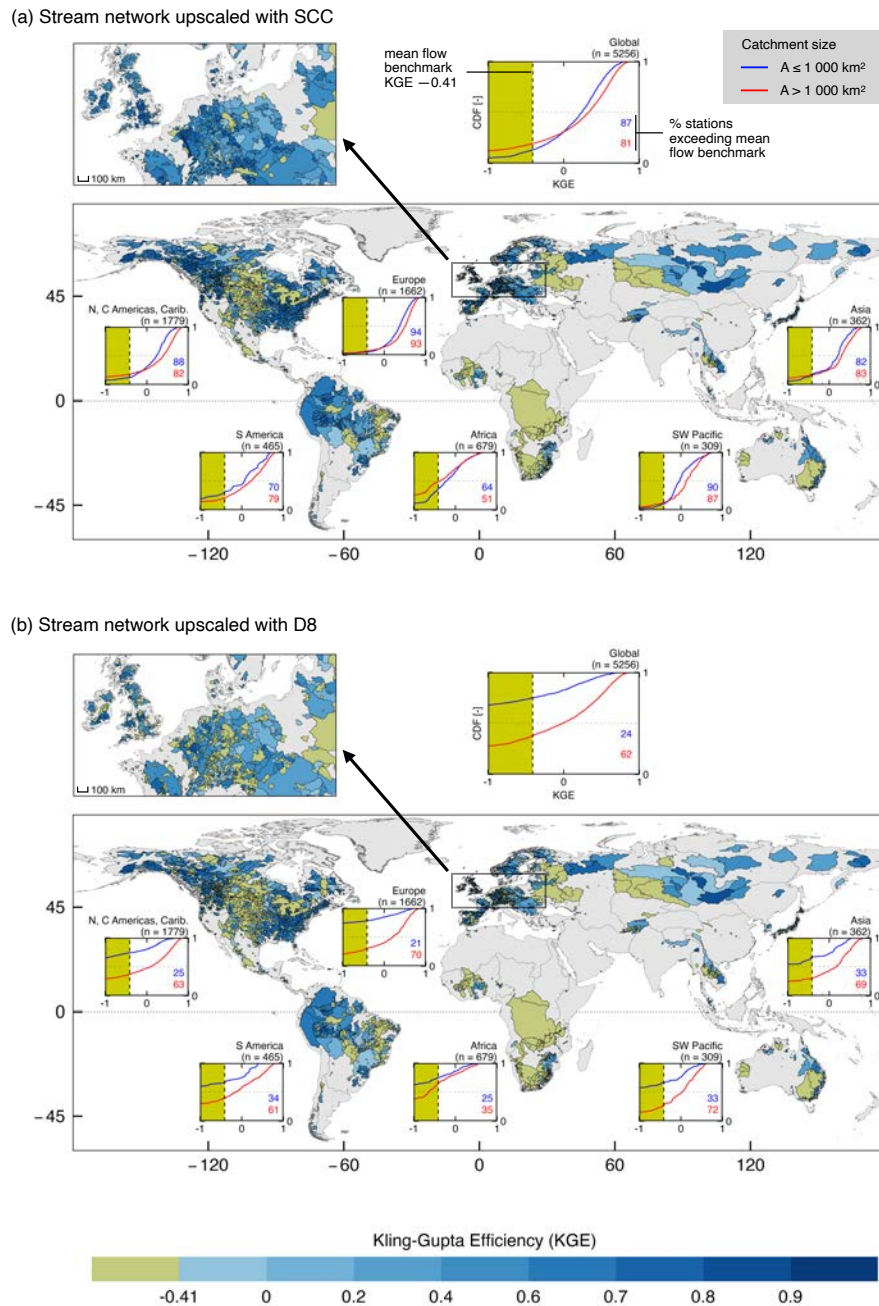


Figure 3.11: Comparison of daily model performance at 5256 streamflow station catchments, worldwide, with subgrid stream networks upscaled to 25 km using (a) SCC, and (b) D8 methods. Global and continent-wise CDFs depict the KGE distribution of small ($< 1000 \text{ km}^2$), and large ($> 1000 \text{ km}^2$) catchments. The light green fill indicate sub-meanflow benchmark (KGE = -0.41) performance.

only 35 catchments, all surpassing 2 500 km², the study mirrors the findings of our study and underscores the effectiveness of multiple downstream connectivity methods (e.g., SCC and HTUs) over single downstream connectivity methods (e.g., D8) for ensuring geographic performance consistency.

Continental-scale (or single-domain) setups are pivotal in global hydrological modeling for several reasons. Firstly, they significantly reduce computational burden primarily by avoiding redundancies in upstream catchments i.e., eliminating the need to simulate the same catchment areas multiple times, as would be the case with multi-domain approach at each basin outlet location. This efficiency translates to reduced storage requirements and simplified output management – a critical consideration in large-scale hydrological modeling. Moreover, employing single-domain promotes seamless analyses compared to managing multiple, geographically overlapping setups.

Despite of these advantages, it would still be insightful to know the computational cost of SCC and break-evens, if any, with respect to single-domain D8 (no catchment conservation) as well as the multi-domain D8 (catchment conservation) as shown in Figure 3.12. Here, the computational nodes are calculated for the three routing approaches by incrementally adding 20 streamflow stations in each run, in the Rhine. In order to mitigate the influence of the ordering of the stations, we applied ten iterations for shuffling the station order, resulting in the ensemble spread. All the iterations converge at $n = 187$ where the ensemble becomes a point. The ensemble spread is not observed for single-domain D8 as the number of nodes is not affected by the number of the stations in the model for the method.

SCC is expensive than the single-domain D8 at all times (refer Figure 3.12). This is expected as SCC is also a single-domain approach and, with increase in points of interest, the SCC will result in additional computational nodes than the single-domain D8. The computational expense increases with the number of stations, but the range of variability reduces drastically as the model resolution increases (100 km to 1 km). In contrast, the multi-scale D8 retains this variability at all model resolutions; around one and half order of magnitude on average. Considering a conservative break-even by comparing the ensemble minimum of multi-domain D8 against the ensemble maximum of the SCC, a break-even is observed roughly around 60 stations at all model resolutions. Thus, for the domain size of the Rhine and the given streamflow stations, SCC would be the more efficient choice to conserve catchment for $n \geq 60$. The maximum contrast in computational size between SCC and the multi-domain D8 occurs at $n = 187$ at 1 km model setup, where SCC is approximately five times faster. Notably, the multi-domain D8 is more efficient than single-domain D8 for a small number of points of interest, especially at fine resolutions. This is because the multi-domain D8 requires minimum bounding domain extent for each catchment, the sum of which can be smaller than the overall domain for small number of catchment outlets. However, this benefit vanishes as soon as the number of points of interest increases due to redundancies in modelled area.

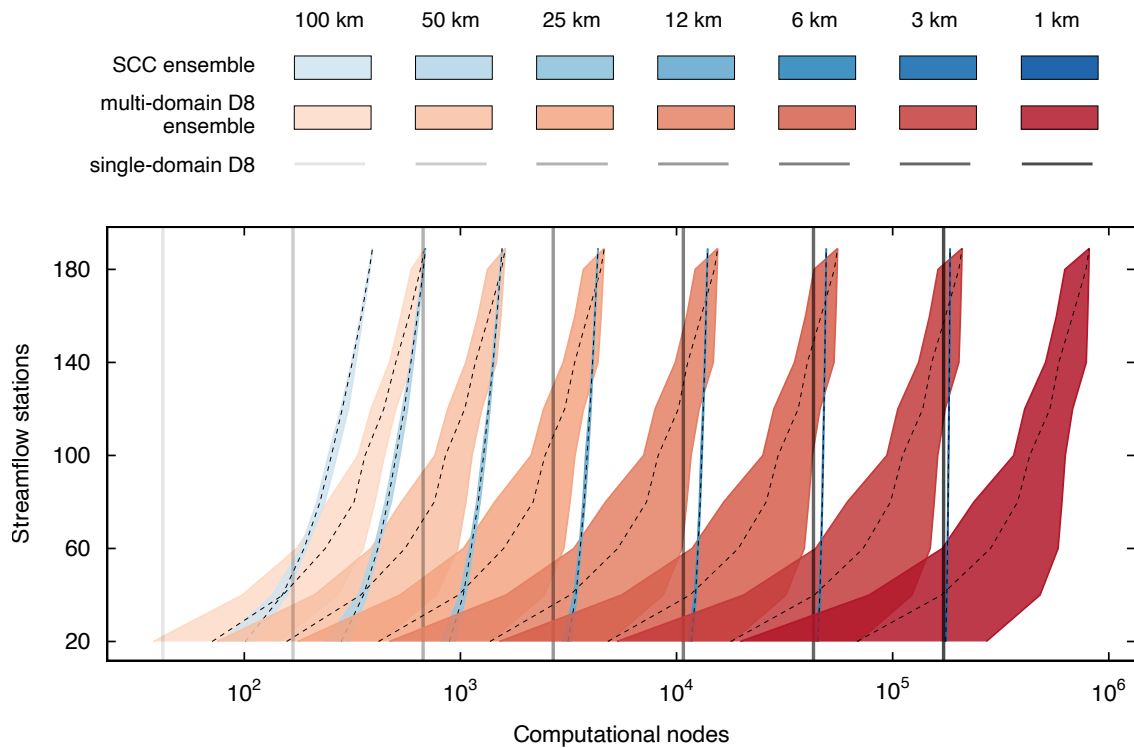


Figure 3.12: Comparison of computational cost (x-axis) among SCC, multi-domain D8, and single-domain D8, showing variation with number of streamflow stations (y-axis) and model resolution (variation in shades) in the regional experiment or The Rhine. The ensemble spread and median (dotted line) for SCC and multi-domain D8 are derived from ten iterations for shuffling the station order. A bin size of 20 stations was applied for the calculation.

3.3.5 Resolving multiple stations in a model grid

Large-scale hydrological models often encounter the issue of multiple streamflow stations within a single grid cell. Figure 3.13 shows the map of the Rhine basin, the 187 streamflow stations, and their corresponding catchments. At 25 km modeling resolution, there are several grids with multiple stations. The bar plots show the mean streamflow \bar{Q} at selected grids.

In grid C4, one station each is positioned on the major stream (station 1) and a minor stream (station 2). D8 simulates the entire grid as a single node, following the main stream's path. However, this approach leads to a significant overestimation of \bar{Q} for station 2 due to its smaller catchment area compared to that of the major stream. SCC, by adhering to catchment conservation principles, offers more realistic estimates of \bar{Q} .

Similarly, grid F7 accommodates two stations each on major (stations 1 and 2) and minor streams (stations 3 and 4). D8's catchment area error becomes evident at stations

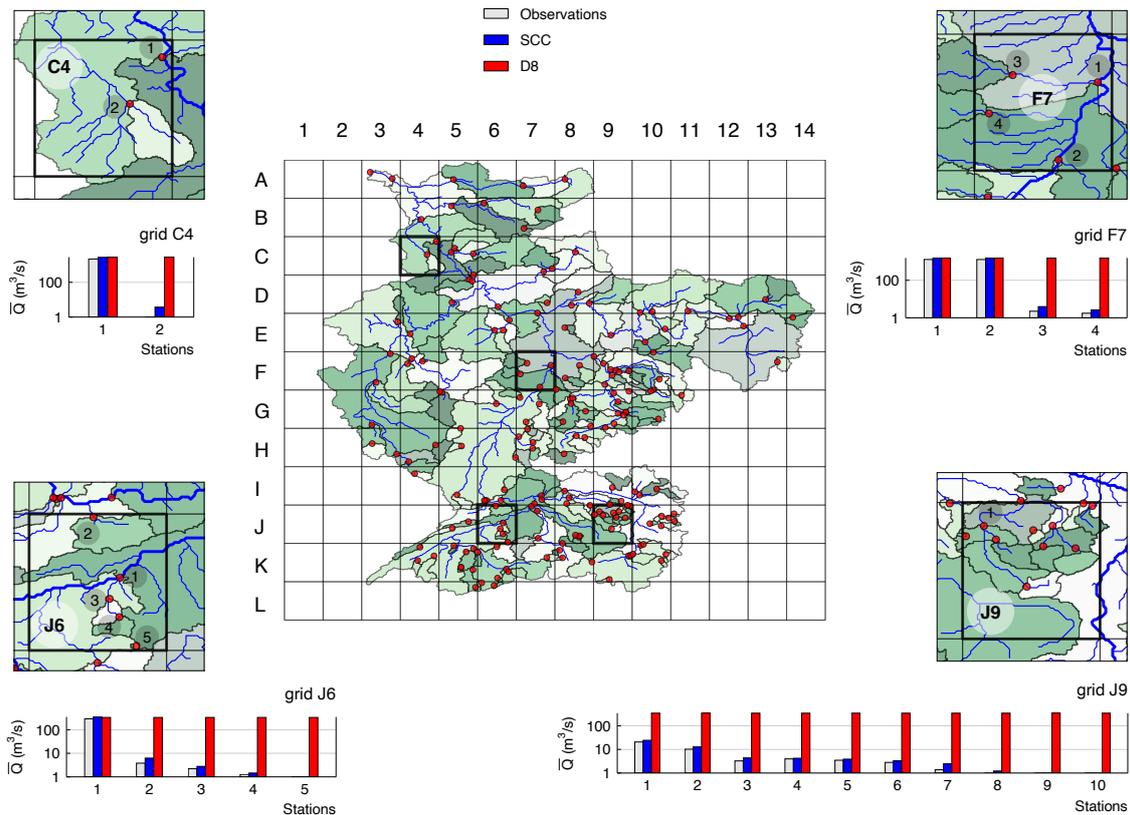


Figure 3.13: Map of the Rhine basin showing 187 stations (red dots), their corresponding catchments, and the 25 km modeling grid. The bar plots, beneath the zoom-in insets for selected grids (C4, F7, J6, and J9), show the mean streamflow values (\bar{Q}) for observations, SCC, and D8 across stations falling in the grids.

3 and 4, where only SCC produces meaningful \bar{Q} estimates. Likewise, in grid J6, D8 substantially overestimates \bar{Q} at stations 2, 3, 4, and 5, all located on minor streams, unlike SCC.

In J9, containing 10 stations, the major stream briefly flows in and loops back to J10. The D8 streamflow simulation, which is based on the catchment area of the major stream, significantly overestimates \bar{Q} at all stations. Since none of the stations are situated directly on the main stream, even the largest catchment among them receives a positive bias of over ten-fold. In summary, SCC effectively handles varying complexities of multiple stations within grid conditions, while D8 consistently introduces positive bias at stations not situated on the major stream within the grid.

Most large-scale streamflow modeling studies set a large catchment area cutoff (Table 3.1), inherently excluding multiple streamflow stations within a grid (Burek et al., 2020; Hou et al., 2023; Droppers et al., 2020; Sutanudjaja et al., 2018; Zhao et al., 2017; Li et al., 2015). Single downstream connectivity methods, such as the D8 and IHU, by

definition, can only resolve single streamflow value in a grid at a time. Whereas, vector based methods like the unit catchment (Yamazaki et al., 2013) with a lower limit on area impedes the ability of the method in resolving multiple points in a grid. Existing multiple downstream connectivity methods (Guo et al., 2004; Nguyen-Quang et al., 2018) can potentially resolve multiple points per grid, though this capacity has not yet been demonstrated (Liang et al., 2004; Wen et al., 2012; Polcher et al., 2023).

In global hydrological modeling, multiple lakes or reservoirs within a grid present similar challenges. Existing literature, primarily using the D8, either classify reservoirs into categories (e.g., “major” and “minor”) and process them differently (Wisser et al., 2010; Hanasaki et al., 2018; Burek et al., 2020; Müller Schmied et al., 2020; Gharari et al., 2024) or limit to one reservoir per grid (Haddeland et al., 2006a; Haddeland et al., 2006b; Biemans et al., 2011; Terink et al., 2015; Zhao et al., 2016; Zajac et al., 2017; Sutanudjaja et al., 2018; Shin et al., 2019; Shin et al., 2020; Dang et al., 2020). Like with streamflow stations, SCC can resolve multiple lake outlets or reservoir dams within a grid (Shrestha et al., 2024).

3.4 CONCLUSIONS AND OUTLOOK

In this study, we developed a new stream network upscaling scheme, Subgrid Catchment Contribution (SCC), for grid based hydrological models with the aim of conserving the catchment at specified points of interest. Applying the SCC in the mesoscale Hydrologic Model (mHM), we conducted extensive testing at 5 256 streamflow stations worldwide, spanning model resolutions from 25 km to 100 km, and compared its performance against the widely-used D8 scheme of Döll and Lehner (2002). Additionally, we conducted a regional-level comparison in the Rhine River basin, utilizing 187 streamflow gauges across model resolutions ranging from 1 km to 100 km, encompassing catchments as small as 1 km² in size.

The newly developed SCC scheme features several distinctive attributes. It includes automated delineation of catchment boundaries within the model establishment framework. SCC, being integrated into mHM, enables on-the-fly upscaling of the stream network tailored to the scale of interest. This scheme ensures absolute conservation of input catchment areas at the subgrid level at all modeling resolutions. This not only allows seamless streamflow simulations across a range of spatial resolutions, but also results in performance consistency across catchments of varying sizes. Furthermore, SCC possesses the capability to resolve multiple streamflow stations or lake/reservoir outlets within each grid.

The proposed SCC scheme and underlying algorithms are transferable to any land-surface or hydrological model through the utilization of the multiscale routing model, mRM, (Samaniego et al., 2010; Thober et al., 2019), mHM’s routing module, to channel the simulated runoff. It is possible since the mRM is stand-alone module that can work with

any gridded model that generates runoff (Thober et al., 2019; Samaniego et al., 2019). This capability is fundamental for the digital twin initiatives.

SCC is a significant advancement over the existing fraction-based methods, like the hydrological transfer units (HTU), in terms of optimizing the number of routing nodes required for conserving catchment at given set of points. This allows us to process and perform computationally demanding tasks of river routing more efficiently. SCC also surpasses the vector based methods since the routing of a catchment in SCC is the culmination of routing through all the catchment fractions and not instantaneous like in the the vector based methods. This accounts for time-delay, resulting in a more realistic representation of in-stream routing processes.

We generated a regime map of area error for the D8 and a regime map of performance gained by substituting D8 with SCC, across a range of catchment sizes and modelling resolutions. Based on the extensive analysis, we introduce a thumb rule suggesting that the effectiveness of D8 diminishes for catchments smaller than 30 times the grid size. These regime maps and the proposed thumb rule are valuable findings for streamflow modelers, aiding in the design of experiments and selection of model resolutions when utilizing the D8 method.

Our demonstration of SCC revealed its capability to generate scalable streamflow, with nine out of ten locations surpassing the mean flow benchmark consistently across all model resolutions in the regional experiment (eight out of ten in the global experiment). In comparison, D8 exhibited inferior performance and lack of scalability.

Beyond scalability, SCC offers consistency in performance across catchment sizes, effectively addressing the “catchment size problem” in gridded hydrology (Fekete et al., 2001; Hanasaki et al., 2006; Yamazaki et al., 2008; Wu et al., 2011; Thober et al., 2019; Eilander et al., 2021; Aerts et al., 2022; Polcher et al., 2023). The disparity in the percentage of locations exceeding the mean flow benchmark between small and large catchments decreased significantly from 40% with D8 to just 6% with SCC, demonstrating substantial performance enhancements, particularly in smaller catchments. This study demonstrates SCC’s ability to resolve catchments as small as 1 km^2 marking a significant milestone for a large-scale gridded hydrological model to accurately simulate locally relevant streamflow.

The locally relevant streamflow using SCC has two fold implications in the calibration of single domain hydrological model. Firstly, by incorporating small catchments into the model calibration process, parameters can be trained to capture headwater hydrology alongside large-scale hydrological processes. This effect contributes to the notion of distributed hydrological modeling at all scales. Secondly, the improved accuracy at small catchments means parameters are less involved in compensating for modeling errors in catchment areas. For instance, if the area of a 10 km^2 catchment is modelled as 20 km^2 then the model parameters will compensate to fit the observed hydrograph at the catchment outlet given there is twice as much water than reality. Therefore, SCC holds the key to more robust model calibration in single domain hydrological modeling.

We further demonstrated SCC's ability to handle the issue of multiple stations falling within a single grid cell. The novel aspect of SCC not only enables the simulation of clusters of streamflow stations but also facilitates the modeling of closely situated lake outlets and cascades of reservoir dams. In other words, SCC bypasses the constraint of model grid size for given set of points of interest, offering greater flexibility in hydrological modeling.

We also report the computational efficacy of SCC, in comparison to the single- and multi-domain D8, at the regional experiment set. Such accounting aligns with the contemporary recommendations made on the environmental impact of computational science research in order to promote a more sustainable future ("[The Carbon Footprint of Computational Research](#)" 2023). Development of "green algorithms" (Lannelongue et al., 2021a), such as SCC, contributes towards digital carbon footprint reduction (Lannelongue et al., 2021b; Lannelongue and Inouye, 2023).

In its current implementation, SCC exclusively partitions the routing grids within mHM, leaving the hydrological grids as regular grids. This means the runoff routed by the routing nodes is estimated as a fraction of the average grid-specific runoff production, assuming uniform runoff production for all areas over a given grid cell. Future work can focus on addressing this "averaging effect" by explicitly resolving sub-grid processes (e.g., soil moisture, evapotranspiration, runoff production) in cells that fractionally contribute to different rivers.

Accurate streamflow simulation is fundamental to flood forecasting. SCC enables models to simultaneously produce accurate and reliable streamflow not only at the basin outlet but also at every desired sections of headwater catchments. This advancement is pivotal for supporting decision-making during local floods, such as the Summer flood of 2021 in Germany (Najafi et al., 2024). This capability holds significant value for large-scale hydrological forecasting systems such as Copernicus Climate Change ULYSSES project, operating globally at 10 km regular grids. Leveraging SCC, these systems can generate flood forecasts at local level, improving their early warning efficiency. The local streamflow simulations with SCC also align with the ambitious target of reliable forecasts from the global scale hyper-resolution hydrologic modelling (Wood et al., 2011a; Beven et al., 2015; Bierkens et al., 2015a) and the initiatives on the digital twin of Earth (Bauer et al., 2021). The annual State of Global Water Resources report by WMO (2023a) could also benefit from SCC with the inclusion of basins smaller than 10 000 km². It is noteworthy that this newfound "eagle vision" in global streamflow modeling and forecasting extends its utility beyond water quantity to areas such as river temperature and water quality (Tang et al., 2019; Wanders et al., 2019; van Vliet et al., 2023; Jones et al., 2023), among others. This broader applicability underscores the transformative potential of SCC in diverse fields of hydrology.

TOWARDS IMPROVED SIMULATIONS OF DISRUPTIVE RESERVOIRS IN GLOBAL HYDROLOGICAL MODELLING

PK Shrestha^{1,2}, et al.

¹Computational Hydrosystems, Helmholtz Centre for Environmental Research – UFZ

²Institute of Environmental Science and Geography, University of Potsdam

Originally published at:

Shrestha, P. K., Samaniego, L., Rakovec, O., Kumar, R., & Thober, S. (2024). Toward Improved Simulations of Disruptive Reservoirs in Global Hydrological Modeling. Water Resources Research, 60(4).

SUMMARY

Accurate simulation of reservoirs has been a challenge for global hydrological models due to highly discontinuous water management and uncertainties in reservoir shape representation. In addition, at a global scale, it is crucial to consider those reservoirs that disrupt the downstream flow regime. We augment mesoscale Hydrologic Model (mHM) with a newly developed lake module that incorporates an existing reservoir regulation scheme with non-consumptive demand predictions from random forest. We also evaluate the sensitivity of reservoir shape on streamflow and evaporation for three shape approximations of varying complexities. We tested the lake module across 31 non-consumptive reservoirs covering an extensive range of hydroclimatic characteristics and demonstrate the applicability by using freely available global reservoir information. Streamflow simulations with reservoirs and model calibration show a median Kling-Gupta Efficiency (KGE) improvement of +0.94 (calibration) and +0.77 (validation) when compared against model simulations without reservoirs and default parameter set. We find reservoir evaporation highly sensitive to reservoir shape with half-pyramid approximation consistently resulting in best fit at reservoirs with surveyed bathymetry. In contrast, the linear approximation (rectangular prism) produced a median bias of +114% relative to half-pyramid, for estimating evaporation, across all the reservoirs. Streamflow simulations were insensitive to the reservoir shape. Our analysis shows that 30% of the non-consumptive hydropower reservoirs of the Global Reservoirs and Dam database (GRanD) dataset are non-disruptive and can be excluded without loss to model realism. Further work is necessary for testing the regulation approach in reservoirs with consumptive water usage.

4.1 INTRODUCTION

In the era of hyper-resolution earth system modelling (Wood et al., 2011a; Beven et al., 2015; Bierkens et al., 2015b; Vergopolan et al., 2020; Hanasaki et al., 2022), and initiatives on digital twins for the best possible estimate of the hydroclimatic state of the Anthropocene (Bauer et al., 2021), reservoirs are prerequisites in earth system simulations. Global reservoirs are estimated to hold three times of the annual average water storage in river channels (Baumgartner and Reichel, 1975; van Beek et al., 2011), which, in turn, it is estimated to have tripled the residence time of the water circulation in the terrestrial water cycle (Vörösmarty et al., 2003; Wisser et al., 2010). Moreover, man-made reservoirs have increased the global terrestrial water surface area by approximately $305,000 \times 10^6 \text{ m}^2$ (Lehner et al., 2011; Zhao and Gao, 2019). This area represents the combined area of the Great Lakes and Lake Victoria. Despite their significant contribution to the water cycle, reservoirs and the losses they incur due to evaporation have received insufficient attention from global hydrologic and land surface modelers, as noted by Telteu et al. (2021). Even among the few models that have attempted to include these features, the representations of lake geometry and water dynamics have been overly simplistic (Turner et al., 2021). This lack of attention towards water reservoirs in the global hydrology modelling community highlights the need for more research and development in this area.

Incorporating reservoirs in large-scale hydrologic models presents several challenges. The first challenge is the intricacies of modeling and predicting the highly dynamic, anthropogenic-driven, and often ad-hoc decisions involved in reservoir regulation. The other conundrum is to accurately estimate the bathymetry of the reservoir and its corresponding elevation-area-volume relationships (i.e., the Elevation Area Volume (hAV) Table). The challenge (and opportunity) to identify the degree of disruptivity of man-made reservoirs so that models only include those that add value to hydrologic simulations is another one. The final challenge is to make all these modeling components scalable and transferable. Due to the complexity of the latter, this publication will focus on the first three challenges and address the latter in a follow-up publication.

Man-made reservoirs alter the natural streamflow regime, with the degree of alteration dependent on the specific regulations implemented (Biemans et al., 2011; Gutenson et al., 2020; Haddeland et al., 2006a; Wisser et al., 2010; Zajac et al., 2017). The regulations may include rules around water release, water diversion, and water level management, among others, which can result in significant changes to the timing, volume, and variability of downstream flows. The reservoir regulations depend on availability of water and demand. Demand is the human response to highly variable events and eventualities that very often can not be forecasted. In general, demand of water from a reservoir can be grouped into consumptive and non-consumptive. The water supplied to consumptive demand from the reservoir (e.g., irrigation, domestic, and industrial) are not registered at the downstream gauge (control point), a distinction from non-consumptive water use

(e.g., hydropower, flood control, navigation, and recreation). Non-consumptive reservoir with control point as downstream streamflow observations is thus an ideal (and basic) setting, especially for testing newly developed reservoir module and evaluating methods to estimate non-consumptive demand.

Table 4.1 shows a non-exhaustive list of twenty-four previous studies on reservoir modeling. This overview unveils the diverse strategies employed in representing regulation at reservoirs, their streamflow disrupting capacity, and the characterization of their underwater topography. The column header “regulation” depicts the evolution of reservoir regulation in HMs. The most basic regulation representation was introduced by Meigh et al. (1999) and later followed by Coe (2000), Döll et al. (2003), and Terink et al. (2015) where reservoir release is a simple function of storage or water level. Neitsch et al. (2011) and the following studies: Burek et al. (2013), Burek et al. (2020), Dang et al. (2020), Yassin et al. (2019), and Zajac et al. (2017), and Zhao et al. (2016), introduced the approach where the release is conditioned based on reservoir levels and discharge thresholds. Wisser et al. (2010), for instance, calculated the release by comparing the simulated inflow with the long-term mean inflow. Other studies proposed the regulation approach by estimating the target release or the storage at the start of of a given year (Haddeland et al., 2006a; Sutanudjaja et al., 2018; van Beek et al., 2011).

Hanasaki et al. (2006) presented a popular method for incorporating reservoirs in large-scale hydrologic models with little or no reservoir data (Biemans et al., 2011; Hanasaki et al., 2008; Pokhrel et al., 2012; Shin et al., 2019; Vanderkelen et al., 2022). This formulation recognizes the variability in reservoir behavior, which can range from inflow-driven to demand-driven. The ratio (c) of reservoir capacity to mean annual inflow is used to make the distinction where inflow-driven ($c < 0.5$) reservoirs are those that regulate their discharges primarily in response to fluctuations in inflows, while demand-driven reservoirs ($c \geq 0.5$) are those that regulate their discharges based on the demand for water downstream. Further, Hanasaki et al. (2006) distinguishes formulation for fulfilled (hedged) demand (refer to Table 4.1) for reservoirs with an irrigation purpose as they will alter their release timing based on the timing of irrigation demands downstream. A similar concept to that proposed by Hanasaki et al. (2006) has been used in other studies (Biemans et al., 2011; Müller Schmied et al., 2020; Shin et al., 2019; Shin et al., 2020; Vanderkelen et al., 2022; Sadki et al., 2023), and is also used in the present study. Shin et al. (2019) further improves the method of Hanasaki et al. (2006) to avoid full-empty oscillations in small reservoirs. Both Hanasaki et al. (2006) and Shin et al. (2019) depend on empirical values in their corresponding formulations of regulation. In contrast, Sadki et al. (2023) introduced these empirical values as parameters and optimized them. Hereafter, we refer to this improved version of Hanasaki et al. (2006) as S_{2023} .

Virtually all of the studies mentioned above have primarily focussed on decoupling seasonality in the water regime, but have not fully examined the specific and often significant variability that can be induced by reservoir operations. Sadki et al. (2023) (S_{2023}) and its predecessors estimate demand, a major source of the regulation variability,

through heuristic modeling which is quite uncertain. Demand is a complex human response and is therefore less amenable to being modeled as a continuous function like other hydrological processes. For this reason, we postulate that techniques such as Machine Learning (ML) could improve estimation of non-consumptive demand and thereby refining the fit of hydrographs below non-consumptive reservoirs, at daily temporal resolution.

Reservoir operation signal can be defined as the difference between the regulated and natural streamflow time series, where the latter would have been measured without the reservoir (Brunner and Naveau, 2023). There are numerous works that reconstruct the reservoir operation signal from observed streamflow time series measured downstream of a reservoir, such as the use of wavelet transform (Shiau and Huang, 2014; White et al., 2005), artificial neural networks (Ehsani et al., 2016; Qie et al., 2022), fuzzy rules (Coerver et al., 2018), harmonic regression models (Turner et al., 2021), Random Forest and Support Vector Machines (Qie et al., 2022), generalized additive models (Brunner and Naveau, 2023), among others. With this in mind, it remains to be seen how useful the S_{2023} would be in conjunction with ML techniques in HMs.

Reservoirs can exacerbate the disruption of the natural hydrologic cycle by significantly increasing evaporation rates, as highlighted by several studies (Friedrich et al., 2017; Shiklomanov, 2009; Zhao and Gao, 2019). This is notable because evaporation is the second most significant component of the global hydrological cycle after precipitation (Beer et al., 2018; Jansen and Teuling, 2020). Zhao and Gao (2019), for example, estimated that the long-term averaged annual evaporation volume from 721 reservoirs in the contiguous United States is equivalent to the 93% of the annual public water supply of the country in 2010. The rate of evaporation in a reservoir is closely tied to its water surface area, as demonstrated by Shin et al. (2019), which, in turn, depends on the reservoir's bathymetry. Bathymetry refers to the underwater topography of a reservoir that shapes its characteristics and influences its behavior, acting as a unique fingerprint for the reservoir.

Despite its importance for reservoir simulations, there is still no global inventory of the actual bathymetry of reservoirs. To date, the gap has been managed with disparate reservoir geometric approximations, as indicated in Table 4.1 under the column header entitled "bathymetry". The range of geometries varies from a linear area-volume relationship (Meigh et al., 1999), to a linear height-volume relationship with constant area i.e., rectangular prism (Döll et al., 2003; Zajac et al., 2017; Burek et al., 2020). Other studies used empirical relationships (Sutanudjaja et al., 2018; Müller Schmied et al., 2020), half-pyramid geometry (van Beek et al., 2011; Shin et al., 2019), and use regression analysis to estimate the height-area-volume relationships at individual reservoirs (Neitsch et al., 2011; Zhou et al., 2016). Some studies even neglected the reservoir evaporation and other lake surface fluxes (Hanasaki et al., 2006; Wisser et al., 2010) while many have not specified their reservoir bathymetry considerations (Haddeland et al., 2006a; Biemans et al., 2011; Burek et al., 2013; Terink et al., 2015; Dang et al., 2020; Shin et al., 2020;

Vanderkelen et al., 2022). Yassin et al. (2019) used the actual bathymetry at 37 reservoirs, which is a data-driven approach with limited applicability.

A significant amount of recent research has focused on using satellite altimeters to estimate the bathymetry of reservoirs (Li et al., 2020; Bacalhau et al., 2022; Chen et al., 2022). The GRanD (Lehner et al., 2011) version 1.3 consists of 7320 global georeferenced dams with attributes of the dam and the reservoir (e.g., volume of the reservoir, height of the dam, etc.) Out of all the new products that have been developed, only ReGeom (Yigzaw et al., 2018) and Global Reservoir Bathymetry dataset (GLOBathy) (Khazaei et al., 2022) offer bathymetry curves for the complete range of reservoirs in the GRanD database. ReGeom utilizes an iterative process to select the optimal geometric shape that minimizes the error in estimated total storage and surface area, and derives bathymetric relationships based on this shape (Yigzaw et al., 2018). In contrast, GLOBathy uses polynomial functions to fit bathymetry relationships to a bathymetry generated using the distance method in a Geographical Information System (GIS) (Khazaei et al., 2022).

This state-of-the-art raises two fundamental questions: First, *how realistic is it to oversimplify reservoir bathymetry, e.g., as a rectangular prism with constant surface area for estimating daily reservoir evaporation?* Second, *given the numerous approximation options available, how sensitive are reservoir simulations to the chosen bathymetry approximations?*

In addition to the reservoir bathymetry, the method used to calculate the evaporation rate also affects the modelled reservoir evaporation. In a comprehensive review of 16 global hydrologic models conducted by Telteu et al. (2021), it was found that reservoir storage was included in only six models, and of those, only four models accounted for reservoir evaporation as part of their hydrologic processes. For example, PCR-GLOBWB uses Potential Evapotranspiration (PET) for reservoir evaporation rate (E), while WaterGAP2 uses PET formulation with albedo (α) = 0.08. CWatM and LPJmL use observed pan evaporation observations, a method that is not applicable when models need to run in forecast mode. Therefore, in addition to over-simplified bathymetry approximations, simplified estimations such as $E = PET$ and/or spatio-temporally fixed albedo raises the question on the credibility of reservoir evaporation simulations from state-of-the-art global HMs.

It should be noted, however, that not all reservoirs are capable of disrupting the natural flow regime of rivers, which means that their impact on streamflow can vary greatly. As a matter of fact, among the 7320 reservoirs of the GRanD database, the top 1% of the highest volume reservoirs account for 50% of the total reservoir volume in the database (Lehner et al., 2011). Nevertheless, size can be relative as the impact of a reservoir can vary significantly depending on the size of the catchment area. In a smaller catchment, a medium-sized reservoir may have a greater disruptive impact because it can store a large portion or even a several times of the annual runoff. A significant alteration of the natural flow regime can have far-reaching consequences, for example, a change in the river temperature regime (Casado et al., 2013; Erickson and Stefan, 2000; Olden and Naiman, 2010) and the damage of its aquatic ecosystem (Lessard and Hayes, 2003). In a larger

catchment, on the contrary, the capacity of the same medium-sized reservoir may have a negligible effect on the total annual runoff at the dam. Meaning, reservoirs that do not disturb the natural streamflow regime (i.e., nondisruptive) may unnecessarily increase the computational effort of hydrological simulations without, however, contributing significantly to improving model accuracy.

Quantification of reservoir disruptivity goes back to Dynesius and Nilsson (1994) (see column header “disruptivity” in Table 4.1) who described “flow regulation” for a river basin as the sum reservoir capacities, interbasin diversions and irrigation consumption expressed as percentage of the mean annual discharge. Another measure of reservoir disruptivity is the Amended Annual Proportional Flow Deviation (AAPFD) index (Gehrke et al., 1995; Ladson and White, 1999) which is a hydrologic indicator for streamflow alteration where monthly observations are compared with natural conditions. Biemans et al. (2011) calculated AAPFD at every grid cell (0.5°) to get a spatial overview of the river stretches most affected by reservoirs and irrigation. Vörösmarty et al. (1997), Nilsson et al. (2005), Lehner et al. (2011), Zajac et al. (2017), and Yassin et al. (2019) used the ratio of reservoir capacity to mean annual inflow for the same purpose but denominated as “degree of regulation” or “regulation scale”. Hanasaki et al. (2006) used the same ratio for comparing seasonality of outflow and inflow, although, without explicitly using it as a measure for disruptivity.

Identifying non-disruptive reservoirs from global reservoir databases opens up the possibility of determining locations with strong anthropogenic impact, which is crucial for prioritizing reservoir modelling activities in large-scale hydrological models. For instance, in mHM, each reservoir adds three or eight parameters to optimisation space depending on whether the reservoir is modelled as a natural lake or a regulated reservoir, respectively. While considering all existing reservoirs would yield the most accurate simulation, prioritizing disruptive reservoirs for modeling optimizes computational resources while still accounting for the substantial impact on the streamflow regime. Yet the literature does not provide clear guidelines for appropriate “exclusion” thresholds for disruptivity indices.

We hypothesize the following about the key challenges in large-scale reservoir modeling:

1. The use of machine learning for modeling the non-consumptive demand improves the streamflow simulation in river networks with reservoirs on a daily time scale.
2. The shape of reservoir (geometry) is of critical importance for reservoir simulations, especially for water level and evaporation fluxes.
3. Only a subset of global reservoirs are disruptive and essential for improving the efficiency of hydrologic models with respect to observed streamflow simulations.

To test these hypotheses, we developed a new lake/reservoir module (Section 4.2.1-4.2.2) for the mesoscale hydrological model (mHM, <https://mhm-ufz.org>) (Samaniego

et al., 2010; Kumar et al., 2013; Thober et al., 2019), which has been shown to be capable of capturing natural hydrologic systems. To test the first hypothesis, we use the random forest technique (Breiman, 2001) to generate the non-consumptive demand use as input for the S_{2023} formulation (Section 4.2.3). To test the second hypothesis, we generated bathymetry curves using two different approximations: a simplified rectangular prism and a more accurate half-pyramid (Liebe et al., 2005). We then compared reservoir simulation outputs from these two approximations to simulations based on ReGeom (Yigzaw et al., 2018) and observed bathymetry, where available. For the third hypothesis, we relate the AAPFD index of reservoirs with a couple of practical disruptivity indices and try to find globally applicable thresholds to distinguish reservoirs that cause disturbance from those that do not. We conducted three experiments covering 31 reservoirs, across the globe exhibiting different hydroclimatic conditions to test these three hypotheses. Reservoirs utilized for consumptive water usage (e.g., irrigation, domestic, and industrial) were excluded from our analysis. Streamflow observations downstream of the dam, the control points in this study, do not register the consumptive water supplied from the reservoir. In absence of measurements for consumptive water use from reservoirs, we specifically focused on reservoirs designed solely for non-consumptive demands for evaluating the efficacy of the new lake module and testing of the above hypotheses.

Table 4.1: Comparison with the state-of-the-art of reservoir representation

Study	HM	No. of dams tested	Regulation	Disruptivity	Bathymetry
This study	mHM-LM	32 non-consumptive reservoirs	<p>Sadki et al. (2023) with non-consumptive demand (\hat{D}^n) based on Random Forest (RF) model based on streamflow gauge downstream of reservoir. κ is a function of instantaneous reservoir volume (V) instead of reservoir volume at start of operational year</p> $\kappa = \left(\frac{V}{\gamma V_f} \right)^\lambda$ <p>Where, V_f is reservoir capacity and λ is a model parameter, in addition to c^*, β, ω, and γ (refer to eqns. in the entry for Hanasaki et al. (2006) below).</p> <p>In contrast to Hanasaki et al. (2006), non-consumptive demand is added to the formulation of \hat{D}^T and all demands are allowed to have variability.</p>	<p>c and c' are used as measures for disruptivity.</p> $c = \frac{V_f}{\bar{T}_0}$ $c' = \frac{V_f}{A_c}$ <p>where, \bar{T}_0 is mean annual inflow volume, and A_c is the reservoir catchment area. Thresholds of c and c' proposed for excluding non-disruptive reservoirs.</p>	<p>Liebe et al. (2005). Comparisons made against $V = Ah$ (linear) and Yigzaw et al. (2018).</p>
State-of-the-art in chronological order					
Dynesius and Nilsson (1994)	-	139 large river system (20% of global river runoff).	Regulation impact assessed as percentage of mean annual discharge of the river system stored in reservoirs.	No analysis or exclusion threshold recommendation.	-
Meigh et al. (1999)	PDM	20 countries in southern and eastern Africa	Outflow given by $Q^T = V^{1.5}$	No analysis or exclusion threshold recommendation.	Linear A - V relationship
Coe (2000)	HYDRA	Parana river basin	Outflow given by $Q^T = \frac{V}{T}$ where T is the residence time	No analysis or exclusion threshold recommendation.	-
Döll et al. (2003)	WaterGAP	680 ($V_f > 500 \times 10^6 \text{ m}^3$)	Outflow given by $Q^T = \kappa V \left(\frac{V}{V_f} \right)^{1.5}$ where κ (0.01/d) is release coefficient	No analysis or exclusion threshold recommendation.	$V = Ah$ (linear)
Nilsson et al. (2005)	-	292 large river systems draining 54% of global land area	Dynesius and Nilsson (1994)	No analysis or exclusion threshold recommendation.	-

Study	HM	No. of dams tested	Regulation	Disruptivity	Bathymetry
Hanasaki et al. (2006)	TRIP (later Ho8)	452 (28 evaluated) ($V_f > 1000 \times 10^6 \text{ m}^3$)	<p>Outflow (monthly) is calculated as</p> $Q^T = \begin{cases} \kappa \hat{D}^T, & c \geq c^* \\ \kappa \rho \hat{D}^T + (1 - \rho) I, & c < c^* \end{cases}$ <p>where, \hat{D}^T is the total hedged demand given by For non-irrigation reservoirs: $\hat{D}^T = I$</p> <p>For irrigation reservoirs: $\hat{D}^T = \begin{cases} \omega \bar{I} + \frac{(1 - \omega)}{\bar{I}} D^T, & \hat{D}^T / \bar{I} > 1 - \omega \\ \bar{I} + D^T - \hat{D}^T, & \hat{D}^T / \bar{I} < 1 - \omega \end{cases}$</p> <p>where, D^T is total demand (irrigation, domestic and industrial supply only) and I is the mean inflow for the month. Bar indicates long-term average value. κ is release coefficient and c is a ratio defined as: $\kappa = \frac{V_1}{\gamma V_f} \quad c = \frac{V_f}{I_v}$</p> <p>where, V_1 is storage at first day of operational year, V_f is the reservoir capacity, I_v is the mean annual reservoir inflow volume. ρ, c^*, ω, and γ are set as: $\rho = 4c^2 \quad c^* = 1/2 \quad \omega = 1/2 \quad \gamma = 0.85$</p>	c used as measure of disruptivity with an empirical threshold of $c^* = 1/2$. No further analysis or exclusion threshold recommendation.	Lake evaporation (E), precipitation (P) and percolation (L) not accounted. Shape not considered
Haddeland et al. (2006a)	VIC	-	Reservoir outflow is optimized based on pre-existing simulated inflow based on the reservoir purpose. The outflow estimates are then bounded by minimum and maximum outflow thresholds.	No analysis or exclusion threshold recommendation.	Not specified
Wisser et al. (2010)	WBM _{plus}	668 ($V_f > 500 \times 10^6 \text{ m}^3$)	<p>Outflow behavior based on comparison of inflow to long term mean inflow.</p> $Q^T = \begin{cases} 0.16I, & I \geq \bar{I} \\ 0.6I + (\bar{I} - I), & I < \bar{I} \end{cases}$	No analysis or exclusion threshold recommendation.	Lake evaporation (E), precipitation (P) and percolation (L) not accounted. Shape not considered.

Study	HM	No. of dams tested	Regulation	Disruptivity	Bathymetry
Biemans et al. (2011)	LPJmL	190 ($V_f > 5000 \times 10^6 \text{ m}^3$)	Hanasaki et al. (2006) with $\omega = 0.1$	Gridded AAPFD (Ladson and White, 1999) showing river stretches most affected by reservoirs and irrigation extractions. No exclusion threshold recommendation.	Not specified
Neitsch et al. (2011)	SWAT (user manual)	-	Outflow based on target storage volumes and outflow thresholds. During flood seasons, the target storage volume is a function of average soil water content in the reservoir catchment. For rest of the year, the target is constant and equal to emergency spillway volume.	No analysis or exclusion threshold recommendation.	$A = \alpha V^\beta$, where α and β are solved from input area and volume corresponding to emergency and principal spillway
van Beek et al. (2011)	PCR-GLOBWB	513	Monthly reservoir target storage estimated at start of year based on expected monthly inflow from retrospective years and monthly outflow derived from a harmonic function. $Q^T = \frac{Q_{\max}^T}{2} \left[1 - \cos \left(\frac{2\pi(m - m_b)}{m_e - m_b} \right) \right]$ where, m is the current month while m_b and m_e are start month and end month of release and refill seasons.	No analysis or exclusion threshold recommendation.	Liebe et al. (2005)
Burek et al. (2013)	LISFLOOD (user manual)	-	Conditional outflow based on storage levels and outflow thresholds. No seasonality control.	No analysis or exclusion threshold recommendation.	Not specified
Terink et al. (2015)	SPHY	-	Outflow can be an exponential or polynomial function of reservoir water level or storage.	No analysis or exclusion threshold recommendation.	Not specified
Zhao et al. (2016)	DHVM	2	Conditional outflow based on storage levels, outflow thresholds and upstream or downstream flow conditions. Monthly demand is either prescribed or calibrated	No analysis or exclusion threshold recommendation.	$A = \alpha_1 V^{\beta_1} + \gamma_1; h = \alpha_2 V^{\beta_2} + \gamma_2$, where α and γ are regression coefficients, and β is $<1, >1$ and 1 for concave, convex and linear relation.
Zajac et al. (2017)	LISFLOOD (GloFAS)	667	Burek et al. (2013)	Global 0.1° map of ratio of upstream cumulative reservoir capacity to the annual natural streamflow volume for illustrating the potential impact of reservoirs on streamflow in the GloFAS. No further analysis or exclusion threshold recommendation.	$V = hA$ (linear)
Sutanudjaja et al. (2018)	PCR-GLOBWB2	≈ 6000	van Beek et al. (2011)	No analysis or exclusion threshold recommendation.	Global relationship (equations not specified)

Study	HM	No. of dams tested	Regulation	Disruptivity	Bathymetry
Yassin et al. (2019)	MESH	37	Comparable to Zhao et al. (2016)	c used as measure of disruptivity and analyzed against model performance. No exclusion threshold recommendation.	Actual bathymetry curves
Shin et al. (2019)	LHFD	1889	Hanasaki et al. (2006) with $\rho = \text{ffc}$, $c^* = 1/\gamma$, and $\omega = 0.1$. ρ treated as a model parameter in one of the experiment.	ρ used as measure of disruptivity. No exclusion threshold recommendation.	Liebe et al. (2005) in conjunction with refining of bed and floodplain elevation (DEM).
Dang et al. (2020)	VIC-ResOpt	2	Conditional outflow based on storage levels and rule curve (semester to monthly) for target water level or demand hedging	No analysis or exclusion threshold recommendation.	Not specified
Müller Schmied et al. (2020)	WaterGAP	1109	Hanasaki et al. (2006)	No analysis or exclusion threshold recommendation.	$A = \left[1 - \left(\frac{ V - V_f }{V} \right)^{2.814} \right] A_f$
Shin et al. (2020)	CamaFlood	86	Shin et al. (2019)	Shin et al. (2019)	Not specified
Burek et al. (2020)	CWatM	-	Burek et al. (2013)	No analysis or exclusion threshold recommendation.	$V = hA$ (linear)
Vanderkelen et al. (2022)	CLM-mizuRoute	1773	Hanasaki et al. (2006)	No analysis or exclusion threshold recommendation.	Not specified.
Sadki et al. (2023)	DROP (reservoir module only)	215 reservoirs in Spain	Hanasaki et al. (2006) and Shin et al. (2019) with parameters. ρ is a function defined by $\rho = \min \left[1, \left(\frac{c}{c^*} \right)^\beta \right]$ c^* , β , ω , and γ are model parameters (refer to eqns. in the entry for Hanasaki et al. (2006) above). In addition, the starting month of the operational year is also a model parameter.	c used as measure of disruptivity and analyzed against model performance. No exclusion threshold recommendation.	Not specified.

4.2 METHODOLOGY

4.2.1 Establishment of a Lake Module for mHM

The mHM (www.ufz.de/mhm) (Samaniego et al., 2010; Kumar et al., 2013; Thober et al., 2019) is a process-based, grid-based distributed hydrologic model, which was developed for operational hydrologic applications at scales ranging from 1 km to 50 km (Zink et al., 2016; Samaniego et al., 2018; Samaniego et al., 2019). Despite of accounting for most of the major hydrological processes (e.g., canopy interception, snow accumulation and melting, soil moisture dynamics, infiltration and surface runoff, evapotranspiration, subsurface storage and discharge generation, deep percolation and base flow, and flood routing) (Rakovec et al., 2016b), mHM has not included reservoirs. Here we augment mHM with a new reservoir/Lake Module (LM) (<https://git.ufz.de/shresthp/mhm>) to account for the anthropogenic effect of natural lakes and man-made reservoirs on hydrological simulations. The overall algorithm and the parameters of LM are provided in C.1 and C.2, respectively.

mHM-LM distinguishes between reservoirs and natural lakes with an input flag. Natural lakes are a consequence of the development of the earth's crust, glacial processes, changing water balance (Shugar et al., 2020), etc. and therefore always exist during a simulation. Artificial lakes (i.e., reservoirs), on the contrary, are created by the construction of a dam that interrupts the natural course of a river, so they require the date of commissioning as input, and appear dynamically in the simulation according to these dates. Further, mHM-LM allows water abstractions (e.g., irrigation, domestic use) from natural lakes to represent regulated natural lakes. mHM-LM represents the bathymetry of the reservoir (or lake) based on the user inputted relationship between elevation (h), surface area (A) and volume (V), which we refer to as the hAV table.

A key feature of the mHM-LM module is that it automatically delineates the reservoir catchment area during run time given the high-resolution Digital Elevation Model (DEM) (at resolution ℓ_0) that forms the basis for the mHM configuration and the user-entered dam location coordinates. A runtime performance test was carried out for mHM where catchment delineation was tested at 169 locations using a 220 m DEM, on a large-scale domain (The Rhine river basin, $160,000 \times 10^6 \text{ m}^2$, system specifications = Dell PowerEdge R940xa 4x 28-Core Intel(R) Xeon(R) Platinum 8280L CPU @ 2.70GHz and 6TB RAM, compiler = GFortran, compiler flags = -O3). The catchment delineation completed in 0.05 s for one location and 12 s for 169 locations which, when extrapolated, would inflate to ≈ 10 minutes for the full set of 7320 GRanD reservoirs. Meaning, catchment delineation of large number of reservoirs is not a computational bottleneck for mHM. Besides, the configuration would be part of the mHM restart files, which then would not matter for subsequent runs (e.g., in forecast mode). After determining the catchment area of the reservoir, mHM-LM simulates the maximum possible inundation area using a specified Dam Crest Level (DCL) as input. If the user does not specify the DCL, mHM-LM estimates

this parameter from the DEM so that the corresponding lake area would be approximately the maximum inundation area in the hAV table.

mHM-LM uses the delineated spatial extent of the reservoir to find lake inlets and outlets, as shown in Figure 4.1a. By definition, any node that touches the maximum extent of the lake is a lake inlet node. The node that includes the dam is the lake outlet node. mHM-LM assumes the lake has the same number of lake inlet nodes throughout the simulation, i.e., the reservoir boundary remains fixed even though the lake states h , A and V vary. This module also uses the delineated extent of the reservoir catchment to preserve reservoir inflow. The new approach of SCC routing allows model grids with multiple subgrid contribution to be partitioned into multiple nodes based on the catchment area of the reservoir. In other words, with SCC, the model grids can now have multiple outlets as shown by the flow direction arrows in Figure 1a. This ensures the area drained by the reservoir is preserved at *each modelling scale*, preventing under- or overestimation of lake inflow, thus preserving subgrid contribution (specified at the resolution ℓ_0) and model efficiency across scales. This feature is consistent with the Multiscale Parameter Regionalization (MPR) paradigm built into mHM (Samaniego et al., 2010; Kumar et al., 2013; Schweppe et al., 2022) which promotes preservation of subgrid information. We intend to demonstrate the impact of the novel SCC upscaling scheme in distributed HMs in a future article.

mHM-LM, currently, does not have an in-built demand estimation or modeling procedure. Consequently, mHM requires demand data as model input for modeling reservoir regulation. This could be records, estimates, or forecasts of demand (e.g., domestic, irrigation, non-consumptive, etc.), either as point or grid time series. Additional information on how mHM processes the input consumptive water demand is available in Supplement S5.

At each model time step, once the inflow from all the lake inlets are accounted, the change in lake volume, area and water level are assumed to be instantaneous. This assumption is based on the fact that the time required for a lake to reach a new water level is less than the integration time step of the model ($= 1$ hour). In next step, the lake's flux exchanges are estimated and the new water balance i.e., new reservoir states are found (refer Section 4.2.2).

The final process of the lake module consist of routing the outflow from the lake (like any other node) to the lake outlet node, as shown in Thober et al. (2019). The equation used for the routing the lake outflow is the same as the original mHM formulation presented in Samaniego et al. (2010) and further developed (e.g., dynamic time stepping) in Thober et al. (2019). For more details refer to the Supplement S1.

4.2.2 Reservoir Water Balance

The proposed mHM-LM module simulates the water balance of a reservoir by treating it as a single entity located in a node of the river network rather than a spatially distributed element. This is advantageous because the presence of a lake or reservoir should be

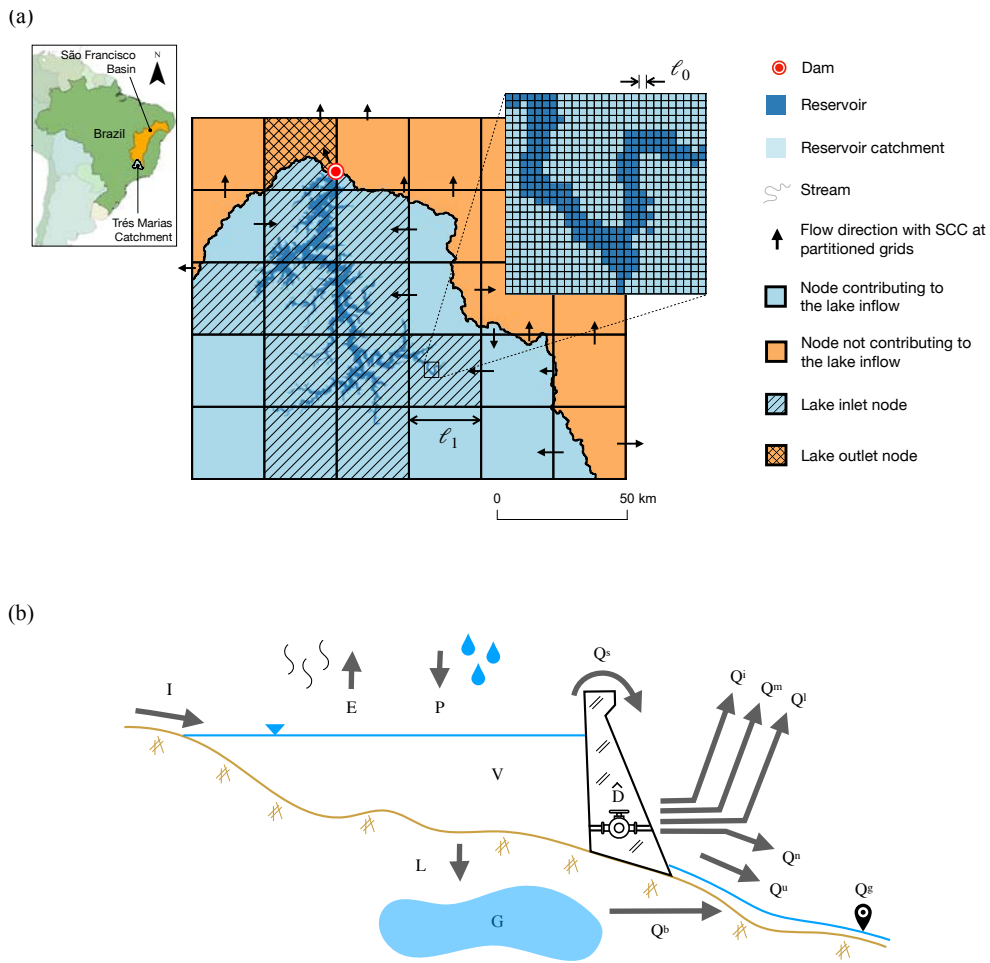


Figure 4.1: (a) Computational grid map of Três Marias reservoir (as an example) in mHM-LM showing the delineated reservoir lake, reservoir catchment, lake inlet nodes, and lake outlet node. Upscaled flow direction arrows at the level ℓ_1 show how a single modelling grid can be split into multiple computational nodes that route water to more than one downstream node. ℓ_0 (≈ 220 m) and ℓ_1 (≈ 25 km) denote the resolution of the level-0 and level-1 of mHM, i.e., the input and the modeling level. (b) Schematics showing Water balance components of reservoir and the lake aquifer beneath the reservoir. Here, the following definitions are use: I [m^3/s] denotes inflow, E [m/s] is lake evaporation, P [m/s] is lake precipitation, L [m/s] is percolation at lake's bed, V [m^3] is lake volume, Q^s [m^3/s] is reservoir spill. Q^i [m^3/s], Q^m [m^3/s], Q^l [m^3/s], and Q^n [m^3/s] are irrigation, domestic, industrial, and non-consumptive abstractions, respectively. Q^u [m^3/s] is unregulated reservoir outflow, \hat{D} represents the reservoir regulation and the demand hedging, G [m^3] is groundwater storage beneath the lake, and Q^b [m^3/s] is shallow groundwater baseflow from G . Q^g [m^3/s] is the streamflow observations at a gauge downstream of the dam.

independent of the modeling resolution (ℓ_1). Most of the models listed in Table 4.1 do not have this property and therefore these HMs can not be labeled as scale independent.

The key state variables and fluxes components of the water balance of a typical reservoir are shown in Figure 4.1b. The finite difference approximation of the water balance equation for this simplified representation is given by:

$$\frac{dV}{dt} \approx \frac{\Delta V}{\Delta t} = \frac{V_t - V_{t-1}}{\Delta t} \approx \left(P_t - E_t - L_t \right) \frac{A_t + A_{t-1}}{2} + I_{t-1} - Q_t^s - Q_t^i - Q_t^m - Q_t^l - Q_t^n - Q_t^u \quad (4.1)$$

Subscripts t and $t - 1$ denote the current and previous time step, respectively. Δt is set here to 1 h, which corresponds to the integration time of the routing algorithm. V [m^3] is the reservoir storage at a point of time. P [m/s] and E [m/s] are the precipitation on the surface of the reservoir and the evaporation from that surface, respectively. L [m/s] is the seepage from the lake bed, and G [m^3] is the groundwater aquifer beneath the lake. A [m^2] represents the simulated surface of the lake, which is also the horizontal projection surface of the lake bottom. The semi-area used is an approximation of the truncated pyramid. I [m^3] is the inflow to the reservoir, which is composed of the inflow from the reservoir catchment and interbasin transfer (from adjacent catchment), if any. Q^s [m^3/s] is the spill from reservoir during overflowing conditions. Q^i , Q^m and Q^l [m^3/s] are the consumptive outflows from the reservoir for irrigation, domestic, and industrial use, respectively. Q^n [m^3/s] is the non-consumptive outflow pertaining to hydropower use, flood control, navigation, and recreation. Q^u [m^3/s] is the unregulated outflow from the reservoir. Q^b [m^3/s] is the shallow groundwater baseflow generated by the aquifer beneath the reservoir.

P_t is estimated by area weighing the input precipitation grids overlaying the delineated lake mask (refer Sect. 4.2.1). E_t is estimated using an implementation of Penman-Monteith equation for potential evaporation (Shuttleworth, 1996), as shown in C.3. The meteorological input required for calculation of E (2-m temperature (T) [$^{\circ}\text{C}$], incident shortwave radiation (S_i) [W/m^2], incident longwave radiation (L_i) [W/m^2], 2-m windspeed (U_2) [m/s], and 2-m dew point temperature (T_d) [$^{\circ}\text{C}$]) are taken from the ERA5 (Copernicus Climate Change Service, 2017) reanalysis database and downscaled to lake representative values by area weighing the input grids overlaying the delineated lake mask. We also introduced dynamic reflectivity of still water, α , which is a function of latitude and the hourly variation of solar elevation angle (refer Eq. C.3). The conceptualization of the percolation flux (L_t) occurring at the bottom of the lake uses a distributed approach using a variable water head and spatially varying soil percolation parameters estimated by the core of the model mHM using the MPR technique. More detail on the procedure to estimate the total water seepage L_t is presented in the Supplement S2 and illustrated in Figure S1. In the current version of this module, the generation of the groundwater flow from the underlying lake aquifer is done via a linear reservoir. We plan to develop a full groundwater model coupled to the mHM-LM in the future. The simplified water balance equations (for G and

Q^b) of the underlying lake aquifer are shown in Supplement S3. LM utilizes the reservoir inflow, collected by the routing model of mHM, from previous time step for the lake water balance. This is because, in mHM, the water balance is followed by the routing at each time step. Equations for Q_t^s are provided in Supplement S4. The regulation scheme employed to estimate Q^i , Q^m , Q^l , Q^n , and Q^u is described in Sect. 4.2.5.

For the sake of simplicity, we assume Q_t^n to be released to the immediate downstream of the reservoir i.e., hydropower station (if any) is located at the base of the dam. The total reservoir outflow leaving the lake, which is then routed to the downstream node, can then be calculated with the following equation:

$$Q_t^d = Q_t^n + Q_t^u + Q_t^s + Q_t^b \quad (4.2)$$

For the initial conditions the lake states (h , A , V) are initialized using the input water level if present, otherwise a half-full reservoir is assumed. The procedure for initializing the aquifer storage (G) beneath the reservoir is described in Supplement S3.

Once all the fluxes are known, V_t and A_t remain unknown in Eq. 4.1 which can be rewritten as:

$$\Delta V = V_t - V_{t-1} = f(A_t) \Delta t \quad (4.3)$$

mHM-LM updates the reservoir states (V , A , and h) at each modelling time step using the secant method (Booth, 1966) root finding algorithm. The corresponding algorithm is presented in C.4.

4.2.3 Estimating Non-consumptive Demand with a Surrogate Model

Non-consumptive use of reservoir water refers to applications where the water remains or is immediately returned to the location in a stream from which it was extracted. Examples of non-consumptive use of water include hydropower generation, flood control, navigation, and recreational uses. Although the non-consumptive water use is returned back without consuming, the timing of water use and return could have significant deviations from reservoir inflow due to reservoir regulation. The management of reservoir is a highly intricate process that relies on numerous external variables, including hydropower energy demands, real-time weather predictions for flood control dams, tourism requirements, etc.

Modelling non-consumptive demand is extremely challenging due to several reasons. Firstly, the data on non-consumptive demand is typically not readily available as open-source. Secondly, often non-consumptive reservoirs are used for more than one non-consumptive applications, making it challenging to disentangle the individual signals. Thirdly, unlike irrigation and domestic demand for which service area can be estimated, once the hydropower produced by a reservoir enters the national grid mix, it is virtually impossible to track the service area. Lastly, the non-consumptive outflow (and reservoir

outflow in general) from a disruptive dam usually bears high degree of discontinuities originating from highly discontinuous regulation decisions. For these reasons, developing an explicit process-based demand model driven by demands from various sectors is outside of the scope of this study.

Despite the lack of readily available data on non-consumptive demand or supply, streamflow gauge observations at a location downstream of dams ($Q^{g,o}$) are available in publicly accessible databases. Non-consumptive water use from a reservoir eventually gets registered downstream at the streamflow gauge. This includes reservoir water released for hydropower use, to maintain water depth for navigation and recreation, and the release corresponding to reservoir level drawdown prior to flood season for flood control. Here, we propose to employ random forest (Breiman, 2001) as a surrogate model to inverse estimate the combined non-consumptive demand from the streamflow gauge observations, $Q^{g,o}$. Random forest (RF) model is a powerful machine learning tool that is highly effective in generating discontinuous functions, which are essential for accurate estimation of non-linear relationships such as reservoir regulation decisions. RFs are an ensemble learning method i.e., they combine the predictions of multiple individual models or decision trees. This ensemble approach often means RFs are less prone to overfitting and less sensitive to outliers, leading to more accurate and stable predictions compared to other multivariate regression approaches (Li et al., 2016; Bachmair et al., 2017; Schoppa et al., 2020; Desai and Ouarda, 2021).

The *predictors* utilized in this study to construct the RF model, their usage proxy and their ranks across the reservoirs based on permutation accuracy importance (Strobl et al., 2007), are shown in Table 4.2. These type of predictors have been widely used in the literature e.g., Qie et al. (2022) and Tounsi et al. (2022). Optimized RF models were obtained for each reservoir of the experiment. The predictors related to the inter-annual water cycle (i.e., *year*, *Pre365*, *Pet365*, *Pre365lag365*, *Pet365lag365*) were within the top six predictors across 75% of the reservoirs. This suggests that, for the majority of these reservoirs, regulatory mechanisms are predominantly influenced by a year-by-year planning approach. Notably, predictors such as *Pet30*, *Pre30*, and *Pre7* exhibited an inter-quartile range exceeding five ranks and an overall range surpassing 10 ranks. This implies the short to medium-term decision-making strategies to be dominant in only a subset of reservoirs.

The RF-model predicted the streamflow at the dam ($Q^{d,RF}$) with KGE values of 0.60 or higher at 90% of reservoirs in both the calibration and validation periods. This suggests that the RF model is a good surrogate for estimating Q^d . The algorithm to predict Q^d using RF and then the non-consumptive reservoir demand from Q^d is presented in C.5.

Table 4.2: Predictors used in constructing random forest model for estimating non-consumptive demand at reservoirs, their explanation (proxy), and the predictor importance ranking across the reservoirs of the experiment.

Predictor	Meaning	Proxy	Predictor rank across reservoirs
Pet365 lag365	Annual PET with 1 year lag	Storage-related decisions. For example, if the past month (or year) was wetter than the corresponding calendar average, this will result in a higher than normal storage. In such case, an above-average release is to be expected in the current month (or year).	
Pet365 lag365	Annual Precipitation with 1 year lag		
Pet30 lag30	Monthly PET with 1 month lag		
Pre30 lag30	Monthly Precipitation with 1 month lag		
Pet365	Annual PET	Decisions based on long-term meteorological conditions, e.g., current year being wetter or drier than the climatological average.	
Pre365	Annual Precipitation		
Tavg30	Average Monthly Temperature	Decisions based on medium-term meteorological conditions, e.g., current month being wetter or drier than the monthly long-term average.	
Pet30	Monthly PET		
Pre30	Monthly Precipitation		
Pet7	PET over last 7 days	Short-term decisions made in response to extreme meteorological conditions, such as flash floods.	
Pre7	Precipitation over last 7 days		
Pet3	PET over last 3 days		
Pre3	Precipitation over last 3 days		
Year	Year of current date	Inter-annual variability of operation decisions.	
Month	Month of current date [1, 12]	Seasonal variability of operation decisions.	
Woy	Week of year for the current date [1, 52]		
Doy	Day of year for the current date [1, 365]		

5 10 15

Rank

4.2.4 Demand Hedging

It is not realistic to fulfill all the demand from the reservoir, at all times. mHM-LM follows the formulation given in Shin et al. (2019) for hedging the demand:

$$\hat{D}_t^T = \begin{cases} \omega \bar{I} + \frac{(1-\omega)}{\bar{D}^T/\bar{I}} D_t^T, & \bar{D}^T/\bar{I} > 1 - \omega \\ \bar{I} + D_t^T - \bar{D}^T, & \bar{D}^T/\bar{I} < 1 - \omega \end{cases} \quad (4.4)$$

$$\text{where, } D_t^T = D_t^i + D_t^m + D_t^l + D_t^n \quad (4.5)$$

\hat{D}_t^T [m³/s] is the total hedged demand for the reservoir. D_t^T [m³/s] is the total demand and is the sum of the irrigation demand (D_t^i), domestic demand (D_t^m), industrial demand (D_t^l), and non-consumptive demand (D_t^n), all in m³/s. \bar{D}^T [m³/s] is the mean annual total demand. \bar{I} [m³/s] is the mean annual inflow rate. \bar{I} is estimated in advance by running the model with the default parameter set. ω is a fraction that ensures minimum value of \hat{D}^T to be at least $\omega \bar{I}$ (Shin et al., 2019; Sadki et al., 2023). Hanasaki et al. (2006) used $\omega = 0.5$, Shin et al. (2019) proposed $\omega = 0.1$, while Sadki et al. (2023) optimized ω . We follow Sadki et al. (2023) and include ω as a model parameter (refer C.2).

The long-term expected value of \hat{D}^T in Eq. 4.4 is mathematically equal to \bar{I} . Hanasaki et al. (2006) advocated for \hat{D}^T to be constrained in this way so that the algorithm can flexibly generate reservoir outflow for biased inflow and argued it to be an essential feature in global river discharge simulations, where inflow can have bias and uncertainties.

The first condition in Eq. 4.4 is comparable with demand hedging rule that preserves some water to meet the future demands because high \bar{D}^T/\bar{I} makes a reservoir susceptible to drought conditions (Shin et al., 2019). The second condition is applied for reservoirs with lesser demand where D_t^T is not curtailed (Sadki et al., 2023). The analytical derivation of the demand hedging criterion $\bar{D}^T/\bar{I} > 1 - \omega$ can be found in Shin et al. (2019).

It is noteworthy that this study deviates from Hanasaki et al. (2006) and the following studies by incorporating non-consumptive demand in Equation 15 and using this formulation for all reservoir usage. Hanasaki et al. (2006) assumes non-irrigation reservoirs to have constant demand at all times, the sum of which is always equal to mean inflow, which is a crude assumption.

The experiment set for this study is described in Sect. 4.3.1 wherein reservoirs with only non-consumptive use are considered. Using the non-consumptive demand estimated from Eq. C.17 (i.e., $D^n = \tilde{D}^n$), Eq. 4.4 reduces to:

$$\hat{D}^n = \begin{cases} \omega \bar{I} + \frac{(1-\omega)}{\tilde{D}^n/\bar{I}} \tilde{D}^n, & \tilde{D}^n/\bar{I} > 1 - \omega \\ \bar{I} + \tilde{D}^n - \tilde{D}^n, & \tilde{D}^n/\bar{I} < 1 - \omega \end{cases} \quad (4.6)$$

4.2.5 Estimating Reservoir Outflow Components

mHM-LM estimates the regulated outflows Q_t^i , Q^m , Q^l , and Q_t^n and the unregulated outflow Q_t^u following a regulation scheme similar to Sadki et al. (2023), which is the revised version of Hanasaki et al. (2006) and Shin et al. (2019). According to the scheme, for reservoirs below a threshold size (c^*), the total outflow constitutes of a fraction (ρ) from the (total hedged) demand and a fraction ($1 - \rho$) from the inflow. While for reservoirs larger than c^* , the outflow is solely governed by the demand:

$$Q_t^T = \begin{cases} \kappa_t \rho \hat{D}_t^T + (1 - \rho) I_t, & 0 \leq c < c^* \\ \kappa_t \hat{D}_t^T, & c \geq c^* \end{cases} \quad (4.7)$$

where Q_t^T [m^3/s] is the total outflow, and I_t [m^3/s] is the reservoir inflow. κ_t [-] is a time varying release coefficient. As ρ [-] varies from 0 to 1, the reservoir regulation changes from run-of-the-river to demand-controlled regulation (Shin et al., 2019). c [-] is the ratio of reservoir capacity (V_f) [m^3] to mean annual reservoir inflow volume (\bar{I}^v) [m^3] and indicates the size of reservoir relative to the catchment. c^* is a threshold above which a reservoir is deemed to be fully demand controlled and is set as a model parameter (refer C.2).

The demand hedging procedure to obtain \hat{D}_t^T (refer Eq. 4.4) doesn't include any checks with prevailing reservoir storage. When the reservoir is in drought conditions, \hat{D}_t^T may require further hedging. κ_t regulates fulfillment of \hat{D}_t^T based on the current reservoir storage. ρ and κ_t are calculated as:

$$\rho = \min \left[1, \left(\frac{c}{c^*} \right)^\beta \right], \quad (4.8)$$

$$\kappa_t = \left(\frac{V_{t-1}}{\gamma V_f} \right)^\lambda, \quad (4.9)$$

where β , γ , and λ are model parameters and dimensionless (ref C.2). V_{t-1} [m^3] is the reservoir volume from previous time step. κ aims to keep the long-term reservoir volume at γV_f . In contrast to Hanasaki et al. (2006) and Shin et al. (2019) who used $\gamma = 0.85$, we follow Sadki et al. (2023) by considering γ as a model parameter as different reservoirs may have different long-term storage goals. λ inhibits the sensitivity of κ to the time varying V . Eqns. 4.7 and 4.8 comprise the generalized form of the regulation scheme originally proposed by Hanasaki et al. (2006). Hanasaki et al. (2006) and Shin et al. (2019) are specific cases where (c^* , β) are set to (0.5, 2) and ($1/\gamma$, 1), respectively. In summary, κ_t "regulates" the demand fulfillment whereas ρ and c^* "partition" the contribution of regulated and unregulated outflows in the total outflow from the reservoir.

Hanasaki et al. (2006) and subsequent studies assume release of the total reservoir outflow downstream, while the water abstraction module was responsible for accounting

for various water uses along the river reaches downstream. Essentially, the reservoir in Hanasaki et al. (2006) served as a regulatory mechanism for the rivers rather than a water usage reserve. Given that the mHM model does not currently include a water abstraction module, we propose an alternative approach for this study. The first term on the R.H.S. of Eq. 4.7 is based on demand, demand hedging, and the evolving reservoir conditions i.e., the regulated outflow from the reservoir. The remaining term is based on the inflow i.e., the unregulated outflow. For reservoirs with only non-consumptive use, $\hat{D}_t^T = \hat{D}_t^n$, and we can thus write:

$$Q_t^n = \begin{cases} \kappa_t \rho \hat{D}_t^n, & 0 \leq c < c^* \\ \kappa_t \hat{D}_t^n, & c \geq c^* \end{cases} \quad (4.10)$$

$$Q_t^u = \begin{cases} (1 - \rho) I_{t-1}, & 0 \leq c < c^* \\ 0, & c \geq c^* \end{cases} \quad (4.11)$$

For consumptive reservoirs including irrigation, domestic, and/or industrial use, individual regulated outflows (Q_t^i , Q_t^m , Q_t^l , and Q_t^n) are calculated by decomposing the total regulated component ($\kappa_t \rho \hat{D}_t^T$ or $\kappa_t \hat{D}_t^T$) with the ratio of individual demand to total demand. In other words, if the consumptive demands (irrigation (D_t^i), domestic (D_t^m), and industrial (D_t^l)) are known and provided as input, mHM holds the capacity to simulate the regulation at consumptive/ multipurpose reservoirs as well. Finally, the reservoir outflows are checked for feasibility with following condition:

$$Q_t^j = \begin{cases} 0, & V_{t-1} = 0 \\ V_{t-1}, & V_{t-1} < Q_t^j \Delta t \\ Q_t^j, & V_{t-1} > Q_t^j \Delta t \end{cases} \quad (4.12)$$

where index j can be i , w , n , or r . The second condition includes compromise of the regulated outflows when reservoir volume is near depletion. The the order of compromise of outflow is considered to be Q_t^n , Q_t^u , Q_t^i , Q_t^l , and Q_t^m .

4.2.6 Reservoir Disruptivity

Reservoirs can significantly impact the natural streamflow patterns of rivers, leading to varying levels of disturbance depending on their disruptive characteristics. Here we employ three indices, two simple and one more complex, to measure reservoir disruptivity. The simple indices, c [-] and c' [m], are defined as:

$$c = \frac{V_f}{\bar{I}_v} \quad \text{and} \quad c' = \frac{V_f}{A_C}, \quad (4.13)$$

where V_f [m^3] denotes the reservoir capacity, \bar{I}_v [m^3] the mean annual inflow volume, and A_C [m^2] the reservoir catchment area. $c = 1$ means that a reservoir can hold one year's runoff from the upstream basin. c' is the equivalent water depth of V_f distributed over the catchment area. The higher the values of c and c' , the more disruptive a reservoir is. The third indicator is the Amended Annual Proportional Flow Deviation (AAPFD) (Gehrke et al., 1995; Ladson and White, 1999) defined as:

$$\text{AAPFD} = \frac{1}{k} \sum_{j=1}^k \left(\sum_{i=1}^{12} \left(\frac{o_{ij} - n_{ij}}{\bar{n}_j} \right)^2 \right)^{\frac{1}{2}}, \quad (4.14)$$

where, o_{ij} is the actual flow, in our case the streamflow observations at a location downstream of dams ($Q^{s,o}$), for month i of year j , n_{ij} is the natural flow, at the same location, for month i of year j , \bar{n}_j is the average monthly flow for year j , and k is the number of evaluation years. AAPFD is zero for an unregulated river and the value increases with streamflow alteration. The selection of AAPFD over other regulation indicators is grounded on its valuable properties that include independence of scale, sensitivity to changes in flow seasonality, sensitivity to changes in flow volume, sensitivity to changes in the shape of the hydrograph (Gehrke et al., 1995) and applicability for ephemeral rivers (dry most of the year) and intermittent rivers (dry during dry season) (Ladson and White, 1999).

AAPFD, although reliable, determines disruption level based on observed and natural hydrographs, which in itself is a constraint for global application. In this context, the value of the modest indicators c and c' becomes more significant. It is therefore necessary to identify thresholds (τ) for these practical indices (i.e., c_τ and c'_τ) that can be used to determine which reservoirs around the world (e.g., those listed in the GRanD database), are or are not disruptive with respect to the hydrological regime.

To identify the disruptivity thresholds (τ), we apply the K-Means clustering (MacQueen, 1967) to find two disjoint sets that minimizes the sum of the intra-cluster variances of AAPFD in correlation to c (and c'). The natural flow (n_{ij}) in the calculation of AAPFD (Eqn. 4.14) is estimated using the optimized M simulations, but without the reservoirs. Values smaller than (c_τ) indicate locations where the inclusion of the existing reservoir does not improve the model performance significantly. Values larger than (c_τ) indicate that reservoirs significantly disrupt the downstream streamflow regime. This is an important finding that will help the hydrological community improve the performance of the existing global hydrological models (e.g., those use in the Copernicus Climate Change Service (C3S) ULYSSES Project, GLOFAS (ECMWF), ISI-MIP, among others).

4.3 EXPERIMENT DESIGN

4.3.1 Data and Setup

This study is carried out on two sets of reservoirs: ones for which high-quality (H) reservoir information is available, and another set for which freely (F) available global reservoir information is used. The main features of the H-reservoirs (coordinates, capacity, dam crest level, maximum surface area, catchment area, commission date) and the time series data of reservoir water elevation and release were obtained from the corresponding local authorities. The H-reservoirs provide the opportunity to test mHM-LM with maximum data certainty. H-reservoirs consist of the Rappbode reservoir in Germany and the Três Marias reservoir in Brazil (Figure 4.2).

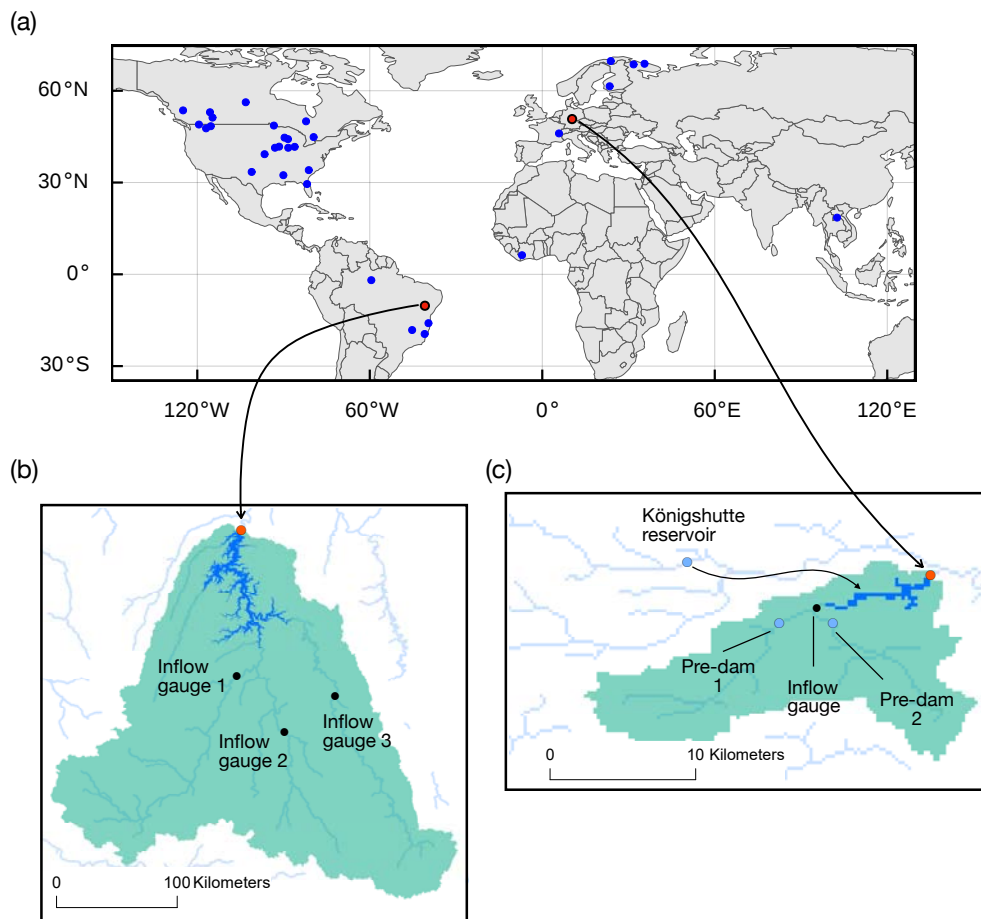


Figure 4.2: (a) Global map showing the geographical distribution of $n = 31$ reservoirs considered for the experiment. Red dots - H-reservoirs, Blue dots - F-reservoirs. Hydrological setting of the (b) Três Marias reservoir, and (c) Rappbode reservoir

The Rappbode reservoir, Germany's largest drinking water reservoir, lies downstream of two pre-dams that reduce its nutrient and sedimentation loading, receives a significant volume of interbasin transfer inflow from the Königshutte reservoir of the adjacent basin and is used mainly for water supply and flood control (Rinke et al., 2013). For Rappbode, the observed inflow data (which includes upstream regulations) was used as a boundary condition. The interbasin transfer and domestic water supply point time series data were model inputs. The `hAV` table for the Rappbode reservoir was derived from the actual elevation map of the reservoir bed (refer to the Software Availability Statement).

Trés Marias is the largest headwater reservoir of the São Francisco basin in North East Brazil, mainly used for hydropower (Lehner et al., 2011). Streamflow data at three inflow gauges were used as a boundary condition. In the case of the Três Marias reservoir, we acquired the `hAV` table from Fundação Cearense de Meteorologia e Recursos Hídricos (FUNCEME).

We explored 7320 reservoirs of the GRanD (version 1.3) database for F-reservoirs using the following screening criteria:

- A reservoir should be exclusively used to fulfill non-consumptive demands (i.e., hydroelectricity, recreation, navigation and flood control). Reservoirs with irrigation, domestic and industrial water use were avoided as estimating consumptive demand or using model-based demand inherits significant uncertainties at daily resolution (Biemans et al., 2011; Voisin et al., 2013b; Voisin et al., 2013a; Zhao et al., 2016) which is not suitable for testing performance of the LM. GRanD consisted of 1513 hydroelectric reservoirs without consumptive use.
- A reservoir should have a GRDC streamflow station available downstream from the dam for applying a Random Forest model for non-consumptive demand estimation/prediction. The search distance downstream was limited to twice the reservoir catchment area in order to get the reservoir regulation signals on the streamflow.
- A reservoir should not have additional reservoirs upstream interfering the inflow to the reservoir for simple hydrological setting.
- The catchment area of the reservoir should be between $5,000$ to $100,000 \times 10^6 \text{ m}^2$ in order to avoid very small (non-disruptive) ones and to ensure feasible runtimes during optimization, respectively.

Only 31 GRanD reservoirs fulfilled these criteria (see Figure 4.2). The geographical coordinates and other key features of the F-reservoirs are taken from the GRanD database (Lehner et al., 2011) and tabulated into the Table S1. We ensured the dams are located on the flow accumulation grid at the nearest catchment area values (refer to the Software Availability Statement). We estimate the effective spillway length of the selected F-reservoirs using Google Earth. The hydrologic model `mHM-LM` requires a high resolution DEM (and its derivatives), soil maps, geological maps, leaf area index (LAI), land cover

and meteorological forcings as described in Table S2. These data sources were also used in Saha et al. (2021).

4.3.2 Modelling Procedure

C.5 provides the steps followed for estimating D^n using RF. Forwards runs in mHM-LM use the RF surrogate \tilde{D}^n as input and simulates reservoir outflow using its regulation scheme. We calibrate mHM-LM using streamflow observations at gauge location downstream ($Q^{g,o}$) of the dams. Each reservoir catchment is setup and modelled as an individual domain. First, each mHM-LM model spins up for ten years. This stabilizes the catchment soil moisture, eventually stabilizing reservoir inflow and storage. The simulation period corresponds to the period for which $Q^{g,o}$ is available which could vary across the reservoirs (refer to Table S1). The first two third of the simulation period is considered for calibration, while the remaining serve for validation. For F-reservoirs, we optimize the full set of parameters of mHM-LM by maximizing the KGE (Gupta et al., 2009), of simulated streamflow at the gauge location. While for H-reservoirs, we use inflow observations as boundary conditions upstream of reservoir. Since we have observations at both the reservoir (water level) and the downstream gauge location, the objective function was set to utilize both set of observations which was to maximize KGE of reservoir volume (derived using water level observations and the hAV table) and streamflow at the gauge location, with equal weights. We employed the DDS (Tolson and Shoemaker, 2007) algorithm to optimize the mHM-LM parameters across 1000 iterations. We set the model resolution to 0.25° (≈ 27 km at the equator).

4.3.3 Experiments

We conducted three experiments to test the hypotheses of this study. The first experiment relates to the performance evaluation of mHM-LM that uses the surrogate RF demand model. We evaluate the simulation of streamflow decoupling at reservoirs on the daily time scale. The added value of reservoirs is then analyzed by comparing the performance of the mHM-LM against naturalized streamflow obtained wMHMalone. To ensure accurate evaluations with minimal data uncertainty, we initially utilize the H-reservoirs for evaluation. Once mHM-LM successfully passes the performance test at the H-reservoirs, we assess the streamflow simulations at the F-reservoirs with freely available global dam information such as reservoir shape and streamflow.

In the second experiment, we analyze the sensitivity of reservoir shape on reservoir simulations because it is known that the reservoir shape affects the variability of reservoir surface area and elevation with time. We use three approximations of reservoir bathymetry. 1) The most basic approximation is called linear. As its name indicates, here it is assumed that the relationship between reservoir volume and water level vary linearly. The reservoir area is kept constant and equal to the area A_f corresponding to reservoir

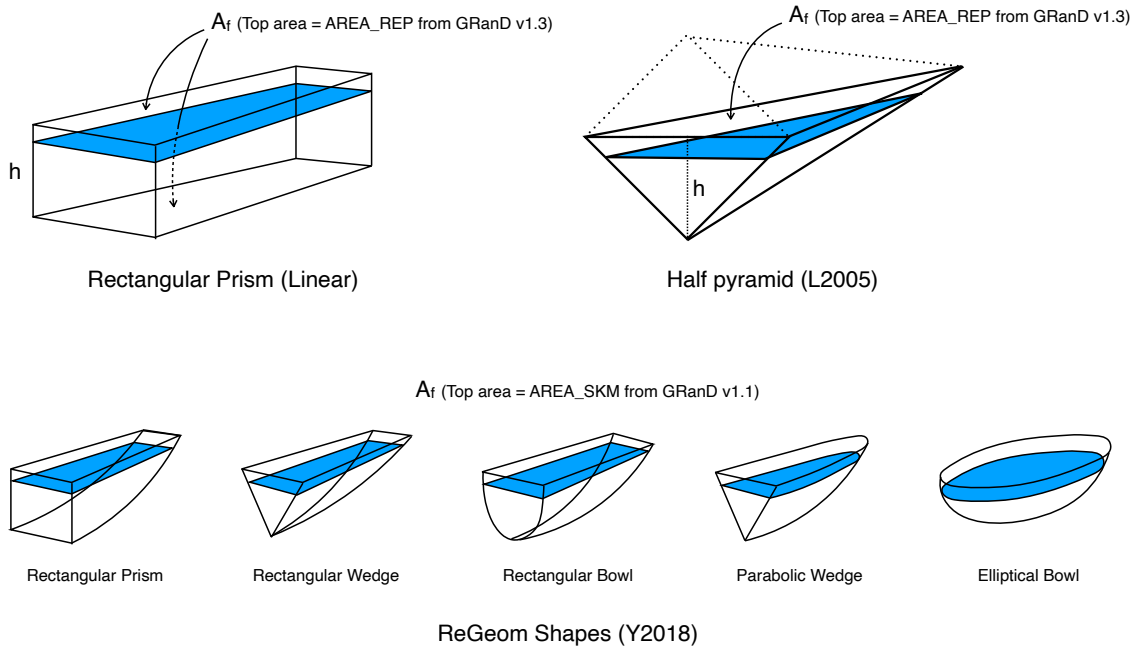


Figure 4.3: Schematics of bathymetry approximations for rectangular prism (Linear), half-pyramid (L2005), and ReGeom shapes (Y2018)

capacity V_f . This means the maximum depth is the ratio of V_f to A_f (refer Figure 4.3). These assumptions are unrealistic because of two reasons. First, reservoirs are impounded on natural terrain where the water surface area changes with reservoir depth and is not constant. Secondly, the average cross-section of reservoirs are generally closer to a conical cross-section than a rectangle. Which means, with rectangular cross-section of the linear bathymetry approximation, we would end up greatly underestimating the maximum depth of the reservoir. Still, we include the linear approximation in this experiment because it is commonly used in literature. 2) The second approximation is denoted as L2005 (Liebe et al., 2005), where the reservoir shape is assumed as a half pyramid with a square base cut diagonally at the base (refer Figure 4.3). This shape approximation gives variability in water surface area with depth as well as variability in the cross-section with distance away from the dam/ outlet, which is more realistic compared to Linear. The derivation of hAV equations for L2005 is provided in Supplement S6 and Figure S2. For L2005, the reservoir is allowed to extend to any distance upstream to achieve a surface area of A_f at maximum capacity, V_f . The GRanD database provides four different keys with four different entries of surface area for each reservoir. Out of the four keys, we use the "AREA_REP" key as A_f for the Linear and L2005 shape approximations since it is defined as the "most reliable reported surface area of reservoir". 3) The third approximation is the ReGeom dataset (Yigzaw et al., 2018) denoted as Y2018 which is essentially the hAV tables

corresponding to the reservoirs of the GRanD database. The five candidates of shapes used in Y_{2018} are shown in Figure 4.3. Y_{2018} iteratively selects the optimal geometric shape out of the candidate shapes by minimizing the error in estimated total storage and maximum surface area (Yigzaw et al., 2018). Yigzaw et al. (2018) use GRanD database entries from the key "AREA_SKM" as the surface area during the optimisation. The simulation performance of the three bathymetry approximations are then put to test at both H and F-reservoirs.

In the third experiment, our aim is to explore potential correlations between performance improvement (i.e., the added value of reservoirs) and disruptivity indices. This analysis specifically focuses on F-reservoirs, which are non-consumptive hydropower reservoirs. By establishing thresholds, we can effectively differentiate potentially disruptive reservoirs from those that are likely to be non-disruptive. These thresholds are then extrapolated to a broader range of reservoirs, such as the non-consumptive hydropower reservoirs in the GRanD dataset, enabling us to offer valuable insights into identifying reservoirs with significant disruptive impacts on the hydrological regime.

4.4 RESULTS AND DISCUSSION

4.4.1 Performance Evaluation of mHM-LM and RF Model

The performance results at two high-quality (H) reservoirs are shown in Figure 4.4 for the Rappbode and in Figure S3 for the Trés Marias reservoir. We compare the streamflow simulations from mHM-LM simulations with full set of parameters optimized with reservoirs (M) with mHM simulations with default parameters without dams (N). Since the streamflow observation (black dashed line) for both the reservoirs are located immediately downstream of the dam, we additionally include $Q^{d,RF}$ fitted by random forest model (RF) in the comparison. For Rappbode, the RF predicts the streamflow at the dam with a Kling-Gupta Efficiency (KGE) of 0.72 and 0.93 during calibration and validation periods, respectively. Similarly, this efficiency metric for Trés Marias are 0.84 and 0.89, respectively. The variability in the performance of RF across the years originates from the randomized distribution of modelling years across training and testing of the RF model.

The streamflow simulation efficiency, KGE, during calibration of the mHM with the lake module (M) compared with the default mHM runs (N), increased by +0.47 (0.16 to 0.63) and +1.19 (-0.43 to 0.76) for the Rappbode and the Trés Marias reservoirs, respectively. The dampened seasonality of the observed streamflow with diminished peaks is well matched with inclusion of the reservoirs, especially at the Trés Marias reservoir. Apart from the improved seasonality, mHM-LM is able to explain the daily reservoir regulation signatures in conjunction with non-consumptive demand predictions obtained with a Random Forest (RF) model. mHM-LM simulation shows satisfactory fit of water level at both reservoirs. We want to mention that model evaluation based on a one-to-one

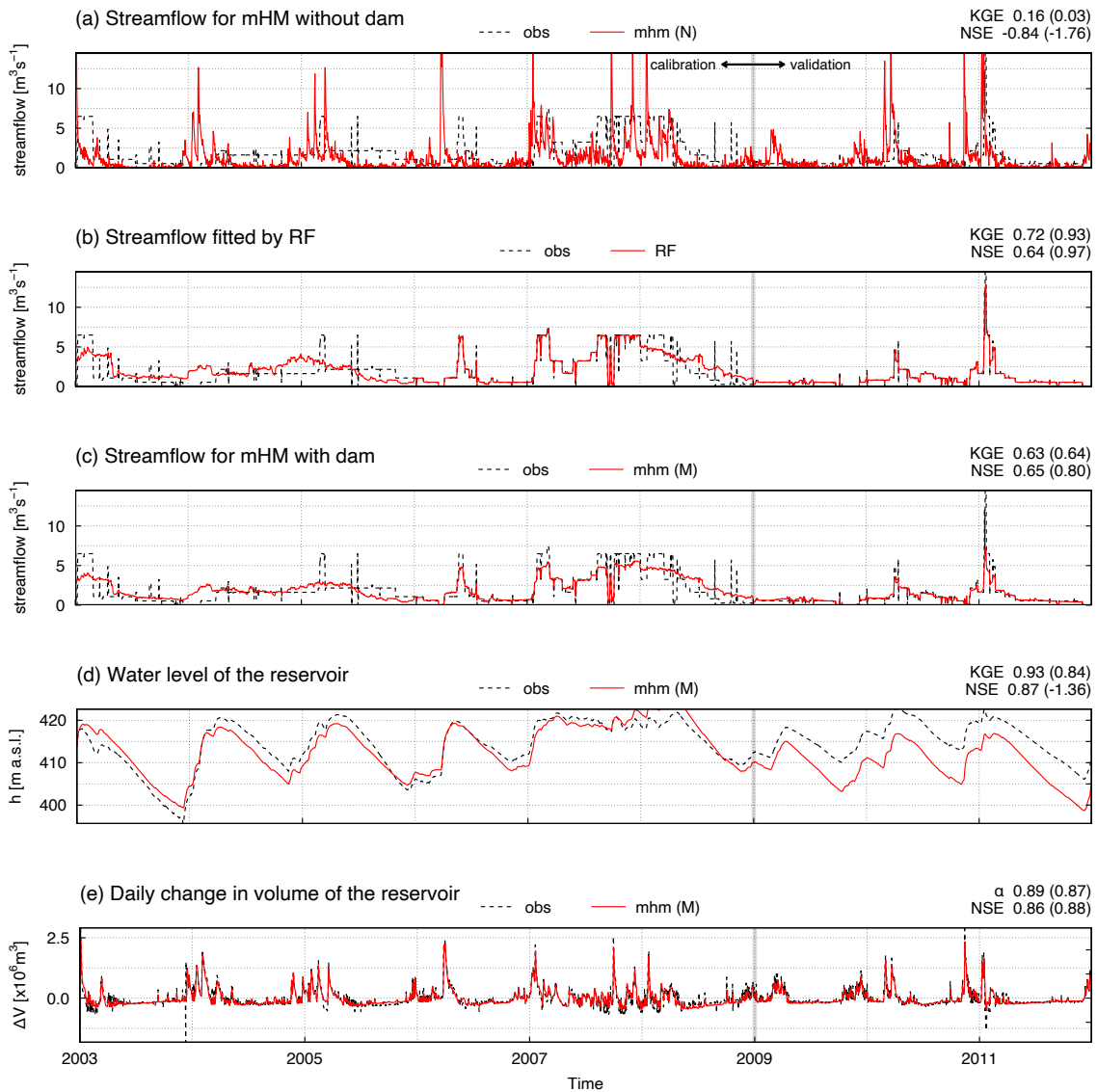


Figure 4.4: mHM-LM prediction efficiency at the Rappbode reservoir compared against observed streamflow. (a) mHM without dam (N), (b) $Q^{d,RF}$ fitted by RF, (c) mHM-LM with a dam (M), (d) reservoir water level performance in mHM-LM, (e) daily change in volume performance in mHM-LM. The performance metrics for the calibration period are followed by the performance during validation period in parentheses.

comparison of water elevation simulations and observations, although necessary, may not be fair. In Figure 4.4d, the overestimated outflow in second half of 2008 results in an underestimation of water level h . This underestimation of the water level is carried over the next three years, although the reservoir outflow was well simulated. This result stems from the fact that the water level is a state variable and thus cumulative. We test the

performance evaluation based on ΔV which is the difference between reservoir volume of current day and the previous day. Unlike water level, ΔV excludes any carryover of the errors from 2008 to the next three years (see Figure 4.4e). This proves metrics based on daily change in volume to be a fair evaluation of reservoir model performance and should be used in conjunction with absolute values such as water elevation or reservoir volume. Since we strip seasonality off while calculating ΔV , we evaluate ΔV with variability ratio α instead of KGE. It is also noteworthy how, in comparison to water level, the Nash-Sutcliffe Efficiency (NSE) of ΔV correctly represents the good model performance during the validation years.

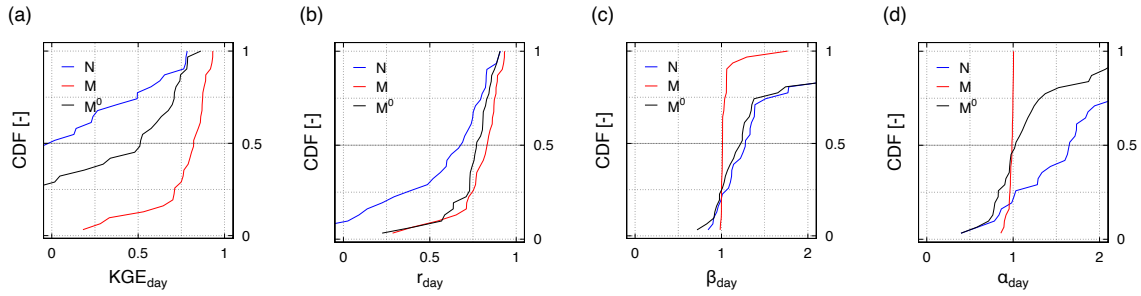
Figure 4.5 illustrates the cumulative distribution functions (CDFs) of KGE at streamflow gauges downstream of F-reservoirs. We obtain a median KGE performance of 0.82 for mHM-LM (M) with a median improvement of +0.88 over mHM without the lake model (N) for the calibration period (figure 4.5a). During the validation (figure 4.5b), the median KGE performance for the M-simulations is 0.67, with a median improvement of +0.84 over the N-simulations. It is important to note that the performance of former reflects the combined effects of optimizing both the LM and mHM parameters. To disentangle the two effects and see the added value of reservoirs, we exclusively calibrated the LM parameters (refer C.2), while maintaining the remaining mHM parameters at their default values. We refer to this simulation as M^0 . M^0 -simulations produced median KGE values of 0.51 and 0.47 for calibration and validation periods, respectively, which still gives an improvement of greater than +0.50 over the N-simulations for both periods.

The CDFs for the KGE components provided in Figure 4.5 shows M^0 to have large contribution in improvement of streamflow variability (α_{day}) over the N-simulations while the M-simulations primarily reduces bias (β_{day}). This observation is sound because the introduction of a reservoir (LM parameters) leads to matching the artificial regulation signatures on streamflow while including non-LM parameters leads to improvements of the reservoir inflow.

Figure 4.6 shows how actual evapotranspiration (aET) simulations in the upstream catchment for the M-simulation leads to improvement in mean annual streamflow at the gauge downstream, compared to the lake-model simulations with default mHM parameters (M^0). Overall, these outcome emphasize the added value of reservoirs in hydrological modeling and underscores the potential of the mHM parameters to improve the streamflow simulations downstream of dams or natural lakes.

The majority of large-scale hydrological modeling studies have mainly focused on matching streamflow seasonality change brought by a reservoir rather than the fine scale (daily to weekly) discontinuities added to the hydrograph, although the performance assessment are made at daily resolution in some cases (Solander et al., 2016; Wada et al., 2016; Zajac et al., 2017; Hanasaki et al., 2018; Shin et al., 2020; Vanderkelen et al., 2022; Sadki et al., 2023). The newly proposed mHM-LM model not only improves the median *daily* KGE of the streamflow simulations from a negative value to 0.82 in 31 globally distributed reservoirs, but also is able to match fine scale reservoir disruption seen in

Calibration



Validation

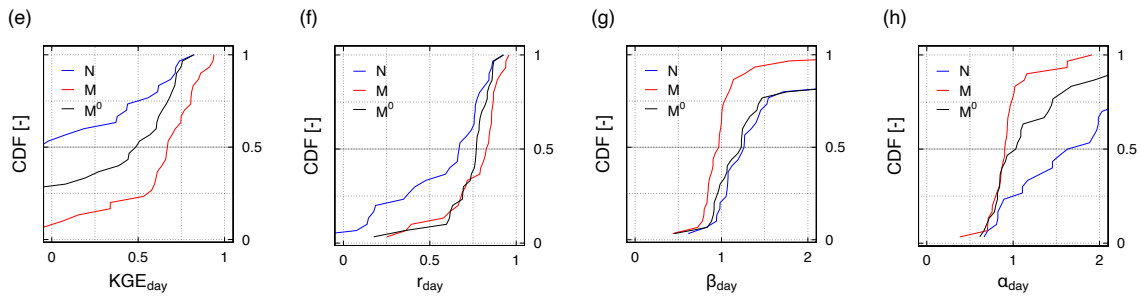


Figure 4.5: CDFs depicting the streamflow performance at downstream gauges ($n = 31$, F-reservoirs) with LM and mHM parameters optimized (M), only LM parameters optimized (M^0), and default parameters without dams (N). Panels (a) – (d) correspond to the calibration period, and panels (e) – (h) correspond to the validation period. The KGE and its three individual components (r – correlation, β – mean bias, α – variability bias) are estimated against observations downstream of the dams.

hydrographs. It should be noted that the best KGE obtained without the LM is less than the median KGE of the model with the LM. Recent studies, in contrast, obtained inferior results to those obtained here when reservoirs were included in a hydrological model. For example, Sadki et al. (2023) obtained a median monthly C_{2M} (a bounded version of NSE, see (Mathevet et al., 2006)) of 0.52, Zajac et al. (2017) got a median daily KGE of 0.20, and Hanasaki et al. (2018) present negative monthly NSE at four out of six cases detailed. Its only Yassin et al. (2019) who demonstrated KGE (daily) greater than 0.75 for 59% reservoirs for dam inclusive simulations, which is comparable to our study, albeit using surveyed bathymetry, observations for water level, inflow and environmental flow. In comparison, we demonstrate the abilities of mHM-LM and RF with freely available global reservoir information. We admit that these comparison are not 1:1 since most of the aforementioned studies include irrigation reservoirs and the methodology introduced in this study is for non-consumptive hydropower reservoirs having a streamflow station

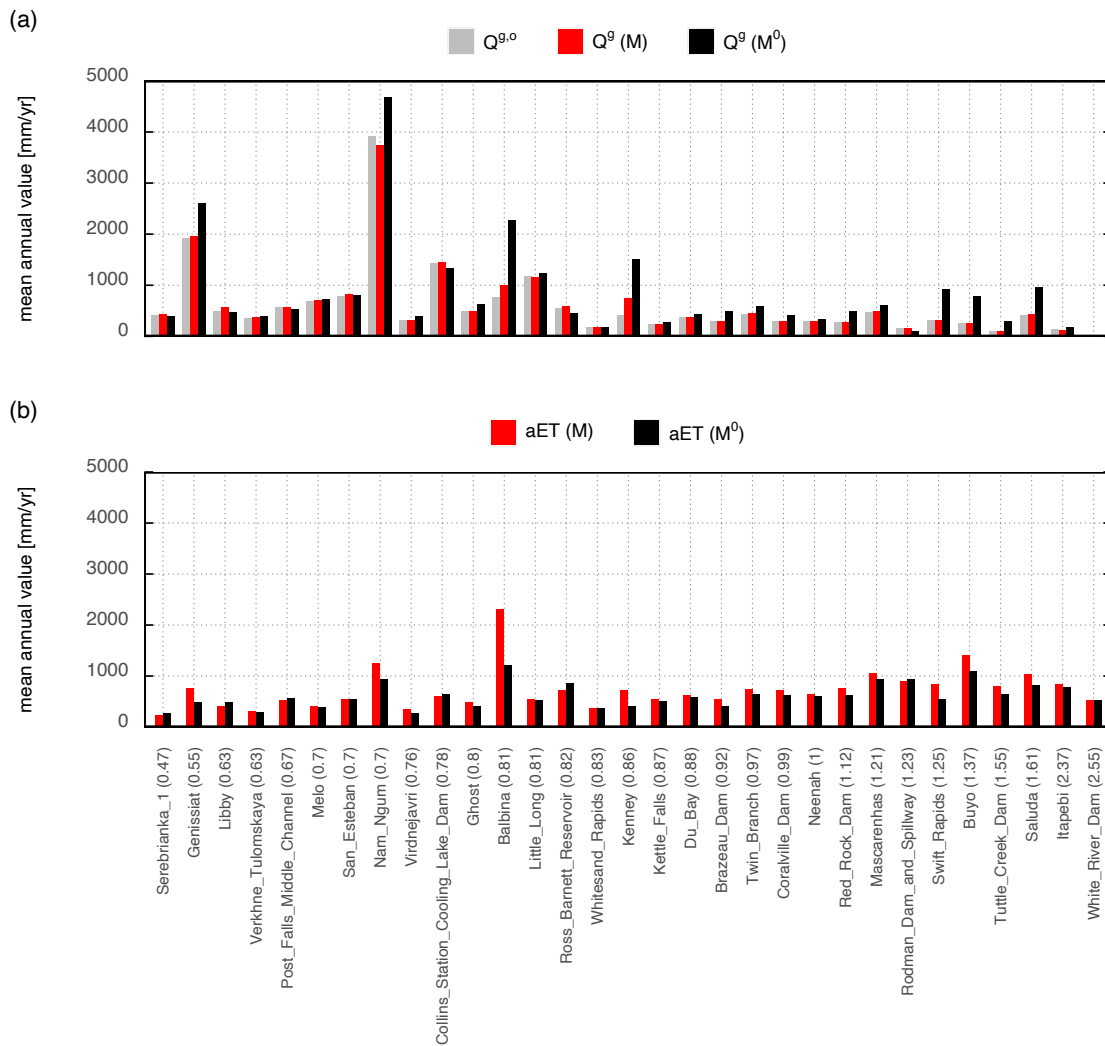


Figure 4.6: Comparison of the mean annual values of M^0 and M simulations for (a) runoff at the location of gauge downstream of the reservoir, and (b) aET from the reservoir catchment across F-reservoirs. M included all parameters in optimization while in M^0 only the reservoir parameters were optimized i.e., simulation from upstream catchment was based on default parameter set. Runoff corresponding to the observed streamflow ($Q^{g,0}$) at the gauge is also included in the subplot (a). The reservoirs are sorted by the aridity index (ratio of PET to P) of the reservoir catchment, which are also enclosed in the parenthesis alongside the name of the dam in the x-axis.

downstream of the reservoir. Still, the results show HMs can match daily reservoir disruption signals by leveraging machine learning techniques.

4.4.2 Sensitivity of Reservoir Shape on Reservoir Simulations

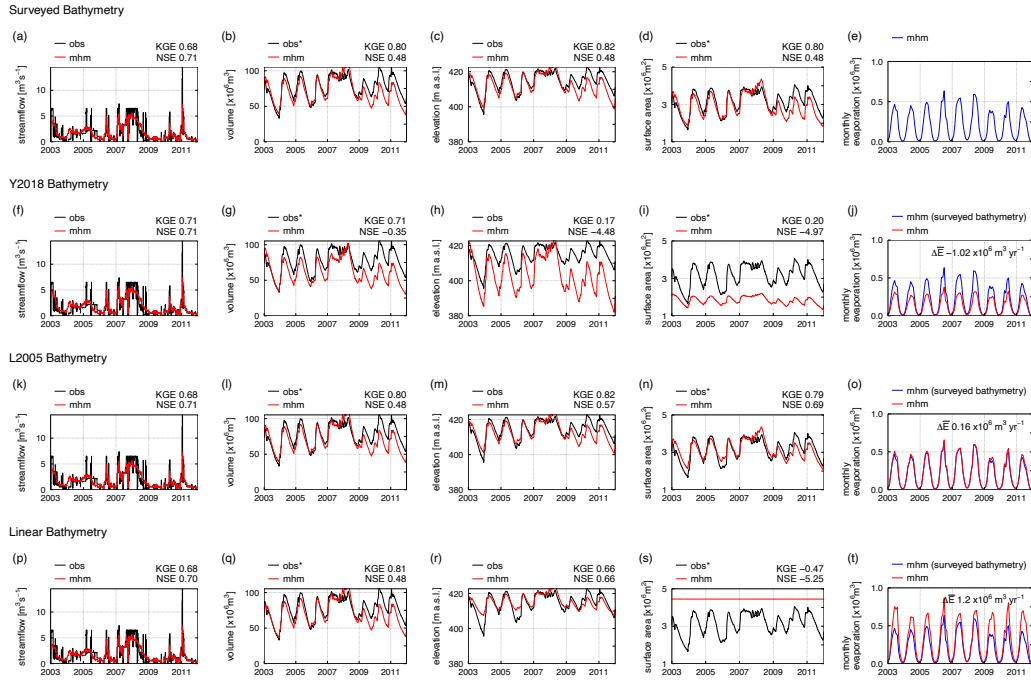


Figure 4.7: Sensitivity of the reservoir shape on streamflow, volume, elevation, surface area and evaporation at the Rappbode reservoir. $\Delta\bar{E}$ is the difference in mean annual evaporation. Note: * derived from actual hAV table using observed elevation. (A corresponding graph for the Três Marias reservoir is presented in Figure S4.)

Figure 4.7 shows the sensitivity of the reservoir shape at the Rappbode reservoir. We initialize all simulations with the same water elevation to ensure comparability between runs. Results indicate that the streamflow downstream (Q) of this dam is virtually unaffected by the shape of the reservoir. This is because the regulations are based on reservoir volume (V), and the latter is not affected by the shape as long as the mean annual evaporation (\bar{E}) is comparatively small compared to the reservoir capacity (V_f). The ratio of \bar{E}/V_f for Rappbode is 2.3%. The errors in the volume simulations V for Y2018 and the linear assumption originate from the start of the modelling period, where different h - V relationships lead to different volume initialization for same elevation.

In contrast to simulated V and Q , simulations for the water level (h), the surface area (A) and the evaporation (E) are very sensitive to reservoir shape. The dynamics of h and A are best fit by the L2005. Consequently, the evaporation E obtained with L2005 exhibits the closest fit to that obtained with the actual bathymetry of the reservoir. In comparison to the surveyed bathymetry, Y2018 and the Linear shape approximation lead to ten times the error in mean annual evaporation $\Delta\bar{E}$. This error is around 1% of the

reservoir capacity of Rappbode. Considering the water level h , the Y_{2018} approximation is the worst one for the Rappbode Dam.

The corresponding figure for Trés Marias ($\bar{E}/V_f = 7.6\%$) is provided in Figure S4 and leads to similar conclusions. The reservoir shape has no significant effect on streamflow Q , but impacts evaporation estimates substantially. For this dam, L_{2005} yields better shape approximation while Linear bathymetry leads to $\Delta\bar{E}$ of $\approx +2.5\%$ of reservoir capacity in comparison to surveyed bathymetry. This can be explained by Figure 4.8a which compares the actual hA relationship for the H-reservoirs against the linear, L_{2005} and Y_{2018} approximations. The optimal surface and profile shapes of the Y_{2018} are based on matching the capacity and maximum surface area of reservoirs (Yigzaw et al., 2018). Although the goodness of fit of hV curve is discussed, the work excludes any verification of the increments of surface area with elevation i.e., the hA curve. Figure 4.8a clearly shows L_{2005} being the best option at matching the evolution of surface area with elevation, which is obviously important for the temporal dynamics of model simulation.

In order to verify these findings, we acquired surveyed bathymetry for 88 reservoirs in Texas, USA, which overlapped with the GRanD dataset and the Y_{2018} bathymetry dataset. These surveyed data are made publicly available by the Texas Water Development Board (<http://www.twdb.texas.gov/surfacewater/surveys/completed/list/index.asp>). Figure 4.8b compares the hA plots for L_{2005} , Linear and Y_{2018} bathymetry approximations to the surveyed bathymetry at the Texan Reservoirs. Based on visual match, L_{2005} is found to be the better approximation at 72 out of 88 reservoirs i.e., majority of the locations. Linear approximation completely misses the graph dynamics with a constant value. While, Y_{2018} is seen to be the better option at only few reservoirs (e.g., Anahuac, Kurth, White Rock, etc.).

Y_{2018} produced downward concave hA relationship in virtually every location although most of the reservoirs have upward concave relationship. The verification of the estimated hA relationship, which was missing in Y_{2018} , would have helped to spot this issue. L_{2005} approximation gives a better fit to the hA relationship. It is noteworthy that L_{2005} and Linear are based on the “CAP_REP” and “AREA_REP” (keys from the GRanD dataset), defined as the most reliable reported values for reservoir capacity (V_f) and corresponding surface area (A_f), respectively. In contrast, Y_{2018} utilizes “CAP_MCM” and “AREA_SKM” (alternative set of keys from the GRanD dataset) as V_f and A_f for the shape optimization. We compared these values from GRanD to the surveyed values of A_f and V_f at the Texan reservoirs (Figure 4.9a and 4.9b). We found the median absolute error for the key “AREA_SKM” to be much higher (26.3%) than that for values given in the key “AREA_REP” (6.9%). This elucidates the substantial conformity to surveyed values of A_f and V_f achieved by L_{2005} and Linear approximations, as opposed to Y_{2018} . There is an overall underestimation of A_f and an overestimation of V_f by the keys “AREA_SKM” and “CAP_MCM”, respectively, in the GRanD v1.3. This finding resonates with the observation made by Steyaert et al. (2022) while comparing “CAP_MCM” to the observed maximum storage volume at 679 major reservoirs across the US. We also noted that the entries

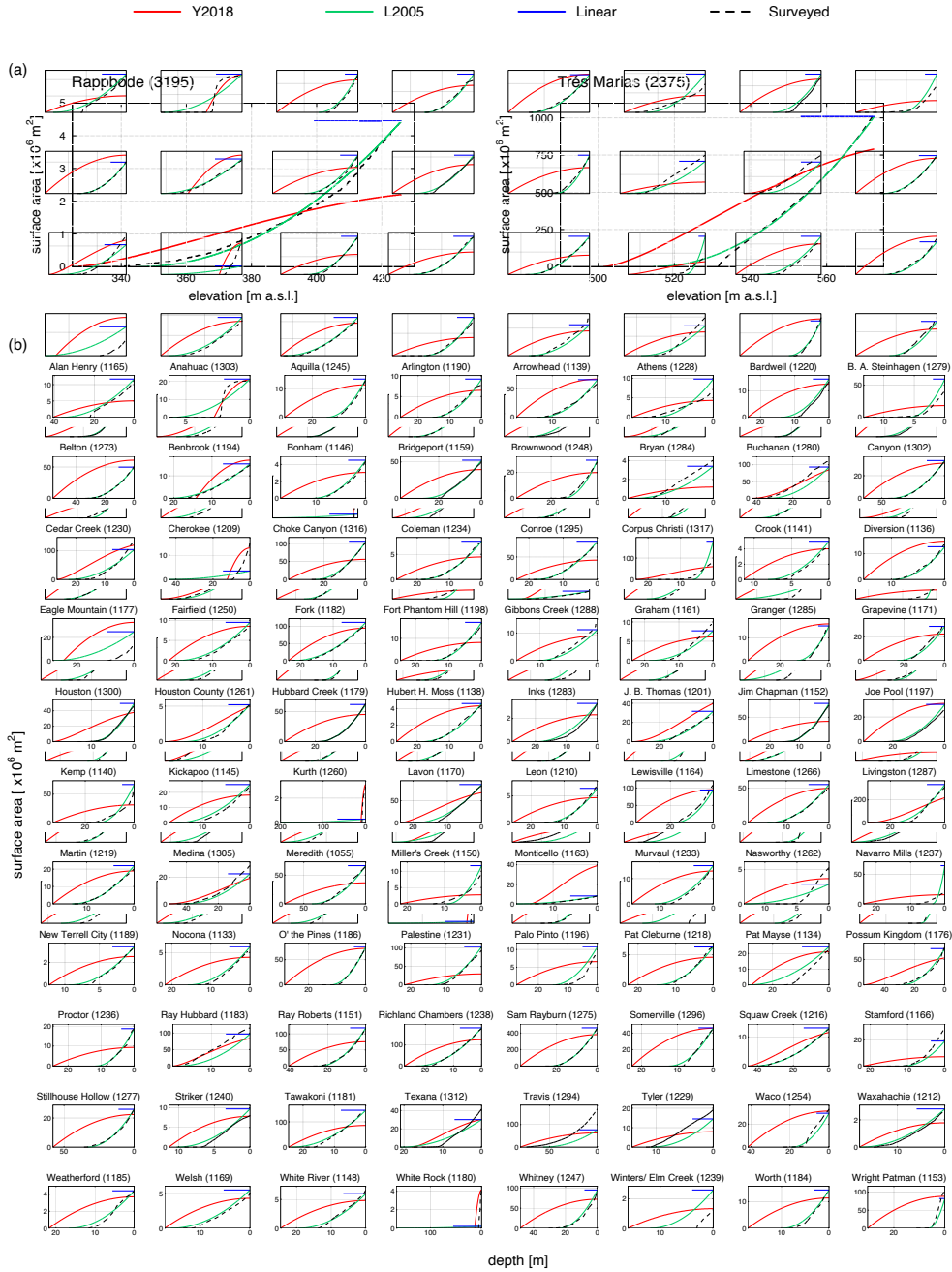


Figure 4.8: hA plots comparing the surveyed bathymetry to Y₂₀₁₈, L₂₀₀₅ and Linear shape approximations at (a) H-reservoirs, and (b) 88 Texan reservoirs. The title of individual plot displays the name of the reservoir with GRanD ID in the parentheses. The corresponding figure for hV plots are provided in Figure S5.

in the key “AREA_SKM” were updated by more than ten percent at 521 reservoirs in GRanD v1.3 compared to the GRanD v1.1, while the entries in the key “CAP_MCM” didn’t receive such large updates (Figure 4.9c and 4.9d). Y₂₀₁₈ was based on GRanD v1.1. From the Figures 4.9a and 4.9c, it is evident that A_f in GRanD v1.1 incurred even greater degree of underestimation than GRanD v1.3. This adds to the reason for Y₂₀₁₈’s inability to outperform a less complex method like L₂₀₀₅. These comparisons underscore the significance of accurate A_f and V_f while making bathymetry approximations. To summarize, L₂₀₀₅ is by far the better alternative to surveyed bathymetry for large-scale hydrological modeling. We employ L₂₀₀₅ to evaluate the simulation performance of mHM-LM at F-reservoirs (Section 4.4.1, Figure 4.5.)

Figure 4.10 shows the CDFs of the KGE metric and its components at freely (F) available reservoirs for the Y₂₀₁₈ and the linear bathymetry approximations. In these experiments the simulations obtained with the L₂₀₀₅ approximation is used as the reference for the estimation of the KGE metric, because it performed best in the reservoirs with high quality reservoir data (H-reservoirs) as well as in conforming to the surveyed hAV relationship at 88 other reservoirs. As in H-reservoirs, it is observed that the streamflow Q downstream of the dams of the F-reservoirs is insensitive to the reservoir shape. The simulations for lake volume exhibit a median KGE of at least 0.95 for both the Y₂₀₁₉ and the linear approximations. This result indicates that volume is, in most cases, insensitive to the reservoir shape. Low KGE values for simulated volume may stem from a poor estimation of the reservoir evaporation at a specific location. The KGE for the simulations for water level, surface area and evaporation (h , A and E) show, on the contrary, a substantial sensitivity to reservoir shape. The KGE for simulated surface areas A with the linear geometry approximation is less than zero at all basins. Instead, with the Y₂₀₁₈ approximation, a median KGE of 0.56 is obtained. The mean KGE efficiency for the simulated evaporation E with the Y₂₀₁₈ and the linear approximations were found to be 0.59 to -0.38, respectively.

The F-reservoirs shown in Figure 4.11 are ranked in ascending order by the ratio of mean annual reservoir evaporation to mean annual reservoir capacity (V_f). In Figure 4.11a, the evaporation obtained with the L₂₀₀₅ reservoir shape assumption is used.

The ratio of maximum reservoir surface area to reservoir capacity (A_f/V_f) shown in panel (b) of this figure, correlates very well with the index \bar{E}_{L2005}/V_f (panel (a)), indicating the close relationship between between surface area A_f and reservoir evaporation \bar{E} , and thus the importance of good bathymetry for reservoir modeling. It can also be generalized that a smaller ratio A_f/V_f reflects a narrower shape of the reservoir shape, while a larger ratio reflects a shallower shape of the reservoir. As a result, reservoirs with shallower shape lead to more evaporation, i.e., higher contribution of the reservoir evaporation to the overall basin water balance. These relationships explain the exceptionally high simulated evaporation (> 20% of V_f) at Kettle Falls dam, even though the aridity index (PET/ P) of the White River (with a very small ratio of \bar{E}_{L2005}/V_f) dam is much higher (2.75) than that of the former (0.8). To summarize, the shape of the reservoir, in addition to

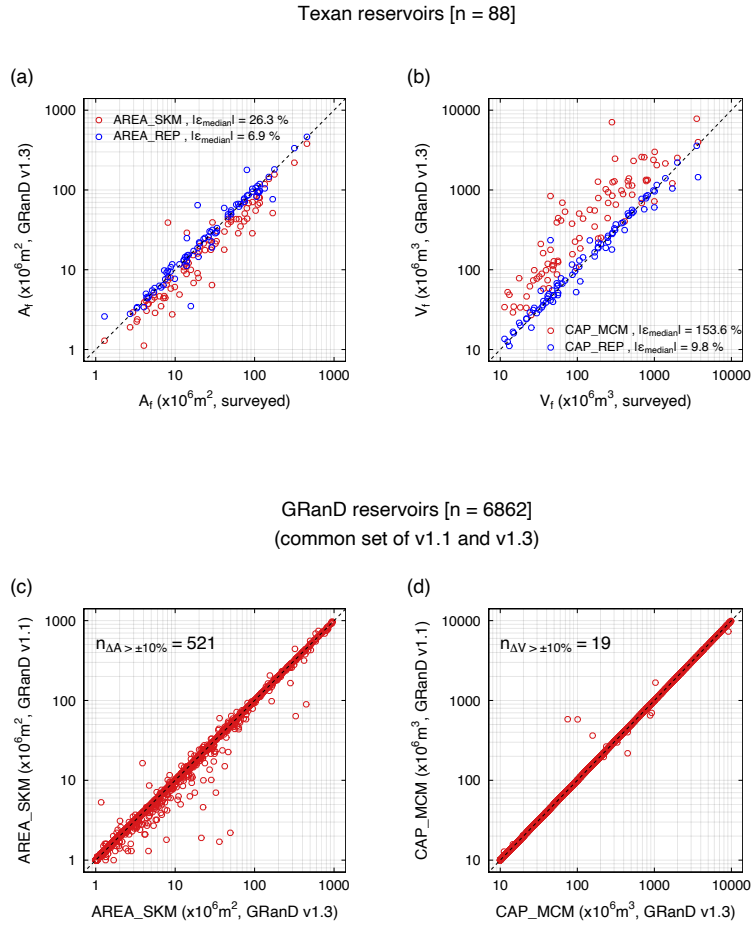


Figure 4.9: Comparison of surveyed and GRanD (v1.3) values of (a) reservoir surface area at full capacity (A_f), and reservoir capacity (V_f) at 88 Texan reservoirs. The legend labels in (a) and (b) include the median absolute error values. Comparison of (c) AREA_SKM, and (d) CAP_MCM values between GRanD v1.1 and v1.3, across the reservoirs of the database. The annotations in (c) and (d) quantify the number of reservoirs with more than 10% change in the value.

local climatic conditions such as the aridity index, play an important role in determining the contribution of the share of evaporation to the water balance of the entire basin.

The ratio of mean annual evaporation (\bar{E}) of either the Y_{2018} or the linear shape approximation, to that obtained with the L_{2005} approximation ($\bar{E}_{L_{2005}}$) for every reservoir in the F set is shown in Figure 4.11c. From this result, it can be concluded that both shape approximations overestimate evaporation compared to L_{2005} . The largest overestimation factor is observed for reservoirs with smaller values of $\bar{E}_{L_{2005}}/V_f$. This could be due to the fact that narrow reservoirs have smaller surface area relative to volume, so errors in estimating area have a greater impact. In general, the linear approximation is the

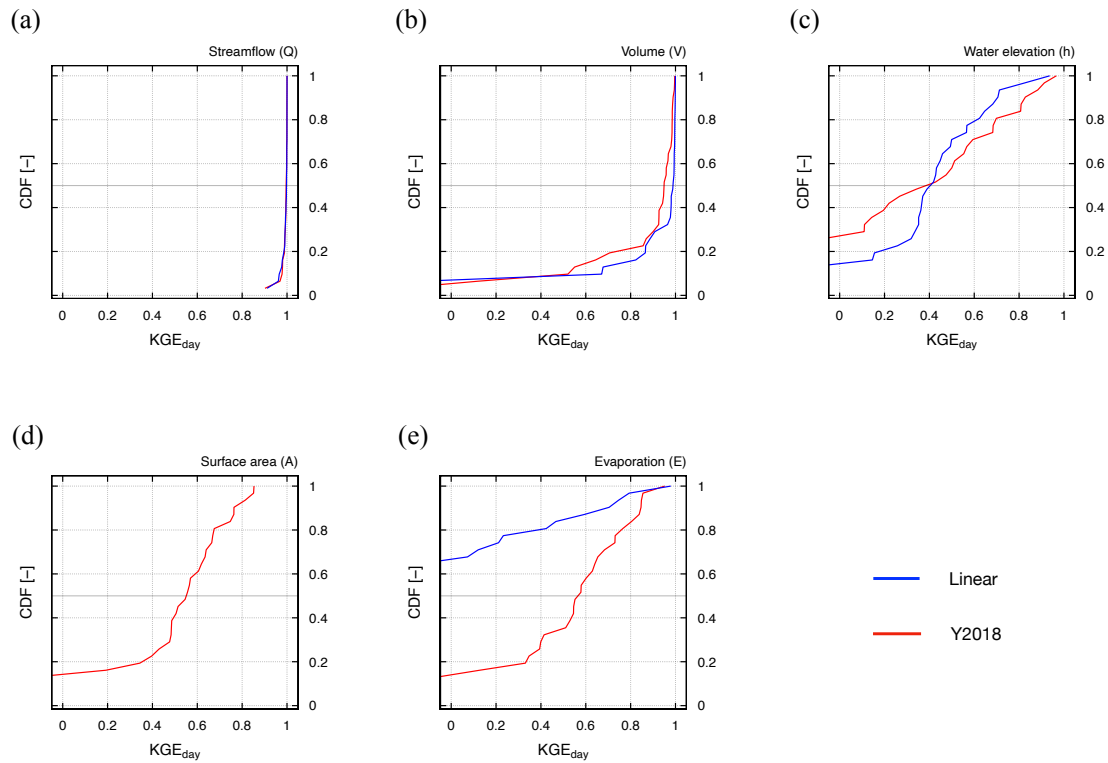


Figure 4.10: Cumulative distribution functions of the mHM lake module performance in 31 reservoirs (F) using two distinct reservoir shape approximations (Y₂₀₁₈ and linear V-h). The KGE metric uses the L₂₀₀₅ bathymetry approximation as the reference. (a) streamflow downstream of the dam, (b) reservoir volume, (c) reservoir water level, (d) reservoir surface area, and (e) reservoir evaporation.

worse of all cases, resulting in an overestimation of at least 100% (w.r.t to L₂₀₀₅) in 60% of the selected reservoirs. The Y₂₀₁₈ approximation, on the other hand, leads to an overestimation in the same proportion for only 6% of the reservoirs in the sample.

This in-depth investigation is the first of its kind to explore the effect of reservoir shape on model simulation, especially on reservoir evaporation. A comprehensive review of existing literature (refer Table 4.1) reveals a notable absence of studies addressing this particular aspect. This could be attributed to the fact that large-scale studies with reservoirs primarily focus on control points such as observed streamflow. Basic examination of “inner states”, like reservoir evaporation, is missing in majority of the studies enlisted in Table 4.1. In fact, none of these studies involve model simulations employing more than one bathymetry approximation. This is alarming, given our findings that streamflow is virtually insensitive to reservoir shape. In essence, if we limit the focus to streamflow, reservoir evaporation can act as a “silent sink”, giving right results for the wrong reasons.

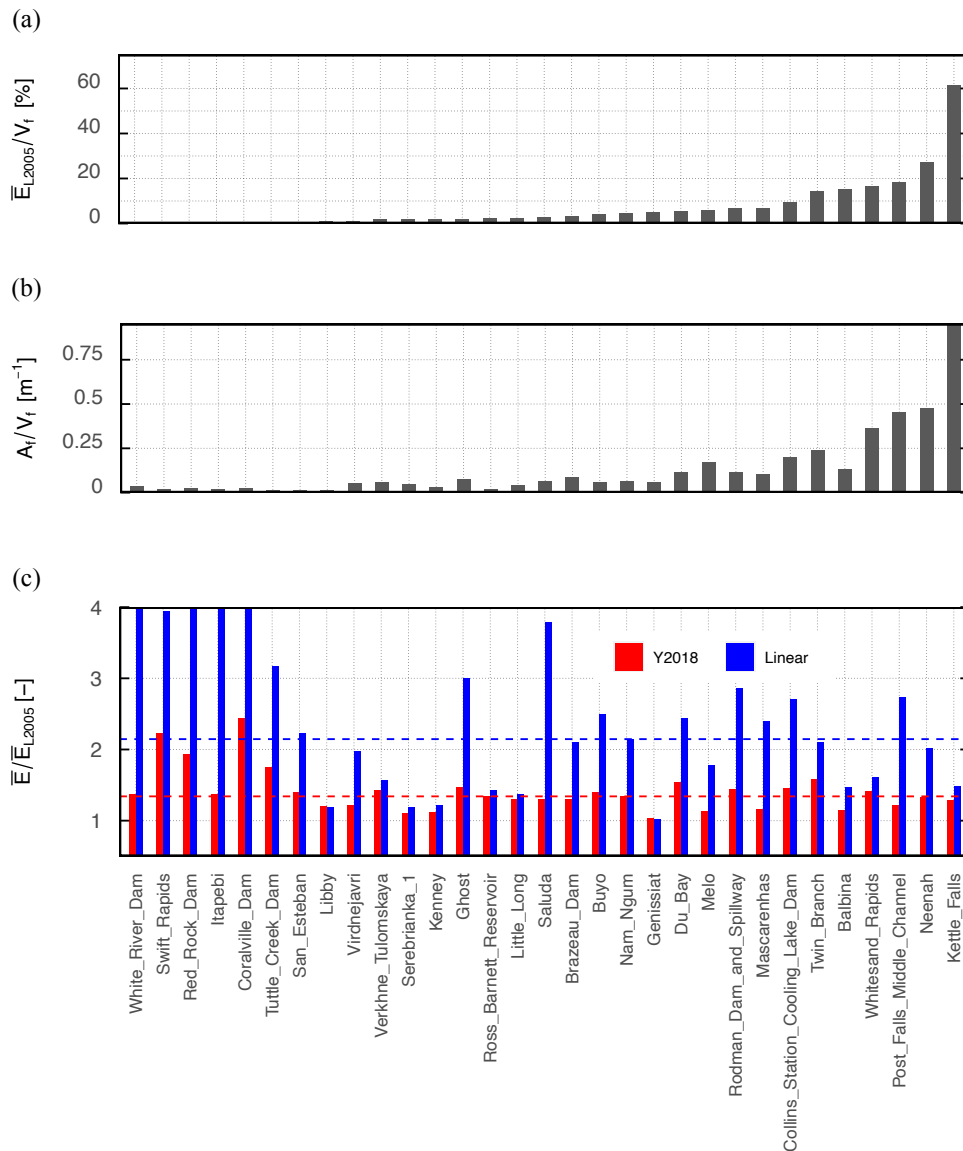


Figure 4.11: (a) Barplot depicting the ratio of mean annual evaporation using L_{2005} shape approximation ($\bar{E}_{L_{2005}}$) to reservoir capacity (V_f). Larger the ratio of $\bar{E}_{L_{2005}}/V_f$, greater the contribution of evaporation in the lake water balance. (b) Barplot depicting the ratio of surface area at reservoir capacity (A_f) to V_f . Larger the ratio of A_f/V_f , flatter the reservoir shape. (c) Barplot depicting the ratio of the mean annual evaporation (\bar{E}) to the mean annual evaporation of L_{2005} ($\bar{E}_{L_{2005}}$) for the linear and Y_{2018} approximations across F-reservoirs. The dotted lines indicate the median values.

4.4.3 Reservoir Disruptivity Analysis

Figure 4.12, panels (a) and (b) depict the relationships of the disruptivity indices c and c' (Eqn. 4.13) versus the indicator that reliability assesses the value of having a given reservoir in a hydrological simulation, namely AAPFD (Eqn. 4.14). These results indicate that both c and c' are covariates and linked to AAPFD in a non-linear way. We identify that the thresholds c_τ and c'_τ are 0.08 and 60 mm, respectively. That is, inclusion of reservoirs with $c < c_\tau$ does not improve significantly the model performance (median AAPFD is low (1.1)). While inclusion of reservoirs with $c > c_\tau$ should significantly improve the model performance (median AAPFD of 2.16).

Figure 4.12c shows the non-linear dependence of the two modest disruptivity indicators (i.e., c and c') for the non-consumptive hydropower reservoirs listed in the GRanD database (note that both axis are logarithmic). The blue dots in this figure are the F-reservoirs selected in this study as a representative sample for this database. To estimate c for the reservoirs not selected in this study, we used dam inflow \bar{I}_v simulated by WaterGAP and routed with the HydroSHEDS flow routing scheme (Döll et al., 2003). The variables for estimating c are provided directly in the GRanD database. Results show that c and c' are strongly correlated for both the F-reservoirs and the GRanD reservoirs, which is expected as inflow is related to catchment area. The 95% prediction intervals (grey lines) enclose most of the non-consumptive hydropower reservoirs contained in the database and entirety of those selected in this study. The thresholds for c and c' still apply to the non-consumptive hydropower reservoirs of the GRanD dataset.

With these indicators, we can identify disruptive non-consumptive hydropower reservoirs at a global scale. This, in turn, opens up the possibility of determining locations with strong anthropogenic impact, which is crucial for prioritizing reservoir modelling activities in large-scale hydrological models. Our analysis of the GRanD reservoir dataset revealed following findings. Out of the 1513 non-consumptive hydropower reservoirs examined, we categorized them into four quadrants based on the thresholds found before, $c_\tau = 0.08$ and $c'_\tau = 60$ mm, as shown in Figure 4.12c. In quadrant I, we find 944 reservoirs with strong potential for disturbing the streamflow regime and the possibility to significantly improve model performance, as shown by the poor KGE values without the F-reservoirs (dark blue points) in the model (e.g., Serebrianka 1 in Figure 4.12d). Quadrant III encompassed 447 reservoirs, which were classified as non-disruptive with little to no space for performance improvement, which is also understood from the higher KGE values without the F-reservoirs (e.g., Virdnejavri and Genissiat in Figures 4.12e and 4.12f, respectively). Quadrant II and IV contain 98 and 16 reservoirs, respectively, where the disruptivity assessment was inconclusive due to conflicting indices. In summary, this result shows that around 30% non-consumptive hydropower dams in the GRanD dataset can be excluded from a global hydrologic model without a significant decrease in streamflow prediction skill. In this sense our study went beyond previous studies (Dynesius and Nilsson, 1994; Nilsson et al., 2005; Zajac et al., 2017; Biemans et al., 2011)

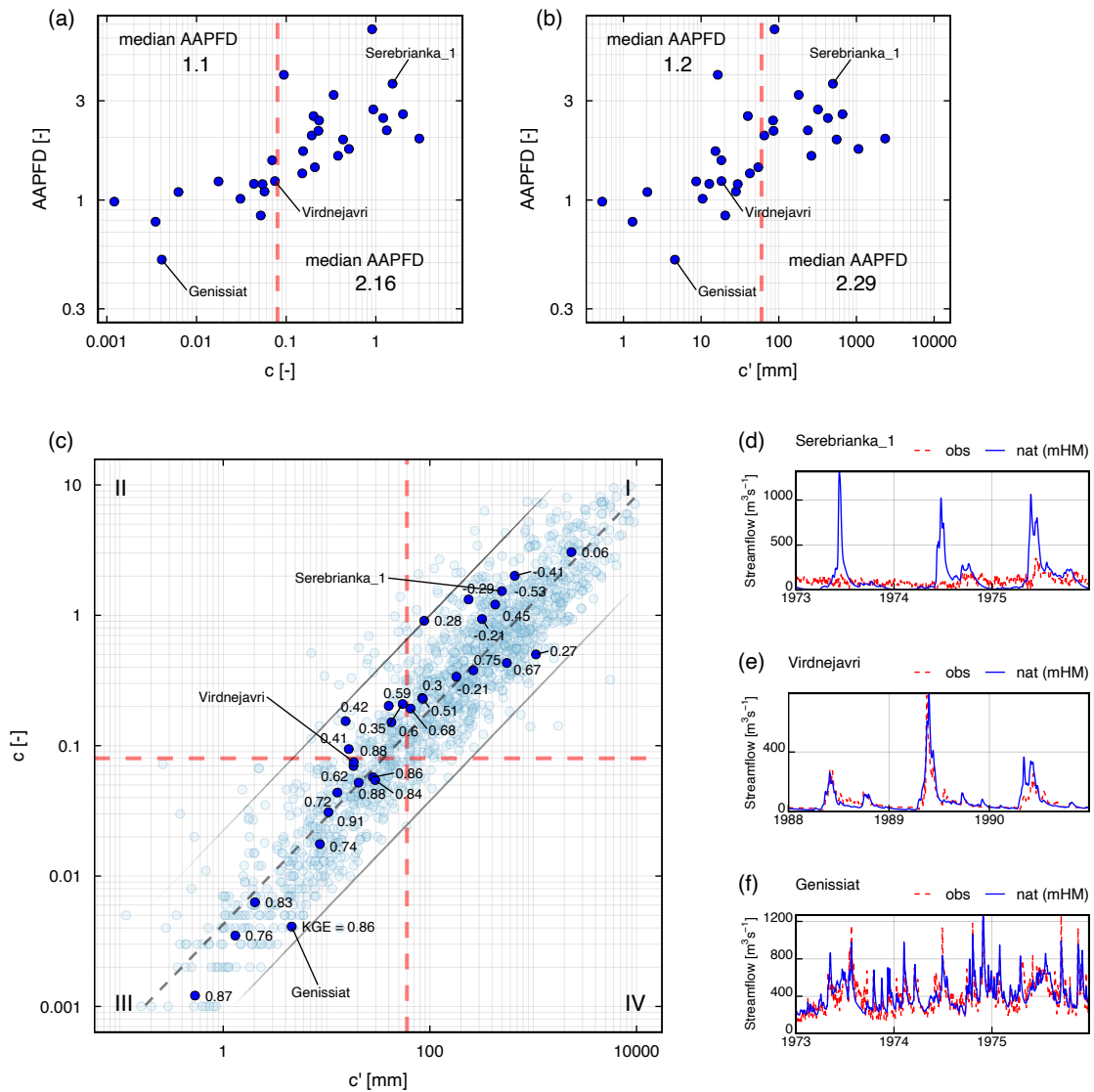


Figure 4.12: Scatterplots between (a) AAPFD vs c , (b) AAPFD vs c' , and (c) c vs c' . Dark blue dots in (a), (b) and (c) are the F-reservoirs, light blue dots in (c) are non-consumptive GRanD reservoirs with hydropower use. The data labels in (c) are the KGE metric between the observations and the naturalized streamflow simulations. AAPFD is an indicator of streamflow regulation (refer Eqn. 4.14). c is the ratio of reservoir capacity to mean annual reservoir inflow volume. c' is the reservoir capacity in terms of the depth of water in the reservoir catchment. Sample size of the non-consumptive hydropower reservoirs in the GRanD without missing values is $n = 1513$. Observed versus naturalized hydrograph comparison at (d) Serebrianka 1, (e) Virdnejavri, and (f) Genissiat reservoirs.

which only identified disruptive reservoirs in the respective modelled regions. Similarly, our analysis supersedes previous studies Biemans et al. (2011), Yassin et al. (2019), and Vanderkelen et al. (2022) that found a relationship between a disruptivity index and model skill for streamflow, but didn't explore thresholds for distinguishing reservoirs for their added value in the model.

It is noteworthy that the disruptivity thresholds proposed here provides a sound justification for excluding less disruptive or non-disruptive reservoirs in a large-scale hydrological modeling. In contrast, previous studies such as Hanasaki et al. (2006) have used thresholds ($c = 0.5$) for parameterisation, which this study includes inherently by following an updated version of the same from Sadki et al. (2023) (refer Eq. 7). The thresholds provided in this study, however, are only tested for non-consumptive hydropower reservoirs and may not be applicable for consumptive reservoirs. Irrigation reservoirs have a distinct disruptive character by supplying water downstream during dry seasons and thereby significantly altering the seasonal pattern of streamflow. Consumptive reservoirs may thus have a notable impact despite their relatively small storage capacity. Identifying "exclusion thresholds" for consumptive reservoirs, thus, remains to be explored.

4.5 CONCLUSIONS AND OUTLOOK

In this study, we presented a novel implementation of a Lake Module (LM) for the mHM model and tested its applicability over two sets of reservoirs worldwide. One set consists of reservoirs with detailed data (e.g., surveyed bathymetry, water level time series, etc.), and the other one consists of reservoirs with limited data (e.g., downstream streamflow gauge and shape approximations from global dataset and the literature). The LM features the following characteristics:

1. The reservoir lake and the reservoir catchment are automatically delineated based on the input dam coordinates and reservoir capacity elevation.
2. The lake is modelled as a single entity such that the lake water balance is not affected by modelling resolution.
3. The reservoir catchment area and inflow are preserved at any modelling resolution.
4. Lake evaporation is estimated based on an energy-based formulation and includes time-varying albedo for the water surface.
5. The default shape of the reservoir is half-pyramid. The user can also specify the bathymetry of the reservoir as elevation, surface area, and volume relationship (hAV) table.

6. The reservoirs are modelled based on the period of commission and decommissioning, i.e., a dam can dynamically appear or disappear depending on the model simulation time-period.

The integration of machine learning techniques, such as random forest, into hydrological modeling has the potential to elucidate complicated non-linear processes, such as reservoir hydropower demand. This approach has shown remarkable potential for refining the fit of hydrographs at daily temporal resolution, and therefore improving the skill of mHM.

While the shape of a reservoir has minimal impact on runoff simulation, care must be taken when reservoir shape approximations are used because they may lead to significant errors in “inner states” like evaporation and the overall water balance of the reservoir. In the absence of observed bathymetry information, the half-pyramid approximation is a more reasonable representation of reservoir bathymetry. In comparison to the half-pyramid shape, the (commonly used) rectangular prism with a constant surface area (or linear shape) simulated unrealistic reservoir surface area dynamics and overestimated evaporation by a factor of two. Despite having the most sophisticated approximation procedure, Y₂₀₁₈ (ReGeom) dataset fell short of being the optimal bathymetry shape for simulating reservoir evaporation. It is essential for efforts such as ReGeom to verify the maximum surface area estimates and the overall shape of the elevation vs. surface area curve, with the half-pyramid shape serving as the benchmark.

There is a non-linear relationship between the streamflow alteration at non-consumptive hydropower reservoirs and the disruptivity indices c (and c'). c and c' are modest yet practical indicators as they are based on easily acquirable information. We postulate that the exclusion of reservoirs (30% of the non-consumptive hydropower reservoirs of the GRanD) based on the proposed thresholds of c and c' do not lead a loss to model realism. This finding represents one of the first attempts to determine “exclusion thresholds” for reservoirs based on their degree of disruptivity of the hydrologic regime.

We demonstrated the potential of employing a Random Forest (RF) surrogate model as a useful intermediate step in understanding non-consumptive demand for hydrological modeling of reservoirs. The demand estimation procedure, however, necessitates streamflow observations downstream of the dam as a control point for training the RF model. Assessing the transferability of RF models for water demand in ungauged reservoirs, therefore, presents an intriguing opportunity. Besides, although not explore in the present study, RF models can be applied for consumptive demand if a reliable control point of the latter can be obtained. Such an investigation could consider using estimates from the existing global demand models (Wada et al., 2014) or demand inferred through satellite soil moisture (Brocca et al., 2018) as first alternatives to missing control points for irrigation and other consumptive demands. Apart from meteorology and time predictors, crop type, cropping calendar, irrigation command area, etc. are the obvious nominations for predictors in such a RF model. If proven successful, the estimation of demand at multipurpose reservoirs, encompassing both non-consumptive and consumptive water

use, could be achieved using multiple RF models simultaneously. This also opens the avenue for exploring possible exclusion thresholds, and/or testing the validity of the ones obtained in this study, for consumptive (e.g., irrigation) reservoirs.

A RF model for non-consumptive demand, once trained, can be used in the forecast mode as it is but a function of time and meteorological predictors, the latter being extracted from the given meteorological forecasts. Yet, it would not be wrong to argue that such one-time-trained RF model, although applicable, would lack the ability to estimate the demand in the changing conditions of the future. A more reliable approach for future simulations would thus be to “recursively” train the RF model up to initialization, provided the updated control data (i.e., streamflow time series) is available. Still, this strategy may remain applicable solely for the short-term forecasts, extending up to the seasonal horizons. Long term forecasts (e.g., decadal horizons) could include much varied changes in the reservoir regulation protocol which may not be possible to predict easily and thus becomes a limitation with the proposed methodology of estimating demand.

The data necessary for large-scale application of mHM with reservoirs includes the coordinates of the dam, reservoir capacity, elevation and surface area corresponding to reservoir capacity, and time series of demand. Although the non-consumptive demand (e.g., hydropower) is better estimated with use of RF model, non-consumptive demand at ungauged reservoirs and consumptive demands can still be generated using existing approaches (e.g., global water demand model from Wada et al. (2014)). Observed streamflow downstream of (some) reservoirs in the domain is sufficient for the model calibration, although some form of validation of reservoir states (water level, surface area, volume) and/or fluxes (evaporation) is highly recommended. The reservoir parameters (Table B1 in C.2) could be set to default at reservoirs where calibration and verification data is not available.

Employing mHM for large-scale simulations with reservoirs has diverse applications across various fields. mHM provides the opportunity for partitioning the reservoir disruption in the hydrological cycle attributable to evaporation, which together with inflow simulations, facilitates in the reservoir budget planning. Likewise, quantifying the distortion of reservoir evaporation from a constant albedo assumption (Shuttleworth, 1996; Wanders et al., 2019) would be another compelling experiment. In hydrological extremes, mHM can be utilized in climate change hotspot regions like the Iberian peninsula, where the drought of 2022 left the average water level in the reservoirs in Catalonia and Andalusia to around 25% (“Severe Drought Spreads in Portugal, Officials Seek EU Help” 2023). mHM can be used to track the impact of such regional droughts on the reservoirs by developing a regional reservoir drought monitoring system. Speaking of depleting reservoirs, the fate of the endoheric lakes (e.g., Lake Urmia of Iran) is another contemporary topic where mHM simulations could play a vital role in scenario analyses for lake sustainability. An application of this nature could leverage cutting-edge satellite technology, like Cyclone Global Navigation Satellite System (CYGNSS) (Al-Khaldi et al., 2021; Wang et al., 2022; Carreno-Luengo et al., 2024), to verify lake surface area evolution

with time. For floods, the other end in the spectrum of the hydrological extremes, mHM allows the possibility to deploy hypothetical reservoirs where its dimensions and flood control regulation scenarios can be played around for optimizing the flood attenuation in future occurrence of an event. In the realm of large-scale ecological studies, mHM enables the investigation of possible connection between reservoir disruptivity and ecological disturbance downstream of reservoirs, and decipher possible thresholds. If proven effective, such straightforward yet effective measures could serve as a starting point for formulating guidelines for designing “eco-friendly” reservoir dams in the future.

SYNTHESIS AND OUTLOOK

5.1 SYNTHESIS AND CONCLUSIONS

Flood is the most persistently deadly and disruptive natural disaster, affecting one in four people worldwide. Small catchment floods have resulted in catastrophic outcomes in the past and should not to be ignored. Global scale Flood Early Warning Systems (FEWS) with timely and effective communication on flood impacts, on-demand in space and time, could, in principle, reduce the death toll and damage attributed to floods, from regional to local scales, every year. This dissertation contributes to this idea and includes some progress demonstrated in the directions of near real-time impact forecasting via inundation modeling and improved streamflow simulation at small and/or regulated catchments in Global Hydrological Model (GHM)s. In the following, the main findings corresponding to each of the seven research statements outlined in Section 1.7 are synthesized and concluded.

R_{1,1}: 2D hydrodynamic models can be incorporated in FEWS for production of near-real-time flood inundation maps and other relevant impact indicators with associated uncertainties.

Rapid map and warning generation is critical for FEWS. But flood inundation modeling has traditionally been computationally demanding. To circumvent this problem, widely recognized FEWS (e.g., GloFAS, EFAS) interpolate pre-calculated flood hazard maps that are spatially inconsistent and do not retain continuity. These methods can be inaccurate, especially when simulating inundation for unprecedented extreme scenarios. Moreover, FEWS that only provide local rainfall depth or gauge water levels often lead to misinformed actions, delayed responses, or no action, highlighting the relevance of impact indicators. The feasibility of the ICON-D2_EPS-mHM-RIM2D operational FEWS is demonstrated in hind-cast for the 2021 European Summer Flood event in the Ahr valley. Parallelized RIM2D 10 m by 10 m flood inundation ensemble runs on GPUs cuts the overall runtime of the FEWS to under three hours. The FEWS delivers probabilistic space-time maps, such as the lead time to specific flood depth thresholds, incorporating the forecast uncertainty and persistency. The forecasts also identifies buildings and transportation infrastructure at risk of flooding. High-resolution DEM is necessary to transfer the system to other regions on the world, while the remaining underlying datasets and modelling tools of the model chain are available freely.

R_{2,2}: SCC preserves the catchment area at predefined points of interest.

The destructive potential of small catchment floods has been proven by past catastrophes and would greatly benefit from accurate impact forecasting via FEWS. State-of-the-art Global Hydrological Model (GHM)s struggle to model contributing area at small catchments accurately, making them unfit for generating boundary conditions of hydrodynamic models in FEWS at local-scales. Existing stream network upscaling techniques, including the widely used D8 method, are largely responsible for the inaccuracies due to the constraint of single outflow direction from a grid. Having a single outflow direction per grid cell makes each grid the smallest unit of the modeled area. The error in the modelled catchment area is fundamentally due to the oversimplification of natural boundaries and domain discretization with simple, geometric- and equally-shaped grids. The novel stream network upscaling scheme, Subgrid Catchment Contribution (SCC), allows model grids to have multiple contribution areas and flow directions, based on subgrid catchments, enabling multiple downstream connectivity. Therefore, with SCC, the model is no longer constrained to grids as the smallest spatial unit and grids fractions can follow natural boundaries which resolves area-related inaccuracies. Regional (Rhine) and global scale experiments show SCC to ensure absolute conservation of catchment areas, at the predefined points of interest in the subgrid level, at all modeling resolutions and catchment sizes. Furthermore, the established regime maps for single domain application of D8 and proposed a thumb rule would aid modellers in their experiment design and selection of model resolutions. Interestingly, SCC is up to five times faster than the multi-domain D8 in the Rhine. The proposed SCC scheme can be employed by any Land Surface Model or Hydrological Model by simply routing the simulated runoff via the routing module of mHM. The improved catchment upscaling with SCC enables GHMs to accurately represent small catchments, facilitating their application in FEWS.

R_{2,3}: SCC eliminates the catchment size problem and enables locally relevant streamflow simulations in gridded hydrological models.

The catchment size problem, which introduces significant errors to small catchments within large modelling domains, is a long-standing challenge in gridded HMs. The accurate catchment upscaling by the SCC abolishes the catchment size problem resulting in locally relevant streamflow for catchments as small as 1 km². A major implication of SCC includes consistency in streamflow simulation across model resolutions of 1 km to 100 km. These breakthroughs implies GHMs augmented with SCC are fit to generate fluvial boundary conditions for hydrodynamic models in FEWS for small catchment floods applications, regardless of the model resolution of the GHM. There are supplementary benefits of SCC in streamflow calibration. Inclusion of small catchment gauges trains parameters to account for headwater processes, in addition to large-scale hydrological processes, promoting distributed modeling across scales. Furthermore, SCC keeps a check

on parameter compensation due to inaccurate upscaling of small catchments, leading to more robust model calibration.

$\mathcal{R}_{2,4}$: SCC enables streamflow estimation at multiple points of interest within a grid cell.

Existing literature does not demonstrate streamflow simulations that resolve multiple stations within a single grid. Large-scale streamflow modeling studies typically set a cutoff for large catchment areas, which inherently excludes multiple streamflow stations within the same grid. This limitation arises because single downstream connectivity methods, such as D8 and IHU, resolve only one streamflow value per grid cell at a time. The multiple downstream connectivity of SCC addresses this issue, demonstrating resolution of complex setting with up to 10 streamflow stations in a single grid. In summary, SCC eliminates the need to adjust the model grid size for a given set of points of interest, providing greater flexibility in hydrological modeling. This feature of SCC can be leveraged for closely situated clusters of reservoir dams or any other type of points of interest where preserving the catchment area is crucial. Thanks to this augmentation, GHMs are now suitable for grids containing the convergence of multiple tributaries, enabling FEWS application to any or all of the tributaries.

$\mathcal{R}_{3,5}$: Machine learning based demand improves the reservoir regulated streamflow simulation.

The available reservoir modeling studies have primarily focused on decoupling seasonality in the water regime rather than the fine scale (daily to weekly) discontinuities in regulated hydrographs. These fine scale regulations reflect demand, a complex human response less amenable to being modeled as a continuous function like other hydrological processes. Machine Learning (ML) based non-consumptive demand is input to the newly developed LM of mHM which automatically delineates the reservoir and enables large-scale hydrological modeling using globally available reservoir data. This approach improves the daily fit of hydrographs downstream of 31 globally distributed non-consumptive reservoirs. ML techniques shows remarkable potential for explaining power for non-linear processes, such as reservoir hydropower demand. The methodology introduced here is designed for non-consumptive hydropower reservoirs with downstream streamflow stations. While ML models could also be applied to consumptive demands (e.g., irrigation), this would require reliable control points, which are not explored in this study. The improved simulation of reservoir regulations enables GHMs to produce accurate streamflow downstream of managed catchments, facilitating their application in FEWS.

$\mathcal{R}_{3,6}$: The bathymetry of the reservoir is critical for the lake surface fluxes.

The reservoir surface area worldwide is equivalent to adding another set of the Great Lakes and Lake Victoria, contributing to global evaporation. Despite the dependence of reservoir evaporation on its underwater shape (or bathymetry), output corresponding to multiple bathymetry approximations have not been compared. This in-depth investigation is the first of its kind to explore the sensitivity of model simulation to reservoir shape. In the absence of observed bathymetry, the half-pyramid approximation is a reasonable proxy to reservoir shape. Oversimplified bathymetry can double the evaporation while causing no alteration to the streamflow. It is critical to include complementary verification of “inner states” like evaporation, in addition to integration variables like streamflow, in order to get the right results for the right reasons. Existing global bathymetry estimates, such as ReGeom, require further refinement, with the half-pyramid shape serving as the benchmark. Furthermore, the Lake Module (LM) of mHM features improved estimation of evaporation rate introducing a new general function for reflectivity of the water surface accounting for latitude and the hourly variation of solar elevation angle. The attention to reservoir bathymetry and evaporation enhances the physical integrity of GHMs and the upstream boundary conditions they generate in FEWS.

$\mathcal{R}_{3.7}$: Only a subset of global reservoirs are disruptive enough to add value to the modelled streamflow.

Top 1% of the largest reservoirs account for 50% of the global reservoir volume. Prioritizing disruptive reservoirs for modeling optimizes computational resources while still accounting for the substantial impact on the streamflow regime. Current literature lacks clear guidelines for appropriate reservoir “exclusion” thresholds. The disruptivity indices c and c' are covariates and show a non-linear relationship with streamflow alteration. Proposed exclusion thresholds for c and c' indicates 30% of the non-consumptive hydropower reservoirs of the GRanD database do not influence modelled streamflow. The reduction of reservoirs has substantial consequences for large-scale HMs, easing parameter calibration and minimizing the runtime needed for generating the boundary conditions for the hydrodynamic model in FEWS. This is one of the first known attempts to determine “exclusion thresholds” for reservoirs based on their disruptivity to the hydrologic regime.

5.2 OUTLOOK

Implications of locally relevant streamflow from GHMs

The Copernicus Climate Change ULYSSES project provides multi-model seasonal prediction system using state-of-the-art GHMs at $0.1^\circ \approx 10$ km resolution (<https://www.ufz.de/>

[index.php?en=47367](#)). The project, currently in its second phase, provides single forecast values at each grids and is limited to forecasts at catchments that are well represented in a 10 km global grid system i.e., $30 \times 100 \text{ km}^2 = 3\,000 \text{ km}^2$ (refer to thumb rule of Equation 3.3). Leveraging SCC, systems such as ULYSSES can generate streamflow forecasts at small catchments ($< 3\,000 \text{ km}^2$), in addition to the larger catchments, without having to change the grid size of the running system. Such use of SCC aligns with the ambitious target of reliable forecasts from the global scale hyper-resolution hydrologic modelling (Wood et al., 2011a; Beven et al., 2015; Bierkens et al., 2015a).

The annual State of Global Water Resources report published by WMO offers another contemporary opportunity for GHMs to leverage SCC. The latest edition of the report (WMO, 2023a) represents global streamflow based on model output from eight GHMs encompassing $\approx 1\,000$ basins, none of which are smaller than $10\,000 \text{ km}^2$, a limitation that would not exist with SCC. It is noteworthy that this integration of small catchments using the newfound “eagle vision” for the GHMs holds significance beyond water quantity to areas such as river temperature and water quality (Tang et al., 2019; Wanders et al., 2019; van Vliet et al., 2023; Jones et al., 2023), among others, underscoring the transformative potential of SCC in diverse fields of hydrology.

Advancing reservoir demand predictions through machine learning techniques

Almost 80% of the 7320 reservoirs of the Global Reservoirs and Dam database (GRanD) cater to at least one consumptive demand. Although not covered in this research, future applications of ML techniques to consumptive demand are possible if a dependable control point is identified. Estimates from the existing global demand models (Wada et al., 2014) or demand inferred through satellite soil moisture (Brocca et al., 2018) can serve as the first alternatives to the missing control points for irrigation and other consumptive demands. Crop type, cropping calendar, irrigation command area, etc. are the obvious nominations for predictors in such a ML model. Testing the transferability of ML models to reservoirs without control points is another paradigm yet to be explored.

A RF model for demand, once trained, can be used in the forecast mode. Forecasting application of ML techniques is yet to be evaluated, specifically answering the question: *Which of the sub-seasonal/seasonal/decadal time horizons would the RF models make sense?* Recursive training of the RF model could add to its longevity and reliability for future simulations, provided the updated control data is available.

A call for comprehensive sensitivity analyses of reservoir simulations

Despite the long history of reservoir representation in large-scale modeling (Haddeland et al., 2006a; Hanasaki et al., 2006), the state-of-the-art is virtually devoid of work pertaining to sensitivity analysis of reservoir simulations. This oversight is especially

concerning given the inherent assumptions in LSMs and GHMs, which ought to be rigorously tested.

This study took the first step in this direction, evaluating the effect of reservoir shape assumptions on evaporation estimations. Future work could include the sensitivity of simulations to rate of change of the hAV (or bathymetry) curves. Majority of the observed bathymetry curves examined in this study have upwards concavity. *What would be the implications of using the downward concavity shapes (e.g., the ReGeom dataset) on these reservoirs?* The simple reservoir shape proposed by Liebe et al. (2005) effectively corresponds to upward concave hAV curves. *What might be a similarly straightforward yet versatile shape for reservoirs exhibiting downward concave hAV curves?* A complementary research question would then be: *can the concavity orientation of the hAV be predicted from the observable topography surrounding the reservoir?*

The geomorphological processes involved in development of topography could help to improve reservoir shape estimation. Steep valleys where fast-flowing water results in the dominance of vertical erosion over lateral erosion lead to V-shape cross section. Leftover valleys eroded by glaciers go through much uniform horizontal and vertical erosion, resulting in flat floor and steep sides. Similarly, low-energy environments with slow moving rivers and flatter gradient favors deposition rather than erosion, resulting in broad and flat cross section. It would, therefore, be worth exploring these different geomorphological mechanisms to find regional clusters at global scale where one shape is more favorable than another while modeling reservoirs.

Another assumption in LSMs that remains largely unexamined is the time-space invariance of the reflectivity (albedo) of water surface, e.g., in Wanders et al. (2019). Surprisingly, even widely respected textbooks like Shuttleworth (1996) endorse this overly simplistic approach. It is known for a fact that the albedo depends on the angle of the sun above the horizon, which is neither constant in space nor in time (Cogley, 1979). Quantifying the sensitivity of reservoir evaporation to different albedo assumptions is another compelling experiment waiting to be demonstrated.

Reservoir monitoring and forecasting systems

In 2022, the Iberian peninsula, a climate change hotspot region, was severely impacted by the European droughts. At the onset of the drought, the average water volume in the reservoirs of Catalonia and Andalusia dropped to about 25% of their total capacity ("[Severe Drought Spreads in Portugal, Officials Seek EU Help](#)" 2023), eventually falling further to just 16% by February 2024 (Biella et al., 2024). Such large-scale events require a regional overview for the decision makers, encompassing the whole reservoir system. The mHM model, given its suitability for large-scale applications using freely accessible data, is well-positioned to serve as the foundation for a regional reservoir drought monitoring system. When enhanced with forecasting capabilities, accurate inflow predictions via SCC can greatly assist reservoir managers in responding to extreme climatic events.

Such systems would be equally useful to monitor the fate of the endoheric lakes around the world, many of which are endangered ecosystems. Once the world's fourth-largest inland body of water, the Aral Sea largely dried up due to extensive irrigation projects initiated during the Soviet era (Micklin, 2007). Lake Urmia in Iran is following the same path, having lost 88% of its surface area with no signs of recovery (AghaKouchak et al., 2015). The only natural way water exits an endoheric lake system is via evaporation from the lake surface. The improved representation of evaporation in mHM could enhance lake water balance simulations and play a vital role in scenario analyses for sustainability of lakes such as Lake Urmia.

The 8000 year return period flood (Vorogushyn et al., 2022) of 2021 in the Ahr valley brought huge loss of life and property. By leveraging mHM, planners can experiment with hypothetical reservoirs and flood control regulations to improve flood attenuation in future events of similar magnitude. In large-scale ecological research, mHM facilitates the exploration of links between reservoir disruptivity and downstream ecological disturbances, helping to identify potential thresholds. Should these findings prove accurate, they could act as a foundation for setting future standards for the design of environmentally responsible reservoir dams.

Towards locally relevant global flood early warning system

The 18th World Meteorological Congress approved eight long term ambitions on global water, first of which is – *No one is surprised by floods* (WMO, 2023b). Currently, only a third of WMO members and territories report having multi-hazard monitoring and forecasting system while only 56% of countries report using hazard, exposure and vulnerability data in their forecasts, restricting the progress on impact-based forecasting and warning (WMO, 2023c).

In 2023, WMO launched *Flood Forecasting Initiative* which aims to improve the capacity of national meteorological and hydrological services in detecting flood-critical situations and providing accurate and timely flood forecasting services. *Flash Flood Guidance System* is another ongoing project from WMO aiming to implement guidance system at country and regional scale, modelling basins as small as 150 km² (HRC, 2019). In Germany, the Hochwasserfrühwarnsystem is the national scale FEWS monitoring and predicting flood events (LfU, 2022) while the National Water Prediction Services provides stage and flow forecasts in the USA (NOAA, n.d.). The Delft-FEWS (<https://oss.deltares.nl/web/delft-fews/>), a commercial software by Deltares, enables tailor-made hydrological forecasting system for individual institutions or nations (e.g., the Australian hydrological forecasting system, HyFs). At continental level, the EFAS provides early warning services across Europe, integrating real-time meteorological data with the LISFLOOD hydrological model at 5 km resolution.

National and regional systems introduce disparity in forecasting capabilities, with developed members benefiting more from these advancements compared to developing

and least developed countries due to limited resources (WMO, 2023b). Global FEWS helps standardize and globalize flood early warning systems. GloFAS, part of the Copernicus Emergency Management Service, integrates weather forecasts from ECMWF-IFS with hydrological models HTESSEL-LISFLOOD to provide consistent and reliable flood forecasting across borders. While the system impressively provides global flood alerts up to 30 days in advance, the information is limited to catchments larger than 500 km² (Harrigan et al., 2020).

The Fathom Global Flood Map (GFM) (Wing et al., 2024; Andreadis et al., 2022; Sampson et al., 2015), produced with the Global Flood Inundation Model, is another global scale inundation modeling effort. Recognizing the extravagant computational cost of downscaling kilometer scale hydrological models to 30 m flood inundation resolution, the system skips hydrological modeling altogether, choosing instead to apply Regional Flood Frequency Analysis to infer historical boundary conditions by extending data from gauged to ungauged sites. While for future simulations, the delta change or “change-factor” approach is adopted to simulate the impact of climate change on flood hazard (Wing et al., 2024). However, with the advent of SCC, these limitations of GFM and GloFAS no longer apply. The next generation of GHM runs would be computationally feasible enough to support GFM for 30 m inundation modeling, while GloFAS can generate flood forecasts for catchments smaller than 500 km².

While weather forecasts have become an integral part of daily life worldwide, flood and inundation forecasts have yet to achieve similar widespread recognition. Windy (<https://www.windy.com/>) is a forecasting platform which has gained popularity for its user-friendly interface and its map-based display, allowing users to zoom in on specific regions to see localized conditions, globally. Windy integrates data from several trusted sources, such as ECMWF and the Global Forecast System (GFS). Despite its impressive offering of 55 forecast variables (including droughts, see Figure 5.1), Windy currently does not provide forecasts or warnings for flood. As future GHMs enhance their ability to simulate local conditions with SCC for FEWS, platforms such as Windy may soon include local flood forecasts powered by global flood early warning systems – GloFEWS.

5.3 THE IRONY OF MYTHS: A FINAL REFLECTION

The mythical story of Shiva taming the mighty Ganga (the river Ganges, refer to Section 1.1) portrays flood as a force that can be controlled or channeled by divine intervention. The Uttarakhand floods of 2013, which ravaged the upper Ganges basin, defy such celestial mastery and stand in stark contrast to the ancient narrative of control and order.

The relentless rain (up to 245 mm) from 15 to 17 June 2013, above the tree line, unleashed torrents of water, boulders, debris, and moraine in the Upper Ganges Basin (NIDM, 2015). The catastrophe, which coincided with peak tourist and pilgrimage season, damaged 2134 km of roads and 112 bridges in the worst affected areas (NIDM, 2015).

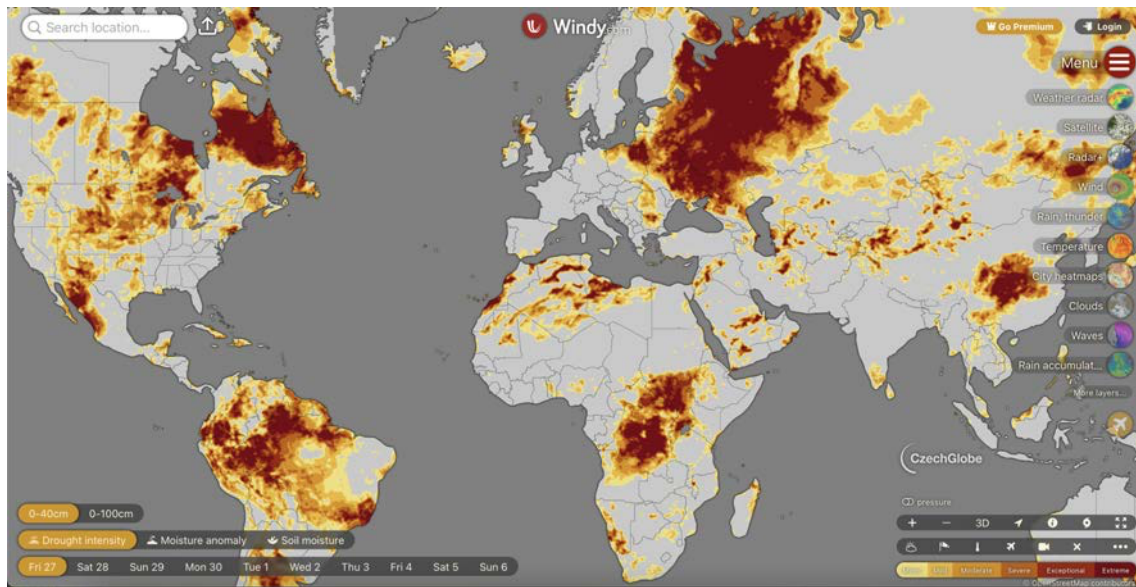


Figure 5.1: Screenshot showing global drought intensity forecasts (source: www.windy.com)

This left more than 110 000 people stranded in inaccessible hilly terrains (Kala, 2014) eventually resulting in a death toll of 4 190, and damage to 19 726 houses (NIDM, 2015).

In the Kedarnath valley, a 50 km² catchment nestled deep in the Himalayas, the post-event destruction around the sacred Kedarnath temple (Figure 5.2b-c) ironically mirrored the very myth of Ganga's descent – a river once believed to be tamed by Shiva had wreaked havoc upon the very lands dedicated to its worship (Note: *Kedarnath* is one of many epithets of Shiva). The flood overwhelmed the town of Uttarkashi (4 609 km²) in the Bhagirathi River catchment (Figure 5.2d) damaging 991 houses (NIDM, 2015). Further downstream, the holy city of Rishikesh witnessed the submergence of its revered Shiva statue, an iconic image of the 2013 floods (Figure 5.2e-f). As floodwaters rose, the statue of the deity, symbolizing control over the Ganga located at the top of the matted hair, was swallowed by the surging river herself, a grim reminder of flood's untamable force.

This stark contrast between flood myth and reality underscores the essential purpose of this research. While myth offers comfort through divine narratives of control, practical flood management in river catchments, big and small, relies on accurate hydrological models, and timely early warning systems. In the end, it is through human effort, technological innovation, and proactive management, rather than divine interventions, that we confront the ever-growing threat of floods in a changing climate.

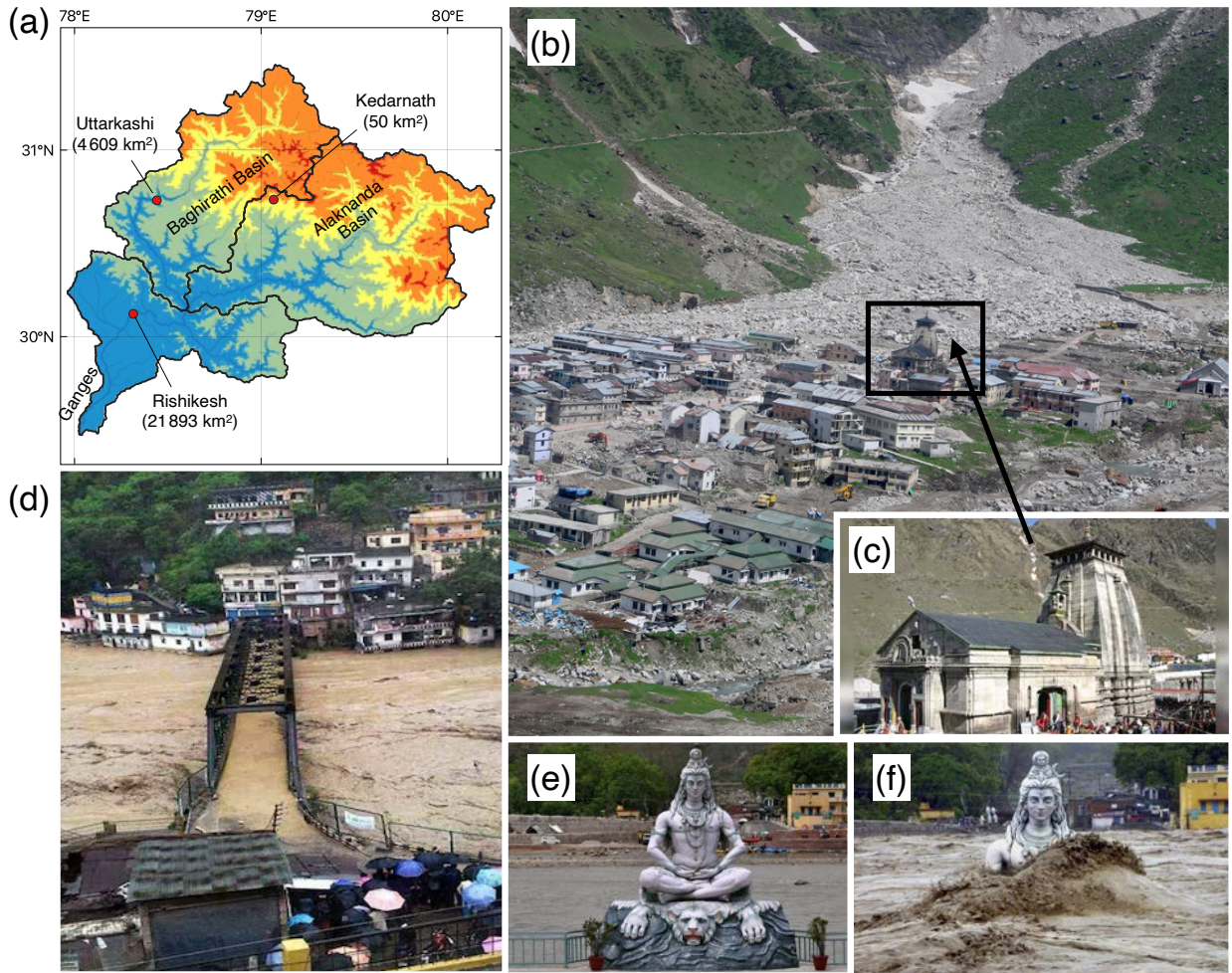


Figure 5.2: The “Descent of Ganga” in the 21st century – the 2013 Uttarakhand floods in Northern India. (a) Map illustrating the Upper Ganges Basin, with highlighted points referencing accompanying photographs. (b) and (c) The Kedarnath valley and the temple of Kedarnath (Shiva) (Firstpost, 2013; Adobe Stock, n.d.). (d) Flooding of a bridge at Uttarkashi in the Bhagirathi catchment (India Today, 2013). (e) and (f) The statue of Shiva at Rishikesh before and during the flood (Amma, 2013; Sommer, 2013).

Part III
APPENDICES

APPENDIX A

This section includes the Appendix and the Supporting Information from the following publication:

Najafi, H., Shrestha, P. K., Rakovec, O., Apel, H., Vorogushyn, S., Kumar, R., Thober, S., Merz, B., & Samaniego, L. (2024). High-resolution impact-based early warning system for riverine flooding. Nature Communications, 15(1), 3726.

A.1 ENSEMBLE WATER LEVEL FORECASTS

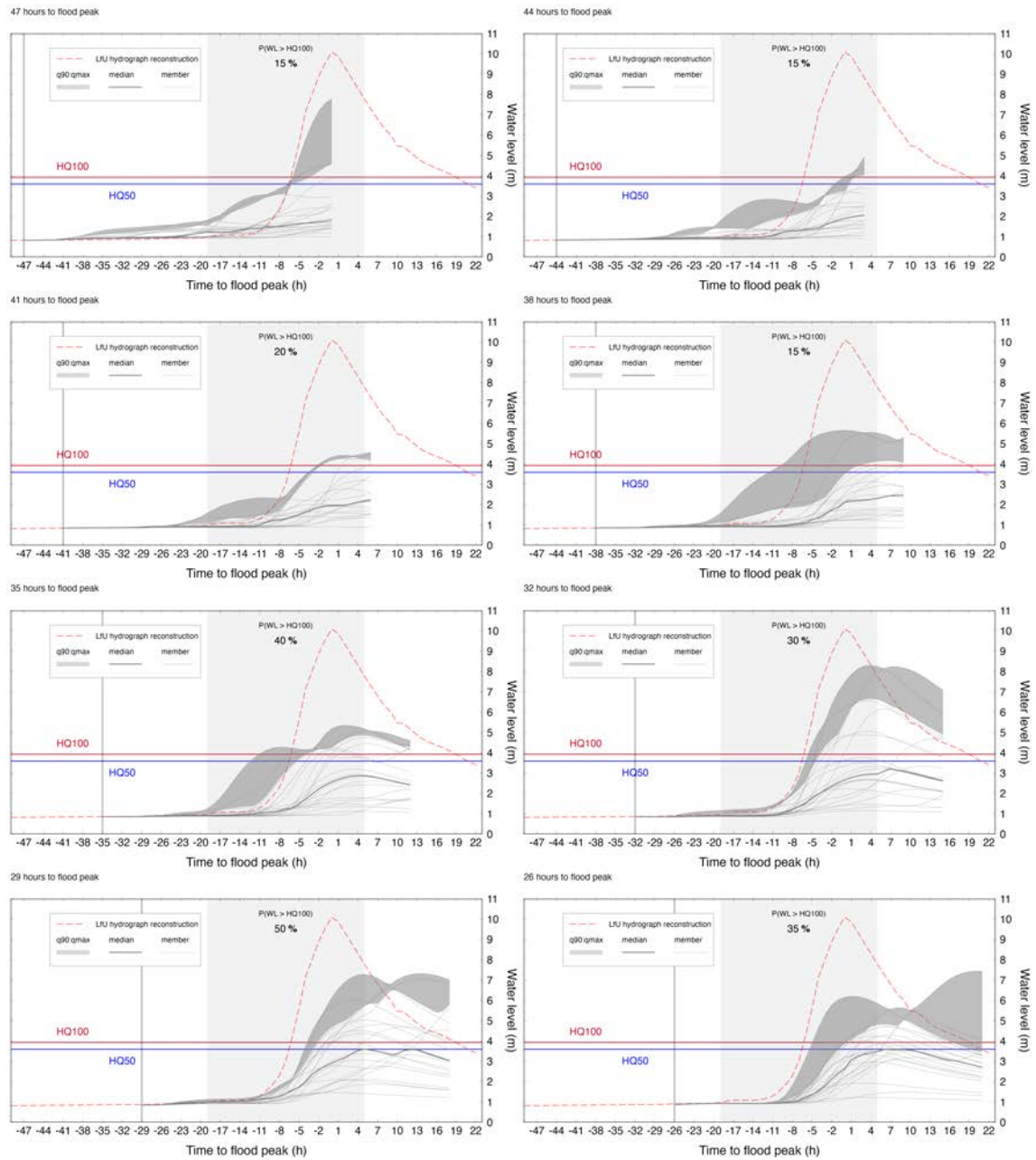


Figure A.1: Ensemble water level forecasts ($n=20$) at gauge Altenahr for 16 initialisations between July 13, 2021 (02 CEST) and July 14, 2021 (23 CEST) based on ICON_D2_EPS - mHM. Initialization timing from 47 h to 26 h before the event. Data Sources: Observed streamflow: LFU. Observed rainfall (RADOLAN) and weather forecast (ICON_D2_EPS): Deutscher Wetterdienst.

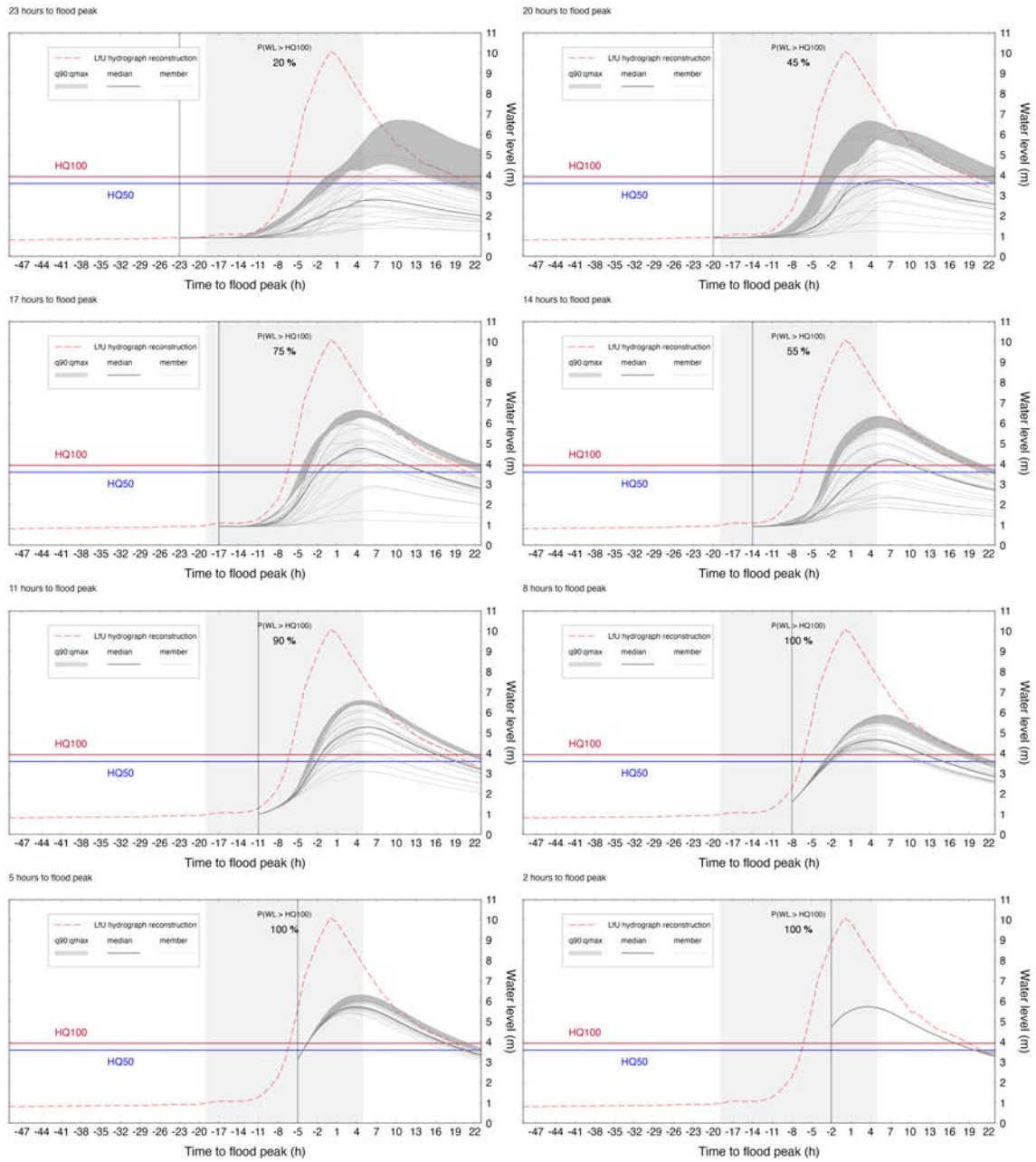


Figure A.1: ... Cont. Ensemble water level forecasts. Initialization timing from 23 h to 2 h before the event.

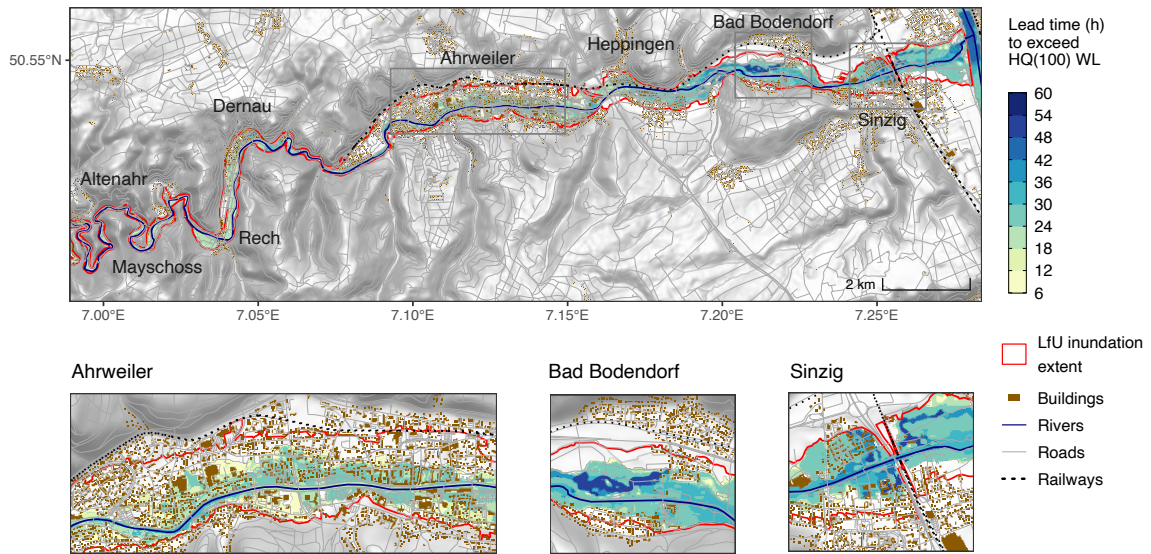


Figure A.2: Raster-based lead-time map of water level downstream Altenahr gauge exceeding HQ₁₀₀ levels based on ensemble median from ICON_D2_EPS-mHM-RIM2D warning chain. The red outlined areas indicate the inundation areas mapped by the State Office for the Environment (LfU) of Rheinland-Pfalz. Supplementary data sources: OSM rivers, roads and buildings: OpenStreetMap/OpenStreetMap, 2017 contributors 2021 distributed under the Open Data Commons Open Database License (ODbL) v1.0. Hillshade: DTMHengl et al., 2021v0.3 (CC BY).

A.2 ENSEMBLE MEDIAN - WITHOUT PERSISTENCE

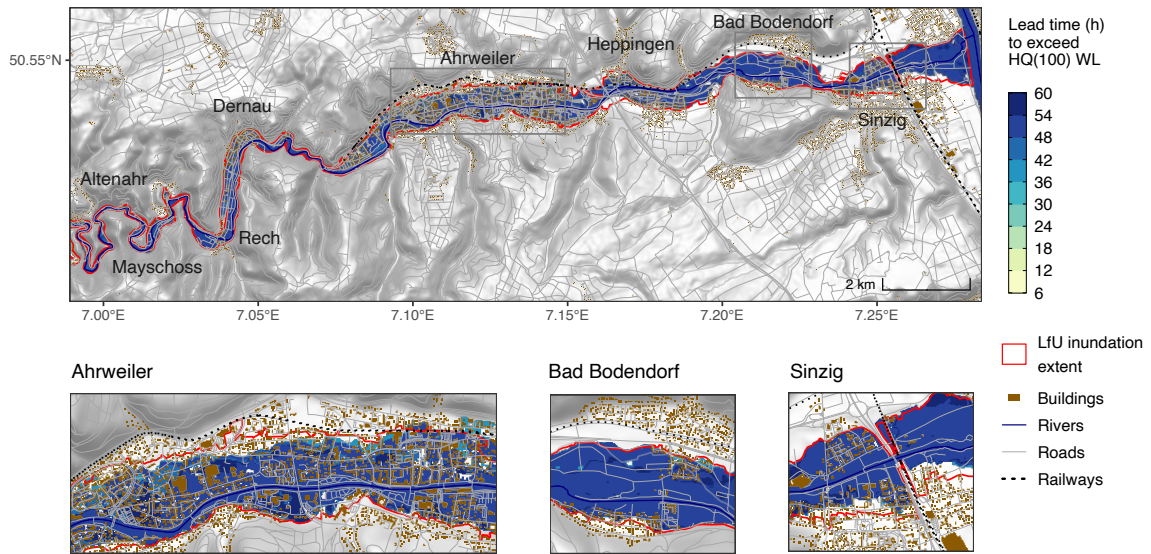


Figure A.3: Raster-based lead-time map of water level downstream Altenahr gauge exceeding HQ_{100} levels based on Maximum ensemble from ICON_D2_EPS-mHM-RIM2D warning chain. The red outlined areas indicate the inundation areas mapped by the State Office for the Environment (LfU) of Rheinland-Pfalz. Supplementary data sources: OSM river, roads and buildings: OpenStreetMapOpenStreetMap, 2017 contributors 2021 distributed under the Open Data Commons Open Database License (ODbL) v1.0. Hillshade: DTM vo.3 (CC BY)Hengl et al., 2021.

A.3 ENSEMBLE MAXIMUM - WITHOUT PERSISTENCE

A.4 FORECASTING CHAIN FOR THE IMPACT-BASED FEWS

Forecasting Chain for an Impact-based Flood Early Warning System

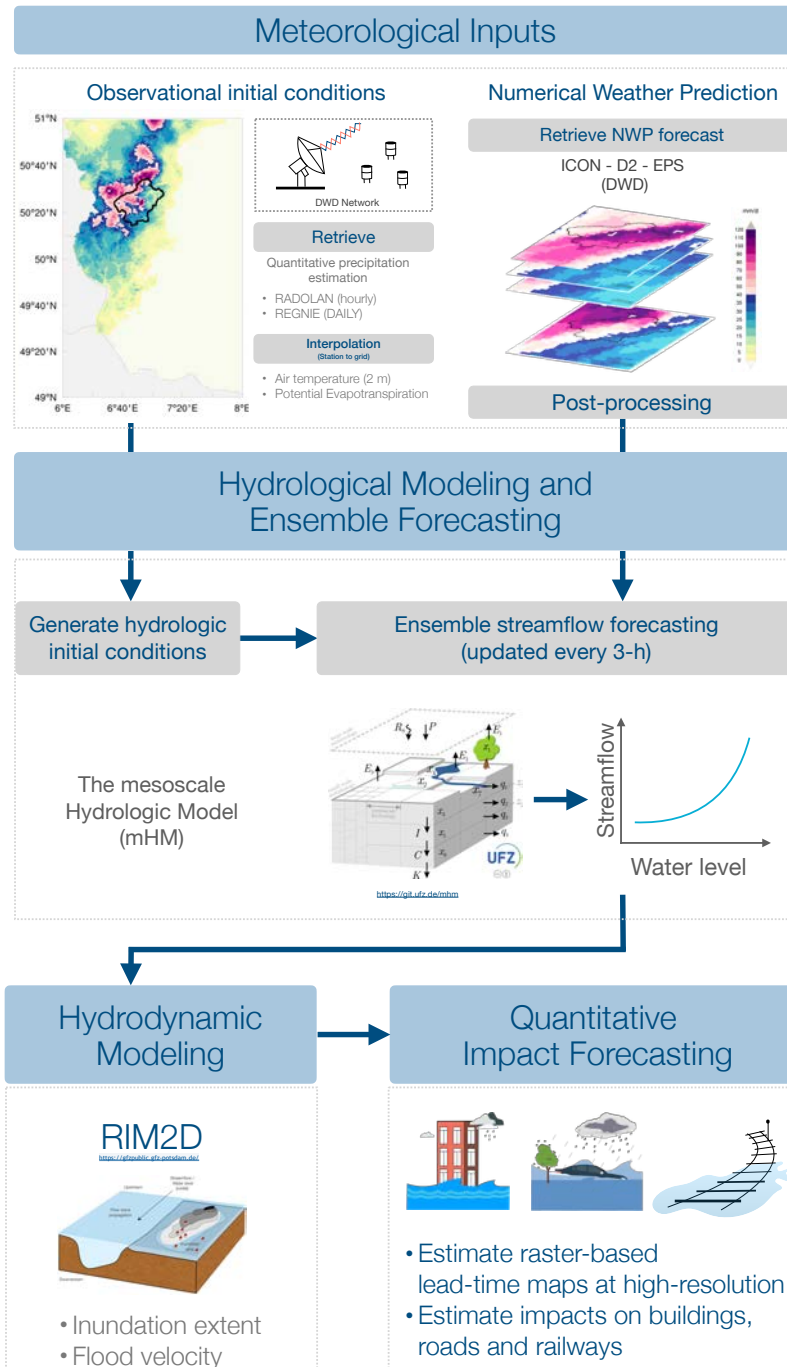


Figure A.4: Schematic of the ICON_D2_EPS-mHM-RIM2D flood warning chain. Data sources: Observed rainfall fields based on RADOLAN and ICON_D2_EPS (Deutscher Wetterdienst).

A.5 MHM PERFORMANCE EVALUATION

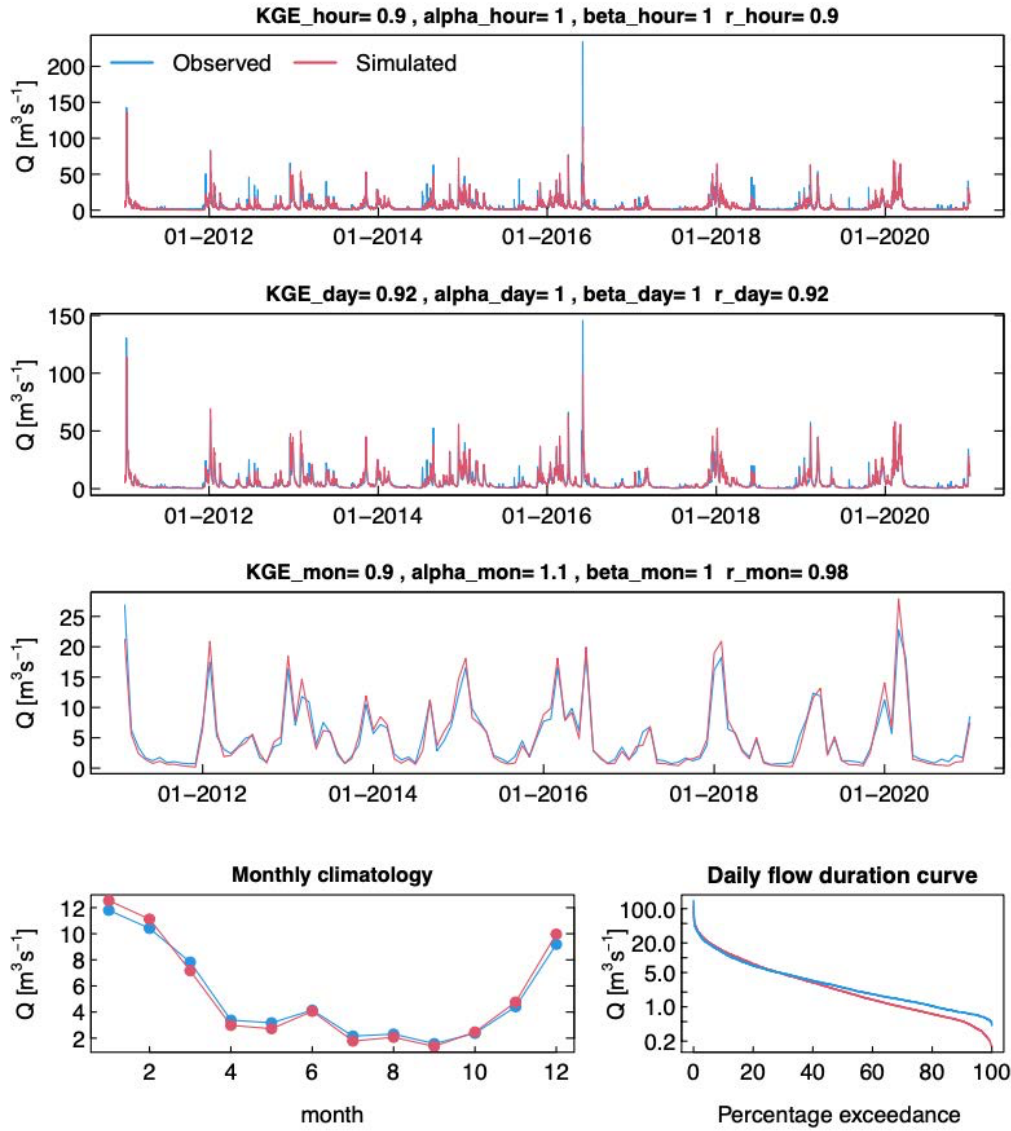
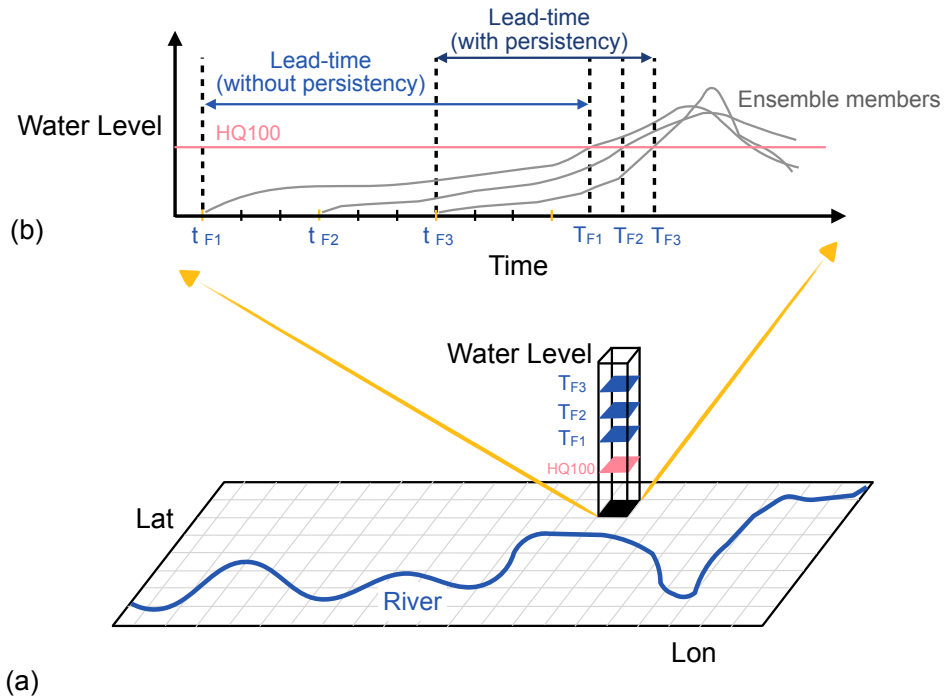


Figure A.5: Time series of streamflow simulations and observation at (a) hourly, (b) daily, (c) monthly time step for the Altenahr gauge. Monthly climatology is shown in panel (d) and daily flow duration curve is shown in panel (e). The respective Kling-Gupta efficiency (KGE) Gupta et al., 2009 values with an optimal value of 1 and the three components of KGE (i.e., α = ratio of variability, β = ratio of bias, r = correlation) are shown in the respective panels. Data source: observed streamflow from LfU.

A.6 PERSISTENCY MAP SCHEMATICS



t_{Fi} : Forecast initialization for which water level exceeds HQ100 for the i^{th} time

T_{Fi} : Forecast time step of hydrodynamic model corresponding to t_{Fi}

Figure A.6: (a) Raster-based inundation forecast and water level shown for three forecast initialisations for a given pixel (b) Definition of maximum lead-time (with and without persistency) for the given pixel and an ensemble member. In defining the term lead-time with persistency, water level for three consecutive forecast initialisations exceed the HQ100.

A.7 LOCATION MAP

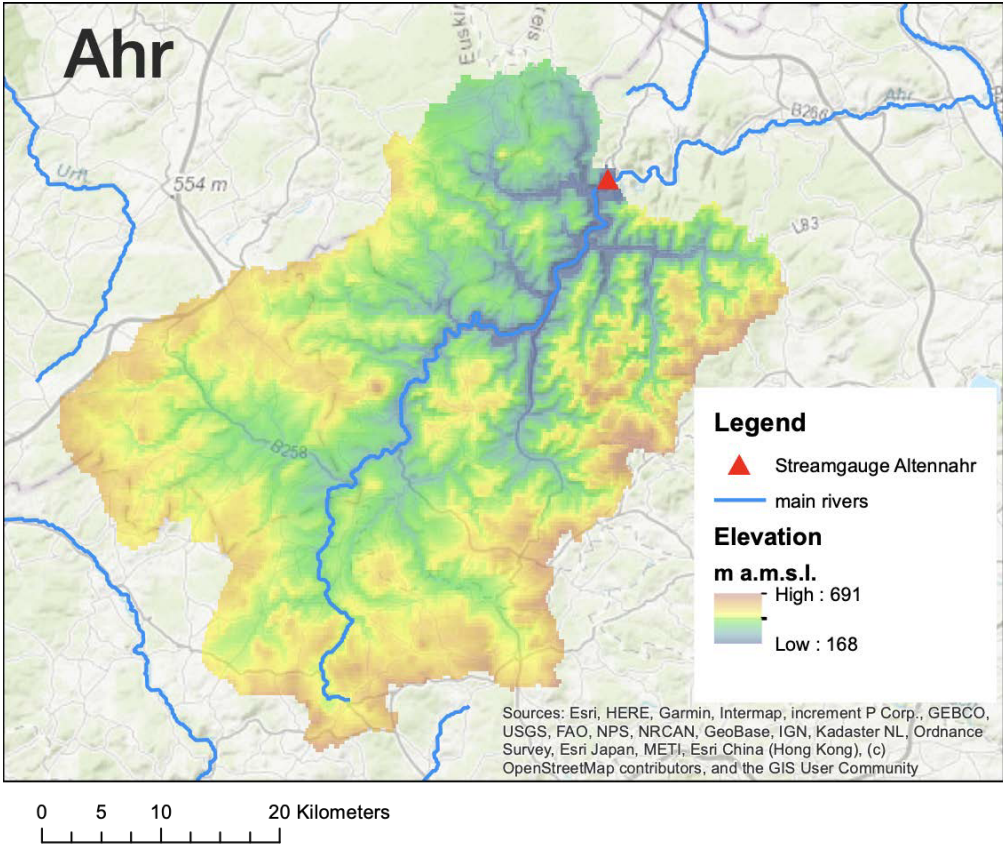


Figure A.7: Topographic map of the Ahr catchment

APPENDIX B

This section includes the Appendix and the Supporting Information from the following publication:

Shrestha, P. K., Samaniego, L., Rakovec, O., Kumar, R., Mi, C. X., Rinke, K., & Thober, S. (under review). Enhancing Global Streamflow Modeling to Enable Locally Relevant Simulations. Water Resources Research.

B.1 GLOBAL DISTRIBUTION OF DATA AVAILABILITY, CATCHMENT AREA ERROR IN THE DEM, AND CATCHMENT SIZE

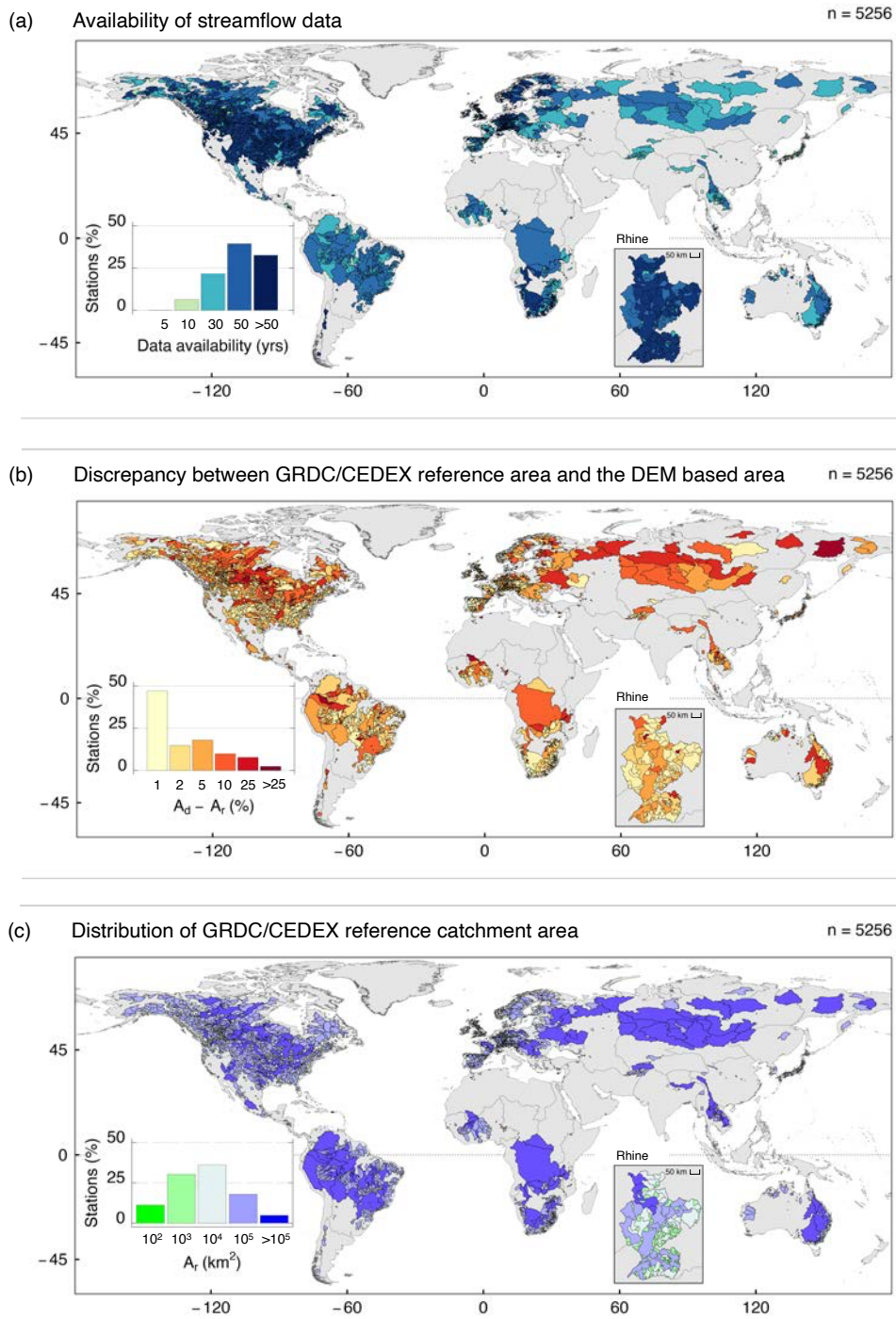


Figure B.1: Attributes of 5 256 streamflow stations of the global experiment. (a) Temporal extent of daily time series streamflow data between 1961 to 2020. n is the number of streamflow stations. (b) Discrepancy between the GRDC/CEDEX reference catchment area (A_r) and the DEM based catchment area (A_d) subsequent to the application of BasinEx. (c) Distribution of the GRDC/CEDEX reference catchment areas (A_r). The insets shows the same for the Rhine basins.

B.2 SCHEMATICS OF THE RESOLUTION LEVELS IN MHM

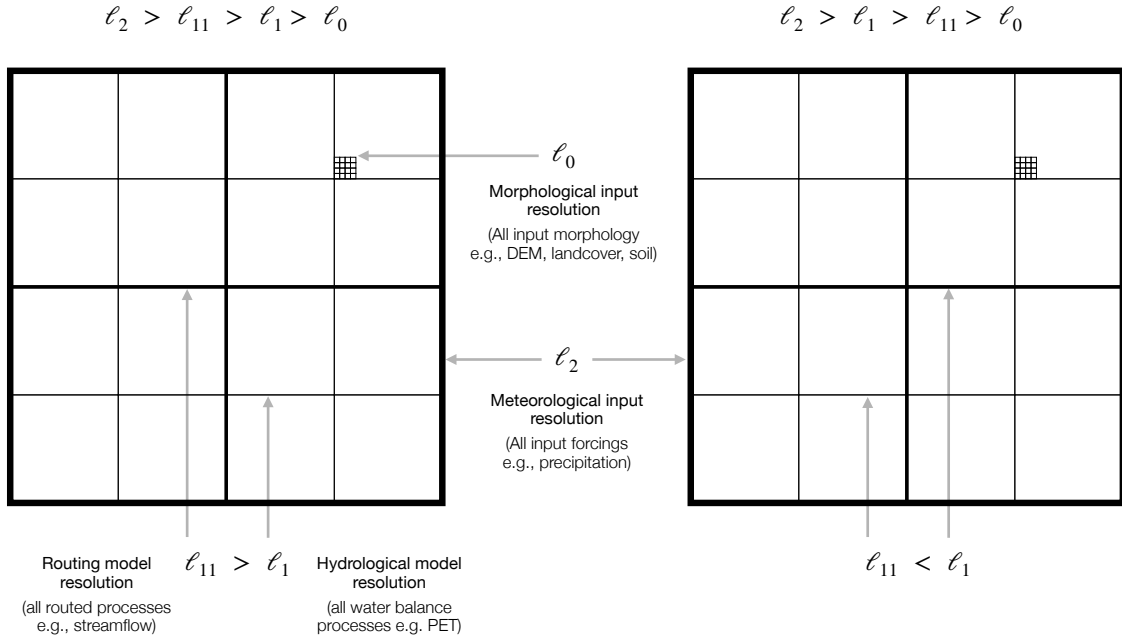


Figure B.2: Resolution levels used in mHM with two possible cases between l_1 and l_{11} . Note that there is a third possible case (not shown here) where l_1 and l_{11} are equal.

B.3 ALGORITHMS FOR UPSCALING THE STREAM NETWORK WITH SCC

Algorithm 1 Delineation of basins at points of interest

(see Figure 3.3a-d)

1. Read the coordinates of a set of locations contained in the set \mathcal{D} , numbered from $i = 1, N$. Here, N denotes the number of streamflow stations where streamflow will be estimated.
2. Delineate l_0 catchment at each point i using flow direction (F_d) at the l_0 level, with the index i as the value, to obtain a vector \mathcal{M} of catchment maps.
3. Co-locate the vector \mathcal{M} into a single map (M') such that each pixel is assigned the index (i) corresponding to the catchment with minimum F_a (flow accumulation at l_0) at the outlet (F_a^o).

$$M' = i_{\min(F_a^o)} \mid \mathcal{M} \tag{B.1}$$

Algorithm 2 Node initialisation

(see Figure 3.3e-f)

1. Intersect the catchment map M' of Algorithm 1 with the ℓ_{11} grid (panel e).
 2. Establish all unique sub-catchments within an ℓ_{11} grid (panel f).
 3. Assign unique IDs to each node.
 4. Estimate the contributing area fraction (f) of each node (to be used in routing).
-

Algorithm 3 Setting the upscaled stream network

(see Figure 3.3g-h)

1. Walk along the border of each node to identify the ℓ_0 cell with the maximum F_a i.e., the subgrid outlet.
 2. Given the F_d of the subgrid outlet, determine the downstream node.
 3. Connect each node to its downstream node by flow direction arrows to represent the upscaled stream network. In Figure 3.3g (zoomed inset), node 2 is the downstream node for node 3.
 4. Store the routing order (to be used in routing).
-

B.4 ROUTING FLOW USING STREAM NETWORK UPSCALED BY SCC

mRM routes the streamflow through links connecting the subgrid outlets of the upstream and downstream nodes. Once the stream network is upscaled by SCC to the user prescribed routing resolution (ℓ_{11}), mRM routes the streamflow through the links in the routing order (see Algorithm 3), at each time step, in the following manner:

Algorithm 4 Streamflow routing

1. Collect the inflow Q_i^t at a link as sum of outflow Q_o^t from the m upstream links at time step t

$$Q_i^t = \sum_{k=1}^m Q_o^{k,t} \quad (\text{B.2})$$

2. Add the fraction f (see Algorithm 2) of streamflow generated from the current node (Q_n^t) to Q_i^t

$$Q_i^t = Q_i^t + fQ_n^t \quad (\text{B.3})$$

3. Route the streamflow downstream (Samaniego et al., 2010; Thober et al., 2019) using Muskingum-Cunge routing parameters (ν_1 and ν_2) regionalized by the multiscale routing model, mRM (Thober et al., 2019).

$$Q_o^t = Q_o^{t-1} + \nu_1 (Q_i^{t-1} - Q_o^{t-1}) + \nu_2 (Q_i^t - Q_i^{t-1}) \quad (\text{B.4})$$

4. Repeat steps 1 – 3 for all the links

B.5 EQUATIONS FOR THE BENCHMARKS

We benchmark SCC against the D8 and other state-of-the-art upscaling methods. The accuracy of the SCC modelled catchment area is benchmarked against D8 based on modeling efficiency (ME) and root mean squared error normalized with standard deviation (Normalized Root Mean Square Error (NRMSE)). The expression of ME as defined by Yamazaki et al. (2009), which is equivalent to the Nash-Sutcliffe Efficiency (NSE) (Nash and Sutcliffe, 1970), is:

$$\text{ME} = \frac{\sum_{i=1}^k (\bar{A}_d - A_d^i)^2 - \sum_{i=1}^k (\hat{A}_i - A_d^i)^2}{\sum_{i=1}^k (\bar{A}_d - A_d^i)^2}, \quad (\text{B.5})$$

where, A_d^i is the DEM based catchment area at a streamflow station, \hat{A}_i is the upscaled catchment area at the station, and \bar{A}_d is the DEM based mean catchment area across all the stations (total = k). The expression of NRMSE is:

$$\text{NRMSE} = \frac{\sqrt{\frac{\sum_{i=1}^k (\hat{A}_i - A_d^i)^2}{k}}}{\sigma}, \quad (\text{B.6})$$

where, σ is the standard deviation of the A_d values. We benchmark the streamflow simulation of SCC against D8 based on change in model performance at individual stations as:

$$\Delta KGE = KGE_{\text{SCC}} - KGE_{\text{D8}} \quad (\text{B.7})$$

Where, KGE is the Kling-Gupta Efficiency metric (Gupta et al., 2009) between daily streamflow simulations and observations. KGE_{SCC} and KGE_{D8} are calculated for SCC and D8 streamflow simulations, respectively.

B.6 COMPARISON OF MODEL UPSCALED CATCHMENT AREA WITH THE GRDC/CEDEX REFERENCE CATCHMENT AREA

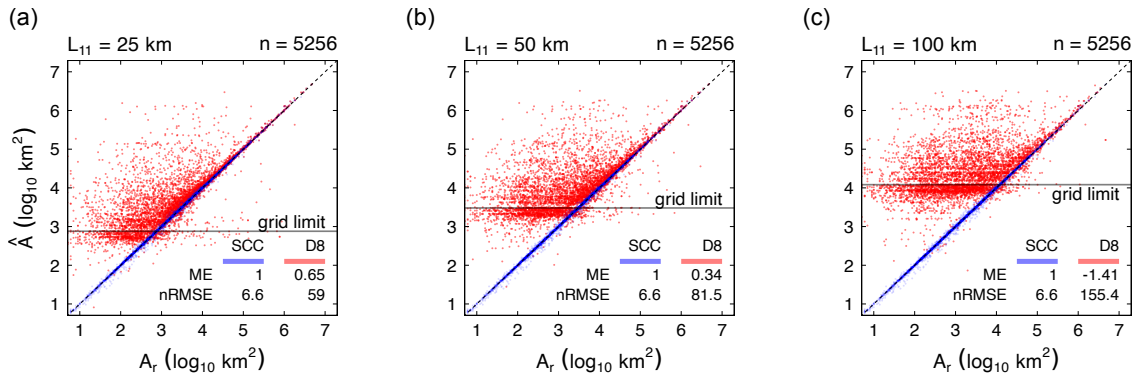


Figure B.3: Scatterplots of GRDC/CEDEX reference area (A_r) on x-axis and model upscaled catchment area (\hat{A}) on y-axis evaluating performance of SCC vs D8 at model resolutions of (a) 25 km, (b) 50 km, and (c) 100 km corresponding to the 5 256 streamflow stations worldwide. The goodness of fit of \hat{A} on A_r is given by the model error (ME, dimensionless) and RMSE (km^2) normalized using standard deviation. The grid limit represents the area of the model grid (ℓ_{11}) and is estimated at the equator. Together with Figure 3.6, this figure highlights that inaccuracies from the upscaling scheme, such as the D8 method, can be orders of magnitude higher than the error in the DEM if not properly addressed. The inconsistencies of SCC against the reference area is thus mainly limited to the errors in the DEM used in this study, which could be improved with a finer resolution and/or better hydrography checks in the DEM (e.g., MERIT Hydro).

B.7 ADDITIONAL FIGURES FOR THE SCALABILITY HYPOTHESIS

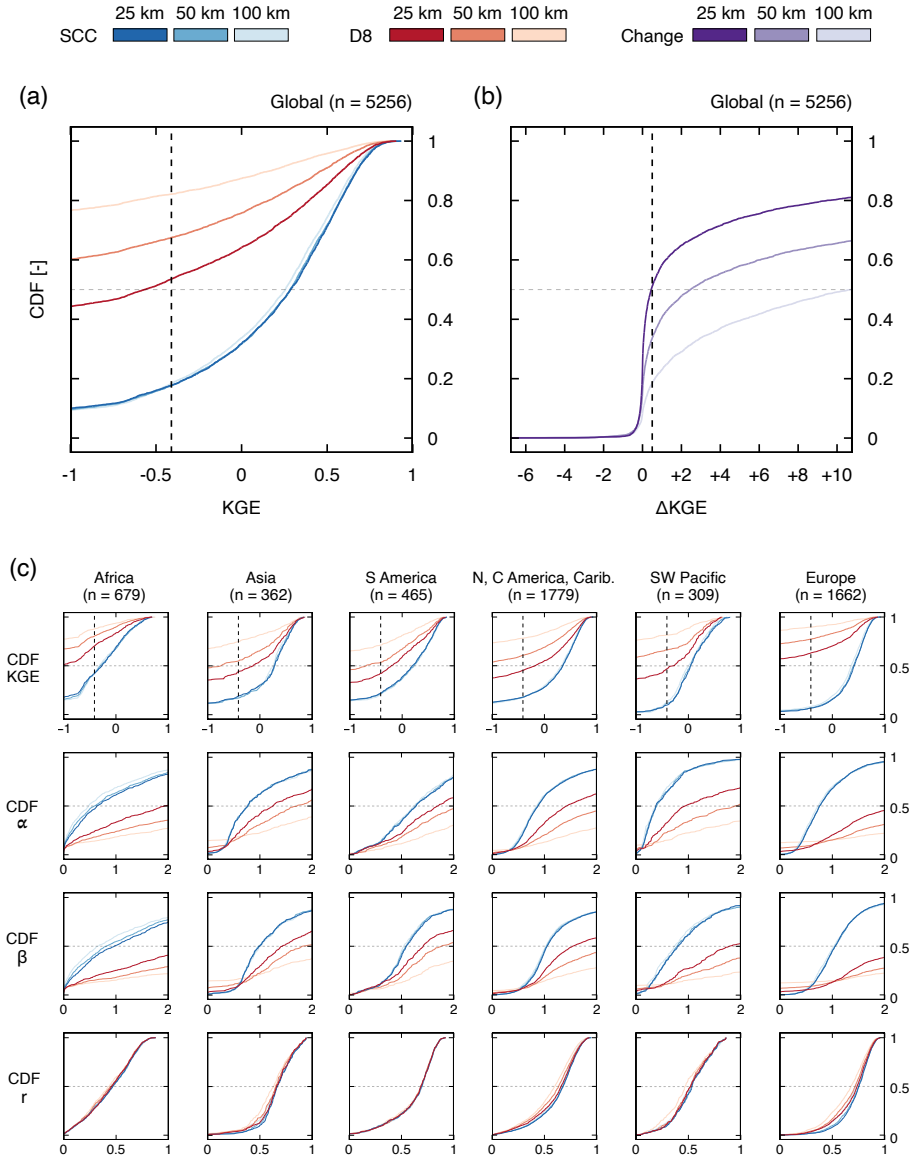


Figure B.4: CDFs comparing streamflow performance across 25 km to 100 km model resolutions, and subgrid stream network upscaling using SCC and D8, for the global experiment. (a) Global CDFs of KGE. (b) Global CDFs showing the corresponding improvements gained by using SCC instead of D8 (i.e., Δ KGE). (c) WMO region-wise CDFs for KGE and its components namely variability measure (α), bias (β), and correlation (r). The vertical lines in the CDFs for KGE correspond to the mean flow benchmark (KGE = -0.41). The vertical line in the panel (b) corresponds to Δ KGE = +0.5.

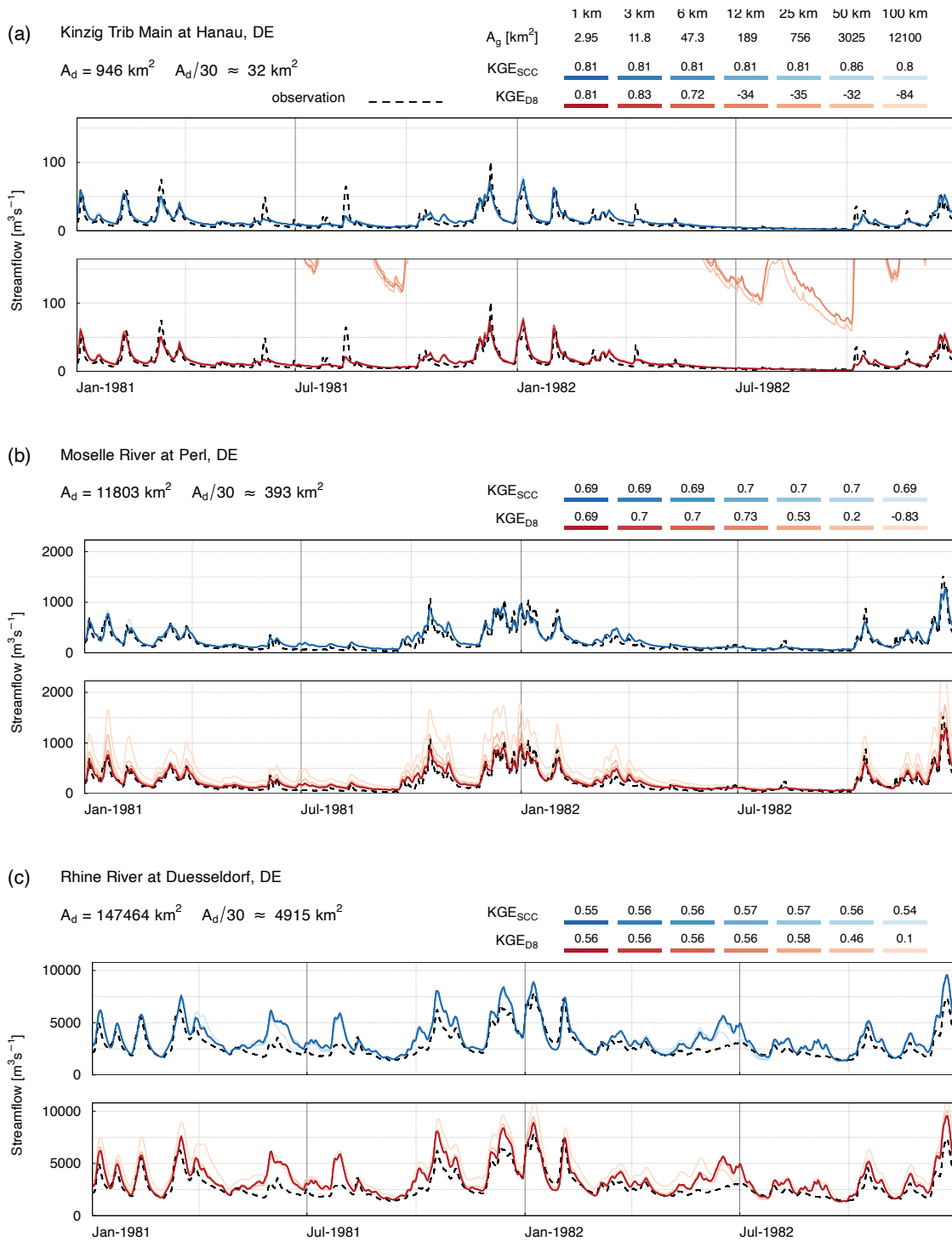


Figure B.5: Hydrographs resulting from SCC and D8 across 1 km to 100 km model resolutions at three different streamflow stations in the Rhine: (a) Kinzig River (tributary of the Main River) at Hanau, DE, (b) Moselle River at Pearl, DE, and (c) Rhine River at Düsseldorf, DE. A_d – DEM based catchment area, A_g – model grid size estimated at the equator. Note: The KGE values correspond to the full evaluation period (1961 – 2020) while the graph viewport zooms to the years 1981 – 1982.

APPENDIX C

This section includes the Appendix and the Supporting Information from the following publication:

Shrestha, P. K., Samaniego, L., Rakovec, O., Kumar, R., & Thober, S. (2024). Toward Improved Simulations of Disruptive Reservoirs in Global Hydrological Modeling. Water Resources Research, 60(4).

C.1 OVERALL ALGORITHM FOR MHM-LM

Algorithm 5 Overall Algorithm for mHM-LM

1. Estimate P_t as described in Sect. 4.2.2.
2. Estimate E_t as described in Sect. 4.2.2 and C.3.
3. Estimate L_t as described in Supplement S2.
4. Collect I_{t-1} from the routing model of mHM.
5. Estimate Q_t^b as described in Supplement S3.
6. Update G_t as described in Supplement S3.
7. Estimate Q_t^s as described in Supplement S4.
8. Estimate D_t^i , D_t^m , and D_t^l , if any, as described in Supplement S5.
9. Estimate Q_t^u using Eq. 4.11.
10. Use $D_t^n = \tilde{D}_t^n$ from Eq. C.17 as described in C.5 based on Random Forest.
11. Hedge the demand D_t^n to obtain \hat{D}_t^n using Eq. 4.6.
12. Adjust \hat{D}_t^n to obtain Q_t^n using Eq. 4.10.
13. Check whether Q_t^n can be fulfilled using Eq. 4.12.
14. Repeat steps 10–12 if D_t^i , D_t^m , and D_t^l are given to obtain Q_t^i , Q_t^m , and Q_t^l , respectively.
15. Solve V_t and A_t using Eq. 4.1 and hAV table as described in C.4.
16. Redistribute Q_t^i , Q_t^m , and Q_t^l , if any, as described in Supplement S5.
17. Estimate Q_t^d using Eq. 4.2.
18. Pass Q_t^d and Q_t^b to the routing model of mHM for further routing downstream.
19. Repeat 1–18 for all model time steps.
20. Optimize mHM and LM parameters for streamflow simulations at gauge location (Q^g), downstream of the reservoir, as described in Sect. 4.3.2.

C.2 LAKE MODULE PARAMETERS

Table C.1: Parameters of LM

Parameter	Process	Value			Reference
		Default	Lower bound	Upper bound	
ω	regulation	0.5	0	1	Eqn. 4.4
c^*	regulation	0.5	0.001	20	Eqn. 4.7
β	regulation	2	0.5	5	Eqn. 4.7
γ	regulation	0.85	0.6	0.95	Eqn. 4.9
λ	regulation	0.5	0.1	1	Eqn. 4.9
ζ	percolation	11	8	15	Supplement S2
\bar{Q}_b	baseflow	1	0.001	1000	Supplement S3
C_d	spill	3	2.64	3.95	Supplement S4

Note: The values for ω , c^* , β , and γ are taken from Sadki et al.

C.3 LAKE EVAPORATION

The lake evaporation (E) is estimated using an implementation of Penman-Monteith equation for potential evaporation (Shuttleworth, 1996):

$$E = \left(\frac{\Delta}{\Delta + \gamma} \right) (R_n + A_n) + \left(\frac{\gamma}{\Delta + \gamma} \right) \frac{\mu_0 (1 + \mu_1 U_2) (e_s - e)}{\lambda}, \quad (\text{C.1})$$

where, Δ is the slope of saturated vapor pressure versus temperature graph, γ is the psychrometric constant, λ is latent heat of vaporization of water, R_n is the net surface solar radiation, A_n is advection rate per unit area of lake, e_s is saturated vapor pressure, and e is ambient vapor pressure. U_2 is windspeed at 2 m above the lake surface and is a model input. This parameterization used the following empirical coefficients: $\mu_0 = 6.43$ and $\mu_1 = 0.536$

The expression for R_n and its components are:

$$\begin{aligned} R_n &= S_n + L_n \\ S_n &= S_i - \alpha S_i \\ L_n &= L_i - L_o \\ L_o &= \epsilon \sigma T^4, \end{aligned} \quad (\text{C.2})$$

where, S is shortwave radiation, L is longwave radiation and the subscripts n , i , and o denote net, incident and outgoing, respectively. The last expression of equation set C.2 is the Boltzmann's formulation where ϵ is the emissivity of water (0.96) and σ is Stefan-Boltzmann constant ($5.67 \times 10^{-8} \text{ W m}^{-2} \text{ K}^{-4}$). S_i and L_i are model inputs. α is the albedo i.e., reflectivity of still water.

The radiative term (first part) in equation C.1 is known to be larger than the aerodynamic term (second part). Shuttleworth mentions the factor by which the radiative term exceeds the aerodynamic term can range from 1.35 (arid locations) to as much as 3.84 (humid locations). The albedo or the reflectivity of water, α , in the radiative term thus has much significance. α depends on the position of the sun above the horizon i.e., the solar elevation angle, θ . θ varies with time of day, day of year and location on Earth. Figure C.1 shows how constant albedo assumptions such as Shuttleworth and Wanders et al. are inaccurate compared to measurements taken from Cogley. Fresnel equation shows good fit but overestimates α at lower values of θ . Here, we rather fit a Weibull type function on the measurements of Figure C.1 which gives α (%) as a function of θ (degrees):

$$\alpha = s \left[\frac{k}{\lambda} \left(\frac{\theta/10}{\lambda} \right)^{k-1} e^{-\left(\frac{\theta/10}{\lambda} \right)^k} \right] + c, \quad (\text{C.3})$$

where k and λ denote shape and scale parameters, respectively. Here the following values were adopted: $k = 1.517$, $\lambda = 1.236$, $s = 53.279$, and $c = 4.493$.

θ is a function of hour of the day, day of the year and latitude, the procedure to calculate which can be referred to from Cogley and Meeus. The expression for advection, A_h , in equation C.1 is:

$$A_h = \rho_w c_w (IT_i - Q_r T_o + PT_p), \quad (\text{C.4})$$

where, ρ_w is density of water and c_w is specific heat capacity of water. T is temperature while subscripts i , o and p denotes inflow, outflow and precipitation. Since temperature routing through reservoirs is not included in current version of mHM-LM, we consider all T_i , T_o and T_p to be equal to model input average daily air temperature, T . I denotes reservoir inflow, Q_r is the reservoir release, and P is precipitation on reservoir surface.

We refer to Tetten's formulations for calculating Δ , e_s and e in equation C.1:

$$\begin{aligned} \Delta &= \frac{\eta e_s}{e^{2 \log(T+\tau)}}, \\ e_s &= \eta e^{\left(\frac{\alpha T}{T+\tau} \right)}, \\ e &= \eta e^{\left(\frac{\alpha T_d}{T_d+\tau} \right)}, \end{aligned} \quad (\text{C.5})$$

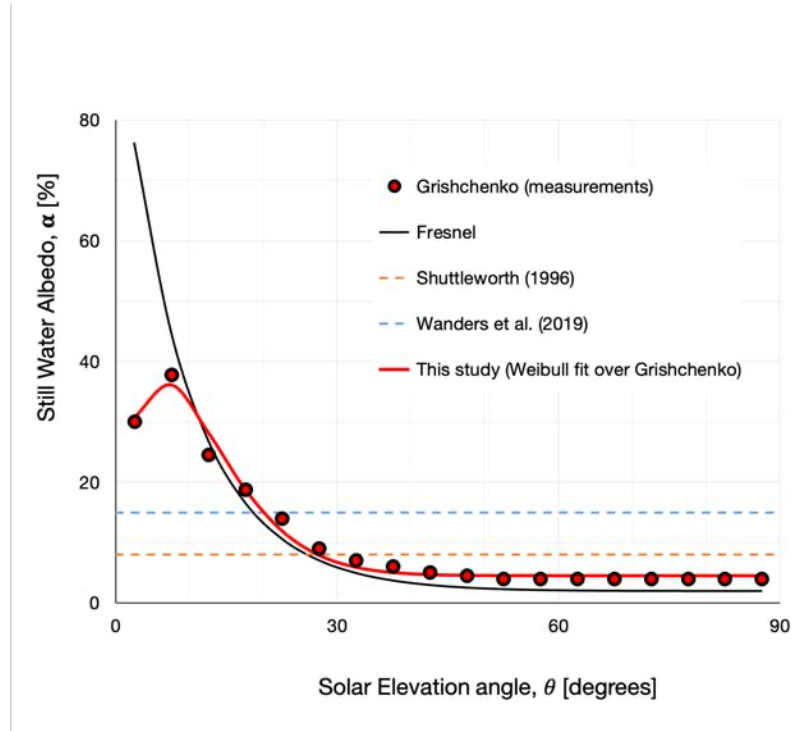


Figure C.1: Albedo of still water for reservoir evaporation. Grishchenko measurements taken from Cogley (1979)

where, $\eta = 0.61078$, $\tau = 237.3$, $\alpha = 17.27$. T_d is the dew point temperature which is a model input. Although λ and γ can be taken as constants, for global experiment such as this study, we opted to go with their temperature and altitude varying formulation (Shuttleworth, 1996):

$$\begin{aligned} \gamma &= \gamma_0 \frac{P}{\lambda}, \\ \lambda &= \beta_0 + \beta_1 T_s, \\ P &= \rho_0 \left(\frac{\zeta_0 + \zeta_1 z}{\zeta_0} \right)^\mu, \end{aligned} \tag{C.6}$$

where, P is atmospheric pressure, z is the altitude of the reservoir water surface, T_s is the temperature of reservoir water surface, assumed to be equal to model input average daily air temperature, T . This parameterization uses the following coefficients: $\gamma_0 = 0.0016286$, $\beta_0 = 2.501$, $\beta_1 = -0.002361$, $\rho_0 = 101.3$, $\zeta_0 = 293$, $\zeta_1 = -0.0065$, $\mu = 5.256$.

C.4 RESERVOIR WATER BALANCE SOLUTION

Algorithm 6 Reservoir Water Balance Solution

1. Given h_{t-1} , A_{t-1} , and V_{t-1} from previous time step ($t - 1$) in the lake model.
2. Set the initial conditions of the solver for states ($k - 1$) and ($k - 2$). Set $k = 1$ for the 1st iteration of the solver.

- a. Estimate h (*), A , V (**), $\Delta\hat{V}$

$$\begin{aligned}
 h_t^{(-1)} &= h_{t-1} - 0.02 & h_t^{(0)} &= h_{t-1} + 0.01 \\
 A_t^{(-1)} &= \text{hAV}(h_t^{(-1)}) & A_t^{(0)} &= \text{hAV}(h_t^{(0)}) \\
 V_t^{(-1)} &= \text{hAV}(h_t^{(-1)}) & V_t^{(0)} &= \text{hAV}(h_t^{(0)}) \\
 \Delta\hat{V}^{(-1)} &= V_t^{(-1)} - V_{t-1} & \Delta\hat{V}^{(0)} &= V_t^{(0)} - V_{t-1}
 \end{aligned} \tag{C.7}$$

- b. Estimate ΔV from Eq. 4.3

$$\Delta V^{(-1)} = f\left(A_t^{(-1)}\right) \Delta t \quad \Delta V^{(0)} = f\left(A_t^{(0)}\right) \Delta t \tag{C.8}$$

- c. Estimate the volume error, ϵ

$$\epsilon^{(-1)} = \Delta\hat{V}^{(-1)} - \Delta V^{(-1)} \quad \epsilon^{(0)} = \Delta\hat{V}^{(0)} - \Delta V^{(0)} \tag{C.9}$$

3. Repeat following steps, for $k = 1, 2, 3, \dots$ until $|\epsilon^{(k)}| \leq 1 \text{ m}^3$.

- a. Estimate $\Delta\hat{V}^{(k)}$ using secant method

$$\Delta\hat{V}^{(k)} = \Delta\hat{V}^{(k-1)} - \epsilon^{(k-1)} \frac{\Delta\hat{V}^{(k-1)} - \Delta\hat{V}^{(k-2)}}{\epsilon^{(k-1)} - \epsilon^{(k-2)}} \tag{C.10}$$

- b. Estimate $V_t^{(k)}$

$$V_t^{(k)} = \Delta\hat{V}^{(k)} + V_{t-1} \tag{C.11}$$

- c. Estimate $A_t^{(k)}$

$$A_t^{(k)} = \text{hAV}(V_t^{(k)}) \tag{C.12}$$

- d. Estimate ΔV from Eq. 4.3

$$\Delta V^{(k)} = f\left(A_t^{(k)}\right) \Delta t \tag{C.13}$$

Algorithm 6 (contd ...)

3. Contd ...

e. Estimate $\epsilon^{(k)}$

$$\epsilon^{(k)} = \Delta \hat{V}^{(k)} - \Delta V^{(k)} \quad (\text{C.14})$$

f. Update the following variables

$$\begin{aligned} \Delta V^{(k-2)} &= \Delta V^{(k-1)} \\ \Delta V^{(k-1)} &= \Delta V^{(k)} \\ \epsilon^{(k-2)} &= \epsilon^{(k-1)} \\ \epsilon^{(k-1)} &= \epsilon^{(k)} \end{aligned} \quad (\text{C.15})$$

4. Estimate h_t using solved V_t

$$h_t = \text{hAV}(V_t) \quad (\text{C.16})$$

Notes:

* We set small fluctuations for the first two iterations of the solver [($k - 2$) and ($k - 1$)] as initial conditions for the solver for every time step t . As a rule of thumb, we fix the elevation fluctuations to -2 and +1 cm respectively.

** $A_t^{(k)}$ and $V_t^{(k)}$ are estimated by linear interpolation in the hAV table using $h_t^{(k)}$.

C.5 RANDOM FOREST BASED PREDICTION OF NON-CONSUMPTIVE DEMAND

\tilde{D}_t^n is input for the mHM-LM regulation scheme (refer Sect. 4.2.4 and 4.2.5) which then estimates the model regulated non-consumptive outflow (Q_t^n).

C.6 ROUTING OF THE RESERVOIR OUTFLOW

The routing equation for a lake-node link i.e., reservoir/lake outflow follows Samaniego et al. (2010) and Thober et al. (2019) as shown below:

$$Q_t^o = Q_{t-1}^o + \nu_1 (Q_{t-1}^i - Q_{t-1}^o) + \nu_2 (Q_t^i - Q_{t-1}^i) \quad (\text{C.18})$$

Where Q^o is streamflow exiting the link, Q^i is streamflow entering the link, ν_1 and ν_2 are Muskingam-Cunge routing parameters regionalized in the stand-alone multiscale routing model, mRM (Thober et al., 2019) that is based on the techniques proposed in Samaniego et al. (2010) and later further developed and tested in Kumar et al. (2013).

Algorithm 7 Random Forest based Prediction of Non-consumptive Demand

1. Adjust $Q^{s,o}$ time series with the ratio of catchments at the gauge and the dam to estimate the hypothetical streamflow observations immediately after the dam (Q^d), for available years (m).
2. Estimate the times series of the predictors described above.
3. Repeat following steps until $\min(1000, C[m, m_t])$ iterations
 - a. Randomly segregate m years into two equal-sized groups, one for training (number of years = m_t) and one for testing.
 - b. Fit a RF model on the training data.
 - c. Test the performance (KGE) of the fitted RF on the testing data.
4. Select the RF model with best performance (KGE) during testing.
5. Prepare the RF model prediction time series ($Q^{d,RF}$) for the m years.
6. Inverse estimate the non-consumptive demand component from $Q^{d,RF}$, on-the-fly during model simulation, by rearranging Eq. 4.2 as

$$\tilde{D}_t^n = Q_t^{d,RF} - Q_t^s - Q_t^u - Q_t^b \quad (C.17)$$

C.7 PERCOLATION FROM RESERVOIR BOTTOM

The percolation, L_t [m/h], from a reservoir in mHM is calculated as -

$$L_t = \sum_{i=1}^n L_t^i \quad (C.19)$$

Where n is number of slices in the input hAV table (refer Figure C.2). L_t^i is the percolation at lake bed for slice i given by -

$$L_t^i = \kappa^p \kappa_t^c (h_{t-1} - \bar{h}_{t-1}^i) \Delta A_{t-1}^i / A_{t-1} \quad (C.20)$$

Where κ^p is the coefficient of percolation for lake bed. κ^c is a multiplier to control the height of percolation water. h_{t-1} [m a.s.l.] is the elevation of water surface and \bar{h}_{t-1}^i [m a.s.l.] is average elevation of the slice. ΔA_{t-1}^i [m²] is the area covered by the slice i , while A_{t-1} [m²] is the area of reservoir water surface.

L_t is based on reservoir depth and surface area from the previous time step as the reservoir states for the current time step will only be known after the water balance. κ^p is calculated using soil properties as predictors in a transfer function within MPR (Samaniego et al., 2010) in mHM. The multiplier κ_t^c is calculated as:

$$\kappa_t^c = (h_t - \bar{h}^b) / e^1 \quad (C.21)$$

Where \bar{h}^b is the average lake bed elevation and ι is a LM parameter that controls value of κ^c .

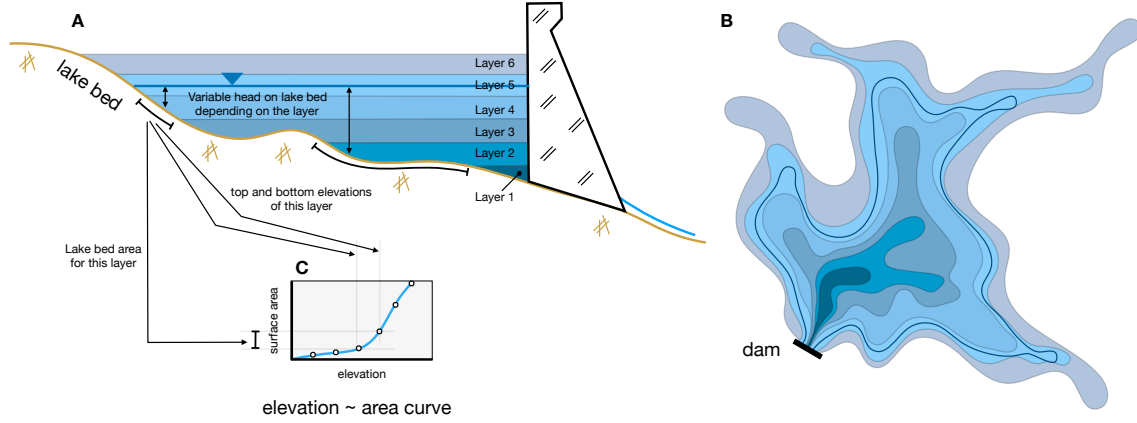


Figure C.2: Percolation in mHM

C.8 WATER BALANCE FOR AQUIFER STORAGE

The water balance equation for storage G underneath a reservoir in mHM is -

$$G_t = G_{t-1} + L_t - Q_t^b \tag{C.22}$$

Where, the shallow groundwater baseflow, Q^b , is calculated from G of previous time step -

$$Q_t^b = k_b G_{t-1} \tag{C.23}$$

Here, k_b is the baseflow recession coefficient (s^{-1}). Soil properties are used as predictors in a transfer function for calculating k_b within MPR (Samaniego et al., 2010) in mHM. G is initialized using equation C.23 -

$$G_1 = \bar{Q}_b / k_b \tag{C.24}$$

Here \bar{Q}_b [m^3/s] is long term baseflow from G and is a model parameter.

C.9 RESERVOIR SPILL

The reservoir spill, Q_t^s [m^3/s], is estimated using the following generalized spill equation:

$$Q_t^s = \begin{cases} 0, & h_{t-1} \leq h^d \\ \zeta (h_{t-1} - h^d)^{1.5}, & h_{t-1} > h^d \end{cases} \quad (\text{C.25})$$

Where h_{t-1} [m] is the elevation of reservoir water level and h^d [m] is the elevation of the dam crest level (DCL). The spill is based on reservoir elevation from the previous time step as the reservoir elevation for the current time step will only be known after the reservoir water balance. ζ is calculated as (USBR, 2011) -

$$\zeta = C_d L_s \quad (\text{C.26})$$

C_d is the coefficient of discharge and L_s [m] is the effective spillway length. We approximated the value of L_s from Google Earth. C_d is a LM parameter. We looked for smallest and largest values of C_d in the literature. We found broad-crested weirs to have the smallest value of 2.64 (USBR, 2011) and 3.95 as maximum value attainable for ogee-shaped weirs (USBR, 1997). We used these values to set bounds of C_d during optimization.

C.10 CONSUMPTIVE WATER USE AT RESERVOIR

At this stage, the mHM-LM does not include an internal water demand model for consumptive use i.e., irrigation, domestic, and industrial use. Therefore, the user must input the consumptive demand either measured or estimated. If consumptive demand is provided as gridded input, the model calculates the domestic demand (D_t^m) [m³/s], industrial demand (D_t^l) [m³/s] and irrigation demand (D_t^i) [m³/s] for current time step by area weighing the input demand grids overlaying the delineated reservoir service area mask. To delineate the reservoir service area mask, LM selects the pixels downstream of the reservoir within an input supply service distance (Note: Sadki et al. (2023) optimizes this service distance for each reservoir). If a downstream reservoir is within the supply service distance of the upstream reservoir, the upstream reservoir's service area is limited to the water divide between the two reservoirs.

mHM-LM uses D_t^i , D_t^m , and D_t^l to estimate the irrigation consumptive outflow (Q_t^i [m³/s]), domestic supply (Q_t^m [m³/s]), and industrial supply (Q_t^l [m³/s]), respectively. Q_t^i , Q_t^m , and Q_t^l are then redistributed to the reservoir service area. If the input consumptive demand was gridded, Q_t^i , Q_t^m , and Q_t^l are redistributed using the reservoir service area mask as overlay, weighed by the grid demand values. If the input consumptive demand was point time series, Q_t^i is redistributed using the reservoir service area mask as overlay, weighed by input irrigation areas map. In case of Q_t^m , and Q_t^l , the weights are generated from input population density map. The irrigation areas map and the population density map were prepared from globally available datasets (refer Table S2). The redistributed

irrigation outflow¹ is incorporated as additional precipitation at model grids (ℓ_1) where it undergoes water balance processes. In other words, the soil moisture located in the agricultural areas will be watered with constant rates over the vegetation growing season. Future versions of this module will implement irrigation scheduling and soil moisture validation capabilities using field-scale soil moisture sensors (e.g., cosmic-ray neutron rover surveys (Schrön et al., 2018)). The redistributed domestic outflow² skips the water balance and gets directly routed by mRM to mimic the reservoir-to-household-to-river movement of domestic return flow.

C.11 INFORMATION ON RESERVOIRS USED IN THE EXPERIMENT

¹ Assuming 50% conveyance and application losses (FAO, 1989)

² Assuming 30% return flow. Similar return fractions are used in Wada et al. (2011), Wada et al. (2014), and Shrestha et al. (2017)

Gtand id	Reservoir impounding Dam	River	Gauge GRDC	Q start	Q end	Co.	Comm. Year	Main use	Lon degree	Lat degree	V_f $\times 10^6 \text{m}^3$	A_f $\times 10^6 \text{m}^2$	A_c $\times 10^6 \text{m}^2$	c	c' $\times 10^{-3} \text{m}$
15	Kenney	Nechako	4207160	1915	2015	CA	1952	H	-124.95	53.58	23800	839.1	13971	6.986	1703.5
245	Brazeau Dam	Brazeau	4213375	1956	2015	CA	1962	H	-115.58	52.97	490	39.49	5593	0.350	87.6
256	Ghost	Bow	4213043	1983	2012	CA	1929	H	-114.71	51.21	132	10.96	6459	0.061	20.4
297	Libby	Kootenai	4115320	1910	1991	US	1973	H	-115.31	48.41	7434.2	163.81	23324	0.784	318.7
315	Post Falls Middle Channel	Spokane	4115403	1913	2017	US	1906	H	-116.95	47.71	277.5	125.54	9853	0.052	28.2
706	Whitesand Rapids	Reindeer	4214285	1985	2016	US	1942	H	-103.15	56.23	14860	5435.48	62727	1.258	236.9
731	Kettle Falls	Namakan	4213210	1905	2015	US	1914	R	-93.36	48.62	866.5	826.48	38038	0.088	22.8
907	Coralville Dam	Iowa	4119251	1903	2017	US	1958	FC	-91.53	41.73	568.9	13.37	8039	0.293	70.8
911	Red Rock Dam	Des Moines	4119280	1903	2017	US	1969	FC	-92.98	41.37	2171.4	59.05	32113	0.518	67.6
965	Tuttle Creek Dam	Big Blue	4122201	1950	2017	US	1962	FC	-96.59	39.26	2784	42.87	24711	2.171	112.7
1148	White River Dam	White	4150507	1924	2017	US	1963	FC	-101.09	33.46	98.7	3.49	7573	2.304	13.0
1207	Ross Barnett Reservoir	Pearl	4149122	1901	2017	US	1965	R	-90.06	32.40	4206.2	89.1	7814	1.050	538.3
1399	Little Long	Mattagami	4214551	1983	2015	US	1963	H	-82.17	50.00	357.6	14.44	34250	0.033	10.4
1477	Swift Rapids	Severn	4234300	1953	2016	US	1917	H	-79.54	44.86	50	1.1	5791	0.048	8.6
1480	Du Bay	Wisconsin	4119452	1914	2016	US	1942	H	-89.65	44.67	164.1	19.33	12824	0.047	12.8
1493	Neenah	Fox	4133200	1917	2013	US	1922	FC	-88.45	44.19	1356.8	645.53	15195	0.367	89.3
1556	Twin Branch	St. Joseph	4133500	1930	2016	US	1903	H	-86.13	41.67	12	2.85	8700	0.004	1.4
1563	Collins Station Cooling Lake Dam	Illinois	4119401	1981	2017	US	1975	O	-88.37	41.36	36.5	7.42	17978	0.006	2.0
1866	Saluda	Saluda	4148535	1925	2017	US	1930	H	-81.22	34.05	2713.7	180.93	6274	2.395	432.5
1919	Rodman Dam and Spillway	Oklawaha	4148555	1968	2017	US	1968	N	-81.81	29.51	160.4	18.56	7315	0.188	21.9
2363	Balbina	Uatuma	3628401	1977	1996	BR	1987	H	-59.48	-1.91	17533	2304.63	18895	1.352	927.9
2375	Trés Marias	São Francisco	*	1957	2006	BR	1962	H	-45.27	-18.22	21000	799.76	50953	1.011	412.1
2534	Itapebi	Jequitinhonha	3652455	1936	2010	BR	2003	H [†]	-39.59	-15.97	2720	60.99	68026	0.262	40.0
2538	Mascarenhas	Doce	3652600	1967	1994	BR	1972	H [†]	-40.92	-19.50	51.8	5.4	74085	0.002	0.7
3044	Buyo	Sassandra	1427500	1970	1996	IC	1980	H	-7.04	6.24	8300	509.2	47871	0.944	173.4
3195	Rappbode	Rappbode	*	1981	2018	DE	1959	WS	10.89	51.74	109.1	2.3	116	4.230	940.5
3373	Genissiat	Rhone	6139391	1920	1992	FR	1948	H	5.81	46.05	56	3.33	10878	0.006	5.1
3683	Virdnejavri	Alta	6731920	1971	2015	NO	1987	H	23.82	69.70	140	6.75	7655	0.091	18.3
3732	Melo	Kokemaenjoki	6854100	1931	1992	FI	1971	H	23.53	61.46	699	121.91	8379	0.152	83.4
4348	Serebrianka 1	Voroniya	6971401	1960	2004	RU	1970	H	35.57	68.82	4170	201.45	8377	1.279	497.8
4349	Verkhne-Tulomskaya	Tuloma	6971130	1935	2011	RU	1965	H	31.74	68.61	11520	585.33	17412	1.858	661.6
5136	Nam Ngum	Nam Ngum	2469141	1966	1994	LA	1972	H	102.55	18.53	7030	436.93	8308	0.846	846.2

where, H - hydropower, R - recreation, FC - flood control, O - others, N - navigation, WS - water supply

Co. - country, Comm. year - commissioned year

* gauge from local authorities

† is information from Wikipedia

source: Gtand v1.3 (Lehner et al., 2011) except for Gauge grdc ID and c'

C.12 DATA SOURCES

Data Type	Dataset name	Processed Resolution	Author, Source
Dam coordinates and salient features	GRanD v1.3	point, -	Lehner et al. (2011)
Reservoir bathymetry (Y2018)	ReGeom	point, -	Yigzaw et al. (2018)
Surveyed Reservoir bathymetry (Texas)	-	point, -	Texas Water Development Board http://www.twdb.texas.gov/surfacewater/surveys/completed/list/index.asp
Streamflow observations	GRDC	point, daily	The Global Runoff Data Centre http://www.bafg.de/\ac{GRDC}/
DEM (+ derivatives)	Global Multi-resolution Terrain Elevation Data (GMTED2010)	1/512°, static	USGS and NGA (2018)
Soil	SoilGrids	1/512°, static	ISRIC - World Soil Information (2017)
Geology	Global Lithological Map (GLiM)	1/512°, static	Hartmann and Moosdorf (2012)
Land cover	Global Land Cover (GlobCover)	1/512°, static	European Space Agency (ESA), Universit Catholique de Louvain (2009)
LAI	Global Inventory Modeling and Mapping Studies (GIMMS)	1/512°, monthly climatology	Tucker et al. (2004)
P, T, U_2, L_i, S_i, T_d	ERA5	0.25°, daily	Copernicus Climate Change Service (2017)
Irrigation areas	Global Map of Irrigation Areas (GMIA) v5	1/512°, static	Siebert et al. (2005)
Population density	Gridded Population of the World (GPW) v4, year 2000	1/512°, static	Center for International Earth Science Information Network (CIESIN)

C.13 DERIVATION OF BATHYMETRIC RELATIONSHIPS FOR HALF OF PYRAMID WITH SQUARE BASE

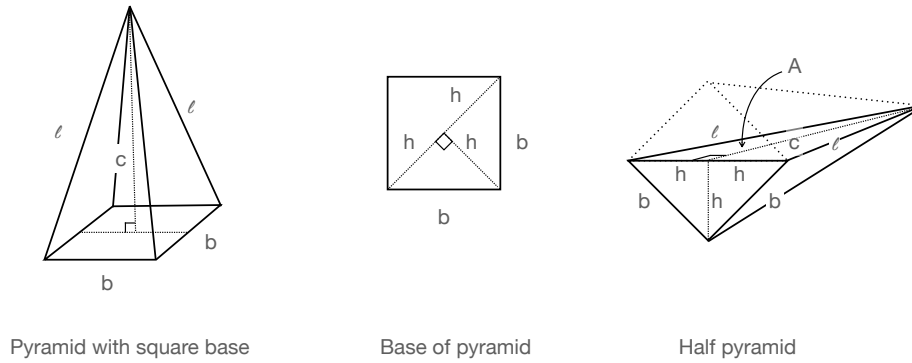


Figure C.3: Schematics for half pyramid

Let us consider a pyramid of height h , having a square base with edges b as shown in Figure C.3. The volume of the full pyramid, V_p , is given by -

$$V_p = \frac{1}{3} b^2 c \quad (\text{C.27})$$

Here b can be replaced by $h\sqrt{2}$.

$$V_p = \frac{2}{3} h^2 c \quad (\text{C.28})$$

The volume of half pyramid, V , would then be half of V_p -

$$V = \frac{1}{3} h^2 c \quad (\text{C.29})$$

The half pyramid, which is cut diagonally at the square base, can be an approximation of reservoir shape. Here, ℓ is known as the characteristic length and is expressed f times depth i.e., $f h$. Expressing c in terms of h and ℓ , V further reduces to -

$$V = \frac{1}{3} h^2 \sqrt{\ell^2 - h^2} \quad (\text{C.30})$$

$$= \frac{1}{3} h^2 \sqrt{f^2 h^2 - h^2} \quad (\text{C.31})$$

$$= \frac{1}{3} h^3 \sqrt{f^2 - 1} \quad (\text{C.32})$$

Similarly, the surface area A can be derived in terms of h and f as -

$$A = \frac{1}{2} 2h c \quad (\text{C.33})$$

$$= h\sqrt{\ell^2 - h^2} \quad (\text{C.34})$$

$$= h\sqrt{f^2 h^2 - h^2} \quad (\text{C.35})$$

$$= h^2\sqrt{f^2 - 1} \quad (\text{C.36})$$

Substituting A into expression of V, we get -

$$V = \frac{1}{3} h A \quad (\text{C.37})$$

When maximum values of V and A are known, maximum depth is obtained from equation C.37. Once maximum depth is known, f can be determined using either equation C.32 or C.36. Thereafter, equations C.32 and C.36 work as hAV or bathymetric relationship for the reservoir shape.

C.14 PERFORMANCE EVALUATION AT TRES MARIAS

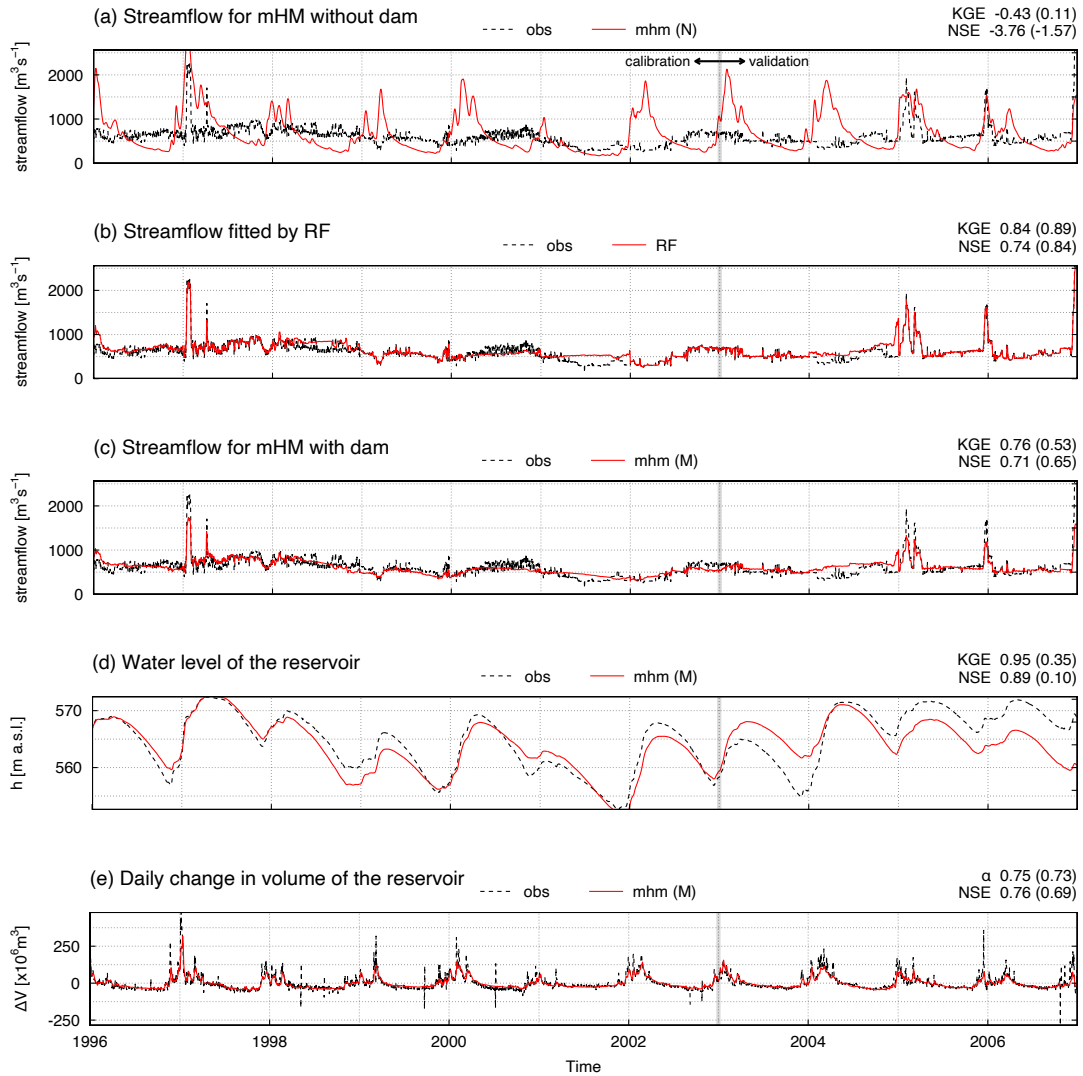


Figure C.4: Performance evaluation of RF and mHM simulations at Três Marias reservoir. Rows 1 to 3 show streamflow downstream of reservoir in mHM without dam (N), $Q^{d,RF}$ fitted by random forest (RF), and mHM with dam (M), respectively. Rows 4 and 5 show performance of reservoir water level and incremental volume simulations, respectively. The performance metrics for calibration is followed by those for validation in parentheses.

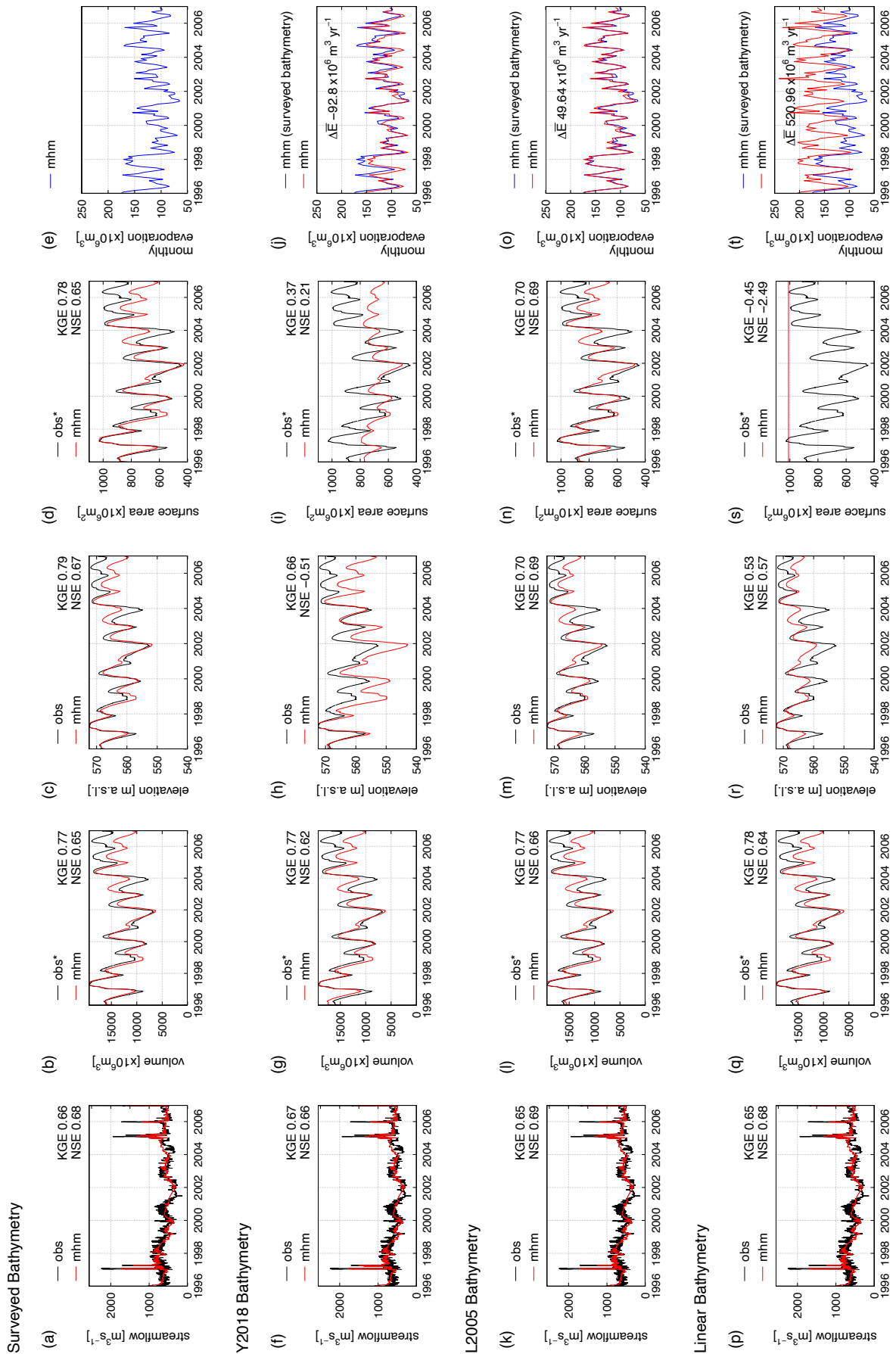


Figure C.5: Sensitivity of reservoir shape on streamflow, volume, elevation, surface area and evaporation for Três Marias reservoir.

C.15 SENSITIVITY OF RESERVOIR SHAPE AT TRES MARIAS

C.16 hv PLOTS COMPARING THE SURVEYED BATHYMETRY TO SHAPE APPROXIMATIONS

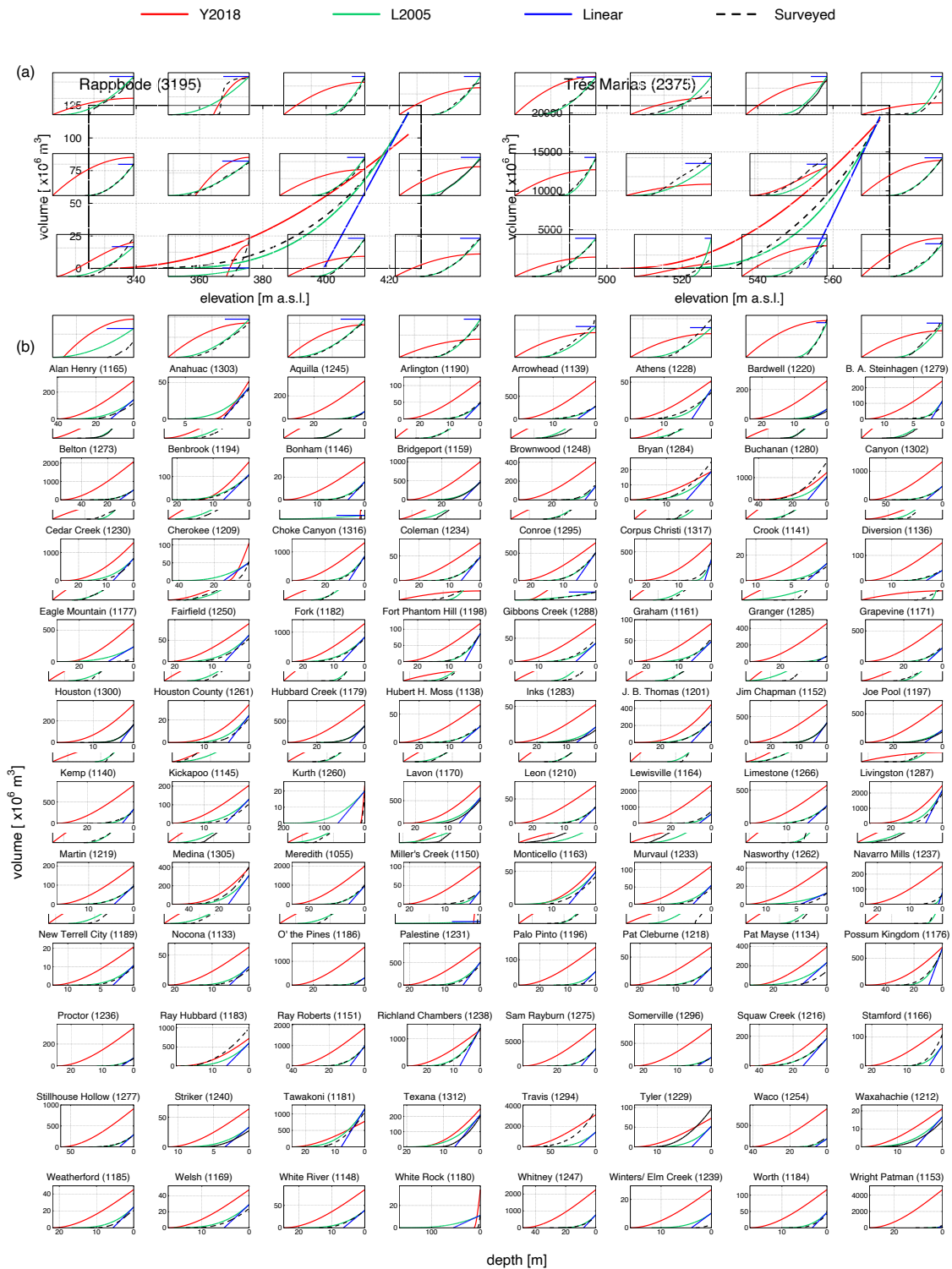


Figure C.6: hV plots comparing the surveyed bathymetry to Y₂₀₁₈, L₂₀₀₅ and Linear shape approximations at (a) H-reservoirs, and (b) 88 Texan reservoirs. The title of individual plot displays the name of the reservoir with GRanD ID in the parentheses. The corresponding figure for hA plots are provided in Figure 8.

BIBLIOGRAPHY

- Adams, Thomas E and Thomas Pagano (2016). *Flood forecasting: A global perspective*. Academic Press.
- Adhikari, Tirtha Raj et al. (Sept. 2023). "Evaluation of Post Extreme Floods in High Mountain Region: A Case Study of the Melamchi Flood 2021 at the Koshi River Basin in Nepal." In: *Natural Hazards Research* 3.3, pp. 437–446. ISSN: 2666-5921. DOI: [10.1016/j.nhres.2023.07.001](https://doi.org/10.1016/j.nhres.2023.07.001). (Visited on 09/06/2024).
- Adobe Stock (n.d.). *Kedarnath temple aerial view after Kedarnath Disaster 2013. Heavy loss to people & property happened. Worst Disaster.landslide, flood, cloudburst in india Stock-Foto*. URL: <https://stock.adobe.com/de/images/kedarnath-temple-aerial-view-after-kedarnath-disaster-2013-heavy-loss-to-people-property-happened-worst-disaster-landslide-flood-cloudburst-in-india/376219171> (visited on 09/26/2024).
- Aerts, Jerom P. M. et al. (Aug. 2022). "Large-Sample Assessment of Varying Spatial Resolution on the Streamflow Estimates of the Wflow_sbm Hydrological Model." In: *Hydrology and Earth System Sciences* 26.16, pp. 4407–4430. ISSN: 1027-5606. DOI: [10.5194/hess-26-4407-2022](https://doi.org/10.5194/hess-26-4407-2022). (Visited on 03/22/2024).
- AghaKouchak, Amir et al. (Mar. 2015). "Aral Sea Syndrome Desiccates Lake Urmia: Call for Action." In: *Journal of Great Lakes Research* 41.1, pp. 307–311. ISSN: 0380-1330. DOI: [10.1016/j.jglr.2014.12.007](https://doi.org/10.1016/j.jglr.2014.12.007). (Visited on 09/25/2024).
- Ajmar, Andrea et al. (2017). "Response to flood events: The role of satellite-based emergency mapping and the experience of the Copernicus emergency management service." In: *Flood damage survey and assessment: New insights from research and practice*, pp. 211–228.
- Al-Khalidi, Mohammad M. et al. (Sept. 2021). "Inland Water Body Mapping Using CYGNSS Coherence Detection." In: *IEEE Transactions on Geoscience and Remote Sensing* 59.9, pp. 7385–7394. ISSN: 1558-0644. DOI: [10.1109/TGRS.2020.3047075](https://doi.org/10.1109/TGRS.2020.3047075). (Visited on 12/15/2023).
- Alcamo, Joseph et al. (June 2003). "Development and Testing of the WaterGAP 2 Global Model of Water Use and Availability." In: *Hydrological Sciences Journal* 48.3, pp. 317–337. ISSN: 0262-6667. DOI: [10.1623/hysj.48.3.317.45290](https://doi.org/10.1623/hysj.48.3.317.45290). (Visited on 04/09/2024).
- Alfieri, Lorenzo et al. (2013). "GloFAS—global ensemble streamflow forecasting and flood early warning." In: *Hydrology and Earth System Sciences* 17.3, pp. 1161–1175.
- Alfieri, Lorenzo et al. (2019). "Range-dependent thresholds for global flood early warning." In: *Journal of Hydrology X* 4, p. 100034.
- Amma (Sept. 2013). *50-Crore Relief and Rehabilitation Package for Uttarakhand*. URL: <https://www.amritapuri.org/16760/uttarakhand.aum> (visited on 09/26/2024).

- Anderson, Cheryl L et al. (2022). "Connecting forecast and warning: a partnership between communicators and scientists." In: *Towards the "Perfect" Weather Warning: Bridging Disciplinary Gaps through Partnership and Communication*. Springer International Publishing Cham, pp. 87–113.
- Andreadis, Konstantinos M. et al. (Sept. 2022). "Urbanizing the Floodplain: Global Changes of Imperviousness in Flood-Prone Areas." In: *Environmental Research Letters* 17.10, p. 104024. ISSN: 1748-9326. DOI: [10.1088/1748-9326/ac9197](https://doi.org/10.1088/1748-9326/ac9197). (Visited on 09/27/2024).
- Apel, Heiko et al. (2022). "Brief communication: Impact forecasting could substantially improve the emergency management of deadly floods: case study July 2021 floods in Germany." In: *Natural Hazards and Earth System Sciences* 22.9, pp. 3005–3014.
- BGR (2020). *Digital soil map of Germany 1 : 200, 000 (BUEK 200) vo.5*. https://www.bgr.bund.de/DE/Themen/Boden/Informationsgrundlagen/Bodenkundliche_Karten-Datenbanken/BUEK200/buek200_node.html.
- Bacalhau, José Ráurium et al. (June 2022). "Bathymetry of Reservoirs Using Altimetric Data Associated to Optical Images." In: *Advances in Space Research* 69.11, pp. 4098–4110. ISSN: 0273-1177. DOI: [10.1016/J.ASR.2022.03.011](https://doi.org/10.1016/J.ASR.2022.03.011).
- Bachmair, Sophie et al. (Nov. 2017). "Developing Drought Impact Functions for Drought Risk Management." In: *Natural Hazards and Earth System Sciences* 17.11, pp. 1947–1960. ISSN: 1561-8633. DOI: [10.5194/nhess-17-1947-2017](https://doi.org/10.5194/nhess-17-1947-2017). (Visited on 11/28/2023).
- Bahra, Avi (Oct. 2011). "Managing work flows with ecFlow." In: *ECMWF Newsletter* 129, pp. 30–32. DOI: [10.21957/nr843dob](https://doi.org/10.21957/nr843dob). URL: <https://www.ecmwf.int/en/eLibrary/80182-managing-work-flows-ecflow>.
- Baker, Victor R. (May 2009). "The Channeled Scabland: A Retrospective." In: *Annual Review of Earth and Planetary Sciences* 37.1, pp. 393–411. ISSN: 0084-6597, 1545-4495. DOI: [10.1146/annurev.earth.061008.134726](https://doi.org/10.1146/annurev.earth.061008.134726). (Visited on 09/03/2024).
- Bartels, H et al. (2004). "Zusammenfassender Abschlussbericht zum Projekt RADOLAN." In: *Deutscher Wetterdienst, Offenbach*.
- Bates, P. D and A. P. J De Roo (Sept. 2000). "A Simple Raster-Based Model for Flood Inundation Simulation." In: *Journal of Hydrology* 236.1, pp. 54–77. ISSN: 0022-1694. DOI: [10.1016/S0022-1694\(00\)00278-X](https://doi.org/10.1016/S0022-1694(00)00278-X). (Visited on 09/16/2024).
- Bates, P D et al. (Sept. 1995). "Initial Comparison of Two Two-Dimensional Finite Element Codes for River Flood Simulation." In: *Proceedings of the Institution of Civil Engineers - Water, Maritime and Energy* 112.3, pp. 238–248. ISSN: 0965-0946. DOI: [10.1680/iwtme.1995.27886](https://doi.org/10.1680/iwtme.1995.27886). (Visited on 09/16/2024).
- Bates, P D et al. (Sept. 1998). "Internal and External Validation of a Two-Dimensional Finite Element Code for River Flood Simulations." In: *Proceedings of the Institution of Civil Engineers - Water, Maritime and Energy* 130.3, pp. 127–141. ISSN: 0965-0946. DOI: [10.1680/iwtme.1998.30972](https://doi.org/10.1680/iwtme.1998.30972). (Visited on 09/16/2024).
- Bates, Paul D (2022). "Flood inundation prediction." In: *Annual Review of Fluid Mechanics* 54, pp. 287–315. DOI: <https://doi.org/10.1146/annurev-fluid-030121-113138>.

- Bates, Paul (2023). "Fundamental limits to flood inundation modelling." In: *Nature Water* 1.7, pp. 566–567.
- Bauer, Peter et al. (2015). "The quiet revolution of numerical weather prediction." In: *Nature* 525.7567, pp. 47–55.
- Bauer, Peter et al. (Feb. 2021). "A Digital Twin of Earth for the Green Transition." In: *Nature Climate Change* 2021 11:2 11.2, pp. 80–83. ISSN: 1758-6798. DOI: [10.1038/s41558-021-00986-y](https://doi.org/10.1038/s41558-021-00986-y).
- Baumgartner, A and E Reichel (1975). 1975: *The World Water Balance: Mean Annual Global Continental and Maritime Precipitation, Evaporation and Runoff*. Amsterdam: Elsevier.
- Beer, Tom et al. (2018). *Global Change and Future Earth: The Geoscience Perspective*. Vol. 3. Cambridge University Press.
- Bertola, Miriam et al. (2023). "Megafloods in Europe can be anticipated from observations in hydrologically similar catchments." In: *Nature Geoscience*, pp. 1–7.
- Beven, Keith et al. (Jan. 2015). "Hyperresolution Information and Hyperresolution Ignorance in Modelling the Hydrology of the Land Surface." In: *Science China Earth Sciences* 58.1, pp. 25–35. ISSN: 16747313. DOI: [10.1007/S11430-014-5003-4/METRICS](https://doi.org/10.1007/S11430-014-5003-4/METRICS).
- Bhatt, C. M. et al. (Dec. 2011). "Potential of High Resolution Satellite Data for Disaster Management: A Case Study of Leh, Jammu & Kashmir (India) Flash Floods, 2010." In: *Geomatics, Natural Hazards and Risk* 2.4, pp. 365–375. ISSN: 1947-5705. DOI: [10.1080/19475705.2011.580014](https://doi.org/10.1080/19475705.2011.580014). (Visited on 09/09/2024).
- Biella, Riccardo et al. (Aug. 2024). *The 2022 Drought Needs to Be a Turning Point for European Drought Risk Management*. DOI: [10.5194/egusphere-2024-2069](https://doi.org/10.5194/egusphere-2024-2069). (Visited on 09/25/2024).
- Biemans, H. et al. (Mar. 2011). "Impact of Reservoirs on River Discharge and Irrigation Water Supply during the 20th Century." In: *Water Resources Research* 47.3. ISSN: 00431397. DOI: [10.1029/2009WR008929](https://doi.org/10.1029/2009WR008929).
- Bierkens, Marc F. P. (2015). "Global Hydrology 2015: State, Trends, and Directions." In: *Water Resources Research* 51.7, pp. 4923–4947. ISSN: 1944-7973. DOI: [10.1002/2015WR017173](https://doi.org/10.1002/2015WR017173). (Visited on 04/09/2024).
- Bierkens, Marc F. P. et al. (2015a). "Hyper-Resolution Global Hydrological Modelling: What Is next? "Everywhere and Locally Relevant"." In: *Hydrological processes* 29.2, pp. 310–320.
- Bierkens, Marc F.P. et al. (Jan. 2015b). "Hyper-Resolution Global Hydrological Modelling: What Is Next?" In: *Hydrological Processes* 29.2, pp. 310–320. ISSN: 1099-1085. DOI: [10.1002/HYP.10391](https://doi.org/10.1002/HYP.10391).
- Bjornstad, Bruce Norman (Feb. 2021). *Ice Age Floodscapes of the Pacific Northwest: A Photographic Exploration*. Springer Nature. ISBN: 978-3-030-53043-3.
- Bjornstad, Bruce (2006). "On the Trail of the Ice Age Floods: A Geological Field Guide to the Mid-Columbia Basin." In: *(No Title)*. (Visited on 09/03/2024).

- Boeing, F. et al. (2022). "High-resolution drought simulations and comparison to soil moisture observations in Germany." In: *Hydrology and Earth System Sciences* 26.19, pp. 5137–5161. DOI: [10.5194/hess-26-5137-2022](https://doi.org/10.5194/hess-26-5137-2022).
- Boelee, Leonore et al. (2019). "Estimation of uncertainty in flood forecasts—A comparison of methods." In: *Journal of Flood Risk Management* 12, e12516.
- Booth, Andrew Donald (1966). *Numerical Methods*. Butterworths.
- Bout, Bastian Van den et al. (2023). "A breakthrough in fast flood simulation." In: *Environmental Modelling & Software* 168, p. 105787.
- Breiman, Leo (Oct. 2001). "Random Forests." In: *Machine Learning* 45.1, pp. 5–32. ISSN: 08856125. DOI: [10.1023/A:1010933404324/METRICS](https://doi.org/10.1023/A:1010933404324/METRICS).
- Bretz, J. Harlen (Nov. 1923). "The Channeled Scablands of the Columbia Plateau." In: *The Journal of Geology* 31.8, pp. 617–649. ISSN: 0022-1376. DOI: [10.1086/623053](https://doi.org/10.1086/623053). (Visited on 09/03/2024).
- Brocca, Luca et al. (Dec. 2018). "How Much Water Is Used for Irrigation? A New Approach Exploiting Coarse Resolution Satellite Soil Moisture Products." In: *International Journal of Applied Earth Observation and Geoinformation* 73, pp. 752–766. ISSN: 1569-8432. DOI: [10.1016/j.jag.2018.08.023](https://doi.org/10.1016/j.jag.2018.08.023). (Visited on 12/11/2023).
- Brunner, Manuela Irene and Philippe Naveau (2023). "Spatial Variability in Alpine Reservoir Regulation: Deriving Reservoir Operations from Streamflow Using Generalized Additive Models." In: *Hydrol. Earth Syst. Sci* 27, pp. 673–687. DOI: [10.5194/hess-27-673-2023](https://doi.org/10.5194/hess-27-673-2023).
- Burek, P. et al. (2013). *LISFLOOD - Distributed Water Balance and Flood Simulation Model - Revised User Manual*. Tech. rep. Joint Research Centre, Institute for Environment and Sustainability, European Commission.
- Burek, Peter and Mikhail Smilovic (Dec. 2023). "The Use of GRDC Gauging Stations for Calibrating Large-Scale Hydrological Models." In: *Earth System Science Data* 15.12, pp. 5617–5629. ISSN: 1866-3508. DOI: [10.5194/essd-15-5617-2023](https://doi.org/10.5194/essd-15-5617-2023). (Visited on 04/09/2024).
- Burek, Peter et al. (July 2020). "Development of the Community Water Model (CWatM v1.04) - A High-Resolution Hydrological Model for Global and Regional Assessment of Integrated Water Resources Management." In: *Geoscientific Model Development* 13.7, pp. 3267–3298. ISSN: 19919603. DOI: [10.5194/gmd-13-3267-2020](https://doi.org/10.5194/gmd-13-3267-2020).
- Campbell, R et al. (2018). "Impact-based forecasting and warning: Weather ready nations." In: *WMO Bulletin* 67.2, pp. 10–13.
- Carreno-Luengo, Hugo et al. (Feb. 2024). "Detection of Inland Water Bodies under Dense Biomass by CYGNSS." In: *Remote Sensing of Environment* 301, p. 113896. ISSN: 0034-4257. DOI: [10.1016/j.rse.2023.113896](https://doi.org/10.1016/j.rse.2023.113896). (Visited on 12/15/2023).
- Casado, Ana et al. (2013). "Influence of Dam-induced Hydrological Regulation on Summer Water Temperature: Sauce Grande River, Argentina." In: *Ecohydrology : ecosystems, land and water process interactions, ecohydrogeomorphology*. DOI: [10.1002/eco.1375](https://doi.org/10.1002/eco.1375).

- Champati Ray, P. K. et al. (Mar. 2016). "Kedarnath Disaster 2013: Causes and Consequences Using Remote Sensing Inputs." In: *Natural Hazards* 81.1, pp. 227–243. ISSN: 1573-0840. DOI: [10.1007/s11069-015-2076-0](https://doi.org/10.1007/s11069-015-2076-0). (Visited on 09/09/2024).
- Chaney, Nathaniel W. et al. (Nov. 2021). "HydroBlocks v0.2: Enabling a Field-Scale Two-Way Coupling between the Land Surface and River Networks in Earth System Models." In: *Geoscientific Model Development* 14.11, pp. 6813–6832. ISSN: 1991-959X. DOI: [10.5194/gmd-14-6813-2021](https://doi.org/10.5194/gmd-14-6813-2021). (Visited on 03/20/2024).
- Chen, Tan et al. (Jan. 2022). "Monitoring Global Reservoirs Using ICESat-2: Assessment on Spatial Coverage and Application Potential." In: *Journal of Hydrology* 604, p. 127257. ISSN: 0022-1694. DOI: [10.1016/J.JHYDROL.2021.127257](https://doi.org/10.1016/J.JHYDROL.2021.127257).
- Cloke, Hannah L and Florian Pappenberger (2009). "Ensemble flood forecasting: A review." In: *Journal of hydrology* 375.3-4, pp. 613–626.
- Coe, Michael T (2000). "Modeling Terrestrial Hydrological Systems at the Continental Scale: Testing the Accuracy of an Atmospheric GCM." In: *Journal of Climate* 13.4.
- Coerver, Hubertus M. et al. (2018). "Deduction of Reservoir Operating Rules for Application in Global Hydrological Models." In: *Hydrology and Earth System Sciences* 22.1, pp. 831–851. ISSN: 16077938. DOI: [10.5194/HESS-22-831-2018](https://doi.org/10.5194/HESS-22-831-2018).
- Cogley, J. G. (June 1979). "The Albedo of Water as a Function of Latitude." In: *Monthly Weather Review* 107.6, pp. 775–781. ISSN: 00270644. DOI: [10.1175/1520-0493\(1979\)107<0775:TAOWAA>2.0.CO;2](https://doi.org/10.1175/1520-0493(1979)107<0775:TAOWAA>2.0.CO;2).
- Copernicus Climate Change Service (2017). *ERA5: Fifth Generation of ECMWF Atmospheric Reanalyses of the Global Climate*.
- Copernicus EMS Mapping products, EMSR517 (2023). Available at: [\[EMSR517\]: Bad Neuenahr-Ahrweiler: Grading Product, Monitoring 1, version 3, release 1, RTP Map 01](#). Accessed on: 4 October 2023.
- Costa-Cabral, Mariza C. and Stephen J. Burges (1994). "Digital Elevation Model Networks (DEMON): A Model of Flow over Hillslopes for Computation of Contributing and Dispersal Areas." In: *Water Resources Research* 30.6, pp. 1681–1692. ISSN: 1944-7973. DOI: [10.1029/93WR03512](https://doi.org/10.1029/93WR03512). (Visited on 04/02/2024).
- Courtney, Chris (2018). *The Nature of Disaster in China: The 1931 Yangzi River Flood*. Studies in Environment and History. Cambridge: Cambridge University Press. ISBN: 978-1-108-41777-8. DOI: [10.1017/9781108278362](https://doi.org/10.1017/9781108278362). (Visited on 09/03/2024).
- DWD–Deutscher Wetterdienst (2021). *Bericht zum Ablauf und Umfang der operationellen Warn- und Beratungstätigkeit des Deutschen Wetterdienstes im Vorlauf und während des Unwetters 12. – 15. Juli 2021 in NRW und Rheinland-Pfalz, ausgelöst durch das Tief „Bernd*. Tech. rep. DWD – Deutscher Wetterdienst. URL: https://www.dwd.de/DE/presse/pressemitteilungen/DE/2021/20210825_dwd_stellungnahme_kritik_news.html.
- Dang, Thanh Duc et al. (Apr. 2020). "A Software Package for the Representation and Optimization of Water Reservoir Operations in the VIC Hydrologic Model." In: *Environ-*

- mental Modelling and Software* 126, p. 104673. ISSN: 13648152. DOI: [10.1016/j.envsoft.2020.104673](https://doi.org/10.1016/j.envsoft.2020.104673).
- Daniels, Ronald et al. (Jan. 2006). *On Risk and Disaster: Lessons from Hurricane Katrina*. University of Pennsylvania Press. ISBN: 978-0-8122-1959-3.
- David, Cédric H. et al. (Oct. 2011). "River Network Routing on the NHDPlus Dataset." In: *Journal of Hydrometeorology* 12.5, pp. 913–934. ISSN: 1525-7541, 1525-755X. DOI: [10.1175/2011JHM1345.1](https://doi.org/10.1175/2011JHM1345.1). (Visited on 04/02/2024).
- Desai, Shitanshu and Taha B. M. J. Ouarda (Mar. 2021). "Regional Hydrological Frequency Analysis at Ungauged Sites with Random Forest Regression." In: *Journal of Hydrology* 594, p. 125861. ISSN: 0022-1694. DOI: [10.1016/j.jhydrol.2020.125861](https://doi.org/10.1016/j.jhydrol.2020.125861). (Visited on 11/28/2023).
- Developers, mHM (July 2022). *Mhm-Ufz/Basinex: Vo.2.0*. DOI: [10.5281/zenodo.6840021](https://doi.org/10.5281/zenodo.6840021). (Visited on 05/31/2023).
- Döll, Petra and Bernhard Lehner (Feb. 2002). "Validation of a New Global 30-Min Drainage Direction Map." In: *Journal of Hydrology* 258.1, pp. 214–231. ISSN: 0022-1694. DOI: [10.1016/S0022-1694\(01\)00565-0](https://doi.org/10.1016/S0022-1694(01)00565-0). (Visited on 08/23/2023).
- Döll, Petra and Stefan Siebert (Apr. 2002). "Global Modeling of Irrigation Water Requirements." In: *Water Resources Research* 38.4, pp. 8–1–8–10. ISSN: 00431397. DOI: [10.1029/2001WR000355](https://doi.org/10.1029/2001WR000355).
- Döll, Petra et al. (Jan. 2003). "A Global Hydrological Model for Deriving Water Availability Indicators: Model Tuning and Validation." In: *Journal of Hydrology* 270.1-2, pp. 105–134. ISSN: 00221694. DOI: [10.1016/S0022-1694\(02\)00283-4](https://doi.org/10.1016/S0022-1694(02)00283-4).
- Dottori, Francesco et al. (2017). "An operational procedure for rapid flood risk assessment in Europe." In: *Natural Hazards and Earth System Sciences* 17.7, pp. 1111–1126.
- Droppers, Bram et al. (Oct. 2020). "Simulating Human Impacts on Global Water Resources Using VIC-5." In: *Geoscientific Model Development* 13.10, pp. 5029–5052. ISSN: 1991-959X. DOI: [10.5194/gmd-13-5029-2020](https://doi.org/10.5194/gmd-13-5029-2020). (Visited on 03/20/2024).
- Dynesius, Mats and Christer Nilsson (Nov. 1994). "Fragmentation and Flow Regulation of River Systems in the Northern Third of the World." In: *Science* 266.5186, pp. 753–762. ISSN: 00368075. DOI: [10.1126/SCIENCE.266.5186.753](https://doi.org/10.1126/SCIENCE.266.5186.753).
- Ehsani, Nima et al. (Apr. 2016). "A Neural Network Based General Reservoir Operation Scheme." In: *Stochastic Environmental Research and Risk Assessment* 30.4, pp. 1151–1166. ISSN: 14363259. DOI: [10.1007/S00477-015-1147-9/TABLES/8](https://doi.org/10.1007/S00477-015-1147-9/TABLES/8).
- Eilander, Dirk et al. (Sept. 2021). "A Hydrography Upscaling Method for Scale-Invariant Parametrization of Distributed Hydrological Models." In: *Hydrology and Earth System Sciences* 25.9, pp. 5287–5313. ISSN: 16077938. DOI: [10.5194/hess-25-5287-2021](https://doi.org/10.5194/hess-25-5287-2021). (Visited on 09/23/2022).
- Emerton, Rebecca E et al. (2016). "Continental and global scale flood forecasting systems." In: *Wiley Interdisciplinary Reviews: Water* 3.3, pp. 391–418.

- Erickson, Troy R. and Heinz G. Stefan (2000). "Linear Air/Water Temperature Correlations for Streams during Open Water Periods." In: *Journal of Hydrologic Engineering*. DOI: [10.1061/\(asce\)1084-0699\(2000\)5:3\(317\)](https://doi.org/10.1061/(asce)1084-0699(2000)5:3(317)).
- European Space Agency (ESA), Universit Catholique de Louvain (2009). *Global Land Cover Map for 2009*. Data Set.
- FAO (1989). *Annex I : Irrigation Efficiencies*. (Visited on 12/13/2020).
- Fekete, Balázs M. et al. (2001). "Scaling Gridded River Networks for Macroscale Hydrology: Development, Analysis, and Control of Error." In: *Water Resources Research* 37:7, pp. 1955–1967. ISSN: 1944-7973. DOI: [10.1029/2001WR900024](https://doi.org/10.1029/2001WR900024). (Visited on 03/21/2024).
- Feldhaus, K. et al. (1992). "Finite Element Simulation of Flow and Pollution Transport Applied to a Part of the River Rhine." In: *Hydraulic and Environmental Modelling: Estuarine and River Waters*. Gower. ISBN: 978-0-429-42693-3.
- Fenn, C. R. et al. (2005). "The Boscastle Flood of 16 August 2004: Characteristics, Causes and Consequences." In: York, UK. (Visited on 09/09/2024).
- Firstpost (June 2013). *Photos: Kedarnath Temple before and after the Uttarakhand Floods*. URL: <https://www.firstpost.com/photos/photos-kedarnath-temple-before-and-after-the-uttarakhand-floods-903375.html> (visited on 09/26/2024).
- Flood Disaster Hits Hispaniola* (June 2004). Text.Article. (Visited on 09/09/2024).
- Flörke, Martina et al. (Feb. 2013). "Domestic and Industrial Water Uses of the Past 60 Years as a Mirror of Socio-Economic Development: A Global Simulation Study." In: *Global Environmental Change* 23.1, pp. 144–156. ISSN: 0959-3780. DOI: [10.1016/j.gloenvcha.2012.10.018](https://doi.org/10.1016/j.gloenvcha.2012.10.018). (Visited on 04/09/2024).
- Fraehr, Niels et al. (2023). "Supercharging hydrodynamic inundation models for instant flood insight." In: *Nature Water*, pp. 1–9.
- Fragoso, M. et al. (Mar. 2012). "The 20 February 2010 Madeira Flash-Floods: Synoptic Analysis and Extreme Rainfall Assessment." In: *Natural Hazards and Earth System Sciences* 12.3, pp. 715–730. ISSN: 1561-8633. DOI: [10.5194/nhess-12-715-2012](https://doi.org/10.5194/nhess-12-715-2012). (Visited on 09/09/2024).
- Freeman, T. Graham (Jan. 1991). "Calculating Catchment Area with Divergent Flow Based on a Regular Grid." In: *Computers & Geosciences* 17.3, pp. 413–422. ISSN: 0098-3004. DOI: [10.1016/0098-3004\(91\)90048-I](https://doi.org/10.1016/0098-3004(91)90048-I). (Visited on 04/04/2024).
- Friedrich, Katja et al. (June 2017). "Reservoir Evaporation in the Western United States: Current Science, Challenges, and Future Needs." In: *Bulletin of the American Meteorological Society* 99.1, pp. 167–187. ISSN: 0003-0007. DOI: [10.1175/bams-d-15-00224.1](https://doi.org/10.1175/bams-d-15-00224.1).
- Fundel, Vanessa J et al. (2019). "Promoting the use of probabilistic weather forecasts through a dialogue between scientists, developers and end-users." In: *Quarterly Journal of the Royal Meteorological Society* 145, pp. 210–231.
- GRDC (n.d.). *Global Daily Streamflow Data Set*.
- Gehrke, P. C. et al. (1995). "River Regulation and Fish Communities in the Murray-Darling River System, Australia." In: *Regulated Rivers: Research & Management* 11.3-4, pp. 363–375. ISSN: 1099-1646. DOI: [10.1002/rrr.3450110310](https://doi.org/10.1002/rrr.3450110310). (Visited on 12/14/2023).

- Gharari, Shervan et al. (2024). "A Flexible Framework for Simulating the Water Balance of Lakes and Reservoirs From Local to Global Scales: mizuRoute-Lake." In: *Water Resources Research* 60.5, e2022WR032400. ISSN: 1944-7973. DOI: [10.1029/2022WR032400](https://doi.org/10.1029/2022WR032400). (Visited on 05/13/2024).
- Gomez, Michael et al. (2019). "Skill of ensemble flood inundation forecasts at short-to medium-range timescales." In: *Journal of Hydrology* 568, pp. 207–220.
- Grogan, Danielle S. et al. (Oct. 2022). "Water Balance Model (WBM) v.1.0.0: A Scalable Gridded Global Hydrologic Model with Water-Tracking Functionality." In: *Geoscientific Model Development* 15.19, pp. 7287–7323. ISSN: 1991-959X. DOI: [10.5194/gmd-15-7287-2022](https://doi.org/10.5194/gmd-15-7287-2022). (Visited on 03/22/2024).
- Gründemann, Gaby Joanne et al. (2022). "Rarest rainfall events will see the greatest relative increase in magnitude under future climate change." In: *Communications Earth & Environment* 3.1, p. 235.
- Guo, Jianzhong et al. (2004). "A New Multiscale Flow Network Generation Scheme for Land Surface Models." In: *Geophysical Research Letters* 31.23. ISSN: 1944-8007. DOI: [10.1029/2004GL021381](https://doi.org/10.1029/2004GL021381). (Visited on 04/02/2024).
- Gupta, Hoshin V. et al. (2009). "Decomposition of the Mean Squared Error and NSE Performance Criteria: Implications for Improving Hydrological Modelling." In: *Journal of Hydrology*. ISSN: 00221694. DOI: [10.1016/j.jhydrol.2009.08.003](https://doi.org/10.1016/j.jhydrol.2009.08.003).
- Gutenson, Joseph L. et al. (May 2020). "Comparison of Generalized Non-Data-Driven Lake and Reservoir Routing Models for Global-Scale Hydrologic Forecasting of Reservoir Outflow at Diurnal Time Steps." In: *Hydrology and Earth System Sciences* 24.5, pp. 2711–2729. ISSN: 1607-7938. DOI: [10.5194/hess-24-2711-2020](https://doi.org/10.5194/hess-24-2711-2020).
- HRC (2019). *Verification Guidelines for the Flash Flood Guidance System Component Products and Derivative Warnings*. Tech. rep. 102. Global Flash Flood Guidance Program | Hydrologic Research Center. (Visited on 09/27/2024).
- Haddeland, Ingjerd et al. (Apr. 2006a). "Anthropogenic Impacts on Continental Surface Water Fluxes." In: *Geophysical Research Letters* 33.8. ISSN: 00948276. DOI: [10.1029/2006GL026047](https://doi.org/10.1029/2006GL026047).
- Haddeland, Ingjerd et al. (June 2006b). "Effects of Irrigation on the Water and Energy Balances of the Colorado and Mekong River Basins." In: *Journal of Hydrology* 324.1-4, pp. 210–223. ISSN: 00221694. DOI: [10.1016/j.jhydrol.2005.09.028](https://doi.org/10.1016/j.jhydrol.2005.09.028).
- Hanasaki, N. et al. (July 2008). "An Integrated Model for the Assessment of Global Water Resources - Part 1: Model Description and Input Meteorological Forcing." In: *Hydrology and Earth System Sciences* 12.4, pp. 1007–1025. ISSN: 16077938. DOI: [10.5194/hess-12-1007-2008](https://doi.org/10.5194/hess-12-1007-2008). (Visited on 01/11/2021).
- Hanasaki, Naota et al. (July 2006). "A Reservoir Operation Scheme for Global River Routing Models." In: *Journal of Hydrology* 327.1-2, pp. 22–41. ISSN: 00221694. DOI: [10.1016/j.jhydrol.2005.11.011](https://doi.org/10.1016/j.jhydrol.2005.11.011).

- Hanasaki, Naota et al. (Jan. 2018). "A Global Hydrological Simulation to Specify the Sources of Water Used by Humans." In: *Hydrology and Earth System Sciences* 22.1, pp. 789–817. ISSN: 1607-7938. DOI: [10.5194/hess-22-789-2018](https://doi.org/10.5194/hess-22-789-2018).
- Hanasaki, Naota et al. (Apr. 2022). "Toward Hyper-Resolution Global Hydrological Models Including Human Activities: Application to Kyushu Island, Japan." In: *Hydrology and Earth System Sciences* 26.8, pp. 1953–1975. ISSN: 1027-5606. DOI: [10.5194/hess-26-1953-2022](https://doi.org/10.5194/hess-26-1953-2022). (Visited on 04/09/2024).
- Hapuarachchi, Hapu Arachchige Prasantha et al. (2022). "Development of a national 7-day ensemble streamflow forecasting service for Australia." In: *Hydrology and Earth System Sciences* 26.18, pp. 4801–4821.
- Harrabin, Roger (July 2021). "Climate Change: Science Failed to Predict Flood and Heat Intensity." In: (visited on 09/16/2024).
- Harrigan, Shaun et al. (Sept. 2020). "GloFAS-ERA5 Operational Global River Discharge Reanalysis 1979–Present." In: *Earth System Science Data* 12.3, pp. 2043–2060. ISSN: 1866-3516. DOI: [10.5194/essd-12-2043-2020](https://doi.org/10.5194/essd-12-2043-2020). (Visited on 10/21/2021).
- Harrowsmith, M et al. (2020). *The Future of Forecasts: Impact-Based Forecasting for Early Action, International Federation of Red Cross and Red Crescent Societies and the UK Met Office*, 84 pp.
- Hartmann, Jörg and Nils Moosdorf (2012). *Global Lithological Map Database v1.0 (Gridded to 0.5 Degree Spatial Resolution)*. Data Set. DOI: [10.1594/PANGAEA.788537](https://doi.org/10.1594/PANGAEA.788537).
- Hengl, Tomislav et al. (Apr. 2021). *Continental Europe Digital Terrain Model at 30 m resolution based on GEDI, ICESat-2, AW3D, GLO-30, EUEM, MERIT DEM and background layers. Version vo.3*. DOI: [10.5281/zenodo.4724549](https://doi.org/10.5281/zenodo.4724549). URL: <https://doi.org/10.5281/zenodo.4724549>.
- Hou, Ying et al. (2023). "Global Evaluation of Runoff Simulation From Climate, Hydrological and Land Surface Models." In: *Water Resources Research* 59.1, e2021WR031817. ISSN: 1944-7973. DOI: [10.1029/2021WR031817](https://doi.org/10.1029/2021WR031817). (Visited on 03/21/2024).
- ISRIC - World Soil Information (2017). *SoilGrids — Global Gridded Soil Information*. Wageningen, The Netherlands.
- India Today (June 2013). *Uttarakhand Flood Survivors Bring Back Harrowing Tales from the Hills*. <https://www.indiatoday.in/india/north/story/uttarakhand-flood-survivors-bring-back-harrowing-tales-from-the-hills-167270-2013-06-18>. (Visited on 09/26/2024).
- Intergovernmental Panel on Climate Change (2021). *Factsheet: People and Oceans*. Tech. rep. IPCC. URL: https://www.ipcc.ch/report/ar6/wg1/downloads/factsheets/IPCC_AR6_WGI_Regional_Fact_Sheet_Europe.pdf.
- Ivanov, Valeriy Y et al. (2021). "Breaking down the computational barriers to real-time urban flood forecasting." In: *Geophysical Research Letters* 48.20, e2021GL093585.
- Jansen, Femke A and Adriaan J Teuling (2020). "Evaporation from a Large Lowland Reservoir-(Dis)Agreement between Evaporation Models from Hourly to Decadal Timescales." In: *Hydrol. Earth Syst. Sci* 24, pp. 1055–1072. DOI: [10.5194/hess-24-1055-2020](https://doi.org/10.5194/hess-24-1055-2020).

- Jones, Edward R. et al. (Aug. 2023). "DynQual v1.0: A High-Resolution Global Surface Water Quality Model." In: *Geoscientific Model Development* 16.15, pp. 4481–4500. ISSN: 1991-959X. DOI: [10.5194/gmd-16-4481-2023](https://doi.org/10.5194/gmd-16-4481-2023). (Visited on 05/28/2024).
- Kala, Chandra Prakash (June 2014). "Deluge, Disaster and Development in Uttarakhand Himalayan Region of India: Challenges and Lessons for Disaster Management." In: *International Journal of Disaster Risk Reduction* 8, pp. 143–152. ISSN: 2212-4209. DOI: [10.1016/j.ijdrr.2014.03.002](https://doi.org/10.1016/j.ijdrr.2014.03.002). (Visited on 09/26/2024).
- Katyal, Ashok K. and Ioana G. Petrisor (Sept. 2011). "Flood Management Strategies for a Holistic Sustainable Development." In: *Environmental Forensics* 12.3, pp. 206–218. ISSN: 1527-5922. DOI: [10.1080/15275922.2011.595051](https://doi.org/10.1080/15275922.2011.595051). (Visited on 09/13/2024).
- Kauffeldt, Anna et al. (2016). "Technical review of large-scale hydrological models for implementation in operational flood forecasting schemes on continental level." In: *Environmental Modelling & Software* 75, pp. 68–76.
- Khazaei, Bahram et al. (Dec. 2022). "GLOBathy, the Global Lakes Bathymetry Dataset." In: *Scientific data* 9.1. ISSN: 2052-4463. DOI: [10.1038/S41597-022-01132-9](https://doi.org/10.1038/S41597-022-01132-9).
- Knoben, Wouter J.M. et al. (2019). "Technical Note: Inherent Benchmark or Not? Comparing Nash-Sutcliffe and Kling-Gupta Efficiency Scores." In: *Hydrology and Earth System Sciences* 23.10, pp. 4323–4331. ISSN: 16077938. DOI: [10.5194/hess-23-4323-2019](https://doi.org/10.5194/hess-23-4323-2019).
- Kotlyakov, V. M. et al. (Jan. 2013). "Flooding of July 6–7, 2012, in the Town of Krymsk." In: *Regional Research of Russia* 3.1, pp. 32–39. ISSN: 2079-9713. DOI: [10.1134/S2079970513010061](https://doi.org/10.1134/S2079970513010061). (Visited on 09/09/2024).
- Kox, Thomas et al. (2018). "Anticipation and response: Emergency services in severe weather situations in Germany." In: *International Journal of Disaster Risk Science* 9, pp. 116–128.
- Kreibich, Heidi et al. (2021). "Knowing what to do substantially improves the effectiveness of flood early warning." In: *Bulletin of the American Meteorological Society*, pp. 1–38.
- Kumar, Rohini et al. (Oct. 2010). "The Effects of Spatial Discretization and Model Parameterization on the Prediction of Extreme Runoff Characteristics." In: *Journal of Hydrology* 392.1-2, pp. 54–69. ISSN: 00221694. DOI: [10.1016/j.jhydrol.2010.07.047](https://doi.org/10.1016/j.jhydrol.2010.07.047). (Visited on 01/18/2022).
- (2013). "Implications of Distributed Hydrologic Model Parameterization on Water Fluxes at Multiple Scales and Locations." In: *Water Resources Research* 49.1, pp. 360–379. ISSN: 00431397. DOI: [10.1029/2012WR012195](https://doi.org/10.1029/2012WR012195).
- Ladson, AR and LJ White (1999). "An Index of Stream Condition: Reference Manual.(9780731143184)." In: *Victoria. Dept. of Natural Resources*.
- Lahsen, Myanna and Jesse Ribot (2022). "Politics of attributing extreme events and disasters to climate change." In: *Wiley Interdisciplinary Reviews: Climate Change* 13.1, e750. DOI: <https://doi.org/10.1002/wcc.750>.
- Lannelongue, Loïc and Michael Inouye (Feb. 2023). "Carbon Footprint Estimation for Computational Research." In: *Nature Reviews Methods Primers* 3.1, pp. 1–2. ISSN: 2662-8449. DOI: [10.1038/s43586-023-00202-5](https://doi.org/10.1038/s43586-023-00202-5). (Visited on 05/17/2024).

- Lannelongue, Loïc et al. (2021a). "Green Algorithms: Quantifying the Carbon Footprint of Computation." In: *Advanced Science* 8.12, p. 2100707. ISSN: 2198-3844. DOI: [10.1002/adv.202100707](https://doi.org/10.1002/adv.202100707). (Visited on 05/17/2024).
- Lannelongue, Loïc et al. (Sept. 2021b). "Ten Simple Rules to Make Your Computing More Environmentally Sustainable." In: *PLOS Computational Biology* 17.9, e1009324. ISSN: 1553-7358. DOI: [10.1371/journal.pcbi.1009324](https://doi.org/10.1371/journal.pcbi.1009324). (Visited on 05/17/2024).
- Lehner, Bernhard and Günther Grill (2013). "Global River Hydrography and Network Routing: Baseline Data and New Approaches to Study the World's Large River Systems." In: *Hydrological Processes* 27.15, pp. 2171–2186. ISSN: 1099-1085. DOI: [10.1002/hyp.9740](https://doi.org/10.1002/hyp.9740). (Visited on 02/01/2024).
- Lehner, Bernhard et al. (Nov. 2011). "High-Resolution Mapping of the World's Reservoirs and Dams for Sustainable River-Flow Management." In: *Frontiers in Ecology and the Environment* 9.9, pp. 494–502. ISSN: 1540-9295. DOI: [10.1890/100125](https://doi.org/10.1890/100125).
- Lessard, Joanna L. and Daniel B. Hayes (2003). "Effects of Elevated Water Temperature on Fish and Macroinvertebrate Communities below Small Dams." In: *River Research and Applications*. DOI: [10.1002/rra.713](https://doi.org/10.1002/rra.713).
- LfU (2022). *Hochwasser im Juli 2021*. Tech. rep. Landesamt für Umwelt (LfU) Rheinland-Pfalz. URL: https://lfu.rlp.de/fileadmin/lfu/Wasserwirtschaft/Ahr-Katastrophe/Hochwasser_im_Juli2021.pdf.
- Li, Bing et al. (July 2016). "Comparison of Random Forests and Other Statistical Methods for the Prediction of Lake Water Level: A Case Study of the Poyang Lake in China." In: *Hydrology Research* 47.S1, pp. 69–83. ISSN: 0029-1277. DOI: [10.2166/nh.2016.264](https://doi.org/10.2166/nh.2016.264). (Visited on 11/28/2023).
- Li, Hong-Yi et al. (Apr. 2015). "Evaluating Global Streamflow Simulations by a Physically Based Routing Model Coupled with the Community Land Model." In: *Journal of Hydrometeorology* 16.2, pp. 948–971. ISSN: 1525-7541, 1525-755X. DOI: [10.1175/JHM-D-14-0079.1](https://doi.org/10.1175/JHM-D-14-0079.1). (Visited on 03/20/2024).
- Li, Hongyi et al. (June 2013). "A Physically Based Runoff Routing Model for Land Surface and Earth System Models." In: *Journal of Hydrometeorology* 14.3, pp. 808–828. ISSN: 1525755X. DOI: [10.1175/JHM-D-12-015.1](https://doi.org/10.1175/JHM-D-12-015.1).
- Li, Yao et al. (July 2020). "A High-Resolution Bathymetry Dataset for Global Reservoirs Using Multi-Source Satellite Imagery and Altimetry." In: *Remote Sensing of Environment* 244, p. 111831. ISSN: 00344257. DOI: [10.1016/j.rse.2020.111831](https://doi.org/10.1016/j.rse.2020.111831).
- Liang, Xu et al. (Oct. 2004). "Assessment of the Effects of Spatial Resolutions on Daily Water Flux Simulations." In: *Journal of Hydrology*. The Distributed Model Intercomparison Project (DMIP) 298.1, pp. 287–310. ISSN: 0022-1694. DOI: [10.1016/j.jhydrol.2003.07.007](https://doi.org/10.1016/j.jhydrol.2003.07.007). (Visited on 04/02/2024).
- Liebe, J. et al. (Jan. 2005). "Estimation of Small Reservoir Storage Capacities in a Semi-Arid Environment." In: *Physics and Chemistry of the Earth* 30.6-7 SPEC. ISS. Pp. 448–454. ISSN: 14747065. DOI: [10.1016/j.pce.2005.06.011](https://doi.org/10.1016/j.pce.2005.06.011).

- Lindell, Michael K and Ronald W Perry (2012). "The protective action decision model: Theoretical modifications and additional evidence." In: *Risk Analysis: An International Journal* 32.4, pp. 616–632.
- Ludwig, Karl (2006). *The water balance model LARSIM: design, content and applications*. Inst. für Hydrologie der Univ.
- MacQueen, J (1967). "Classification and Analysis of Multivariate Observations." In: *5th Berkeley Symp. Math. Statist. Probability*. University of California Los Angeles LA USA, pp. 281–297.
- Mateo, Cherry May R. et al. (Oct. 2017). "Impacts of Spatial Resolution and Representation of Flow Connectivity on Large-Scale Simulation of Floods." In: *Hydrology and Earth System Sciences* 21.10, pp. 5143–5163. ISSN: 1027-5606. DOI: [10.5194/hess-21-5143-2017](https://doi.org/10.5194/hess-21-5143-2017). (Visited on 03/25/2024).
- Mathevet, Thibault et al. (2006). "A Bounded Version of the Nash-Sutcliffe Criterion for Better Model Assessment on Large Sets of Basins." In: *Large Sample Basin Experiments for Hydrological Model Parameterization: Results of the Model Parameter Experiment—MOPEX*. Vol. 307. IAHS Publ.
- Mazzoleni, Maurizio et al. (Nov. 2022). "Deciphering Human Influence on Annual Maximum Flood Extent at the Global Level." In: *Communications Earth & Environment* 3.1, pp. 1–10. ISSN: 2662-4435. DOI: [10.1038/s43247-022-00598-0](https://doi.org/10.1038/s43247-022-00598-0). (Visited on 09/05/2024).
- Meeus, Jean (1991). "Astronomical Algorithms." In: *Richmond*.
- Meigh, J. R. et al. (1999). "A Grid-Based Approach to Water Scarcity Estimates for Eastern and Southern Africa." In: *Water Resources Management* 13.2, pp. 85–115. ISSN: 09204741. DOI: [10.1023/A:1008025703712/METRICS](https://doi.org/10.1023/A:1008025703712/METRICS).
- Merz, Bruno et al. (2020). "Impact forecasting to support emergency management of natural hazards." In: *Reviews of Geophysics* 58.4, e2020RG000704.
- Merz Blöschl, Vorogushyn et al. (2021). "Causes, impacts and patterns of disastrous river floods." In: *Nature reviews earth and environment* 2.7817, pp. 592–609. DOI: <https://doi.org/10.1038/s43017-021-00195-3>.
- Micklin, Philip (May 2007). "The Aral Sea Disaster." In: *Annual Review of Earth and Planetary Sciences* 35. Volume 35, 2007, pp. 47–72. ISSN: 0084-6597, 1545-4495. DOI: [10.1146/annurev.earth.35.031306.140120](https://doi.org/10.1146/annurev.earth.35.031306.140120). (Visited on 09/25/2024).
- Mizukami, Naoki et al. (June 2016). "mizuRoute Version 1: A River Network Routing Tool for a Continental Domain Water Resources Applications." In: *Geoscientific Model Development* 9.6, pp. 2223–2238. ISSN: 1991-959X. DOI: [10.5194/gmd-9-2223-2016](https://doi.org/10.5194/gmd-9-2223-2016). (Visited on 03/20/2024).
- Mool, Pradeep K. et al. (Mar. 2011). *Glacial Lakes and Glacial Lake Outburst Floods in Nepal*. Tech. rep. (Visited on 09/12/2024).
- Mueller, Sonja et al. (Feb. 2019). "Disaster Scenario Simulation of the 2010 Cloudburst in Leh, Ladakh, India." In: *International Journal of Disaster Risk Reduction* 33, pp. 485–494. ISSN: 2212-4209. DOI: [10.1016/j.ijdrr.2018.09.004](https://doi.org/10.1016/j.ijdrr.2018.09.004). (Visited on 09/09/2024).

- Müller Schmied, Hannes et al. (2020). "The Global Water Resources and Use Model WaterGAP v2.2d: Model Description and Evaluation." In: *Geoscientific Model Development Discussions*, pp. 1–69. ISSN: 1991-959X. DOI: [10.5194/gmd-2020-225](https://doi.org/10.5194/gmd-2020-225).
- NIDM (2015). *Uttarakhand Disaster 2013*. Tech. rep. New Delhi: National Institute of Disaster Management, Ministry of Home Affairs, Govt. of India.
- NOAA (n.d.). *National Water Prediction Service - NOAA*. <https://water.noaa.gov/>. Forecast Portal. (Visited on 09/27/2024).
- Najafi, Husain et al. (2022). "Post-Assessment of ECMWF-mHM ensemble flood forecasting for 2021 summer flood in west Germany." In: *AGU Fall Meeting Abstracts*. Vol. 2022, H35I–1221.
- Najafi, Husain et al. (May 2024). "High-Resolution Impact-Based Early Warning System for Riverine Flooding." In: *Nature Communications* 15.1, p. 3726. ISSN: 2041-1723. DOI: [10.1038/s41467-024-48065-y](https://doi.org/10.1038/s41467-024-48065-y). (Visited on 05/02/2024).
- Nash, JE and JV Sutcliffe (1970). "River Flow Forecasting through Conceptual Models Part I—A Discussion of Principles." In: *Journal of hydrology*.
- Neitsch, S.L et al. (2011). *Soil & Water Assessment Tool Theoretical Documentation Version 2009*. Tech. rep., pp. 1–647. DOI: [10.1016/j.scitotenv.2015.11.063](https://doi.org/10.1016/j.scitotenv.2015.11.063).
- Nguyen-Quang, Trung et al. (Dec. 2018). "ORCHIDEE-ROUTING: Revising the River Routing Scheme Using a High-Resolution Hydrological Database." In: *Geoscientific Model Development* 11.12, pp. 4965–4985. ISSN: 1991-959X. DOI: [10.5194/gmd-11-4965-2018](https://doi.org/10.5194/gmd-11-4965-2018). (Visited on 03/21/2024).
- Nilsson, Christer et al. (Apr. 2005). "Fragmentation and Flow Regulation of the World's Large River Systems." In: *Science* 308.5720, pp. 405–408. ISSN: 00368075. DOI: [10.1126/SCIENCE.1107887/SUPPL_FILE/NILSSON.SOM.PDF](https://doi.org/10.1126/SCIENCE.1107887/SUPPL_FILE/NILSSON.SOM.PDF).
- O'Callaghan, J. F. and D. M. Mark (Dec. 1984). "The Extraction of Drainage Networks from Digital Elevation Data." In: *Computer Vision, Graphics, & Image Processing* 28.3, pp. 323–344. ISSN: 0734189X. DOI: [10.1016/S0734-189X\(84\)80011-0](https://doi.org/10.1016/S0734-189X(84)80011-0).
- O'Donnell, Greg et al. (1999). "A Simple Algorithm for Generating Streamflow Networks for Grid-Based, Macroscale Hydrological Models." In: *Hydrological Processes* 13.8, pp. 1269–1275. ISSN: 1099-1085. DOI: [10.1002/\(SICI\)1099-1085\(19990615\)13:8<1269::AID-HYP806>3.0.CO;2-R](https://doi.org/10.1002/(SICI)1099-1085(19990615)13:8<1269::AID-HYP806>3.0.CO;2-R). (Visited on 03/27/2024).
- Oki, Taikan and Y. C. Sud (Jan. 1998). "Design of Total Runoff Integrating Pathways (TRIP)—A Global River Channel Network." In: *Earth Interactions* 2.1, pp. 1–37. ISSN: 1087-3562. DOI: [10.1175/1087-3562\(1998\)002<0001:DOTRIP>2.3.CO;2](https://doi.org/10.1175/1087-3562(1998)002<0001:DOTRIP>2.3.CO;2). (Visited on 05/02/2024).
- Olden, Julian D. and Robert J. Naiman (2010). "Incorporating Thermal Regimes into Environmental Flows Assessments: Modifying Dam Operations to Restore Freshwater Ecosystem Integrity." In: *Freshwater Biology*. DOI: [10.1111/j.1365-2427.2009.02179.x](https://doi.org/10.1111/j.1365-2427.2009.02179.x).
- Olivera, Francisco et al. (Nov. 2002). "Extracting Low-Resolution River Networks from High-Resolution Digital Elevation Models." In: *Water Resources Research* 38.11, pp. 13–1. ISSN: 0043-1397. DOI: [10.1029/2001WR000726](https://doi.org/10.1029/2001WR000726). (Visited on 03/27/2024).

- OpenStreetMap (2017). *OpenStreetMap contributors 2021 distributed under the Open Data Commons Open Database License (ODbL) v1.0., last access: 30 January 2022.*
- Pappenberger, Florian et al. (2015). "The monetary benefit of early flood warnings in Europe." In: *Environmental Science & Policy* 51, pp. 278–291. ISSN: 1462-9011. DOI: <https://doi.org/10.1016/j.envsci.2015.04.016>. URL: <https://www.sciencedirect.com/science/article/pii/S1462901115000891>.
- Pappenberger, Florian et al. (2019). "Hydrological ensemble prediction systems around the globe." In: *Handbook of hydrometeorological ensemble forecasting*. Springer Berlin/Heidelberg, pp. 1187–1221.
- Patel, Pratiman et al. (Dec. 2022). "Revisiting 2013 Uttarakhand Flash Floods through Hydrological Evaluation of Precipitation Data Sources and Morphometric Prioritization." In: *Geomatics, Natural Hazards and Risk* 13.1, pp. 646–666. ISSN: 1947-5705. DOI: [10.1080/19475705.2022.2038696](https://doi.org/10.1080/19475705.2022.2038696). (Visited on 09/09/2024).
- Paz, Adriano Rolim et al. (2006). "Improvements in Large-Scale Drainage Networks Derived from Digital Elevation Models." In: *Water Resources Research* 42.8. ISSN: 1944-7973. DOI: [10.1029/2005WR004544](https://doi.org/10.1029/2005WR004544). (Visited on 04/02/2024).
- Piccolroaz, Sebastiano et al. (May 2016). "HYPERstream: A Multi-Scale Framework for Streamflow Routing in Large-Scale Hydrological Model." In: *Hydrology and Earth System Sciences* 20.5, pp. 2047–2061. ISSN: 1027-5606. DOI: [10.5194/hess-20-2047-2016](https://doi.org/10.5194/hess-20-2047-2016). (Visited on 03/27/2024).
- Pokhrel, Yadu N. et al. (June 2012). "Model Estimates of Sea-Level Change Due to Anthropogenic Impacts on Terrestrial Water Storage." In: *Nature Geoscience* 5.6, pp. 389–392. ISSN: 17520894. DOI: [10.1038/ngeo1476](https://doi.org/10.1038/ngeo1476).
- Polcher, Jan et al. (May 2023). "Hydrological Modelling on Atmospheric Grids: Using Graphs of Sub-Grid Elements to Transport Energy and Water." In: *Geoscientific Model Development* 16.9, pp. 2583–2606. ISSN: 1991-959X. DOI: [10.5194/gmd-16-2583-2023](https://doi.org/10.5194/gmd-16-2583-2023). (Visited on 03/21/2024).
- Qie, Guangping et al. (2022). "Comparison of Machine Learning Models Performance on Simulating Reservoir Outflow: A Case Study of Two Reservoirs in Illinois, U.S.A." In: *Journal of the American Water Resources Association*. ISSN: 17521688. DOI: [10.1111/1752-1688.13040](https://doi.org/10.1111/1752-1688.13040).
- Quiggin, Daniel et al. (2021). *What near-term climate impacts should worry us most*. The Royal Institute of International Affairs Chatham House: London.
- Quinn, P. et al. (1991). "The Prediction of Hillslope Flow Paths for Distributed Hydrological Modelling Using Digital Terrain Models." In: *Hydrological Processes* 5.1, pp. 59–79. ISSN: 1099-1085. DOI: [10.1002/hyp.3360050106](https://doi.org/10.1002/hyp.3360050106). (Visited on 04/02/2024).
- Rakovec, O. et al. (Oct. 2016a). "Improving the Realism of Hydrologic Model Functioning through Multivariate Parameter Estimation." In: *Water Resources Research* 52.10, pp. 7779–7792. ISSN: 00431397. DOI: [10.1002/2016WR019430](https://doi.org/10.1002/2016WR019430). (Visited on 01/18/2022).

- Rakovec, Oldrich et al. (2016b). "Multiscale and Multivariate Evaluation of Water Fluxes and States over European River Basins." In: *Journal of Hydrometeorology* 17.1, pp. 287–307. ISSN: 15257541. DOI: [10.1175/JHM-D-15-0054.1](https://doi.org/10.1175/JHM-D-15-0054.1).
- Rakovec, Oldrich et al. (Dec. 2019a). "Diagnostic Evaluation of Large-Domain Hydrologic Models Calibrated Across the Contiguous United States." In: *Journal of Geophysical Research: Atmospheres* 124.24, pp. 13991–14007. ISSN: 21698996. DOI: [10.1029/2019JD030767](https://doi.org/10.1029/2019JD030767). (Visited on 01/18/2022).
- Rakovec, Oldrich et al. (Dec. 2019b). "Diagnostic Evaluation of Large-Domain Hydrologic Models Calibrated Across the Contiguous United States." English. In: *Journal of Geophysical Research-Atmospheres* 124.24, pp. 13991–14007. DOI: [10.1029/2019jd030767](https://doi.org/10.1029/2019jd030767).
- Rauthe, Monika et al. (2013). "A Central European precipitation climatology–Part I: Generation and validation of a high-resolution gridded daily data set (HYRAS)." In: *Meteorologische Zeitschrift* 22.3, pp. 235–256.
- Reed, Seann M. (2003). "Deriving Flow Directions for Coarse-Resolution (1–4 Km) Gridded Hydrologic Modeling." In: *Water Resources Research* 39.9. ISSN: 1944-7973. DOI: [10.1029/2003WR001989](https://doi.org/10.1029/2003WR001989). (Visited on 03/27/2024).
- Reinert, D et al. (2020). "DWD database reference for the global and regional ICON and ICON-EPS forecasting system." In: *Technical report Version 2.1. 8, Deutscher Wetterdienst*.
- Rentschler, Jun et al. (June 2022). "Flood Exposure and Poverty in 188 Countries." In: *Nature Communications* 13.1, p. 3527. ISSN: 2041-1723. DOI: [10.1038/s41467-022-30727-4](https://doi.org/10.1038/s41467-022-30727-4). (Visited on 09/05/2024).
- Rinke, Karsten et al. (2013). "Reservoirs as Sentinels of Catchments: The Rappbode Reservoir Observatory (Harz Mountains, Germany)." In: *Environmental Earth Sciences* 69.2, pp. 523–536. ISSN: 18666299. DOI: [10.1007/s12665-013-2464-2](https://doi.org/10.1007/s12665-013-2464-2).
- Robinson, Alexander et al. (2021). "Increasing heat and rainfall extremes now far outside the historical climate." In: *NPJ Climate and Atmospheric Science* 4.1, p. 45.
- Ross, S. R. J. (Simon R. J.) (2012). *AQA GCSE Geography A*. Cheltenham : Nelson Thornes. ISBN: 978-1-4085-1708-6. (Visited on 09/09/2024).
- Sadki, Malak et al. (2023). "Implementation and Sensitivity Analysis of the Dam-Reservoir Operation Model (DROP v1.0) over Spain." In: *Geosci. Model Dev* 16, pp. 427–448. DOI: [10.5194/gmd-16-427-2023](https://doi.org/10.5194/gmd-16-427-2023).
- Saha, Toma Rani et al. (Apr. 2021). "A Drought Monitoring Tool for South Asia." In: *Environmental Research Letters* 16.5, p. 054014. ISSN: 1748-9326. DOI: [10.1088/1748-9326/ABF525](https://doi.org/10.1088/1748-9326/ABF525).
- Salwey, Saskia et al. (Sept. 2024). "Developing Water Supply Reservoir Operating Rules for Large-Scale Hydrological Modelling." In: *Hydrology and Earth System Sciences* 28.17, pp. 4203–4218. ISSN: 1027-5606. DOI: [10.5194/hess-28-4203-2024](https://doi.org/10.5194/hess-28-4203-2024). (Visited on 09/13/2024).
- Samaniego, L. et al. (2018). "Anthropogenic Warming Exacerbates European Soil Moisture Droughts." In: *Nature Climate Change* 8.5, pp. 421–426. ISSN: 17586798. DOI: [10.1038/s41558-018-0138-5](https://doi.org/10.1038/s41558-018-0138-5).

- Samaniego, Luis et al. (2010). "Multiscale Parameter Regionalization of a Grid - Based Hydrologic Model at the Mesoscale." In: *Water Resources Research* 46, pp. 1–25. DOI: [10.1029/2008WR007327](https://doi.org/10.1029/2008WR007327).
- Samaniego, Luis et al. (2017). "Toward Seamless Hydrologic Predictions across Spatial Scales." In: *Hydrology and Earth System Sciences*, pp. 4323–4346. DOI: [10.5194/hess-21-4323-2017](https://doi.org/10.5194/hess-21-4323-2017).
- Samaniego, Luis et al. (Dec. 2019). "Hydrological Forecasts and Projections for Improved Decision-Making in the Water Sector in Europe." In: *Bulletin of the American Meteorological Society* 100.12, pp. 2451–2472. ISSN: 0003-0007, 1520-0477. DOI: [10.1175/BAMS-D-17-0274.1](https://doi.org/10.1175/BAMS-D-17-0274.1). (Visited on 05/27/2024).
- Sampson, Christopher C. et al. (2015). "A High-Resolution Global Flood Hazard Model." In: *Water Resources Research* 51.9, pp. 7358–7381. ISSN: 1944-7973. DOI: [10.1002/2015WR016954](https://doi.org/10.1002/2015WR016954). (Visited on 09/16/2024).
- Sato, Teruko and Tadashi Nakasu (May 2011). *2009 Typhoon Ondoy Flood Disasters in Metro Manila*. Tech. rep. DOI: [10.13140/RG.2.1.2817.5121](https://doi.org/10.13140/RG.2.1.2817.5121).
- Schoppa, Lukas et al. (Nov. 2020). "Evaluating the Performance of Random Forest for Large-Scale Flood Discharge Simulation." In: *Journal of Hydrology* 590, p. 125531. ISSN: 0022-1694. DOI: [10.1016/j.jhydrol.2020.125531](https://doi.org/10.1016/j.jhydrol.2020.125531). (Visited on 11/28/2023).
- Schrön, M et al. (Sept. 2018). "Cosmic-Ray Neutron Rover Surveys of Field Soil Moisture and the Influence of Roads." In: *Water Resources Research* 54.9, pp. 6441–6459. DOI: [10.1029/2017wr021719](https://doi.org/10.1029/2017wr021719).
- Schubert, Jochen E et al. (2022). "A framework for mechanistic flood inundation forecasting at the metropolitan scale." In: *Water Resources Research* 58.10, e2021WR031279.
- Schumann, GJ-P et al. (2013). "A first large-scale flood inundation forecasting model." In: *Water Resources Research* 49.10, pp. 6248–6257.
- Schweppe, Robert et al. (Jan. 2022). "MPR 1.0: A Stand-Alone Multiscale Parameter Regionalization Tool for Improved Parameter Estimation of Land Surface Models." In: *Geoscientific Model Development* 15.2, pp. 859–882. ISSN: 1991-959X. DOI: [10.5194/gmd-15-859-2022](https://doi.org/10.5194/gmd-15-859-2022). (Visited on 05/30/2023).
- "Severe Drought Spreads in Portugal, Officials Seek EU Help" (May 2023). In: *Reuters*. URL: <https://www.reuters.com/world/europe/severe-drought-spreads-portugal-officials-seek-eu-help-2023-05-10/> (visited on 12/12/2023).
- Shiau, Jenq Tzong and Chian You Huang (Mar. 2014). "Detecting Multi-Purpose Reservoir Operation Induced Time-Frequency Alteration Using Wavelet Transform." In: *Water Resources Management* 28.11, pp. 3577–3590. ISSN: 09204741. DOI: [10.1007/S11269-014-0688-X/FIGURES/9](https://doi.org/10.1007/S11269-014-0688-X/FIGURES/9).
- Shiklomanov, Igor A. (2009). "Appraisal and Assessment of World Water Resources." In: <http://dx.doi.org/10.1080/02508060008686794> 25.1, pp. 11–32. ISSN: 02508060. DOI: [10.1080/02508060008686794](https://doi.org/10.1080/02508060008686794).

- Shin, Sanghoon et al. (Jan. 2019). "High-Resolution Modeling of Reservoir Release and Storage Dynamics at the Continental Scale." In: *Water Resources Research* 55.1, pp. 787–810. ISSN: 19447973. DOI: [10.1029/2018WR023025](https://doi.org/10.1029/2018WR023025).
- Shin, Sanghoon et al. (May 2020). "High Resolution Modeling of River-floodplain-reservoir Inundation Dynamics in the Mekong River Basin." In: *Water Resources Research* 56.5. ISSN: 0043-1397. DOI: [10.1029/2019WR026449](https://doi.org/10.1029/2019WR026449).
- Shrestha, P K et al. (2024). "Toward Improved Simulations of Disruptive Reservoirs in Global Hydrological Modelling." In: *Water Resources Research* 60, e2023WR035433. DOI: [10.1029/2023WR035433](https://doi.org/10.1029/2023WR035433).
- Shrestha, Pallav Kumar et al. (Dec. 2017). "Model-Based Estimation of Land Subsidence in Kathmandu Valley, Nepal." In: *Geomatics, Natural Hazards and Risk* 8.2, pp. 974–996. ISSN: 1947-5705. DOI: [10.1080/19475705.2017.1289985](https://doi.org/10.1080/19475705.2017.1289985).
- Shugar, Dan H. et al. (Oct. 2020). "Rapid Worldwide Growth of Glacial Lakes since 1990." In: *Nature Climate Change* 10.10, pp. 939–945. ISSN: 1758-6798. DOI: [10.1038/s41558-020-0855-4](https://doi.org/10.1038/s41558-020-0855-4). (Visited on 09/19/2023).
- Shuttleworth, W. James (1996). "Evaporation." In: *Handbook of Hydrology*. Ed. by David R Maidment. McGraw-Hill, Inc.
- Siebert, S. et al. (Nov. 2005). "Development and Validation of the Global Map of Irrigation Areas." In: *Hydrology and Earth System Sciences* 9.5, pp. 535–547. ISSN: 1607-7938. DOI: [10.5194/hess-9-535-2005](https://doi.org/10.5194/hess-9-535-2005).
- Smith, PJ et al. (2016). "On the operational implementation of the European Flood Awareness System (EFAS)." In: *Flood forecasting*. Elsevier, pp. 313–348.
- Solander, Kurt C. et al. (Mar. 2016). "Simulating Human Water Regulation: The Development of an Optimal Complexity, Climate-Adaptive Reservoir Management Model for an LSM." In: *Journal of Hydrometeorology* 17.3, pp. 725–744. ISSN: 15257541. DOI: [10.1175/JHM-D-15-0056.1](https://doi.org/10.1175/JHM-D-15-0056.1).
- Sommer, Manfred (Apr. 2013). *India - Uttarakhand - Rishikesh - Shiva - 20*. (Visited on 09/26/2024).
- Sood, Aditya and Vladimir Smakhtin (Apr. 2015). "Global Hydrological Models: A Review." In: *Hydrological Sciences Journal* 60.4, pp. 549–565. ISSN: 0262-6667. DOI: [10.1080/02626667.2014.950580](https://doi.org/10.1080/02626667.2014.950580). (Visited on 04/09/2024).
- Speight, Linda J et al. (2021). "Operational and emerging capabilities for surface water flood forecasting." In: *Wiley Interdisciplinary Reviews: Water* 8.3, e1517.
- Stacke, Tobias and Stefan Hagemann (Dec. 2021). "HydroPy (v1.0): A New Global Hydrology Model Written in Python." In: *Geoscientific Model Development* 14.12, pp. 7795–7816. ISSN: 1991-959X. DOI: [10.5194/gmd-14-7795-2021](https://doi.org/10.5194/gmd-14-7795-2021). (Visited on 03/19/2024).
- Steyaert, Jennie C. et al. (Feb. 2022). "ResOpsUS, a Dataset of Historical Reservoir Operations in the Contiguous United States." In: *Scientific Data* 9.1, p. 34. ISSN: 2052-4463. DOI: [10.1038/s41597-022-01134-7](https://doi.org/10.1038/s41597-022-01134-7). (Visited on 12/17/2023).

- Strobl, Carolin et al. (2007). "Bias in Random Forest Variable Importance Measures: Illustrations, Sources and a Solution." In: *BMC Bioinformatics* 8, p. 25. ISSN: 14712105. DOI: [10.1186/1471-2105-8-25](https://doi.org/10.1186/1471-2105-8-25).
- Sutanudjaja, Edwin H. et al. (June 2018). "PCR-GLOBWB 2: A 5 Arcmin Global Hydrological and Water Resources Model." In: *Geoscientific Model Development* 11.6, pp. 2429–2453. ISSN: 19919603. DOI: [10.5194/gmd-11-2429-2018](https://doi.org/10.5194/gmd-11-2429-2018).
- Szönyi, M. et al. (2021). *PERC floods following "Bernd"*. Tech. rep. Zurich Insurance Company.
- Tang, Ting et al. (Feb. 2019). "Bridging Global, Basin and Local-Scale Water Quality Modeling towards Enhancing Water Quality Management Worldwide." In: *Current Opinion in Environmental Sustainability*. Environmental Change Assessment 36, pp. 39–48. ISSN: 1877-3435. DOI: [10.1016/j.cosust.2018.10.004](https://doi.org/10.1016/j.cosust.2018.10.004). (Visited on 05/28/2024).
- Technology Readiness Level (TRL)* (n.d.). https://www.nasa.gov/pdf/458490main_TRL_Definitions.pdf. Accessed on October 20, 2023.
- Tellman, B. et al. (Aug. 2021). "Satellite Imaging Reveals Increased Proportion of Population Exposed to Floods." In: *Nature* 596.7870, pp. 80–86. ISSN: 1476-4687. DOI: [10.1038/s41586-021-03695-w](https://doi.org/10.1038/s41586-021-03695-w). (Visited on 09/06/2024).
- Telteu, Camelia Eliza et al. (June 2021). "Understanding Each Other's Models An Introduction and a Standard Representation of 16 Global Water Models to Support Intercomparison, Improvement, and Communication." In: *Geoscientific Model Development* 14.6, pp. 3843–3878. ISSN: 19919603. DOI: [10.5194/GMD-14-3843-2021](https://doi.org/10.5194/GMD-14-3843-2021).
- Teng, Jin et al. (2017). "Flood inundation modelling: A review of methods, recent advances and uncertainty analysis." In: *Environmental modelling & software* 90, pp. 201–216.
- Terink, W et al. (2015). "SPHY v2 . 0 : Spatial Processes in Hydrology." In: *Geoscientific Model Development*, pp. 2009–2034. DOI: [10.5194/gmd-8-2009-2015](https://doi.org/10.5194/gmd-8-2009-2015).
- "The Carbon Footprint of Computational Research" (Aug. 2023). In: *Nature Computational Science* 3.8, pp. 659–659. ISSN: 2662-8457. DOI: [10.1038/s43588-023-00506-2](https://doi.org/10.1038/s43588-023-00506-2). (Visited on 05/09/2024).
- Thober, Stephan et al. (Jan. 2018). "Multi-Model Ensemble Projections of European River Floods and High Flows at 1.5, 2, and 3 Degrees Global Warming." In: *Environmental Research Letters* 13.1, p. 014003. ISSN: 17489326. DOI: [10.1088/1748-9326/aa9e35](https://doi.org/10.1088/1748-9326/aa9e35). (Visited on 01/18/2022).
- Thober, Stephan et al. (2019). "The Multiscale Routing Model mRM v1 . 0 : Simple River Routing at Resolutions from 1 to 50 Km." In: *Geoscientific Model Development* 12. February, pp. 2501–2521.
- Tolson, Bryan A. and Christine A. Shoemaker (Jan. 2007). "Dynamically Dimensioned Search Algorithm for Computationally Efficient Watershed Model Calibration." In: *Water Resources Research* 43.1. ISSN: 00431397. DOI: [10.1029/2005WR004723](https://doi.org/10.1029/2005WR004723).
- Tounsi, Achraf et al. (June 2022). "On the Use of Machine Learning to Account for Reservoir Management Rules and Predict Streamflow." In: *Neural Computing and Applications*, pp. 1–15. ISSN: 0941-0643. DOI: [10.1007/s00521-022-07500-1](https://doi.org/10.1007/s00521-022-07500-1).

- Tucker, C. J. et al. (2004). *Global Inventory Modeling and Mapping Studies*. College Park, Maryland.
- Turner, Sean W.D. et al. (Dec. 2021). "Water Storage and Release Policies for All Large Reservoirs of Conterminous United States." In: *Journal of Hydrology* 603, p. 126843. ISSN: 0022-1694. DOI: [10.1016/J.JHYDROL.2021.126843](https://doi.org/10.1016/J.JHYDROL.2021.126843).
- Tversky, Amos and Daniel Kahneman (1992). "Advances in prospect theory: Cumulative representation of uncertainty." In: *Journal of Risk and Uncertainty* 5.4, pp. 297–323.
- UNDRR (2015). *Sendai framework for disaster risk reduction 2015–2030*. Tech. rep. United Nations Office for Disaster Risk Reduction. URL: https://www.preventionweb.net/files/43291_sendaiframeworkfordrren.pdf.
- UNSIDR and CRED (2018). *Economic Losses, Poverty & Disasters (1998 - 2017)*. Tech. rep. United Nations International Strategy for Disaster Reduction Secretariat and Centre for Research on the Epidemiology of Disasters. URL: <https://www.cred.be/unisdr-and-cred-report-economic-losses-poverty-disasters-1998-2017>.
- USBR (1997). *Design of Small Dams*. Tech. rep. United States Bureau of Reclamation, pp. 109–129.
- (2011). *Design Standards No. 14: Appurtenant Structures for Dams (Spillway and Outlet Works) Design Standards. Chapter 1 Introduction*. Tech. rep. 14. United States Bureau of Reclamation, p. 55.
- USGS and NGA (2018). *Global Multi-Resolution Terrain Elevation Data 2010 (GMTED 2010)*. Data Set.
- Vanderkelen, Inne et al. (2022). "Evaluating a Reservoir Parametrization in the Vector-Based Global Routing Model mizuRoute (v2.0.1) for Earth System Model Coupling." In: *Geosci. Model Dev* 15, pp. 4163–4192. DOI: [10.5194/gmd-15-4163-2022](https://doi.org/10.5194/gmd-15-4163-2022).
- Vergopolan, Noemi et al. (June 2020). "Combining Hyper-Resolution Land Surface Modeling with SMAP Brightness Temperatures to Obtain 30-m Soil Moisture Estimates." In: *Remote Sensing of Environment* 242, p. 111740. ISSN: 0034-4257. DOI: [10.1016/J.RSE.2020.111740](https://doi.org/10.1016/J.RSE.2020.111740).
- Voisin, N. et al. (Sept. 2013a). "On an Improved Sub-Regional Water Resources Management Representation for Integration into Earth System Models." In: *Hydrology and Earth System Sciences* 17.9, pp. 3605–3622. ISSN: 1607-7938. DOI: [10.5194/hess-17-3605-2013](https://doi.org/10.5194/hess-17-3605-2013).
- Voisin, N. et al. (Nov. 2013b). "One-Way Coupling of an Integrated Assessment Model and a Water Resources Model: Evaluation and Implications of Future Changes over the US Midwest." In: *Hydrology and Earth System Sciences* 17.11, pp. 4555–4575. ISSN: 1607-7938. DOI: [10.5194/hess-17-4555-2013](https://doi.org/10.5194/hess-17-4555-2013).
- Vorogushyn, Sergiy et al. (2022). "Analyse der Hochwassergefährdung im Ahrtal unter Berücksichtigung historischer Hochwasser." In: *Hydrologie und Wasserbewirtschaftung* 66.5, pp. 244–254.
- Vörösmarty, Charles J et al. (1997). "The Storage and Aging of Continental Runoff in Large Reservoir Systems of the World." In: *Ambio (Sweden)*.

- Vörösmarty, Charles J. et al. (July 2000). "Global Water Resources: Vulnerability from Climate Change and Population Growth." In: *Science* 289. DOI: [10.1126/science.289.5477.284](https://doi.org/10.1126/science.289.5477.284). (Visited on 09/04/2024).
- Vörösmarty, Charles J. et al. (Oct. 2003). "Anthropogenic Sediment Retention: Major Global Impact from Registered River Impoundments." In: *Global and Planetary Change* 39.1-2, pp. 169–190. ISSN: 09218181. DOI: [10.1016/S0921-8181\(03\)00023-7](https://doi.org/10.1016/S0921-8181(03)00023-7).
- WMO (n.d.). *World's Deadliest Tropical Cyclone Was 50 Years Ago* | World Meteorological Organization. (Visited on 09/03/2024).
- (2023a). *State of Global Water Resources Report 2022*. (Visited on 04/03/2024).
 - (2023b). *Vision and Strategy for Hydrology and Associated Plan of Action and WMO Hydrological Research Strategy*. Tech. rep. 1319. Geneva: World Meteorological Organization. (Visited on 09/27/2024).
 - (Feb. 2023c). *WMO and the Early Warnings for All Initiative*. URL: <https://wmo.int/activities/early-warnings-all/wmo-and-early-warnings-all-initiative> (visited on 09/27/2024).
- Wada, Y et al. (2011). "Modelling Global Water Stress of the Recent Past: On the Relative Importance of Trends in Water Demand and Climate Variability." In: *Hydrol. Earth Syst. Sci* 15, pp. 3785–3808. DOI: [10.5194/hess-15-3785-2011](https://doi.org/10.5194/hess-15-3785-2011).
- Wada, Y. et al. (Jan. 2014). "Global Modeling of Withdrawal, Allocation and Consumptive Use of Surface Water and Groundwater Resources." In: *Earth System Dynamics* 5.1, pp. 15–40. ISSN: 2190-4987. DOI: [10.5194/esd-5-15-2014](https://doi.org/10.5194/esd-5-15-2014).
- Wada, Yoshihide et al. (2010). "Global Depletion of Groundwater Resources." In: *Geophysical Research Letters* 37.20. ISSN: 1944-8007. DOI: [10.1029/2010GL044571](https://doi.org/10.1029/2010GL044571). (Visited on 04/09/2024).
- Wada, Yoshihide et al. (2013). "Multimodel Projections and Uncertainties of Irrigation Water Demand under Climate Change." In: *Geophysical Research Letters* 40.17, pp. 4626–4632. ISSN: 1944-8007. DOI: [10.1002/grl.50686](https://doi.org/10.1002/grl.50686). (Visited on 04/09/2024).
- Wada, Yoshihide et al. (June 2016). "High-Resolution Modeling of Human and Climate Impacts on Global Water Resources." In: *Journal of Advances in Modeling Earth Systems* 8.2, pp. 735–763. ISSN: 19422466. DOI: [10.1002/2015MS000618](https://doi.org/10.1002/2015MS000618).
- Wanders, Niko et al. (Apr. 2019). "High-Resolution Global Water Temperature Modeling." In: *Water Resources Research* 55.4, pp. 2760–2778. ISSN: 1944-7973. DOI: [10.1029/2018WR023250](https://doi.org/10.1029/2018WR023250).
- Wang, Ji et al. (Jan. 2022). "A New Coherence Detection Method for Mapping Inland Water Bodies Using CYGNSS Data." In: *Remote Sensing* 14.13, p. 3195. ISSN: 2072-4292. DOI: [10.3390/rs14133195](https://doi.org/10.3390/rs14133195). (Visited on 12/15/2023).
- Wang, Menghua et al. (2000). "Dem Aggregation for Watershed Modeling." In: *JAWRA Journal of the American Water Resources Association* 36.3, pp. 579–584. ISSN: 1752-1688. DOI: [10.1111/j.1752-1688.2000.tb04288.x](https://doi.org/10.1111/j.1752-1688.2000.tb04288.x). (Visited on 04/01/2024).
- Warmedinger, Leena et al. (July 2023). "The New Hydrographic Hydrosheds Database Derived from the Tandem-X Dem." In: *IGARSS 2023 - 2023 IEEE International Geoscience*

- and Remote Sensing Symposium*, pp. 1485–1488. DOI: [10.1109/IGARSS52108.2023.10282244](https://doi.org/10.1109/IGARSS52108.2023.10282244). (Visited on 06/28/2024).
- Wen, Zhiqun et al. (2012). “A New Multiscale Routing Framework and Its Evaluation for Land Surface Modeling Applications.” In: *Water Resources Research* 48.8. ISSN: 1944-7973. DOI: [10.1029/2011WR011337](https://doi.org/10.1029/2011WR011337). (Visited on 04/02/2024).
- Weyrich, Philippe et al. (2018). “Effects of impact-based warnings and behavioral recommendations for extreme weather events.” In: *Weather, climate, and society* 10.4, pp. 781–796.
- White, Michael A. et al. (June 2005). “Application of Wavelet Analysis for Monitoring the Hydrologic Effects of Dam Operation: Glen Canyon Dam and the Colorado River at Lees Ferry, Arizona.” In: *River Research and Applications* 21.5, pp. 551–565. ISSN: 1535-1467. DOI: [10.1002/RRA.827](https://doi.org/10.1002/RRA.827).
- Wing, Oliver E. J. et al. (2024). “A 30 m Global Flood Inundation Model for Any Climate Scenario.” In: *Water Resources Research* 60.8, e2023WR036460. ISSN: 1944-7973. DOI: [10.1029/2023WR036460](https://doi.org/10.1029/2023WR036460). (Visited on 09/16/2024).
- Winterrath, Tanja et al. (2012). “On the DWD quantitative precipitation analysis and nowcasting system for real-time application in German flood risk management.” In: *IAHS-AISH publication* 351, pp. 323–329.
- Wisser, D. et al. (Jan. 2010). “Reconstructing 20th Century Global Hydrography: A Contribution to the Global Terrestrial Network- Hydrology (GTN-h).” In: *Hydrology and Earth System Sciences* 14.1, pp. 1–24. ISSN: 1607-7938. DOI: [10.5194/hess-14-1-2010](https://doi.org/10.5194/hess-14-1-2010).
- Wood, Eric F. et al. (May 2011a). “Hyperresolution Global Land Surface Modeling: Meeting a Grand Challenge for Monitoring Earth’s Terrestrial Water.” In: *Water Resources Research* 47.5. ISSN: 1944-7973. DOI: [10.1029/2010WR010090](https://doi.org/10.1029/2010WR010090).
- Wood, Eric F. et al. (2011b). “Hyperresolution global land surface modeling: Meeting a grand challenge for monitoring Earth’s terrestrial water.” In: *Water Resources Research* 47.5.
- World Bank Group (Aug. 2017). *Sierra Leone Rapid Damage and Loss Assessment of August 14th, 2017 Landslides and Floods in the Western Area*. World Bank, Washington, DC. DOI: [10.1596/28836](https://doi.org/10.1596/28836). (Visited on 09/09/2024).
- Wu, Huan et al. (2011). “Automated Upscaling of River Networks for Macroscale Hydrological Modeling.” In: *Water Resources Research* 47.3. ISSN: 1944-7973. DOI: [10.1029/2009WR008871](https://doi.org/10.1029/2009WR008871). (Visited on 03/27/2024).
- Wu, Wenyan et al. (2020). “Ensemble flood forecasting: Current status and future opportunities.” In: *Wiley Interdisciplinary Reviews: Water* 7.3, e1432.
- Yamazaki, D. et al. (Nov. 2009). “Deriving a Global River Network Map and Its Sub-Grid Topographic Characteristics from a Fine-Resolution Flow Direction Map.” In: *Hydrology and Earth System Sciences* 13.11, pp. 2241–2251. ISSN: 1027-5606. DOI: [10.5194/hess-13-2241-2009](https://doi.org/10.5194/hess-13-2241-2009). (Visited on 08/11/2023).

- Yamazaki, Dai et al. (2008). "An Improved Upscaling Method to Construct a Global River Map." In: *Proceedings of the 4th Asia-Pacific Hydrology and Water Resources (APHW) Conference*. Beijing.
- Yamazaki, Dai et al. (2011). "A Physically Based Description of Floodplain Inundation Dynamics in a Global River Routing Model." In: *Water Resources Research* 47.4. ISSN: 1944-7973. DOI: [10.1029/2010WR009726](https://doi.org/10.1029/2010WR009726). (Visited on 04/09/2024).
- Yamazaki, Dai et al. (2013). "Improving Computational Efficiency in Global River Models by Implementing the Local Inertial Flow Equation and a Vector-Based River Network Map." In: *Water Resources Research* 49.11, pp. 7221–7235. ISSN: 1944-7973. DOI: [10.1002/wrcr.20552](https://doi.org/10.1002/wrcr.20552). (Visited on 08/11/2023).
- Yamazaki, Dai et al. (2019). "MERIT Hydro: A High-Resolution Global Hydrography Map Based on Latest Topography Dataset." In: *Water Resources Research* 55.6, pp. 5053–5073. ISSN: 1944-7973. DOI: [10.1029/2019WR024873](https://doi.org/10.1029/2019WR024873). (Visited on 08/11/2023).
- Yassin, Fuad et al. (Sept. 2019). "Representation and Improved Parameterization of Reservoir Operation in Hydrological and Land-Surface Models." In: *Hydrology and Earth System Sciences* 23.9, pp. 3735–3764. ISSN: 16077938. DOI: [10.5194/HESS-23-3735-2019](https://doi.org/10.5194/HESS-23-3735-2019).
- Yigzaw, Wondmagegn et al. (2018). "TECHNICAL REPORTS : DATA a New Global Storage-Area-Depth Data Set for Modeling Reservoirs in Land Surface and Earth System Models." In: *Water Resources Research* 1959, pp. 372–386. DOI: [10.1029/2017WR022040](https://doi.org/10.1029/2017WR022040).
- Yumul, Graciano P. et al. (June 2013). "Abnormal Weather Events in 2009, Increased Precipitation and Disastrous Impacts in the Philippines." In: *Climatic Change* 118.3, pp. 715–727. ISSN: 1573-1480. DOI: [10.1007/s10584-012-0661-8](https://doi.org/10.1007/s10584-012-0661-8). (Visited on 09/09/2024).
- Zajac, Zuzanna et al. (May 2017). "The Impact of Lake and Reservoir Parameterization on Global Streamflow Simulation." In: *Journal of Hydrology* 548, pp. 552–568. ISSN: 00221694. DOI: [10.1016/j.jhydrol.2017.03.022](https://doi.org/10.1016/j.jhydrol.2017.03.022).
- Zhao, Fang et al. (June 2017). "The Critical Role of the Routing Scheme in Simulating Peak River Discharge in Global Hydrological Models." In: *Environmental Research Letters* 12.7, p. 075003. ISSN: 1748-9326. DOI: [10.1088/1748-9326/aa7250](https://doi.org/10.1088/1748-9326/aa7250). (Visited on 03/19/2024).
- Zhao, Gang and Huilin Gao (June 2019). "Estimating Reservoir Evaporation Losses for the United States: Fusing Remote Sensing and Modeling Approaches." In: *Remote Sensing of Environment* 226, pp. 109–124. ISSN: 00344257. DOI: [10.1016/j.rse.2019.03.015](https://doi.org/10.1016/j.rse.2019.03.015).
- Zhao, Gang et al. (2016). "Integrating a Reservoir Regulation Scheme into a Spatially Distributed Hydrological Model." In: *Advances in Water Resources* 98, pp. 16–31. ISSN: 03091708. DOI: [10.1016/j.advwatres.2016.10.014](https://doi.org/10.1016/j.advwatres.2016.10.014).
- Zhongming, Zhu et al. (2020). *WMO Updates Guidelines on Multi-Hazard Impact-Based Forecast and Warning Services*. Tech. rep. WMO.
- Zhou, Tian et al. (Jan. 2016). "The Contribution of Reservoirs to Global Land Surface Water Storage Variations." In: *Journal of Hydrometeorology* 17.1, pp. 309–325. ISSN: 15257541. DOI: [10.1175/JHM-D-15-0002.1](https://doi.org/10.1175/JHM-D-15-0002.1).

- Zink, Matthias et al. (July 2016). "The German Drought Monitor." In: *Environmental Research Letters* 11.7, p. 074002. ISSN: 1748-9326. DOI: [10.1088/1748-9326/11/7/074002](https://doi.org/10.1088/1748-9326/11/7/074002).
- Zink, Matthias et al. (2017). "A high-resolution dataset of water fluxes and states for Germany accounting for parametric uncertainty." In: *Hydrology and Earth System Sciences* 21.3, pp. 1769–1790. DOI: [10.5194/hess-21-1769-2017](https://doi.org/10.5194/hess-21-1769-2017).
- van Beek, L. P. H. et al. (July 2011). "Global Monthly Water Stress: 1. Water Balance and Water Availability." In: *Water Resources Research* 47.7. ISSN: 00431397. DOI: [10.1029/2010WR009791](https://doi.org/10.1029/2010WR009791).
- van Vliet, Michelle T. H. et al. (Oct. 2023). "Global River Water Quality under Climate Change and Hydroclimatic Extremes." In: *Nature Reviews Earth & Environment* 4.10, pp. 687–702. ISSN: 2662-138X. DOI: [10.1038/s43017-023-00472-3](https://doi.org/10.1038/s43017-023-00472-3). (Visited on 05/28/2024).

Helmholtz Centre for
Environmental Research – UFZ
Permoserstraße 15
04318 Leipzig | Germany
www.ufz.de